Université de Montréal

# Caractérisation de matériaux moléculaires amorphes pour optimiser leur préparation et leurs applications

par
Audrey Laventure

Département de chimie
Faculté des arts et des sciences

Thèse présentée à la Faculté des études supérieures et postdoctorales
en vue de l'obtention du grade de Philosophiae Doctor (Ph.D.)
en chimie

Mars 2017

# Résumé

Les matériaux moléculaires amorphes, aussi appelés verres moléculaires, sont constitués de molécules organiques de petite taille capables de s'organiser de façon désordonnée. En plus de présenter certaines des propriétés analogues à celles des polymères, ils offrent des avantages supplémentaires, puisqu'ils sont des espèces isomoléculaires dont la synthèse, la purification et la mise en œuvre sont facilitées par leur viscosité relativement faible. Toutefois, la préparation souvent exigeante de ces matériaux et leur durée de vie utile limitée par leur tendance à relaxer vers l'état cristallin demeurent des obstacles à leur utilisation pour certaines applications, e.g. opto-électronique, nanolithographie, pharmaceutique. Le développement de stratégies visant à faciliter la préparation de la phase vitreuse et éviter sa cristallisation est donc essentiel à la conception de matériaux moléculaires amorphes fonctionnels.

L'objectif principal de cette thèse est d'établir des relations entre la structure moléculaire des verres moléculaires et leurs propriétés. Pour y arriver, différentes librairies de composés modèles, des dérivés analogues de triazine ayant démontré une excellente capacité à former une phase vitreuse, sont utilisées pour i) déterminer l'influence de la nature et de la position des groupements sur la triazine; ii) explorer l'influence des liaisons hydrogène sur les propriétés des verres lorsque leur structure comporte des groupements fonctionnels reconnus pour faciliter la cristallisation et lorsque leurs conditions de préparation se rapprochent de celles employées en industrie et iii) exploiter la phase amorphe afin d'étudier la photosensibilité des azobenzènes (azo) en vue d'optimiser leur utilisation dans des applications.

Tout d'abord, l'influence des différents groupes substituants sur la triazine (groupements de tête, auxiliaires et liants) sur la capacité des composés à former une phase vitreuse (GFA), sur sa stabilité cinétique (GS) et sur sa température de transition vitreuse ($T_g$) est étudiée. Un système de classification des composés développé à partir de mesures de calorimétrie différentielle à balayage (DSC) et des mesures de spectroscopie infrarouge (IR) à température variable combinées à des analyses chimiométriques facilitent la rationalisation des rôles joués par chaque groupe. L'impact des liaisons hydrogène (H), de la barrière énergétique de rotation et de l'encombrement stérique des groupements est ainsi déterminé, permettant de conclure que

le groupe de tête est le plus influent et que la présence de liaisons H n'est pas essentielle au GFA mais qu'elle est importante pour obtenir une $T_g$ élevée.

Ensuite, l'influence des liaisons H sur les propriétés des verres se rapprochant de ceux exploités dans l'industrie est explorée. Des mesures de spectroscopie IR à température variable, de DSC et de résolution de structures cristallines ont permis de conclure que les liaisons H réussissent à nuire à la cristallisation des composés et ce, même s'ils sont simultanément fonctionnalisés avec des motifs qui favorisent la cristallisation (empilements π-π entre dérivés stilbènes fluorés et non fluorés). De plus, trois composés analogues fonctionnalisés avec un groupement de tête possédant une capacité décroissante à établir des liaisons H (donneur, accepteur, aucune) ont été déposés en phase vapeur (PVD), une technique employée entre autres dans l'industrie opto-électronique pour évaluer leur capacité à former des verres ultrastables. Les films ainsi préparés présentent tous des propriétés similaires à celles des verres ultrastables précédemment étudiés, telles qu'une plus grande densité et anisotropie, et sont tous plus stables que ceux préparés par refroidissement à partir de l'état liquide. Toutefois, le verre formé du composé avec un groupement de tête donneur de liaisons H est moins stable que les autres d'au moins un ordre de grandeur, suggérant que les liaisons H limitent le niveau de stabilité atteignable par PVD.

Finalement, un verre à base de triazine fonctionnalisé avec un groupement azo est employé pour étudier d'un point de vue moléculaire les perturbations provoquées par la photoisomérisation de l'azo. Grâce à une nouvelle méthode de spectroscopie IR, il est possible d'observer un gradient d'environnement moléculaire le long de la molécule lors de la photoisomérisation, permettant de soutenir certaines hypothèses relatives au déplacement macroscopique de la matière qui en résulte. Les mélanges de verres à base de triazine servent aussi de plateforme idéale pour découpler l'influence de la $T_g$ et du contenu en azo sur la photo-orientation de l'azo, mais aussi sur la cinétique d'écriture et l'efficacité des réseaux de diffraction (SRG). Ce travail permet ainsi de déterminer une zone optimale de $T_g$ pour l'inscription de SRG. Ces nouvelles connaissances mèneront à la conception plus rationnelle de nouveaux verres moléculaires, pouvant s'étendre à d'autres matériaux amorphes.

**Mots-clés**: verre moléculaire; transition vitreuse; capacité à former un verre; cristallisation; liaison hydrogène; spectroscopie infrarouge; chimiométrie; dépôt physique en phase vapeur; azobenzène.

# Abstract

Amorphous molecular materials, also known as molecular glasses, are small organic molecules capable of being organized in a disordered manner. In addition to sharing some of the useful properties of polymers, they offer additional advantages because they are isomolecular species for which synthesis, purification and processing are facilitated by a relatively low viscosity. However, the usually demanding preparation conditions of these materials and their limited functional lifetime due to their tendency to relax to the crystalline state remain obstacles to their use for certain applications, e.g. opto-electronics, nanolithography, pharmaceuticals. The development of strategies to facilitate the preparation of the vitreous phase and avoid its crystallization is therefore essential for the design of functional amorphous molecular materials.

The main objective of this thesis is to establish relationships between the molecular structure of molecular glasses and their properties. To achieve it, various libraries of model compounds, analogues of triazine derivatives that have demonstrated excellent glass-forming ability, are used to (i) determine the influence of the nature and the position of the groups on the triazine; (ii) explore the influence of hydrogen (H) bonds on the properties of glasses when their structure includes functional groups known to facilitate crystallization and when their preparation conditions are similar to those used in industry; and (iii) exploit the amorphous phase in order to study the photoresponsiveness of azobenzenes (azo) in order to optimize their use in different applications.

The influence of the various substituent groups on the triazine (headgroup, ancillary and linkers) on the glass-forming ability (GFA), the kinetic glass stability (GS) and the glass transition temperature ($T_g$) of the compounds is first studied. A classification system based on differential scanning calorimetry (DSC) and variable temperature infrared spectroscopy (IR) measurements combined to chemometrics analyses facilitate the rationalization of the roles played by each group. The impact of the H-bonds, the energy of the rotation barrier, and the steric hindrance of the groups is determined, leading to the conclusion that the headgroup is the most influential group and that the presence of H-bonds is not essential to the GFA, but important to obtain a high $T_g$.

The influence of the H-bonds on the properties of glasses approaching those exploited in industry is then explored. Variable temperature IR spectroscopy measurements, DSC studies, and single crystal structure resolution have led to the conclusion that H-bonds impede the crystallization of the compounds even though they are simultaneously functionalized with moieties that promote crystallization (π-π stacking between fluorinated and non-fluorinated stilbene groups). In addition, three similar compounds functionalized with a headgroup presenting a decreasing capability to establish H-bonds (donor, acceptor, none) were vapor-deposited (PVD), a technique used, among others, in the opto-electronic industry, to evaluate their capability to form ultrastable glasses. These PVD glasses all show properties that are similar to those previously reported for ultrastable glasses, including higher density and anisotropy, and are all more kinetically stable than glasses prepared by cooling from the viscous state. However, the PVD glasses prepared with a H-bond donor headgroup are less stable than the others by at least an order of magnitude, suggesting that H-bonds limit the level of kinetic stability achievable by PVD.

Finally, a triazine molecular glass functionalized with an azo group is used to study, from a molecular point of view, the perturbations caused by the photoisomerization of the azo. A new IR spectroscopy method was developed to observe a molecular environment gradient along the molecule during photoisomerization, making it possible to support certain hypotheses concerning the resulting macroscopic transport of the material. Triazine-based molecular glass blends are also used as an ideal platform for decoupling the influence of $T_g$ and azo content on the azo photo-orientation, but also on the inscription kinetics and the diffraction efficiency of surface relief gratings (SRGs). This work enables the determination of an optimal $T_g$ range for the inscription of SRGs. Altogether, these new insights will lead to a more rational design of new molecular glasses, which can extend to other amorphous molecular materials.

**Keywords**: molecular glass; glass transition; glass-forming ability; crystallization; hydrogen bonding; infrared spectroscopy; chemometrics; physical vapor deposition; azobenzene.

# Table des matières

# Liste des tableaux

# Liste des schémas

# Liste des figures

# Liste des symboles et abréviations

| | |
|---|---|
| $A$ | Absorbance |
| $A_0$ | Absorbance structurale |
| $A_p$ | Absorbance parallèle à la direction de référence |
| $A_s$ | Absorbance perpendiculaire à la direction de référence |
| ATR | Réflexion totale atténuée (*Attenuated Total Reflection*) |
| Azo | Azobenzène |
| $D$ | Coefficient de diffusion |
| $D_s$ | Diffusion de surface |
| DE | Efficacité de diffraction (*Diffraction efficiency*) |
| DMF | Diméthylformamide |
| DR1 | *Disperse Red 1* |
| DSC | Calorimétrie différentielle à balayage (*Differential Scanning Calorimetry*) |
| DTGS | Sulfate de triglycine deutérée (*Deuterated Triglycine Sulfate*) |
| $F_5$-stilbene | 2,3,4,5,6-pentafluorostilbène |
| FT-IR | Spectroscopie infrarouge à transformée de Fourier (*Fourier Transform Infrared Spectroscopy*) |
| gDR1 | Verre moléculaire à base de triazine fonctionnalisé avec l'azo DR1 |
| GFA | Capacité à former une phase vitreuse (*Glass-Forming Ability)* |
| GS | Stabilité cinétique de la phase vitreuse (*Glass Stability)* |
| $H$ | Enthalpie |
| H | Hydrogène |
| IMC | Indométacine |
| IR | Infrarouge |
| LED | Diode électroluminescente (*Light-emitting diode*) |
| $m$ | Fragilité |
| MCR | Résolution multivariée de courbe (*Multivariate Curve Resolution*) |
| MCT | Tellurure de mercure-cadmium (*Mercury-Cadmium Telluride*) |
| NMR | Résonance magnétique nucléaire (*Nuclear Magnetic Resonance*) |
| NR | *Nile Red* |

| | |
|---|---|
| OTP | *ortho*-terphényle |
| P4VP | Poly(4-vinylpyridine) |
| PCA | Analyse en composantes principales (*Principal Components Analysis*) |
| PDI | Pérylène diimide |
| pDR1A | *Poly(Disperse Red 1 acrylate)* |
| PET | Poly(éthylène téréphtalate) |
| PM-IRSAS | Spectroscopie infrarouge d'absorbance structurale par modulation de la polarisation (*Polarization Modulation Infrared Structural Absorbance Spectroscopy*) |
| PMMA | Poly(méthacrylate de méthyle) |
| PS | Polystyrène |
| PVD | Dépôt physique en phase vapeur (*Physical Vapor Deposition*) |
| $R_c$ | Vitesse critique de refroidissement |
| RMN | Résonance magnétique nucléaire |
| $S_z$ | Paramètre d'ordre |
| SMMA | Self-Modeling Mixture Analysis |
| SRG | Réseau de diffraction (*Surface Relief Grating*) |
| $T$ | Température |
| $T_c$ | Température de cristallisation |
| $T_{eff}$ | Température effective |
| $T_f$ | Température de fusion |
| $T_g$ | Température de transition vitreuse |
| $T_m$ | Température de fusion |
| $T_{onset}$ | Température du début de la transformation d'un verre |
| $T_{ramping}$ | Température lors d'un balayage en température |
| $T_{substrate}$ | Température du substrat |
| TNB | Trisnaphtylbenzène |
| TTT | Transformation temps-température |
| $V_{sp}$ | Volume spécifique |
| WAXS | Diffusion des rayons X aux grands angles (*Wide Angle X-ray Scattering*) |
| $\Delta A$ | Différence dichroïque |

| | |
|---|---|
| $\Delta\rho$ | Densité relative |
| $\tau_\alpha$ | Temps de relaxation alpha |
| $\lvert\Delta H\rvert_{tot}$ | Valeur absolue de l'enthalpie de formation de liaisons H |
| $<P_2>$ | Paramètre d'orientation |
| $<P_2>_{max}$ | Paramètre maximal d'orientation |
| $<P_2>_{res}$ | Paramètre résiduel d'orientation |

*Entre l'ordre et le désordre règne un moment délicieux.*
Paul Valéry

# Remerciements

Je me considère particulièrement privilégiée d'avoir complété mon parcours académique à l'Université de Montréal. Ces années m'auront permis de découvrir les rouages du monde de la recherche scientifique, de développer mon sens critique, d'entretenir mon désir d'apprendre, et surtout, de faire des rencontres qui ont guidé mon développement dans son ensemble.

D'un point de vue professionnel, je commencerai par remercier mon directeur de thèse, Christian Pellerin, qui m'a permis d'effectuer des stages de recherche en tant qu'étudiante au baccalauréat, de l'été 2011 jusqu'en mai 2013, puis de poursuivre au doctorat dans son laboratoire. Je lui suis reconnaissante pour la liberté qu'il m'a accordée à plusieurs niveaux, me permettant d'explorer différentes expériences scientifiques en plus d'expériences professionnelles, que ce soit pour aller présenter des conférences de vulgarisation par l'entremise du projet SEUR, pour agir en tant qu'auxiliaire d'enseignement dans différents cours ou même pour prendre part au programme de transfert technologique Technopreneur du Centre d'entrepreneuriat Poly-UdeM. Je le remercie également de m'avoir permis d'effectuer un stage de recherche à l'automne 2015 à la *University of Wisconsin – Madison*, et aussi de m'avoir donné la chance de présenter mes travaux à de nombreux congrès nationaux et internationaux, tout en ayant contribué à l'amélioration continue de mes habiletés à présenter oralement. Depuis la première rencontre d'embauche en décembre 2010, il aura su repousser les limites de mon souci du détail et aiguiser mon sens de la répartie!

Je tiens aussi à remercier Olivier Lebel (Collège militaire royal du Canada) pour sa productivité et son enthousiasme contagieux, qui auront été tout au long de mon parcours une excellente source de motivation. Je remercie également Armand Soldera (Université de Sherbrooke), qui a su se montrer disponible malgré un horaire chargé, donnant lieu à des échanges stimulants. Ils ont tous deux été de précieux collaborateurs dans le projet des verres moléculaires.

Je souligne également la contribution des co-auteurs des six articles scientifiques qui sont présentés dans cette thèse. La mise en commun de nos expertises et ressources respectives ont permis de compléter des travaux dont nous pouvons être fiers.

Je dois mes connaissances et compétences de base en laboratoire à Frédéric Byette, qui m'a recrutée en CHM1501 pour mon premier stage. Le temps d'un été, j'ai été un *padawan*, pour le paraphraser, qui apprenait à nettoyer du byssus de moules et à le transformer en films ou en fibres! Plus sérieusement, cette expérience a été très formatrice et m'a définitivement aiguillée pour la suite de mon parcours. Comme ce stage était effectué à temps partiel à l'UQAM, j'aimerais remercier Isabelle Marcotte, Alexandre Arnold, ainsi que les membres du groupe de m'avoir accueillie à bras ouverts. Nos discussions ont toujours été enrichissantes, j'en garde un bon souvenir.

*I would like to express my deepest gratitude to Dr. Mark D. Ediger and his research group. I feel privileged to have been able to work during four months with such a professional scientist. I greatly appreciated his availability, his high standards and his genuine interest in science, which I found truly inspirational. The lab members, Maddy Beasley, Jaritza Gomez, Ankit Gujral, Kelly Hebert, Travis Powell, Yue Qiu, Josh Ricci, Kelly Suralik, Micheal Tylinski and Diane Walters are amazing! They made me feel like a full member of the lab, in which the work atmosphere they create and maintain is excellent. I will keep good memories of this internship in Wisconsin, including all the laughter, the hard work and the group activities.*

Ce stage aux États-Unis m'a permis de constater à quel point la formation reçue durant mon parcours est solide. C'est tout à l'honneur des professeurs de chimie du département, et je tiens à le souligner. Un merci tout spécial est adressé à mes enseignants du secondaire et du cégep en chimie (Chantale Girard, Martin Desrochers, Daniel Gareau et Carl Ouellet) sans qui je n'aurais probablement jamais envisagé la chimie comme parcours universitaire!

Je voudrais remercier Sylvain Essiembre pour sa constante disponibilité concernant les divers appareils de caractérisation utilisés, mais aussi pour les discussions à dimension plus humaine. Je voudrais également saluer l'équipe de l'atelier mécanique, notamment Jean-François Myre pour son efficacité dans le design de certains accessoires infrarouge et l'expertise d'Yves Teasdale en électronique, sans qui je n'aurais jamais pu compléter toutes ces mesures de DSC!

J'ai également eu la chance de travailler avec trois étudiants stagiaires motivés, efficaces et surtout, capables de suivre un rythme de travail assez effréné! Je remercie Dominic Lauzon

(été 2014), Jérémie Bourotte (hiver 2015) et Sébastien Néron (été 2015). Le travail qu'ils ont accompli dans le temps qui leur était alloué m'a impressionnée et je leur souhaite le meilleur dans leurs futurs projets: vous êtres sur la bonne voie, ne lâchez pas, peu importe ce que vous entreprendrez!

Mes expériences d'auxiliaire d'enseignement ont toutes été très stimulantes. D'emblée, je voudrais en profiter pour remercier tous les étudiants à qui j'ai enseigné ou que j'ai suivis en tutorat – ils réussissaient à me faire voir la matière sous un autre angle grâce à leurs questions et leurs interventions toujours pertinentes. Tout d'abord, j'aimerais remercier Anne-Marie Faucher, avec qui j'ai fait mes premières armes en tant que répétitrice. Par la suite, je veux exprimer ma gratitude à Karen Waldron pour avoir pensé à m'offrir un poste de « super démonstrateur ». Je remercie aussi les professeurs Géraldine Bazuin et Julian Zhu pour toute la confiance et la latitude qu'ils m'ont accordées pour les répétitions du cours CHM2410, avec qui ce fut un réel plaisir de travailler. Je leur suis également reconnaissante d'avoir pris l'initiative de soumettre ma candidature au prix d'auxiliaire d'enseignement André-Beauchamp – cela m'a fait particulièrement chaud au cœur de le recevoir. Finalement, j'aimerais remercier André Beauchamp, de qui j'ai beaucoup appris, notamment depuis l'automne 2015 en tant que réviseure scientifique pour le cours en ligne CHM1963. Sa philosophie et ses méthodes pédagogiques efficaces et rigoureuses sont des éléments qui continueront de guider ma vision de l'enseignement. J'ai également eu la chance de co-animer à trois reprises le séJOUR découvertes en chimie avec Julien Gravel, Denis Deschênes et Pierre Chaurand, avec lesquels la bonne humeur était toujours au rendez-vous, et ce, même un 3 janvier à 8h30! J'ai également une pensée pour Nicolas Bélanger-Desmarais et Julien Poupart avec qui j'ai participé à l'hiver 2015 au tutorat offert par le département.

Je suis infiniment reconnaissante pour l'ensemble du financement qui m'a été accordé tout au long de mon parcours par l'entremise des divers organismes suivants: le Conseil de recherches en sciences naturelles et en génie du Canada, l'Association des Universités et Collèges du Canada, le *Senior Women Academic Administrators of Canada*, la Société canadienne de chimie, l'Ordre des chimistes du Québec et l'Université de Montréal. J'adresse de sincères remerciements à Richard Giasson, Michel Lafleur, Robert E. Prud'homme et Christian Reber, qui m'ont permis de croire en ma candidature, du baccalauréat au doctorat, et

également à tous ceux qui, à un moment ou à un autre, ont accepté d'écrire une lettre de recommandation!

Je remercie également les membres du jury, Géraldine Bazuin, Michel Lafleur et Yue Zhao (Université de Sherbrooke) d'avoir accepté d'évaluer cette thèse. Leurs commentaires constructifs qui ont contribué à l'amélioration de ce travail ont été grandement appréciés.

D'un point de vue personnel, j'enchaînerai avec les remerciements destinés à mes collègues de bureau dont le support a permis d'alléger l'atmosphère de travail: merci à Alice, Catherine, Damien, Giovanni, Patricia, Xiaoxiao, Yann et Zeinab. Mes remerciements s'adressent également aux membres des groupes Badia, Bazuin, Lafleur, Martel, Prud'homme, Reber, Skene, Winnik, Wuest et Zhu, avec qui les discussions au détour d'un corridor du PJAB ont toujours été très agréables et divertissantes au fil des années. Depuis le baccalauréat, Catherine et Rémi sont de précieux amis, avec qui j'ai passé à travers les diverses étapes de ce parcours, mais aussi, à travers celles de la vie – je dois une grande partie de mon bien-être à tous les éclats de rire que nous partageons, je vous en remercie!

Mes plus sincères remerciements vont à ma famille. Le soutien constant de mes parents m'a permis de me consacrer entièrement à cette thèse, et je suis convaincue que leur intérêt pour tout ce que ma sœur et moi entreprenons est l'une des clés de nos accomplissements. Merci à Martine, ma sœur, pour m'avoir encouragée en partageant tant d'efforts (et de trajets!) depuis l'école primaire! Merci aussi à mes beaux-parents pour leur support plus récent, mais tout aussi apprécié. Je remercie finalement Nicolas, qui a réussi à me rappeler l'importance de vivre une vie équilibrée, et surtout, de l'apprécier pleinement. Son positivisme, sa résilience et sa présence à mes côtés (malgré la distance!) m'inspirent à donner le meilleur de moi-même jour après jour et à avoir confiance en la vie. C'est grâce à toi si j'ai notamment appris à écouter un peu plus mon cœur et un peu moins ma tête… merci pour tout ce bonheur ×××××!

Je terminerai en témoignant ma gratitude à tous ceux et celles qui ont cru en moi, me donnant ainsi le courage nécessaire pour tenter de relever de nouveaux défis.

# Chapitre 1: Introduction

## 1.1 L'état amorphe

Station Université de Montréal, lundi matin, 8 h 25. En pleine heure de pointe, circuler à la sortie du métro pour se rendre sur le campus constitue un défi de taille. Si l'on profite de ce moment pour réfléchir à la situation au lieu de s'impatienter (ce qui est aussi un défi supplémentaire!) il est possible de réaliser que la foule dans laquelle nous nous retrouvons est analogue à un matériau amorphe, caractérisée par un certain degré de désordre et une dynamique lente. Maintes fois utilisée pour illustrer l'état amorphe (illustré à la Figure 1.1), cette analogie[1] s'applique à des entités aussi variées qu'un algorithme de compression d'images, une diffusion d'une protéine dans un milieu cellulaire encombré, une solution colloïdale concentrée,[2] et même un empilement de jouets désordonné,[3] pour lesquels une multitude de « solutions », de « chemins » ou de « positions » équivalents existent simultanément, ralentissant ainsi le déroulement du phénomène en cours.[1]

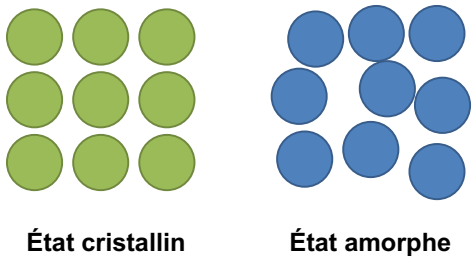


**Figure 1.1.** Représentation de l'état cristallin et de l'état amorphe.

Le désordre qui caractérise l'état amorphe, par opposition à l'ordre à grande distance retrouvé dans l'état cristallin[4] (*voir* Figure 1.1), est une propriété largement exploitée dans la fabrication de plusieurs matériaux. L'exemple le plus courant est celui de la vitre, l'oxyde de silicium ($SiO_2$), qui constitue les fenêtres, la vaisselle, les lentilles, ou les objets d'art, auquel on associe le terme « verre ». Toutefois, ce terme peut également englober plusieurs autres matériaux de différentes compositions.[5] Le verre possède des propriétés essentielles au bon fonctionnement de plusieurs objets et procédés: il est utilisé pour stocker de façon sécuritaire

des déchets nucléaires,[6] pour agir en tant que barrière de diffusion atomique dans les circuits intégrés,[7] pour recouvrir les miroirs de l'interféromètre ayant réussi à enregistrer pour la première fois les ondes gravitationnelles;[8] il est aussi retrouvé au cours des fouilles archéologiques (glacis des faïences égyptiennes,[9] ambre[10] ou obsidienne[1]), dans les poudres de produits laitiers, généralement sous forme de sucres amorphes,[11] et même chez les animaux vivant dans des conditions extrêmes dans un but de préservation biologique.[12-13] L'état figé et désordonné, qui est propre au verre, se retrouve également dans une montagne de sable ou de neige, qui suite à une déstabilisation quelconque, peut se transformer en glissement de terrain ou en avalanche.[14]

L'état amorphe est d'ailleurs étudié et exploité dans les matériaux reliés à des domaines aussi distincts que ceux pharmaceutique,[15-16] alimentaire,[17] opto-électronique[18] et de la nanolithographie.[19] D'un point de vue pharmaceutique, il a été démontré que l'état amorphe facilite la dissolution du principe actif,[20] e.g. deux fois plus rapide pour l'atorvastatine de calcium,[21] ou même la biodisponibilité lors d'administration de médicaments par voie pulmonaire, e.g. environ quatre fois plus dans le cas de l'itraconazole.[22] Par exemple, le naloxone, un composé qui est utilisé pour contrer les effets d'une surdose d'opioïdes, est actuellement administré par voies intraveineuse et intramusculaire, ce qui permet une biodisponibilité rapide, mais qui nécessite l'intervention de personnel qualifié, limitant son accessibilité dans les cas d'urgence. Sa forme amorphe pourrait être administrée oralement à un patient inconscient avec un temps de dissolution de moins de 10 s.[23] Les dispositifs opto-électroniques et les matériaux semi-conducteurs peuvent également bénéficier de l'état amorphe, puisque l'absence de structure périodique permet l'obtention de films uniformes et transparents, élimine les court-circuits dus aux joints de grains et offre une plus grande flexibilité au niveau de la composition des matériaux sans risque d'induire une détérioration des propriétés conductrices.[24] De plus, l'efficacité des photocatalyseurs amorphes destinés à la séparation de l'eau en hydrogène et en oxygène,[25-26] la capacité de stockage d'énergie de certains matériaux amorphes à l'échelle nanoscopique[27] et la performance des piles au lithium amorphes sont améliorées par rapport à leurs analogues cristallins.[28]

Compte tenu des nombreux avantages de l'état amorphe pour certaines applications, il n'est pas étonnant que plusieurs instituts et organisations de recherche, reliés autant aux sciences

des matériaux que de la physique de la matière condensée, en reconnaissent l'importance en l'incluant dans leurs listes d'objectifs à atteindre: les matériaux loin de l'équilibre font l'objet du *Grand Challenge #5* du *U.S. Department of Energy*,[29] tandis que le *National Institute for Pharmaceutical Technology and Education*[30] et la communauté des matériaux électroniques composés d'oxyde[31] en font mention dans leur *Roadmap*. Encore faut-il réussir à générer cet état amorphe et à maintenir ses propriétés sur une échelle de temps pertinent à son étude ou son application, pour arriver à exploiter son plein potentiel.

## 1.1.1 Formation d'un état désordonné

### 1.1.1.1 Types de matériaux pouvant former un verre

Lorsque Turnbull et Cohen ont émis l'hypothèse en 1958 que tout matériau avait la possibilité d'être transformé en son état amorphe,[32] la communauté scientifique était sceptique. Ce doute s'est dissipé avec le temps et de nos jours, l'état amorphe est recherché pour une multitude de matériaux, comme ceux métalliques, inorganiques et organiques, qui peuvent se retrouver dans leur phase vitreuse. Les verres métalliques sont particulièrement intéressants, entre autres pour leur plus grande résistance à la corrosion et leur élasticité. Par exemple, ils peuvent être utilisés pour des applications biomédicales[33] ou même pour rendre les bâtons de golf plus performants.[34]

Les verres organiques incluent les matériaux composés de molécules polymères, mais aussi de molécules de petite taille, pouvant inclure les liquides ioniques[35] et les cristaux liquides.[36] Plusieurs polymères, amorphes ou semi-cristallins, sont utilisés dans les produits de consommation, entre autres le poly(éthylène téréphtalate) (PET) pour les bouteilles de boisson gazeuse, le polystyrène (PS) atactique pour les récipients en styromousse, ou le nylon qui entre dans la composition de certains vêtements.[37] Ils peuvent également être utilisés dans des dispositifs opto-électroniques ou dans le domaine pharmaceutique, tout comme les molécules organiques de petite taille. Ces dernières peuvent aussi être employées pour former des matériaux poreux amorphes pour le stockage de gaz[38] ou des réseaux métallo-organiques amorphes.[39] Les liquides ioniques peuvent se retrouver sous forme amorphe dans les piles au lithium,[40] tout comme certains nanopoints de carbone[41] et aérosols organiques qui peuvent se retrouver eux aussi à l'état amorphe.[42-43]

#### 1.1.1.2 Processus de vitrification

Bien que plusieurs des matériaux nommés dans la section précédente existent naturellement à l'état amorphe, il est parfois nécessaire d'utiliser certaines techniques physiques, plus ou moins exigeantes, pour rendre un matériau amorphe. Certaines d'entre elles sont mécaniques et consistent à détruire le réseau cristallin, par exemple par broyage ou compactage.[15] D'autres visent à frustrer la cristallisation d'une molécule en la mélangeant à d'autres pour obtenir un mélange ou une dispersion amorphe.[44] Il est également possible de piéger l'état non-cristallin, impliquant la précipitation ou la lyophilisation à partir d'une solution,[15] le dépôt physique en phase vapeur (PVD) avec[45] ou sans assistance laser,[46] ou encore le séchage par vaporisation.[47] Lorsqu'il est possible d'obtenir la phase liquide d'un matériau, l'option d'un refroidissement « rapide » (trempe) à partir de cette phase liquide est l'une des méthodes les plus évidentes pour éviter la cristallisation.

#### 1.1.1.3 Vitrification à partir de l'état visqueux (liquide)

Le schéma de gauche à la Figure 1.2 illustre le processus général de cristallisation et de vitrification d'un matériau à partir de son état liquide en représentant son volume spécifique ($V_{sp}$) ou son enthalpie ($H$) en fonction de la température, à pression constante.[48-49] Afin d'éviter d'alourdir le texte, uniquement $V_{sp}$ sera utilisé pour la suite de la description. À haute température, le matériau se trouve sous sa forme liquide. À mesure que la température diminue, $V_{sp}$ diminue (représenté en noir). Lorsque la température atteint la température de fusion ($T_f$, qui correspond à la température de cristallisation dans un cas idéal) le matériau peut soit cristalliser ou passer dans un état surrefroidi, i.e. un état métastable dont les propriétés correspondent à celles extrapolées du liquide à des températures inférieures à $T_f$. L'état dans lequel le matériau se retrouve dépend de sa cinétique de cristallisation: si cette dernière est plus rapide que la vitesse de refroidissement, le matériau cristallisera (transition de 1$^{er}$ ordre selon la classification d'Ehrenfest)[50] et $V_{sp}$ diminuera drastiquement (en vert). L'eau est une exception du point de vue du volume mais suit le comportement représenté du point de vue de l'enthalpie. Toutefois, si sa cinétique de cristallisation est moins rapide que la vitesse de refroidissement, le matériau se retrouvera sous sa forme surrefroidie (en rouge). $V_{sp}$ continuera à diminuer à mesure que la température s'abaisse et la viscosité du matériau augmentera, ayant comme conséquence

de ralentir sa dynamique. Lorsque cette dernière deviendra plus lente que celle imposée par la vitesse de refroidissement, le matériau ne sera plus à l'équilibre et il sera transformé en verre (en bleu), instable d'un point de vue thermodynamique.

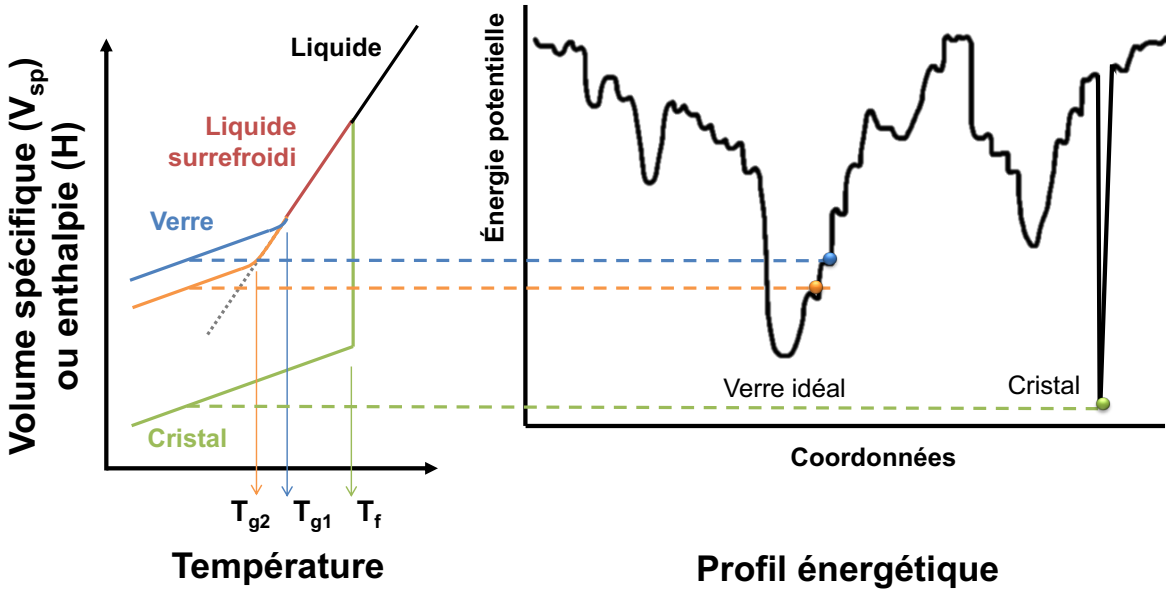


**Figure 1.2.** Processus de cristallisation et de vitrification et correspondance des différents états obtenus selon le profil énergétique.

La différence de stabilité entre le verre et le cristal peut être visualisée dans la portion droite de la Figure 1.2, où l'énergie potentielle des différents états est représentée en fonction des différentes coordonnées possibles pour un matériau qui subit un refroidissement.[51] Dans ce profil énergétique, chaque bosse correspond à un état de transition et chaque bassin correspond à un minimum relatif. D'un point de vue thermodynamique, le cristal correspond au bassin avec l'énergie potentielle la plus faible. Les autres bassins correspondent aux multitudes de verres qui peuvent être formés lors du refroidissement. En effet, l'état vitreux n'est pas un état unique de la matière. L'histoire thermique subie par le matériau influence les propriétés du verre formé: un refroidissement rapide (en bleu à la Figure 1.2) mène à un verre encore plus instable qu'un verre formé par un refroidissement plus lent (en orangé à la Figure 1.2). En effet, plus le refroidissement est lent, plus il sera possible au matériau de rester en équilibre sur une période

de temps prolongée puisqu'il aura la possibilité d'échantillonner une plus grande variété de coordonnées dans l'espace. Cet échantillonnage lui permettra de rejoindre un bassin d'énergie potentielle plus faible, et ce, à une température inférieure, que dans le cas d'un refroidissement rapide, où le temps d'échantillonnage est limité. Un refroidissement infiniment lent, qui suivrait le trait pointillé gris à la Figure 1.2 (panneau gauche), pourrait donc permettre, en théorie, d'atteindre le bassin d'énergie potentielle correspondant au verre « idéal ». Le verre représenté par le point bleu pourrait atteindre ce bassin, ou tout autre bassin possédant une énergie potentielle inférieure, après le refroidissement, lorsqu'il relaxe vers son état le plus stable thermodynamiquement. Bien que très intéressants, les phénomènes reliés à la relaxation des matériaux amorphes, tels que le recuit et le vieillissement physique[52] en dessous de leur $T_g$ ne seront pas abordés dans le cadre de cette thèse.

### 1.1.2 Transition vitreuse

La transition vitreuse se produit sur une gamme de températures dans laquelle on détermine une température de transition vitreuse ($T_g$). Cette dernière dépend de la vitesse de balayage et/ou de la fréquence à laquelle le matériau est perturbé, d'où la présence, à la Figure 1.2, de la $T_{g1}$ pour le verre en bleu (refroidissement rapide) et de la $T_{g2}$ pour le verre en orangé (refroidissement lent).[49] Elle correspond au passage d'un matériau de son état visqueux à son état vitreux dans le cas décrit dans la section précédente, i.e. en refroidissement, ou de l'état vitreux à l'état visqueux en chauffe. À l'état visqueux, les molécules du matériau se retrouvent à l'équilibre et possèdent suffisamment d'énergie pour se mouvoir les unes par rapport aux autres et ainsi explorer les coordonnées du profil énergétique. À l'état vitreux, où les molécules se retrouvent hors-équilibre, seuls des mouvements de vibration des atomes ou de rotation de groupements latéraux sont possibles.[48] Bien que le matériau soit en constante évolution vers l'état le plus stable thermodynamiquement (cristal), on dit de la structure du verre qu'elle est figée, puisque l'échelle de temps sur laquelle les réarrangements moléculaires se produisent est beaucoup plus longue que l'échelle du temps expérimental, et par le fait même, justifiant l'utilisation du terme « métastable » parfois utilisé pour qualifier le verre, alors qu'au sens strict, il est « instable ».[49]

#### 1.1.2.1 Mesure de la température de transition vitreuse

Historiquement, la $T_g$ a été définie, pour les verres non polymériques, comme étant la température à laquelle le temps de relaxation $\tau_\alpha$ d'un matériau, en refroidissement, était de 100 s,[51] mais aussi comme étant la température à laquelle sa viscosité en cisaillement correspondait à $10^{12}$ Pa·s ou $10^{13}$ poises.[48] Une règle empirique rapporte également que la $T_g$ correspond à 2/3 de la valeur de $T_f$.[51] Étant donné que la $T_g$ définit les propriétés mécaniques d'un matériau amorphe et par le fait même, ses applications, il est primordial de la déterminer adéquatement. L'analyse calorimétrique différentielle à balayage (DSC), l'analyse mécanique dynamique et les mesures de viscosité sont parmi les méthodes les plus employées pour déterminer la $T_g$ d'un matériau.[48] Dans cette thèse, la DSC, qui permet de suivre l'évolution de la capacité calorifique de l'échantillon en fonction de la température, est l'outil privilégié pour déterminer les températures de transition des matériaux étudiés. La spectroscopie infrarouge à température variable sera également utilisée au chapitre 6 pour évaluer les $T_g$ des matériaux étudiés. Toutefois, toute propriété affectée par la transition vitreuse peut servir à la déterminer, comme le volume, l'indice de réfraction et la fluorescence. Les spectroscopies diélectrique et de résonance magnétique nucléaire sont également des alternatives intéressantes aux mesures thermiques, puisqu'elles donnent accès aux temps de relaxation du matériau, tout comme les méthodes mécaniques.[48]

#### 1.1.2.2 Théories de la transition vitreuse

Étant donné que la transition vitreuse correspond à une divergence entre un temps expérimental et un temps de relaxation moléculaire, la $T_g$ dépend de la méthode employée, mais aussi de la vitesse de balayage ou de la fréquence de la perturbation utilisée pour la mesurer. Par exemple, pour une même méthode, une variation d'un ordre de grandeur a typiquement une influence de 3-5 °C sur la $T_g$.[49] Cette dépendance cinétique de la $T_g$ complique son interprétation d'un point de vue thermodynamique. Bien qu'on retrouve une discontinuité dans le tracé du coefficient d'expansion thermique ou de la capacité calorifique d'un matériau amorphe, correspondant tous deux à une dérivée partielle d'ordre 2 de l'énergie de Gibbs du matériau, la transition vitreuse peut seulement être considérée comme analogue à une transition de deuxième ordre, sans toutefois en être une d'un point de vue purement thermodynamique.[50]

Toutefois, dans le cas d'un refroidissement infiniment lent, Kauzmann soulève l'idée qu'une transition de second ordre (la transition vitreuse) doit se produire pour éviter que l'entropie du liquide surrefroidi ne devienne inférieure à zéro avant d'atteindre le zéro absolu, ce qui enfreindrait la troisième loi de la thermodynamique.[53] Avec raison, ce paradoxe, et le phénomène de la transition vitreuse en général, a soulevé et soulève encore plusieurs interrogations. Ce n'est pas une coïncidence si le terme « transition vitreuse » est le deuxième mot clé, après « cristallisation » qui est le plus employé dans les publications relatives aux verres depuis 1850.[54] Considérant le nombre impressionnant de théories proposées sans atteinte de consensus au sein de la communauté scientifique, un bref survol des plus classiques a été préféré à une revue plus exhaustive.

Deux des théories les plus classiques ont tenté d'expliquer la transition vitreuse comme étant respectivement gouvernée par 1) l'entropie configurationnelle et 2) le volume libre. Dans le premier cas, la théorie de Gibbs-DiMarzio se base sur le modèle de Flory-Huggins, où des espaces vides et des molécules se partagent des cases d'une matrice.[55] À mesure que la température diminue, de plus en plus de cases deviennent occupées, augmentant la viscosité du système. Cette dernière empêche d'observer la transition de phase d'un point de vue thermodynamique (transition de l'état visqueux à un état vitreux unique), mais permet de s'en approcher. Dans le deuxième cas, Doolittle suggère qu'un lien peut être établi entre la viscosité d'un matériau et sa fraction de volume libre (cases vides de la Figure 1.3).[56-58] La transition vitreuse se produit, en chauffe, lorsque la fraction de volume libre atteint une assez grande valeur pour permettre aux molécules qui composent le matériau de se mouvoir de façon coopérative. La transition vitreuse se produit donc quand le volume libre n'est plus constant en augmentant la température. Le volume libre, en gris dans la Figure 1.3, est donc lié à la mobilité des molécules. Williams, Landel et Ferry ont ensuite supposé que le volume libre augmentait de façon linéaire pour en venir à calculer qu'à la $T_g$ d'un matériau, son pourcentage est de 2,5%.[59] Bien que le modèle de Gibbs-DiMarzio n'ait jamais été démontré expérimentalement, ses prédictions concordent avec celles obtenues à l'aide de la théorie du volume libre, permettant notamment de prévoir la $T_g$ en fonction de la masse molaire, de la composition d'un copolymère et d'un mélange, ou même du contenu en plastifiant.[60]

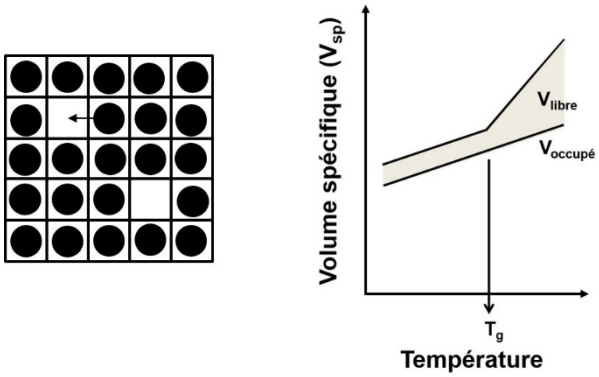


**Figure 1.3.** Représentation schématique du réseau de cases et de l'évolution du volume spécifique d'un matériau en fonction de la température.

Adam et Gibbs ont ensuite tenté de joindre les deux théories en introduisant le concept de régions de réarrangement coopératif, en reliant la viscosité et l'entropie configurationnelle aux minima d'énergie potentielle observés dans le profil énergétique.[61] Bien que l'existence de ces régions et leur taille soient encore débattues, la communauté en a retenu que la transition vitreuse est un phénomène hétérogène,[62] qui implique que le passage de l'état visqueux à l'état vitreux ne tend pas vers une configuration unique, mais vers plusieurs configurations plus ou moins équivalentes en énergie. Bien d'autres théories ont été développées et approchent le phénomène d'un point de vue plus moléculaire pour les polymères,[63] impliquant l'approximation d'un champ moyen dans le cas de la théorie des couplages de modes, ou tentant de s'adapter à des matériaux très précis, comme les films ultraminces,[64] mais aucune n'a encore réussi à capturer toutes les subtilités de la transition vitreuse.

### 1.1.3 Fragilité

La viscosité d'un matériau, i.e. sa résistance à l'écoulement, est une propriété très sensible à la température, surtout dans les alentours de la $T_g$, tel qu'illustré à la Figure 1.4. Selon le matériau, la dépendance en température de la viscosité peut être de type Arrhenius, comme pour $SiO_2$, ou de type Vogel-Tammann-Fulcher, comme pour l'*ortho*-terphényle (OTP),

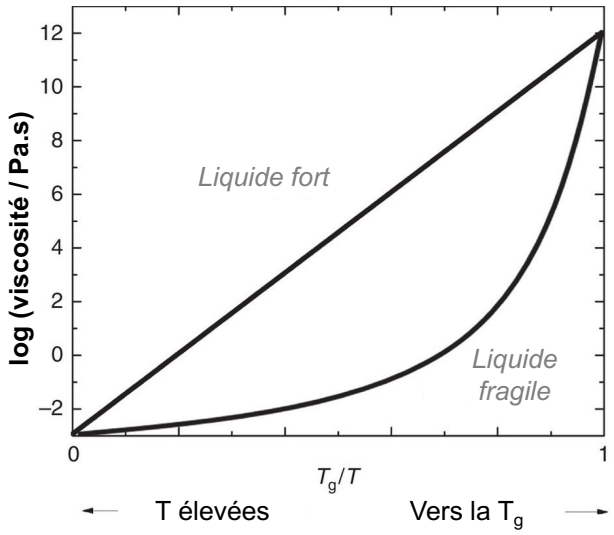


**Figure 1.4.** Représentation du diagramme de fragilité illustrant l'allure de la dépendance en température relative de la viscosité pour un liquide fort et un liquide faible. Adaptée et traduite avec la permission de Macmillan Publishers Ltd: Nature Communications, référence 67 © 2014.

où l'augmentation de viscosité en fonction de la diminution de température est beaucoup plus abrupte près de la $T_g$.[65-67] Le groupe de recherche Angell a utilisé ces différences de dépendances pour classer les liquides selon leur fragilité. La principale différence entre les deux catégories est que l'énergie d'activation nécessaire à la transition vitreuse est quasi constante dans le cas des liquides forts, alors qu'elle évolue en fonction de la température dans le cas des liquides fragiles.[51] La fragilité, *m*, est un paramètre calculé selon l'équation 1.1 où $\tau_\alpha$ est le temps de relaxation $\alpha$ à une température T. Une valeur faible de *m* est associée à un liquide fort (pour $SiO_2$, *m* est autour de 20 et pour $B_2O_3$, autour de 50) et où une valeur supérieure est associée aux liquides fragiles. Pour les polymères, *m* se situe entre 150 et 200 alors que les molécules organiques de petite taille ont un *m* intermédiaire, entre 80 et 100.[68-70] Cette augmentation de la valeur de la fragilité suit généralement l'augmentation de la « rigidité » d'une molécule, qui rend moins efficace son empilement pendant le refroidissement de l'état liquide à l'état vitreux.

$$m = \left.\frac{\mathrm{d}\log\tau_\alpha}{\mathrm{d}T_g/T}\right|_{T_g} \tag{1.1}$$

Récemment, Dalle-Ferrier *et al.* ont raffiné cette hypothèse en proposant que l'augmentation de la fragilité avec la rigidité est due au fait que la rigidité de la molécule la prive d'explorer certaines coordonnées configurationnelles. Son entropie configurationnelle totale varierait donc moins rapidement avec la température que l'ensemble des configurations possibles.[70] Des exceptions intéressantes sont les vitrimères, développés par le groupe de recherche Leiber, qui sont des verres organiques forts, puisque constitués d'atomes liés de façon covalente qui résulte en un réseau dont la topologie est réversible.[71-72]

### 1.1.4 Capacité d'un matériau à former un verre et à résister à la dévitrification

La plupart des matériaux peuvent se retrouver à l'état amorphe à partir de leur état liquide sans devoir appliquer des vitesses de refroidissement extrêmes. En effet, leur capacité à former un verre (*glass-forming ability*, GFA) dépend de leur capacité à résister à la cristallisation en refroidissement. Le GFA est souvent évalué en fonction de la vitesse de refroidissement critique ($R_c$), i.e. la vitesse minimale à laquelle un matériau peut être refroidi sans présenter de signe détectable de cristallisation. Un verre ayant un bon GFA sera donc associé à une vitesse critique de refroidissement lente alors qu'un verre avec un mauvais GFA sera associé à une vitesse critique de refroidissement plus rapide. Tel qu'illustré à la Figure 1.5, ces vitesses de refroidissement critiques peuvent varier de l'ordre de $10^{-6}$ K/s pour le $SiO_2$ jusqu'à $10^9$ K/s pour les verres métalliques.[1] Un matériau peut avoir un bon GFA parce que i) sa capacité à germer est faible et/ou que ii) la croissance de cristaux à partir des germes est lente, i.e. ralentie par la viscosité, comparativement à la vitesse de refroidissement appliquée. La résistance à la dévitrification (*glass stability*, GS) est la capacité du verre formé à résister à la cristallisation lors de la chauffe ou même sous conditions isothermes de recuit ou d'utilisation. Le GS ne sera que brièvement abordé dans le chapitre 2 de cette thèse, d'un point de vue de conditions de chauffe, alors que le GFA sera l'un des paramètres qui fera l'objet d'une étude plus approfondie.

Les concepts de GFA et de GS sont principalement exploités dans l'industrie des verres métalliques (leur relation étant encore débattue),[73-74] tandis que le GFA est de plus en plus étudié pour les verres organiques, notamment dans le domaine pharmaceutique. Plusieurs tests de

| Matériau | Vitesse de refroidissement critique, $R_c$ (K/s) |
|---|---|
| $SiO_2$ ou PS atactique | $10^{-6}$ |
| Glycérol | $10^{-2}$ |
| PET trempé avec $N_{2\,(l)}$ | $10^{2}$ |
| Verre métallique | $10^{7}$-$10^{9}$ |

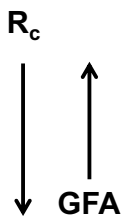


**Figure 1.5.** Relation entre la vitesse de refroidissement critique, $R_c$, et la capacité d'un matériau à former une phase vitreuse, GFA.

prédiction de GFA basés sur la structure des molécules ou sur leur cinétique de cristallisation ont été développés dans le but de rendre plus efficace la détermination du GFA d'un nouveau matériau, pour économiser temps, argent et matériel. Dans le domaine des verres métalliques, le premier test rapporté provenant des travaux de Goldschmidt est de type structural: les mélanges ioniques binaires pouvaient former un verre si le ratio du rayon du cation et de l'anion se trouvait entre 0,2 et 0,4.[75] Toutefois, les valeurs limites incluaient des matériaux qui ne formaient pas de phase vitreuse.[76] D'autres tests tentent de prédire le GFA d'un matériau en tenant compte des températures de transition vitreuse, de cristallisation et/ou de fusion. Kauzmann[53] et Turnbull et Cohen[77] estiment qu'un matériau peut former un verre si $T_g/T_m > 2/3$. Turnbull et Cohen proposent aussi qu'un matériau peut former un verre si le ratio de ses températures d'ébullition et de fusion est plus grand que 2. Dans le premier cas, cette limite semble être la limite inférieure observée et dans le deuxième cas, l'estimation fait totalement abstraction de la dynamique du verre, ce qui peut faire douter de sa pertinence.[78] D'autres, justement pour tenir compte de cette dynamique, ont tenté de relier le GFA à la fragilité, mais avec un succès mitigé.[79-80] Le nombre d'exceptions étant quasi égal au nombre de cas qui confirment les prédictions de ce type de tests, il s'en dégage qu'il est pratiquement impossible d'établir des intervalles universels pour les matériaux.

Des tests basés sur la cinétique de cristallisation ont donc été mis au point pour permettre de tester le GFA des matériaux de manière individuelle. Ces derniers sont illustrés à la Figure 1.6. Uhlmann[81] a développé une méthode pour estimer la vitesse de refroidissement critique en se servant de la cinétique de cristallisation d'un matériau pour calculer la fraction de la phase cristallisée après un certain temps à une température définie, ce qui mène à une courbe de

transformation temps-température (diagramme de type TTT).[82] En pratique, ce test consiste à faire subir des isothermes à différentes températures après la trempe du matériau depuis son état liquide (pointillés rouges, Figure 1.6A). Cette méthode permet d'obtenir une courbe semblable à celle représentée en noir à la Figure 1.6A. La vitesse de refroidissement critique peut donc être estimée en traçant une droite (en trait plein rouge sur la Figure 1.6A) entre la température de fusion du matériau et le sommet de la courbe noire. Cette méthode est laborieuse et peu efficace si la capacité à germer d'un matériau est faible. Une autre méthode est celle du refroidissement en continu, aussi illustrée à la Figure 1.6A, où le matériau est refroidi depuis son état liquide à différentes vitesses de refroidissement (pointillés bleus). Cette dernière est la plus répandue puisqu'elle est la plus pratique, surtout lorsque les mesures sont faites par DSC. Si la fraction de phase cristalline est calculée pour chaque vitesse de refroidissement, il est possible de construire un graphique analogue à celui de la Figure 1.6B, où la fraction de phase cristalline est tracée en fonction de la vitesse de refroidissement appliquée.[78] La vitesse de refroidissement critique correspond donc à la vitesse de refroidissement pour laquelle la fraction de phase cristalline est jugée négligeable. Une méthode similaire à celle du refroidissement en continu est employée dans cette thèse pour évaluer le GFA des composés.

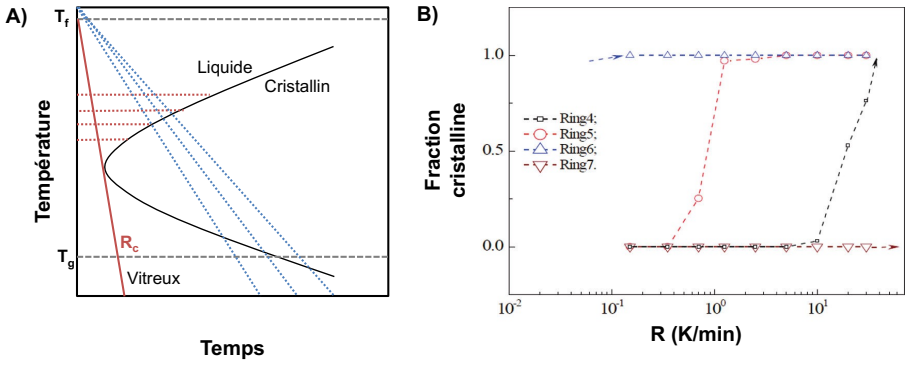


**Figure 1.6.** Méthodes pour estimer la vitesse de refroidissement critique et le GFA des composés. A) Méthode de transformation temps-température (TTT, en trait pointillé rouge) et du refroidissement continu (trait pointillé bleu). B) Méthode pour estimer la vitesse de refroidissement critique de différents composés stilbènes (*Ring4* à *Ring7*) à partir du calcul de la fraction de phase cristalline obtenue à différentes vitesses de refroidissement R. Adaptée et traduite avec la permission de la référence 78 © 2011 American Chemical Society.

## 1.2 Verres moléculaires

Un intérêt certain pour les verres composés de molécules de petite taille est présent au sein de la communauté scientifique puisqu'elles peuvent présenter un état vitreux, analogue à celui obtenu avec des polymères, tout en présentant des avantages supplémentaires. Étant des espèces isomoléculaires, leurs propriétés sont mieux définies et plus facilement reproductibles que celles des polymères, qui sont des espèces polymoléculaires, ce qui facilite leur synthèse et leur purification. Leur viscosité inférieure à celle des polymères facilite également leur mise en œuvre.

Quelques travaux ont été effectués sur des molécules organiques de petite taille par divers groupes de recherche pour tirer des lignes directrices empiriques favorisant la formation d'une phase vitreuse et ainsi contourner des méthodes de préparation exigeante, dont la trempe. Par exemple, les travaux de Salbeck *et al.* ont montré que des molécules non planes, comme les spirofluorènes illustrés à la Figure 1.7A, peuvent former facilement une phase vitreuse.[83] Le groupe de Shirota a conclu que la présence de groupements substituants encombrants, l'absence de planarité et une possibilité d'exister sous différentes conformations facilite la formation d'une phase vitreuse.[18] Certaines des molécules en forme « d'étoile » sont représentées à la Figure 1.7B. Cette dernière règle abonde dans le même sens que celle de la nécessité d'une certaine flexibilité (possibilité de rotation de certains groupements) proposée par Yu *et al*.[84] Naito *et al.* du département recherche et développement de la compagnie Toshiba, ont mentionné qu'il est préférable que les molécules soient de grande taille, possèdent une certaine symétrie, soient globulaires et assez rigides, tout en possédant des groupements chimiques qui ne favorisent pas la cohésion moléculaire.[85] Pedersen *et al.* ont également fait référence à la symétrie, mais cette fois-ci à l'absence de symétrie, comme paramètre favorisant la formation d'une phase vitreuse.[86] À quelques différences près, toutes ces règles empiriques sont conformes aux résultats de l'une des études du groupe de Glotzer, portant sur le type d'arrangement obtenu pour plus de 145 polyèdres de formes différentes, concluant que ceux avec des formes asymétriques avaient une plus grande probabilité de s'arranger de façon désordonnée étant donné leur incapacité à former des empilements compacts.[87]

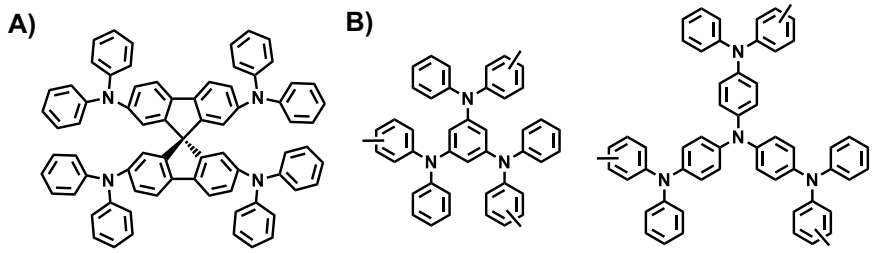


**Figure 1.7.** Représentation de structures moléculaires capables de former facilement une phase vitreuse. A) Dérivé spirofluorène et B) Molécules en forme d'étoile.

## 1.2.1 Verres moléculaires à base de triazine

Lebel *et al.* ont synthétisé en 2006 une série de molécules à base de triazine,[88] maintenant brevetées,[89] dont la structure est représentée à la Figure 1.8. Même si ces dérivés ne suivent pas tous les lignes directrices empiriques mentionnées dans la section précédente, ils présentent, pour la plupart, une excellente capacité à former une phase vitreuse. Fonctionnalisés par un groupement de tête (*headgroup*, $R_1$), des groupements liants (*linkers*, $R_2$ et $R_3$) et des groupements auxiliaires (*ancillary groups*, $R_4$ et $R_5$), ces composés sont relativement symétriques et planes, en plus d'être capables d'établir des liaisons hydrogène dans le cas où certains des groupements de tête $R_1$ ou liants $R_2$ et $R_3$ sont des donneurs de liaisons hydrogène, tel qu'illustré dans l'encadré de la Figure 1.8.

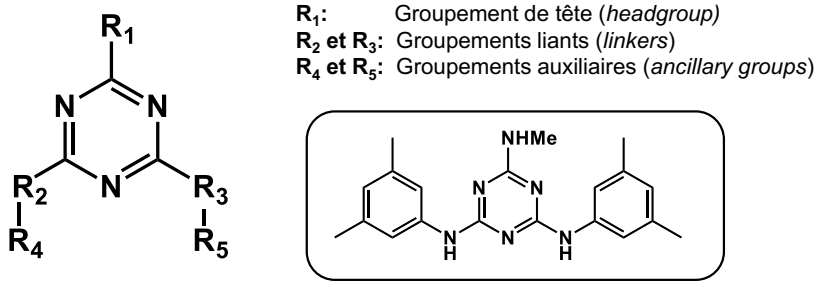


**Figure 1.8.** Structure de base des dérivés de triazine et identification de ses groupes substituants. Un exemple de composé est illustré dans l'encadré.

### 1.2.2 Choix des verres moléculaires à base de triazine comme système modèle

Le fait que ces verres moléculaires à base de triazine soient capables de former une phase vitreuse même à des vitesses de refroidissement aussi lentes que 0,05 °C/min et de résister à la cristallisation pendant plusieurs mois à température ambiante,[90] malgré leurs caractéristiques qui ne suivent pas nécessairement les lignes directrices empiriques énoncées précédemment, est intrigant. De plus, selon certains diagrammes de prédiction de cristallinité, les verres moléculaires à base de triazine se retrouvent à la frontière entre l'état cristallin et non-cristallin, tel que représenté par un rectangle jaune à la Figure 1.9. C'est le cas pour celui établi par Wicker *et al.*,[91] à la Figure 1.9A, qui utilisait un algorithme incluant le nombre de liaisons capables de faire des rotations et ${}^{0}\chi^{v}$, un paramètre analogue au volume moléculaire. Les verres se retrouvent également à la frontière du test de prédiction de Wyttenbach *et al.*,[92-93] illustré à la Figure 1.9B, pour lequel les paramètres importants, comme le volume molaire (< 150 $cm^3$/mol), le nombre de liens capables de faire des rotations (entre 2 et 5) et le nombre effectif de liaisons H (inférieur à $H_{eff}$ = 7.5 x $10^{-3}$, calculé selon l'équation 1.2[92]) ont été sélectionnés comme des paramètres influençant la capacité d'une molécule à former un verre. Le nombre $H_{eff}$ pour les verres à base de triazine a été calculé en approximant que $NH_2$ ~ NH

$$H_{eff} = \frac{\sqrt{OH+COOH}+0{,}33\sqrt{NH_2}}{Masse\ molaire\ du\ composé} \qquad (1.2)$$

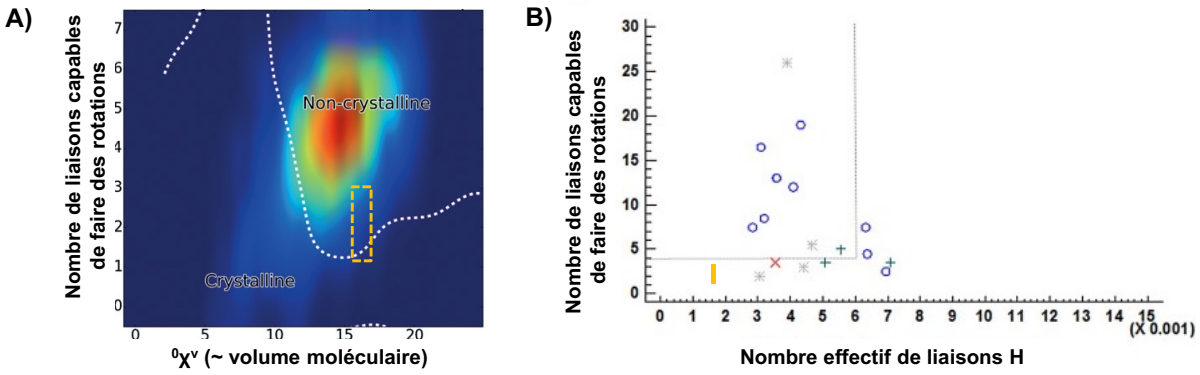


**Figure 1.9.** Diagramme de prédiction de cristallinité, selon A) Wicker *et al.* (adaptée et traduite de la référence 91 avec la permission de The Royal Society of Chemistry) et B) Wyttenbach *et al.* (adaptée et traduite de la référence 93 © 2016 avec la permission de Elsevier).

Ces observations portent à croire que la facilité des dérivés de triazine à former une phase vitreuse et à rester dans cet état tire son origine d'autres paramètres que d'uniquement son volume moléculaire et du nombre de liens capables d'effectuer des rotations. Il devient donc intéressant de tenter d'établir des relations entre leur structure moléculaire, i.e. les groupements substituants qui les composent, et leur GFA, mais aussi leur GS et leur $T_g$. Les travaux de cette thèse utilisent donc des librairies de dérivés de triazine comme système modèle pour les trois raisons principales suivantes: i) la structure de base du verre permet de faire des études systématiques sur l'influence de la nature des groupements; ii) la gamme de $T_g$, allant de -25 °C à près de 200 °C permet d'étudier les phases vitreuse et visqueuse sans devoir recourir à des méthodes pour maintenir la température extrêmement basse ou élevée, comme c'est le cas avec l'OTP ou le $SiO_2$; et iii) leur excellente capacité à former un verre permet d'appliquer des vitesses de refroidissement relativement lente, permettant de faire des mesures *in situ* avec une bonne résolution temporelle tout en évitant d'être confronté au phénomène de cristallisation pendant la mesure.

## 1.3 Relations entre la structure et les propriétés des verres moléculaires

Il est bien connu que la masse molaire d'un composé et les différentes interactions qu'il peut établir peuvent faire varier la $T_g$ d'un matériau.[94] Par exemple, une $T_g$ élevée peut être reliée à la présence de groupements fonctionnels encombrants ou à des interactions intermoléculaires relativement fortes puisqu'ils restreignent la mobilité du composé. Ils limitent la création de volume libre, par opposition à de longues chaînes alkyles, qui elles, favorisent la création de volume libre, menant à une $T_g$ inférieure. Bien que peu communes, certaines études systématiques réalisées sur des séries de verres moléculaires analogues ont réussi à dégager des relations structure-propriétés intéressantes.

Des mesures impliquant des dérivés de xylènes ont montré que la position *meta* sur un cycle aromatique favorisait le GFA, et que la $T_g$ de ces composés augmentait avec la force des liaisons H qu'ils pouvaient établir.[95] Une autre étude, portant sur la comparaison entre le toluène et son analogue saturé, le méthylcyclohexane, a permis d'en conclure que la structure aromatique du toluène le rendait plus fragile que le méthylcyclohexane, dont la fragilité

avoisinait celle des alcools aliphatiques, i.e. intermédiaire entre les catégories « fragile » et « fort ».[96] Par ailleurs, les structures aliphatiques présentent généralement des $T_g$ inférieures à celles des aromatiques puisque les interactions qu'elles établissent sont moins fortes. D'autres études, effectuées sur une série d'isomères de trisnaphtylbenzène (TNB, reconnus pour leur excellent GFA), ont démontré l'importance des rotations intramoléculaires pour favoriser le GFA en permettant la coexistence de certaines conformations.[97] Une étude plus récente sur des analogues du TNB a conclu que l'augmentation de la masse molaire des composés provoquait une augmentation de $T_g$ et que la présence de fortes interactions π augmentait la fragilité des composés et leur $T_g$, mais abaissait leur GFA.[98] Finalement, des travaux sur une librairie de molécules comportant toutes un groupement *cis*-stilbène composés de cycles de différentes tailles suggèrent que les cycles aromatiques à six atomes de carbone favorisent le GFA par rapport à des cycles à moins ou plus d'atomes.[78]

La plupart de ces études sont menées sur des verres dont les principales interactions intermoléculaires sont relativement faibles. Pourtant, d'autres types d'interactions non covalentes plus fortes, telles que les liaisons H, sont couramment retrouvées dans les composés pharmaceutiques, dont le GFA et la $T_g$ sont des propriétés importantes à considérer, tel que discuté dans les travaux du groupe de recherche Taylor.[80, 99] D'ailleurs, certains algorithmes employés pour les tests de prédiction de cristallinité incluent le nombre de liaisons H comme paramètre clé pour prévoir le GFA et le GS de certains composés.[100-102] Il est donc essentiel de procéder à des études systématiques sur des librairies de composés qui comportent des groupements capables de participer à des liaisons H pour dégager des lignes directrices en vue d'optimiser la préparation de matériaux moléculaires amorphes. Les liaisons H et leur influence seront donc étudiées tout au long de cette thèse à l'aide des dérivés de triazine pour atteindre cet objectif, qui est analogue à celui de la tectonique moléculaire (*crystal engineering*), dont le but est de « comprendre les interactions moléculaires dans le contexte des empilements cristallins pour les utiliser dans la conception de nouveaux solides qui possèdent des propriétés physiques et chimiques désirées ».[103]

### 1.3.1 Liaisons hydrogène

#### 1.3.1.1 Utilisation

La liaison H, souvent représentée par X – H ··· A, s'établit entre un atome H lié à un atome électroattracteur X (O, N, halogène) et un autre atome A qui est aussi électroattracteur (O, N, S, halogène) et possède une énergie de dissociation allant de ~ 1 à 165 kJ/mol.[104-105] Cette interaction joue sans contredit un rôle essentiel d'un point de vue biologique, e.g. eau, ADN, protéines,[106-107] mais elle est aussi un incontournable pour le domaine de la tectonique moléculaire.[108] À la fois directionnelle et capable d'offrir une certaine flexibilité du point de vue de l'angle auquel elle peut être établie, cette interaction peut être utile pour « contrôler » l'arrangement des molécules en une structure périodique. Par exemple, les liaisons H sont assez robustes pour créer un réseau tridimensionnel hôte, mais aussi assez flexibles pour lui permettre de s'adapter à différentes molécules invitées.[109] Elles peuvent également contribuer à la stabilisation et à l'optimisation des performances des cellules photovoltaïques si elles sont utilisées stratégiquement pour obtenir la morphologie désirée.[110] Dans le cas d'une utilisation non stratégique, elles peuvent toutefois induire une séparation de phase qui nuit à leur performance.[111] Les liaisons H peuvent également contribuer au désordre d'un matériau et modifier ses propriétés mécaniques. Par exemple, une prédiction de structure cristalline de l'aspirine a suggéré qu'une paire de liaisons H rendait plus difficile son empilement[112] et que la présence de groupements OH dans des molécules analogues composant des aérosols atmosphériques peut augmenter leur viscosité par jusqu'à quatre ordres de grandeur.[113] Ces quelques exemples illustrent l'importance de bien comprendre le comportement des liaisons H pour les utiliser efficacement.

#### 1.3.1.2 Caractérisation

Une méthode particulièrement intéressante pour l'étude des liaisons H est la spectroscopie infrarouge (IR). Grâce à la sélectivité de cette technique, il est possible de faire le suivi, dans le moyen IR, des groupements liés, i.e. qui participent aux liaisons H, et libres (qui n'y participent pas), mais aussi de comparer les états amorphe et cristallin, puisque les caractéristiques d'un spectre IR dépendent de l'environnement moléculaire du composé à l'étude. En effet, lorsqu'un échantillon passe de l'état cristallin à amorphe, les bandes du spectre

IR s'élargissent et se déplacent.[114] Cette approche a notamment été employée dans le domaine pharmaceutique par le groupe de Taylor[115-117] et par Kaushal *et al.*[118] pour étudier les liaisons H en présence, mais aussi pour étudier celles établies entre un composé actif et le polymère utilisé pour stabiliser sa phase vitreuse. Des mesures de spectroscopie IR à température variable permettent aussi de suivre l'évolution d'une bande (largeur, position, absorbance) en fonction de la température. Par exemple, à la Figure 1.10, la position de la bande d'élongation des groupements OH d'une série de disaccharides est tracée en fonction de la température.[119] L'allure de la courbe correspond à celle d'une transition de second ordre: un changement de pente se produit à des températures qui correspondent à leur $T_g$, puisque l'environnement moléculaire des groupes OH est perturbé par la transition vitreuse. Un tel suivi constitue une alternative intéressante pour déterminer la $T_g$ d'un matériau. Il sera justement discuté au chapitre 3 que la perturbation de l'environnement moléculaire des OH peut être à l'origine de la transition vitreuse.

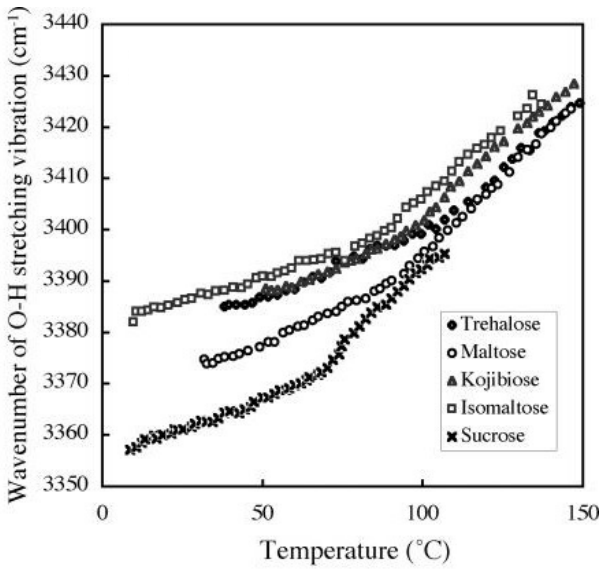


**Figure 1.10.** Variation de la position de la bande d'élongation OH en fonction de la température pour différents saccharides. Adaptée avec la permission de la référence 119 © 2006 American Chemical Society.

La largeur des bandes correspondant aux groupements amino (NH) ou OH liés et libres complique toutefois l'analyse spectrale en vue de quantifier les liaisons H. Dans le cas où il est

difficile de procéder à un étalonnage fiable, il est possible de combiner des mesures IR à une analyse chimiométrique.[120] Cette approche a d'ailleurs été employée pour estimer l'évolution du nombre de groupements OH liés et libres au cours du processus de fusion de l'eau.[121] La section suivante expliquera les raisons qui ont motivé l'utilisation de cette méthodologie, décrite et exploitée dans les chapitres 3, 4 et 5.

### 1.3.2 Études antérieures sur les verres moléculaires à base de triazine

Depuis la parution du premier article sur les verres moléculaires à base de triazine en 2006,[88] plus d'une centaine de composés ont été préparés par le groupe de recherche de Lebel, dont la plupart ont été synthétisés spécifiquement dans le contexte des études de cette thèse. La plupart ont été regroupés en librairies de molécules afin de faciliter l'étude systématique de l'influence de la nature et de la position des groupements substituants $R_1$ à $R_5$ sur la triazine (Figure 1.8) sur leur GFA, leur GS et leur $T_g$, et ainsi établir des relations structure-propriétés. Tel qu'illustré à la Figure 1.11A, la première étude systématique portait sur l'influence du groupement de tête sur plus d'une quarantaine de composés, permettant de déterminer que près des trois quarts de ces derniers formaient facilement une phase vitreuse.[90] Les groupements liants NH et les groupements auxiliaires mexyles (3,5-diméthylphényle) avaient été retenus puisqu'ils favorisaient un bon GFA. Ensuite, le rôle d'un des groupements auxiliaires a été exploré (entre autres par l'auteure de cette thèse) en choisissant le groupement de tête NHMe et les groupements liants NH et en conservant seulement un groupement auxiliaire mexyle.[122] Il a été démontré que le changement du groupement mexyle par d'autres groupements alkyles ou aromatiques portant des méthyles, des alkoxys ou des halogènes ne détériorait pas le GFA des composés, mais pouvait modifier leur $T_g$.

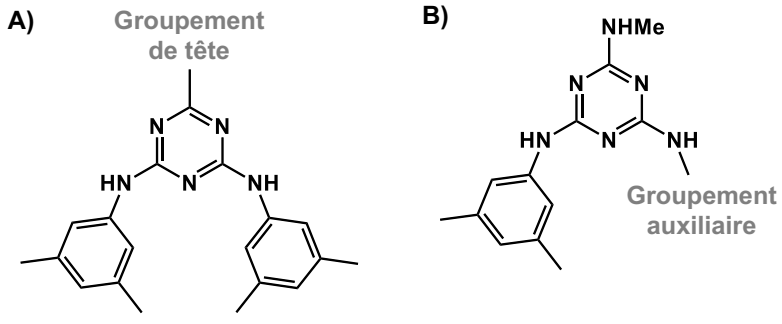


**Figure 1.11.** Structure des molécules étudiées dans les travaux précédents.

D'autres études ont ensuite approfondi l'influence du groupement de tête à l'aide, entre autres, de mesures de viscosité, de calculs de constantes d'association, de résolution de structures cristallines et de spectroscopie IR.[123-124] Les résultats ont mené à l'hypothèse suivante: les liaisons H, rendues possibles par la présence de donneur de liaison H sur les groupements liants (NH) mais aussi sur le groupement de tête dans certains cas, permet aux molécules de former des agrégats qui interagissent faiblement entre eux. Ces derniers empêchent les molécules de s'empiler efficacement tout en limitant leur réarrangement vers l'état cristallin.

Pour mieux comprendre le rôle des liaisons H, des mesures de spectroscopie IR à température variable ont été réalisées.[123] Le ratio normalisé de l'absorbance de la bande d'élongation des groupements NH liés et libres a été tracé en fonction de la température pour une série de composés avec différents groupements de tête (Figure 1.12). Bien que ce paramètre permette d'identifier la $T_g$ des composés (correspondant au changement de pente) et de les comparer de manière relative, il ne renseigne pas sur le nombre de liaisons H dans les phases vitreuse et visqueuse. L'analyse chimiométrique, mentionnée à la section 1.3.1.2 est donc employée dans les travaux de cette thèse pour tenter d'obtenir une estimation quantitative, pouvant être reliée à la $T_g$ des composés.

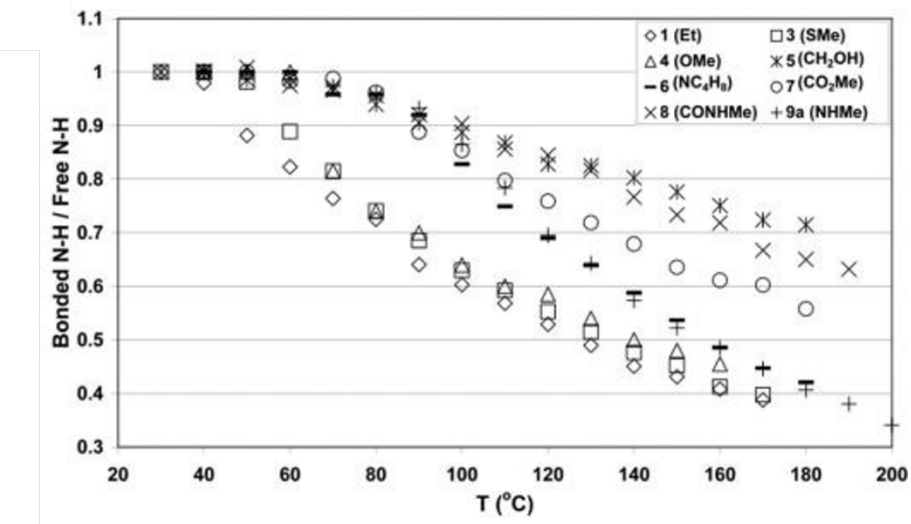


**Figure 1.12.** Évolution du ratio normalisé de l'absorbance des bandes d'élongation des groupements NH liés et libres en fonction de la température pour une série de composés avec différents groupements de tête. Adaptée avec la permission de la référence 123 © 2009 American Chemical Society.

D'autre part, des simulations atomistiques ont été réalisées pour tenter d'établir un lien entre la dynamique des groupements de tête et auxiliaires et la $T_g$ des composés.[125] Cette étude a mis en évidence que la proportion des différents conformères était équivalente, suggérant que la coexistence de conformations d'énergie similaire avait un rôle à jouer dans le GFA des composés. L'ensemble de ces études antérieures confirme l'importance d'approfondir dans cette thèse non seulement l'influence de la nature et de la position des groupements (étudiés au chapitre 2), mais aussi l'intérêt de considérer d'autres paramètres que les liaisons H comme la barrière énergétique de rotation (chapitre 3) et l'influence d'autres types d'interactions (empilements π-π, chapitre 4) pour établir des relations structure-propriétés.

## 1.4 Matériaux moléculaires amorphes fonctionnels et applications

Les verres moléculaires présentés à la section 1.2 étaient principalement étudiés par Shirota, Salbeck et Naito en vue de les intégrer dans des dispositifs opto-électroniques. L'intérêt pour de tels composés fonctionnels est encore présent de nos jours puisqu'une entreprise, *Molecular Glass* Inc., a récemment été fondée par Michel Molaire, dont les verres peuvent agir en tant que transporteurs de charges et même trouver des applications en luminescence, en électronique organique et en photonique.[126] D'ailleurs, des compagnies comme 3M, Xerox, Samsung, Dow, IBM et Kodak détiennent plus d'une centaine de brevets relatifs aux « verres moléculaires » selon la base de données *Lens.org*. Différentes techniques peuvent être employées pour réussir à intégrer ces composés fonctionnalisés dans certains dispositifs opto-électroniques. L'une des méthodes employées par l'industrie est le dépôt physique en phase vapeur (PVD), puisqu'il n'implique pas la présence de solvant.[127]

### 1.4.1 Verres ultrastables

#### 1.4.1.1 Méthode de préparation: dépôt physique en phase vapeur

Le groupe de recherche Ediger a été le premier à démontrer que la déposition en phase vapeur d'un composé peut produire un verre ultrastable, i.e. qui possède les propriétés d'un verre qui aurait subi un recuit de plus d'un millier d'années.[46] Le procédé, tel qu'illustré à la

Figure 1.13A, consiste à chauffer un composé dans une chambre dont la pression est de l'ordre de $10^{-7}$ torr afin de faciliter la vaporisation des molécules. Une fois passées en phase vapeur, elles se déposent sur un substrat. La température du substrat est l'un des paramètres qui permet de contrôler les propriétés résultantes des verres. Un gradient de températures peut donc être appliqué au substrat (d'où la présence de $T_1$ et $T_2$ à la Figure 1.13A) pour produire de façon simultanée différents verres.[128]

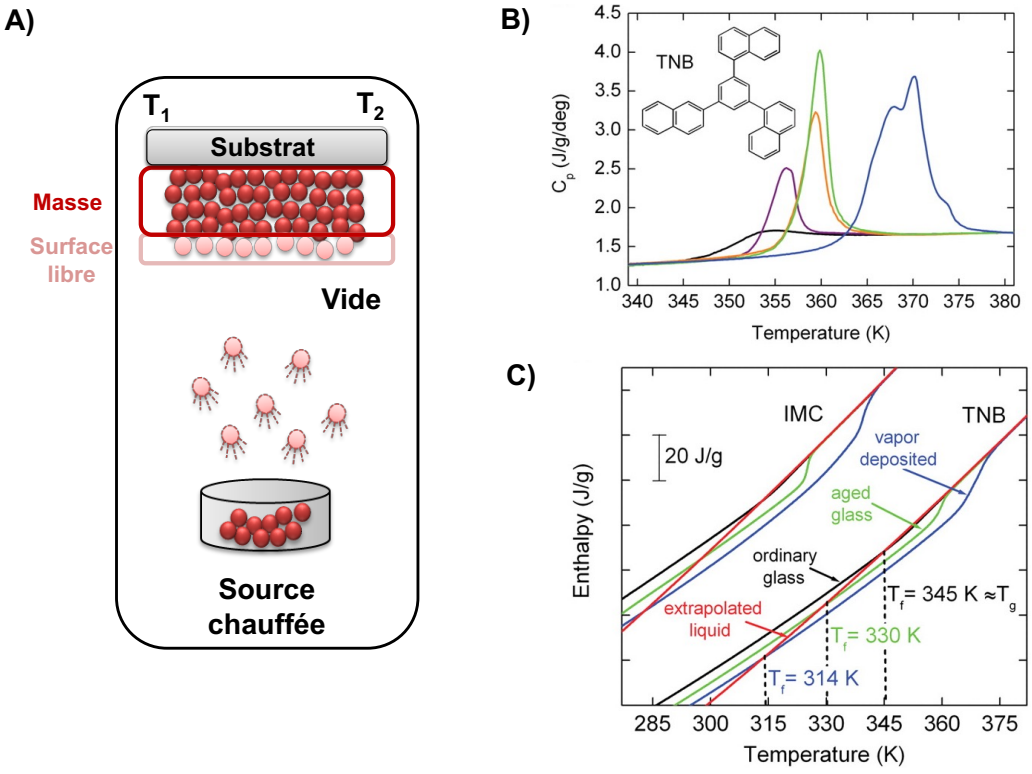


**Figure 1.13.** Fonctionnement général du dépôt physique en phase vapeur (PVD) et exemples représentatifs des propriétés des verres ainsi préparés. A) Schéma du processus PVD utilisant un gradient de températures (de $T_1$ à $T_2$). B) Thermogrammes DSC du verre TNB préparé par PVD à une température de substrat de 296 K à une vitesse de déposition de 5 nm/s (bleu) et refroidi à partir de l'état liquide à 40 K/min (noir). Les autres courbes correspondent à des recuits pendant 174 j à 296 K (violet), 9 j (orangé) et 15 j (vert) à 328 K. C) Comparaison de l'enthalpie en fonction de la température des verres de l'indométacine (IMC) et de TNB déposés par PVD (bleu), ayant subi un recuit (vert, 15 j à 328 K pour le TNB, conditions similaires pour l'IMC), ayant été refroidis à partir de l'état liquide (noir), et de celle extrapolée du liquide (rouge). $T_f$ est la température fictive. Adaptée de la référence 46 avec la permission de AAAS.

### 1.4.1.2 Propriétés des verres préparés par PVD

Si la température du substrat est près de la $T_g$ du composé, entre 0,8 et 0,9 $T_g$, la stabilité du verre sera maximisée.[129] Cette température de substrat serait suffisante pour procurer assez de mobilité aux molécules à la surface libre (Figure 1.13A) du substrat, et éventuellement du film, pour explorer leur profil énergétique (illustré à la Figure 1.2) et ainsi opter pour une conformation qui leur est favorable avant d'être enfouies dans le film suite à l'arrivée des molécules suivantes.[130] Cette possibilité d'explorer le profil énergétique mène à des verres qui ont des propriétés différentes de celles d'un verre qui a été formé par le refroidissement de son état liquide. Tel qu'illustré à la Figure 1.13B et 1.13C, un verre préparé par PVD présente une $T_g$ plus élevée et une enthalpie plus faible que celle d'un verre préparé par le refroidissement depuis son état liquide ou même ayant subi des recuits de l'ordre d'une centaine de jours à la température de déposition sur le substrat. Les verres préparés par PVD sont également plus denses, présentant une différence de densité pouvant aller jusqu'à 1,35%.[129] Les verres PVD présentent également une certaine anisotropie, i.e. que les molécules ont tendance à s'orienter de manière parallèle au substrat lorsque la température de ce dernier est faible ($< 0,7\ T_g$).[129, 131] Finalement, les verres PVD présentent une plus grande stabilité, puisque leur temps de relaxation α ($\tau_\alpha$) peut être jusqu'à $10^5$ plus long que pour un verre préparé par refroidissement dans des conditions isothermes identiques.[132]

### 1.4.1.3 Facteurs influençant les propriétés des verres PVD

Outre la forme de la molécule,[129, 133] les interactions qu'elle peut établir sont susceptibles d'influencer le niveau de stabilité atteignable par les verres préparés par PVD. En effet, il semble y avoir un lien entre la mobilité de surface des molécules et la stabilité que les verres peuvent atteindre. Des mesures de diffusion de surface sur des verres formés par refroidissement du groupe Yu, illustrées à la Figure 1.14, ont montré une certaine corrélation entre la force des interactions intermoléculaires que pouvaient établir certains composés et leur coefficient de diffusion ($D$).[134] En effet, il s'avère que l'indométacine (IMC, en vert), qui est capable d'établir des liaisons H, présente un $D$ plus faible que celui de l'OTP (en bleu), et que sa stabilité est inférieure au verre PVD de l'OTP. Ces résultats suggèrent que les interactions intermoléculaires peuvent ralentir la diffusion de surface et ainsi limiter l'exploration du profil énergétique des

molécules lorsqu'elles atteignent le substrat pendant le PVD. Cette hypothèse est en partie renforcée par des mesures de diffusion de surface sur du PS bien en dessous de sa masse molaire critique d'enchevêtrements (en noir), qui présente un $D_s$ encore plus faible que pour l'IMC et pour lequel la diffusion serait limitée par l'enfouissement de la chaîne de polymère dans l'épaisseur du film et le nombre d'interactions qu'elle peut établir.[135] Ces résultats ont d'ailleurs motivé une récente étude sur des verres PVD préparés à partir de molécules fonctionnalisées avec des groupements OH, montrant qu'une gamme de stabilité cinétique allant de $10^{0,7}$ jusqu'à $10^{3,4}$ $\tau_\alpha$ pouvait être atteinte.[132] Cette étude prouve que les liaisons H jouent un rôle dans la stabilité cinétique d'un verre. C'est pour cette raison que le chapitre 5 relate l'étude de l'influence des liaisons H sur la stabilité cinétique de verres PVD préparés à partir de trois dérivés de la triazine possédant les mêmes groupes liants et auxiliaires, mais dont le groupement de tête présente différentes capacités d'établir des liaisons H (NHMe, OMe et Et).

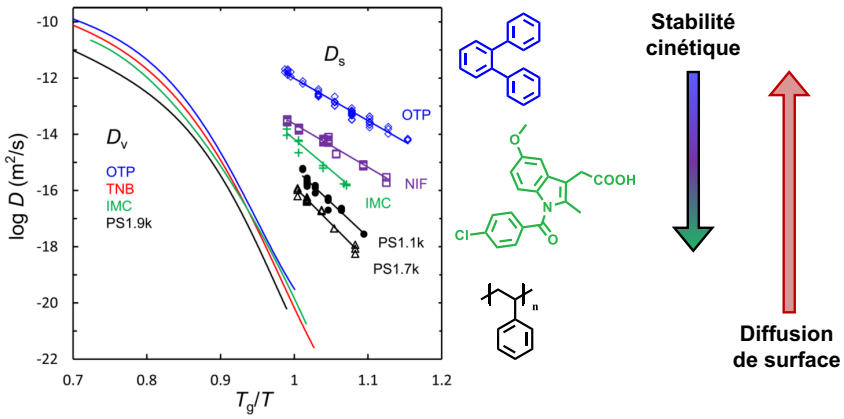


**Figure 1.14.** Coefficients de diffusion de surface ($D_s$) et massique ($D_v$) de différents composés en fonction de la température et suggestion de la relation entre la stabilité cinétique et $D_s$. Adaptée avec la permission de la référence 135 © 2016 American Chemical Society.

## 1.4.2 Verres moléculaires photosensibles

Il est également possible de tirer avantage du GFA des verres moléculaires à base de triazine pour étudier des phénomènes qui sont facilités par l'état amorphe, comme c'est le cas

pour la photoisomérisation des azobenzènes (azo). Bien que des travaux aient déjà été réalisés sur des verres moléculaires fonctionnalisés avec des azos, leur structure n'est pas assez analogue pour permettre une comparaison systématique.[136] Dans le cas des dérivés à base de triazine, il est possible de modifier seulement le groupement azo[137] tout en conservant le GFA des verres, ce qui est particulièrement utile pour isoler l'influence de la nature des groupements azos sur les phénomènes liés à leur photosensibilité. Ces travaux, présentés aux chapitres 6 et 7, sont d'autant plus pertinents considérant que le gDR1, un dérivé de triazine fonctionnalisé avec l'azo *Disperse Red 1* (DR1), illustré à la Figure 1.15A, peut former des réseaux de diffraction (SRG)[138] avec une efficacité similaire à d'autres matériaux amorphes fonctionnalisés avec des azos, mais qu'il peut aussi être utilisé pour des applications de nanolithographie[139] ou d'optique non linéaire.[140]

### 1.4.2.1 Propriétés des azobenzènes

Les dérivés d'azos sont des colorants qui possèdent deux transitions électroniques dans l'UV-visible, i.e. une de type π-π* impliquant les électrons qui sont délocalisés sur l'ensemble de la molécule, et une de type n-π* impliquant les paires d'électrons libres du groupement azo, N=N.[141] Suite à une irradiation dans le domaine de longueurs d'onde correspondant à l'absorption de la transition π-π*, le groupement azo peut subir une photoisomérisation de la forme *trans* à la forme *cis*, tel qu'illustré à la Figure 1.15A. Cette dernière est rapide, soit de l'ordre de quelques picosecondes, et réversible suite à une relaxation thermique ou à une irradiation dans le domaine des longueurs d'ondes de la transition n-π*. Le passage de la forme *trans* à la forme *cis* cause un changement de polarité et une diminution de la distance entre les atomes de carbone aux positions 4 et 4' de l'azo, qui passe de 0,9 nm (*trans*) à 0,55 nm (*cis*).[142] Le processus de photoisomérisation et celui de relaxation sont influencés par le type de groupement substituant sur le dérivé azo (électroattracteur ou électrodonneur) mais aussi par l'environnement des molécules.[143] Par exemple, les verres azo préparés par PVD présentent une plus grande photostabilité, i.e. résistance à la photoisomérisation, que ceux préparés par refroidissement.[144]

Les changements provoqués au niveau moléculaire par la photoisomérisation se reflètent sur les propriétés macroscopiques du matériau, rendant possible des changements de volume,

mais aussi des effets photo-mécaniques.[145-146] Ces déplacements de masse se déroulent souvent bien en dessous de la $T_g$, où les mouvements sont limités, tel qu'explicité à la section 1.1.2. Des hypothèses de « photofluidisation » et/ou de « photoramollissement »[147-148] ont donc été émises autant à partir de travaux expérimentaux que computationnels et sont encore débattues au sein de la communauté scientifique.[149-151] C'est donc dans cette optique que la photoisomérisation du gDR1 est étudiée d'un point de vue moléculaire au chapitre 6.

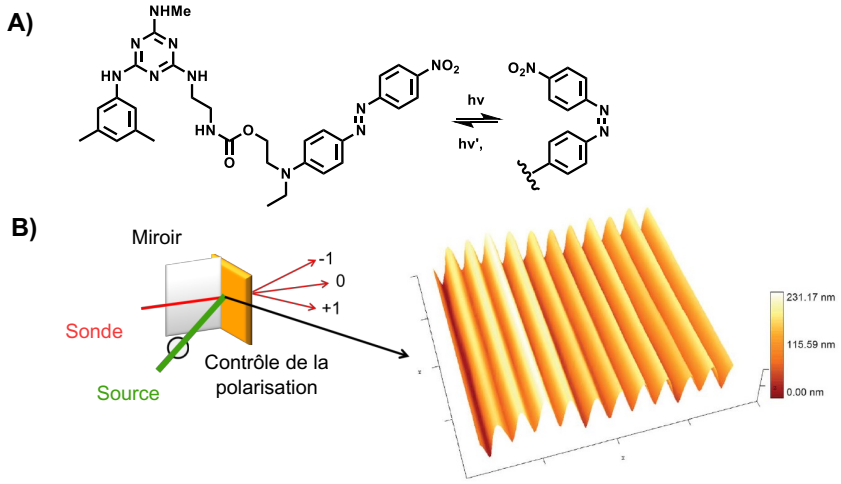


**Figure 1.15.** A) Verre à base de triazine fonctionnalisé avec un azo (gDR1) et son processus de photoisomérisation. B) Montage employé pour l'inscription de SRG et image de microscopie à force atomique d'un SRG préparé à partir d'un film de gDR1. Adaptée de la référence 138 avec la permission de The Royal Society of Chemistry.

Dans le cas où l'irradiation des azos se fait de manière polarisée linéairement, seules les molécules dont le moment dipolaire est partiellement aligné avec le vecteur du champ électrique de la radiation absorbent la lumière, ce qui fera en sorte de créer une anisotropie dans le matériau. En effet, les azos subiront des cycles *trans-cis-trans* qui mèneront éventuellement à l'alignement perpendiculaire des molécules par rapport à la polarisation de l'irradiation.[146] Cette photo-orientation peut être étudiée en temps réel par PM-IRSAS (*polarization modulation infrared structural absorbance spectroscopy*),[152] une méthode de spectroscopie IR polarisée qui permet entre autres de suivre l'orientation de l'azo de manière sélective. Si un patron d'interférence est utilisé pour illuminer la surface d'un film à base d'azo (*voir* Figure 1.15B),

un réseau sera créé à sa surface (SRG).[153-154] La formation de SRGs (qui peuvent être utilisés comme matériel d'optique ou de nanolithographie)[155-158] est influencée par plusieurs paramètres dont les impacts sont difficiles à isoler. L'utilisation de mélanges de verres moléculaires, i.e. des mélanges à bases de gDR1 et de verres non sensibles à la lumière, facilite le découplage de l'effet de la $T_g$ et du contenu en azo. Ces concepts, présentés au chapitre 7, ont permis de dégager des lignes directrices pour optimiser l'inscription de SRG tout en tenant compte de la photo-orientation de l'azo.

## 1.5 Objectifs de la thèse

Le but principal de ce travail doctoral est d'établir des relations entre les caractéristiques moléculaires et le comportement macroscopique des verres moléculaires à base de triazine pour optimiser la préparation et l'utilisation de tels matériaux amorphes dans diverses applications. Les études menées précédemment sur ces composés ont permis de dégager deux hypothèses expliquant leur excellente capacité à former une phase vitreuse, la première étant la présence de liaisons H à l'état visqueux et la seconde étant les agrégats formés par les molécules qui empêchent leur réarrangement efficace en leur état cristallin. Ces hypothèses servent donc de prémisse à l'élaboration des trois objectifs de la thèse, chacun couvert par deux projets. La Figure 1.16 résume les relations entre ces éléments.

Le premier objectif consiste à mieux comprendre l'influence de la position et de la nature des groupements substituants de la triazine sur le GFA et la $T_g$ de ces composés. Deux études antérieures ont permis de déterminer, respectivement, l'influence du groupement de tête et d'un des groupements auxiliaires. Le rôle des deux groupements auxiliaires et celui des deux groupements liants doit être exploré pour rendre possible une synthèse des rôles de chacun. La poursuite du travail préalablement entamé vise également à approfondir l'hypothèse reliant les liaisons H et le GFA en vérifiant notamment si un lien quantitatif existe entre les liaisons H et les valeurs de $T_g$, mais aussi en évaluant si d'autres paramètres, comme l'encombrement stérique ou les énergies de barrières de rotation, influencent le GFA, le GS et la $T_g$ des composés. Cette étape est essentielle pour orienter la conception rationnelle de nouvelles molécules présentant les propriétés désirées.

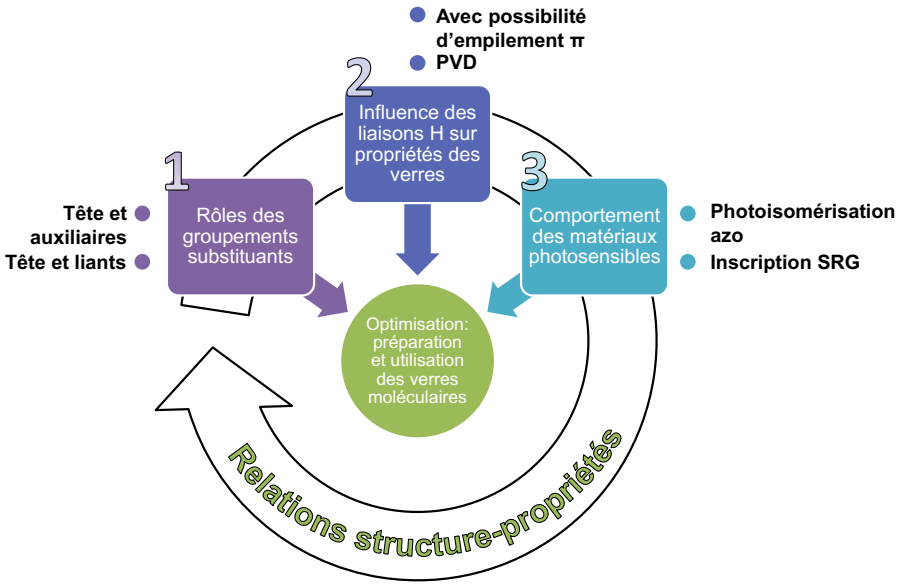


**Figure 1.16**. Schéma des relations entre les trois objectifs de la thèse et des travaux présentés.

Le deuxième objectif consiste à évaluer l'influence des liaisons H sur les propriétés de matériaux amorphes dont la structure moléculaire ou la méthode de préparation diffèrent de celles précédemment étudiées. Tout d'abord, il s'agit de vérifier si les liaisons H peuvent empêcher la cristallisation des composés lorsque d'autres interactions intermoléculaires, reconnues pour leur capacité à entraîner la cristallisation, sont simultanément présentes dans le matériau. Ces interactions sont les empilements π entre des cycles aromatiques perfluorés et non fluorés, qui sont couramment utilisés en tectonique moléculaire pour la conception de structures cristallines. Dans le deuxième cas, il est question d'étudier l'influence des liaisons H impliquant des groupements NH sur la stabilité cinétique des verres préparés par PVD, une méthode fréquemment utilisée en industrie pour préparer des couches minces amorphes.

L'atteinte de ce deuxième objectif est incontournable pour réussir à faire un pont entre l'aspect plus fondamental du premier objectif et celui plus pratique du troisième. Ce dernier consiste à mieux comprendre certains phénomènes reliés à la photosensibilité des matériaux fonctionnalisés avec des azos pour optimiser leur utilisation dans certaines applications. D'abord, le GFA des verres facilite l'étude des changements d'environnement moléculaire impliqués lors de la photoisomérisation d'un azo. L'isomolécularité et la structure des composés permettent aussi de déterminer la $T_g$ idéale pour inscrire des SRGs, un paramètre dont l'influence demeure ambiguë lorsque des matériaux polymériques sont employés. L'atteinte de

cet objectif est complémentaire à celle du premier, c'est-à-dire qu'en connaissant la $T_g$ optimale d'un matériau, il est possible de procéder à un design plus rationnel de verres moléculaires fonctionnels en exploitant les connaissances acquises à propos de l'influence des groupements substituants de la triazine.

## 1.6 Contenu de la thèse

Cette thèse se décline en huit chapitres, dont les six du centre portent chacun sur une librairie de molécules différentes, choisie stratégiquement pour atteindre les objectifs décrits dans la section précédente. La Figure 1.17 illustre ces librairies pour faire ressortir les différences structurales qui ont motivé leur sélection.

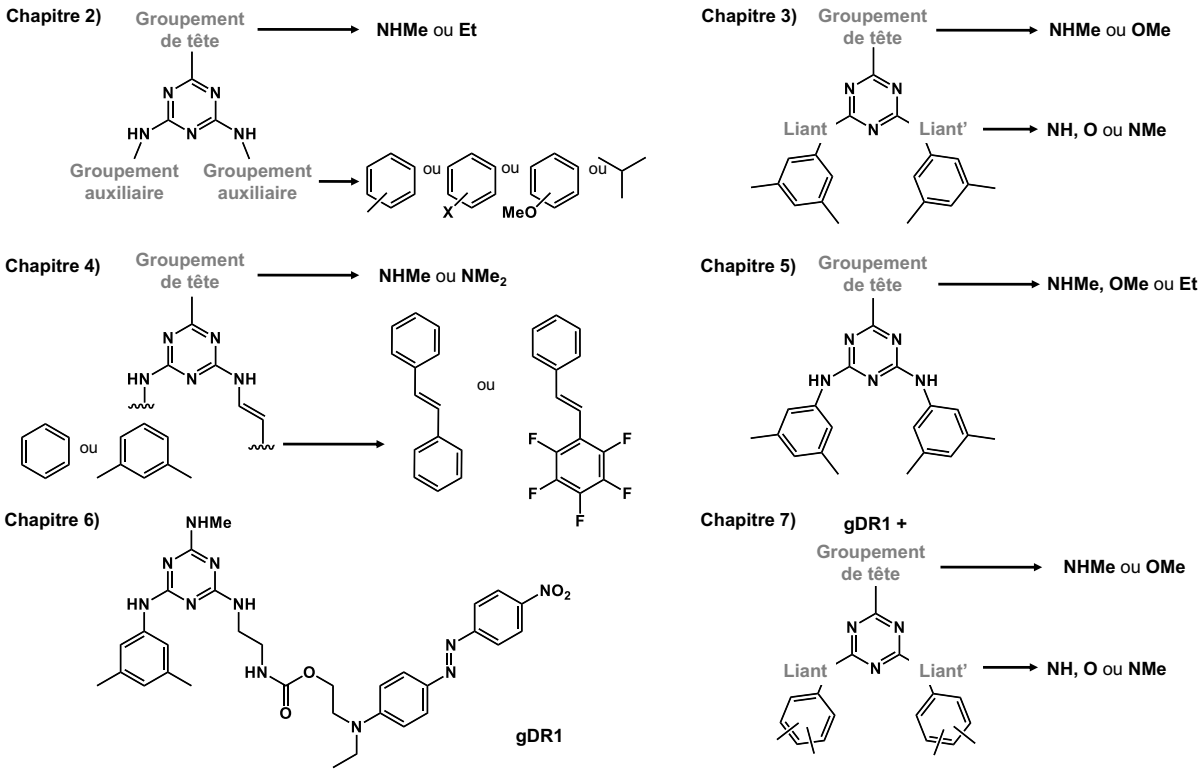


**Figure 1.17.** Répertoire des librairies de composés étudiés dans chaque chapitre.

À la suite de ce chapitre d'introduction, le chapitre 2 porte sur l'influence du groupement de tête et des groupements auxiliaires sur le GFA, le GS et la $T_g$ des composés à l'étude. La moitié d'entre eux comportent une tête NHMe, capable d'établir des liaisons H, alors que l'autre moitié possède une tête Et, incapable d'établir des liaisons H, et sont substitués par deux

groupements auxiliaires identiques qui sont aromatiques (substitués par des méthyles, des alkoxys ou des halogènes) ou alkyles. Une méthode impliquant des mesures de DSC pour comparer et classer les composés selon leur GFA est établie et est d'ailleurs reprise dans les chapitres 3 et 4. Ce chapitre est publié sous forme d'article dans *New Journal of Chemistry* (Laventure, A.; Soldera, A.; Pellerin, C.; Lebel, O. *New J. Chem.* **2013**, *37*, 3881-3889).

Le chapitre 3 concerne l'influence des groupements liants sur le GFA et la $T_g$ des composés. La moitié des composés étudiés porte une tête NHMe et l'autre une tête OMe et ils portent des groupements liants NH, O ou NMe. Chacun d'entre eux permet d'évaluer l'effet d'un paramètre sur le GFA et la $T_g$: la possibilité d'établir une liaison H, la barrière énergétique de rotation et l'encombrement stérique. Le nombre de liaisons H a pu être corrélé à la $T_g$ et à l'enthalpie de formation des liaisons H lors de la vitrification grâce à des mesures de spectroscopie IR à température variable et à une analyse chimiométrique des résultats, approche reprise aux chapitres 4 et 5, tandis que les énergies de barrière de rotation sont estimées par des simulations. Le travail du chapitre 3 est publié sous forme d'article dans *Physical Chemistry Chemical Physics* (Laventure, A.; De Grandpré, G.; Soldera, A.; Lebel, O.; Pellerin, C. *Phys. Chem. Chem. Phys.* **2016**, *18*, 1681-1692).

Le chapitre 4 implique une série de quatre molécules, substituées par un groupement de tête pouvant établir des liaisons H (NHMe) ou ne le pouvant pas ($NMe_2$) et par des groupements auxiliaires stilbènes fluorés et non fluorés. Il démontre que les liaisons H peuvent empêcher la cristallisation d'un composé malgré la présence simultanée d'interactions intermoléculaires $\pi$ qui sont des motifs reconnus pour entraîner la cristallisation. Cette conclusion est appuyée par des résultats de DSC et de spectroscopie IR à température variable, des résolutions de structures cristallines et des estimations d'énergies d'interaction provenant de simulations. Ce chapitre est publié en tant qu'article dans *Crystal Growth & Design* (Laventure, A.; Maris, T.; Pellerin, C.; Lebel, O. *Cryst. Growth Des.* **2017**, doi 10.1021/acs.cgd.6b01567).

Le chapitre 5 porte sur la stabilité cinétique relative de verres préparés par PVD à partir de trois composés qui possèdent une capacité décroissante à établir des liaisons H (groupement de tête NHMe – donneur, OMe – accepteur et Et – aucune). Il est montré que les liaisons H affectent la stabilité cinétique des verres préparés par PVD, puisque les verres du composé substitués d'un groupement de tête NHMe préparés par PVD, dont l'analyse chimiométrique

montre une plus grande quantité de liaisons H à l'état visqueux et vitreux, sont à peine plus stables que les verres NHMe préparés par refroidissement. Toutefois, des mesures d'ellipsométrie, de spectroscopie IR et de diffusion des rayons X aux grands angles permettent de montrer que peu importe le groupement de tête, les verres présentent des propriétés similaires (densité et anisotropie) à celles observées dans de précédentes études sur les verres ultrastables préparés par PVD. Ce chapitre est publié en tant qu'article dans *Journal of Physical Chemistry B* (Laventure, A.; Gujral, A.; Lebel, O.; Pellerin, C.; Ediger, M.D. *J. Phys. Chem. B* **2017**, *121*, 2350-2358).

Le chapitre 6 démontre que la photoisomérisation de l'azobenzène crée un gradient d'environnements moléculaires le long de la molécule substituée par un azo, et ce, autant pour un polymère fonctionnalisé avec un azo en chaîne latérale que pour un verre moléculaire substitué par un azo. L'environnement de la chaîne principale du *poly(Disperse Red 1 acrylate*) (pDR1A) et du cœur du verre triazine reste quasi inchangé tandis que celui de l'azo ressent un effet équivalent à une augmentation de température qui peut atteindre 200 °C. Cette démonstration est rendue possible grâce à l'élaboration d'une nouvelle méthode impliquant des mesures de spectroscopie IR permettant de relier l'environnement moléculaire présent à une certaine température et celui généré par l'irradiation. Elle offre une piste de réflexion au sujet des déplacements macroscopiques athermaux. Ce chapitre est publié en tant qu'article dans *Journal of the American Chemical Society* (Vapaavuori, J.[*]; Laventure, A.[*]; Bazuin, C. G.; Lebel, O.; Pellerin, C., *J. Am. Chem. Soc.* **2015**, *137*, 13510-13517. [*] = contribution égale).

La stratégie employée au chapitre 7 permet de déterminer la $T_g$ idéale pour maximiser la vitesse d'inscription de SRG tout en obtenant une efficacité de diffraction maximale. La structure analogue des verres triazine et leur large gamme de $T_g$ permet de préparer des mélanges photoactifs aux propriétés optiques similaires, et surtout de découpler l'influence de la $T_g$ et du contenu en azo pour en arriver à une conclusion plus générale que certaines obtenues avec des systèmes polymériques. L'étude permet également de montrer que la photo-orientation est un bon indicateur pour prévoir l'efficacité des matériaux à former des SRGs, mais que la rigidité de la matrice doit tout de même être prise en compte. Ce chapitre est publié en tant qu'article dans *ACS Applied Materials & Interfaces* (Laventure, A.; Bourotte, J.; Vapaavuori, J.;

Karperien, L.; Sabat, R.G.; Lebel, O.; Pellerin, C. *ACS Appl. Mater. Interfaces*, **2017**, *9*, 798-808).

Le dernier chapitre consiste en une conclusion, divisée en quatre parties. Les trois premières permettent de faire un retour global sur les trois objectifs principaux de la thèse tandis que la dernière suggère des travaux futurs, répartis selon cinq grands axes de recherche. Ces derniers sont inspirés par les résultats obtenus au cours de ce travail et pourront contribuer à l'avancement des connaissances tant fondamentales que pratiques pour exploiter le plein potentiel des matériaux moléculaires amorphes.

## 1.7 Références


1. Berthier, L.; Ediger, M. D., *Phys. Today* **2016,** *69*, 40-46.
2. Weeks, E. R., *ACS Macro Lett.* **2017,** *6*, 27-34.
3. Salmon, P., *Nat. Mater.* **2002,** *1*, 87-88.
4. Sperling, L. H., The Amorphous State. In *Introduction to Physical Polymer Science*, John Wiley & Sons, Inc.: Hoboken, NJ, 2005; pp 197-238.
5. Jacoby, M., *Chem. Eng. News Archive* **2012,** *90*, 34-36.
6. Pegg, I. L., *Phys. Today* **2015,** *68*, 33-39.
7. Wiley, J. D.; Perepezko, J. H.; Nordman, J. E.; Guo, K. J., *IEEE Trans. Ind. Electron.* **1982,** *IE-29*, 154-157.
8. Abbott, B. P., et al., *Phys. Rev. Lett.* **2016,** *116*, 061102.
9. Tite, M.; Shortland, A.; Paynter, S., *Acc. Chem. Res.* **2002,** *35*, 585-593.
10. Zhao, J.; Simon, S. L.; McKenna, G. B., *Nat. Commun.* **2013,** *4*, 1783.
11. Foster, K. D.; Bronlund, J. E.; Paterson, A. H. J., *J. Food Eng.* **2006,** *77*, 997-1006.
12. Crowe, J. H.; Carpenter, J. F.; Crowe, L. M., *Annu. Rev. Physiol.* **1998,** *60*, 73-103.
13. Fahy, G. M.; MacFarlane, D. R.; Angell, C. A.; Meryman, H. T., *Cryobiology* **1984,** *21*, 407-426.
14. Berthier, L.; Charbonneau, P.; Zamponi, F., *La Recherche* **2016,** 68-72.
15. Hancock, B. C.; Zografi, G., *J. Pharm. Sci.* **1997,** *86*, 1-12.
16. Yu, L., *Adv. Drug. Deliv. Rev.* **2001,** *48*, 27-42.

17. Levine, H., *Amorphous Food and Pharmaceutical Systems*. Royal Society of Chemistry: Cambridge, 2002.
18. Shirota, Y., *J. Mater. Chem.* **2005,** *15*, 75-93.
19. De Silva, A.; Felix, N. M.; Ober, C. K., *Adv. Mater.* **2008,** *20*, 3355-3361.
20. Paus, R.; Ji, Y.; Vahle, L.; Sadowski, G., *Mol. Pharm.* **2015,** *12*, 2823-2833.
21. Shete, G.; Puri, V.; Kumar, L.; Bansal, A. K., *AAPS PharmSciTech* **2010,** *11*, 598-609.
22. Yang, W.; Johnston, K. P.; Williams Iii, R. O., *Eur. J. Pharm. Biopharm.* **2010,** *75*, 33-41.
23. Alqurshi, A., et al., *Mol. Pharm.* **2016,** *13*, 1688-1698.
24. Anseau, M. R.; Weller, P. F., *J. Chem. Educ.* **1973,** *50*, 506.
25. Grewe, T.; Tüysüz, H., *ACS Appl. Mater. Interfaces* **2015,** *7*, 23153-23162.
26. Indra, A.; Menezes, P. W.; Sahraie, N. R.; Bergmann, A.; Das, C.; Tallarida, M.; Schmeisser, D.; Strasser, P.; Driess, M., *J. Am. Chem. Soc.* **2014,** *136*, 17530-6.
27. Li, H. B.; Yu, M. H.; Lu, X. H.; Liu, P.; Liang, Y.; Xiao, J.; Tong, Y. X.; Yang, G. W., *ACS Appl. Mater. Interfaces* **2014,** *6*, 745-749.
28. Tian, F.; Radin, M. D.; Siegel, D. J., *Chem. Mater.* **2014,** *26*, 2952-2959.
29. US Department of Energy - Office of Science. "Research: Grand Challenges". https://science.energy.gov/bes/efrc/research/grand-challenges/ (page consultée le 20 février 2017).
30. The National Institute for Pharmaceutical Technology and Education. "Pharmaceutical Research Impact". http://www.nipte.org/content/pharmaceutical-research-impact (page consultée le 20 février 2017).
31. Lorenz, M., et al., *J. Phys. D: Appl. Phys.* **2016,** *49*, 433001.
32. Turnbull, D.; Cohen, M. H., *J. Chem. Phys.* **1958,** *29*, 1049-1054.
33. Li, H. F.; Zheng, Y. F., *Acta Biomater.* **2016,** *36*, 1-20.
34. Plummer, J., *Nat. Mater.* **2015,** *14*, 553-555.
35. Zhang, S.; Lu, X.; Zhou, Q.; Li, X.; Zhang, X.; Li, S., *Ionic Liquids: Physicochemical Properties*. Elsevier Science: Amsterdam, 2009.
36. Collings, P. J.; Hird, M., *Introduction to Liquid Crystals: Chemistry and Physics*. Taylor & Francis: London, Bristol PA, 1997.

37. Sperling, L. H., Multicomponent Polymeric Materials. In *Introduction to Physical Polymer Science*, John Wiley & Sons, Inc.: Hoboken, NJ, 2005; pp 687-756.
38. Evans, J. D.; Huang, D. M.; Hill, M. R.; Sumby, C. J.; Sholl, D. S.; Thornton, A. W.; Doonan, C. J., *J. Phys. Chem. C* **2015,** *119*, 7746-7754.
39. Bennett, T. D.; Cheetham, A. K., *Acc. Chem. Res.* **2014,** *47*, 1555-1562.
40. Sangoro, J.; Kremer, F., *Acc. Chem. Res.* **2011,** *45*, 525-532.
41. Margraf, J. T.; Strauss, V.; Guldi, D. M.; Clark, T., *J. Phys. Chem. B* **2015,** *119*, 7258-7265.
42. Dette, H. P.; Koop, T., *J. Phys. Chem. A* **2014,** *119*, 4552-61.
43. Koop, T.; Bookhold, J.; Shiraiwa, M.; Pöschl, U., *Phys. Chem. Chem. Phys.* **2011,** *13*, 19238-55.
44. Laitinen, R.; Löbmann, K.; Grohganz, H.; Strachan, C.; Rades, T., *Mol. Pharm.* **2014,** *11*, 2381-2389.
45. Guo, Y., et al., *Nat. Mater.* **2012,** *11*, 337-343.
46. Swallen, S. F.; Kearns, K. L.; Mapes, M. K.; Kim, Y. S.; McMahon, R.; Ediger, M. D.; Wu, T.; Yu, L.; Satija, S., *Science* **2006,** *315*, 353-356.
47. McNamara, D.; Yin, S.; Pan, D.; Crull, G.; Timmins, P.; Vig, B., *Mol. Pharm.* **2017,** *14*, 377-385.
48. Sperling, L. H., Glass-Rubber Transition Behavior. In *Introduction to Physical Polymer Science*, John Wiley & Sons, Inc.: Hoboken, NJ, 2005; pp 349-425.
49. Ediger, M. D.; Angell, C. A.; Nagel, S. R., *J. Phys. Chem.* **1996,** *100*, 13200-13212.
50. McKenna, G. B.; Simon, S. L., Chapter 2 - The glass transition: its measurement and underlying physics. In *Handbook of Thermal Analysis and Calorimetry*, Cheng, S. Z. D., Ed. Elsevier Science B.V.: Amsterdam, 2002; Vol. 3, pp 49-109.
51. Debenedetti, P. G.; Stillinger, F. H., *Nature* **2001,** *410*, 259-267.
52. Angell, C. A.; Ngai, K. L.; McKenna, G. B.; McMillan, P. F.; Martin, S. W., *J. Appl. Phys.* **2000,** *88*, 3113-3157.
53. Kauzmann, W., *Chem. Rev.* **1948,** *43*, 219-256.
54. Mauro, J. C.; Zanotto, E. D., *Int. J. Appl. Glass Sci.* **2014,** *5*, 313-327.
55. Gibbs, J. H.; DiMarzio, E. A., *J. Chem. Phys.* **1958,** *28*, 373-383.
56. Doolittle, A. K., *J. Appl. Phys.* **1951,** *22*, 1031-1035.

57. Doolittle, A. K., *J. Appl. Phys.* **1951,** *22*, 1471-1475.
58. Doolittle, A. K.; Doolittle, D. B., *J. Appl. Phys.* **1957,** *28*, 901-905.
59. Williams, M. L.; Landel, R. F.; Ferry, J. D., *J. Am. Chem. Soc.* **1955,** *77*, 3701-3707.
60. Di Marzio, E. A.; Yang, A. J. M., *J. Res. Natl Inst. Stand. Technol.* **1997,** *102*, 135-157.
61. Adam, G.; Gibbs, J. H., *J. Chem. Phys.* **1965,** *43*, 139-146.
62. Ediger, M. D., *Annu. Rev. Phys. Chem.* **2000,** *51*, 99-128.
63. Freed, K. F., *Acc. Chem. Res.* **2011,** *44*, 194-203.
64. Mirigian, S.; Schweizer, K. S., *J. Chem. Phys.* **2015,** *143*, 244705.
65. Angell, C. A., *J. Non-Cryst. Solids* **1991,** *131*, 13-31.
66. Martinez, L. M.; Angell, C. A., *Nature* **2001,** *410*, 663-667.
67. Mauro, N. A.; Blodgett, M.; Johnson, M. L.; Vogt, A. J.; Kelton, K. F., *Nat. Commun.* **2014,** *5*, 4616.
68. Wang, L.-M.; Mauro, J. C., *J. Chem. Phys.* **2011,** *134*, 044522.
69. Webb, S. L., Silica melts at extreme conditions. In *European Mineralogical Union Notes in Mineralogy*, Papp, G.; Weiszburg, T. G., Eds. Eötvös University Press: Budapest, 2005; Vol. 7.
70. Dalle-Ferrier, C.; Kisliuk, A.; Hong, L.; Carini Jr., G.; Carini, G.; D'Angelo, G.; Alba-Simionesco, C.; Novikov, V. N.; Sokolov, A. P., *J. Chem. Phys.* **2016,** *145*, 154901.
71. Montarnal, D.; Capelot, M.; Tournilhac, F.; Leibler, L., *Science* **2011,** *334*, 965-968.
72. Capelot, M.; Unterlass, M. M.; Tournilhac, F.; Leibler, L., *ACS Macro Lett.* **2012,** *1*, 789-792.
73. Lu, Z. P.; Liu, C. T., *Acta Mater.* **2002,** *50*, 3501-3512.
74. Nascimento, M. L. F.; Souza, L. A.; Ferreira, E. B.; Zanotto, E. D., *J. Non-Cryst. Solids* **2005,** *351*, 3296-3308.
75. Goldschmidt, V. Skrifter Norske Videnskaps. Akad. (Oslo) I, *Matematisch-Naturwiss. Klasse 1* **1926,** 7.
76. Gutzow, I. S.; Schmelzer, J. W. P., *The Vitreous State: Thermodynamics, Structure, Rheology, and Crystallization*. Springer: Berlin Heidelberg, 2013.
77. Turnbull, D.; Cohen, M. H., *J. Chem. Phys.* **1958,** *29*, 1049-1054.
78. Ping, W.; Paraska, D.; Baker, R.; Harrowell, P.; Angell, C. A., *J. Phys. Chem. B* **2011,** *115*, 4696-4702.

79. Kawakami, K.; Harada, T.; Yoshihashi, Y.; Yonemochi, E.; Terada, K.; Moriyama, H., *J. Phys. Chem. B* **2015,** *119*, 4873-4880.
80. Baird, J.; Santiago-Quinonez, D.; Rinaldi, C.; Taylor, L. S., *Pharm. Res.* **2012,** *29*, 271-84.
81. Uhlmann, D. R., *J. Non-Cryst. Solids* **1972,** *7*, 337-348.
82. Blaabjerg, L. I.; Lindenberg, E.; Lobmann, K.; Grohganz, H.; Rades, T., *Mol. Pharm.* **2016,** *13*, 3318-25.
83. Salbeck, J.; Yu, N.; Bauer, J.; Weissörtel, F.; Bestgen, H., *Synth. Met.* **1997,** *91*, 209-215.
84. Yu, L.; Reutzel-Edens, S. M.; Mitchell, C. A., *Org. Process Res. Dev.* **2000,** *4*, 396-402.
85. Naito, K.; Miura, A., *J. Phys. Chem.* **1993,** *97*, 6240-6248.
86. Pedersen, U. R.; Harrowell, P., *J. Phys. Chem. B* **2011,** *115*, 14205-14209.
87. Damasceno, P. F.; Engel, M.; Glotzer, S. C., *Science* **2012,** *337*, 453-457.
88. Lebel, O.; Maris, T.; Perron, M.-È.; Demers, E.; Wuest, J. D., *J. Am. Chem. Soc.* **2006,** *128*, 10372-10373.
89. Lebel, O. Molecular glasses with functionalizable groups - US009346768B2. 2016.
90. Wuest, J. D.; Lebel, O., *Tetrahedron* **2009,** *65*, 7393-7402.
91. Wicker, J.; Cooper, R., *CrystEngComm* **2014,** *17*, 1927-1934.
92. Wyttenbach, N.; Kirchmeyer, W.; Alsenz, J.; Kuentz, M., *Mol. Pharm.* **2016,** *13*, 241-50.
93. Wyttenbach, N.; Kuentz, M., *Eur. J. Pharm. Biopharm.* **2017,** *112*, 204-208.
94. Cowie, J. M. G., *Polymers: Chemistry and Physics of Modern Materials, 2nd Edition*. Taylor & Francis: Boca Raton, FL, 1991.
95. Alba-Simionesco, C.; Fan, J.; Angell, C. A., *J. Chem. Phys.* **1999,** *110*, 5262-5272.
96. Alba, C.; Busse, L. E.; List, D. J.; Angell, C. A., *J. Chem. Phys.* **1990,** *92*, 617-624.
97. Whitaker, C. M.; McMahon, R. J., *J. Phys. Chem.* **1996,** *100*, 1081-1090.
98. Liu, T.; Cheng, K.; Salami-Ranjbaran, E.; Gao, F.; Glor, E. C.; Li, M.; Walsh, P. J.; Fakhraai, Z., *Soft Matter* **2015,** *11*, 7558-7566.
99. Baird, J. A.; Van Eerdenbrugh, B.; Taylor, L. S., *J. Pharm. Sci.* **2010,** *99*, 3787-3806.
100. Alhalaweh, A.; Alzghoul, A.; Kaialy, W.; Mahlin, D.; Bergström, C. A. S., *Mol. Pharm.* **2014,** *11*, 3123-3132.

101. Mahlin, D.; Ponnambalam, S.; Heidarian Höckerfelt, M.; Bergström, C. A. S., *Mol. Pharm.* **2011,** *8*, 498-506.
102. Nurzyńska, K.; Booth, J.; Roberts, C. J.; McCabe, J.; Dryden, I.; Fischer, P. M., *Mol. Pharm.* **2015,** *12*, 3389-3398.
103. Desiraju, G. R., *Crystal engineering: the design of organic solids*. Elsevier: Amsterdam and New York, 1989.
104. Steiner, T., *Angew. Chem. Int. Ed.* **2002,** *41*, 48-76.
105. Jeffrey, G. A., *An Introduction to Hydrogen Bonding*. Oxford University Press: New York, 1997.
106. Saenger, W., Forces Stabilizing Associations Between Bases: Hydrogen Bonding and Base Stacking. In *Principles of Nucleic Acid Structure*, Springer New York: New York, NY, 1984; pp 116-158.
107. Mignon, P.; Loverix, S.; Steyaert, J.; Geerlings, P., *Nucleic Acids Res.* **2005,** *33*, 1779-1789.
108. Desiraju, G. R., *Acc. Chem. Res.* **2002,** *35*, 565-573.
109. Xiao, W. C.; Hu, C. H.; Ward, M. D., *J. Am. Chem. Soc.* **2014,** *136*, 14200-14206.
110. Aytun, T.; Barreda, L.; Ruiz-Carretero, A.; Lehrman, J. A.; Stupp, S. I., *Chem. Mater.* **2015,** *27*, 1201-1209.
111. Xiao, Z.; Sun, K.; Subbiah, J.; Ji, S.; Jones, D. J.; Wong, W. W. H., *Sci. Rep.* **2014,** *4*, 5701.
112. Habgood, M.; Lancaster, R. W.; Gateshki, M.; Kenwright, A. M., *Cryst. Growth Des.* **2013,** *13*, 1771-1779.
113. Rothfuss, N. E.; Petters, M. D., *Environ. Sci. Technol.* **2017,** *51*, 271-279.
114. Chalmers, J. M., Mid-Infrared Spectroscopy of the Condensed Phase. In *Handbook of Vibrational Spectroscopy*, Chalmers, J.; M.; Griffiths, P. R., Eds., Eds. John Wiley & Sons, Ltd: Chichester, 2001; Vol. 1, p 128.
115. Tang, X. C.; Pikal, M. J.; Taylor, L. S., *Pharm. Res.* **2002,** *19*, 477-483.
116. Van Eerdenbrugh, B.; Lo, M.; Kjoller, K.; Marcott, C.; Taylor, L. S., *J. Pharm. Sci.* **2012,** *101*, 2066-2073.
117. Wegiel, L. A.; Mauer, L. J.; Edgar, K. J.; Taylor, L. S., *J. Pharm. Pharmacol.* **2014,** *66*, 244-255.

118. Kaushal, A. M.; Chakraborti, A. K.; Bansal, A. K., *Mol. Pharm.* **2008,** *5*, 937-945.
119. Imamura, K.; Sakaura, K.; Ohyama, K.-i.; Fukushima, A.; Imanaka, H.; Sakiyama, T.; Nakanishi, K., *J. Phys. Chem. B* **2006,** *110*, 15094-15099.
120. Gemperline, P., *Practical Guide To Chemometrics, Second Edition*. CRC Press: Boca Raton, FL, 2006.
121. Šašić, S.; Segtnan, V. H.; Ozaki, Y., *J. Phys. Chem. A* **2002,** *106*, 760-766.
122. Eren, R. N., et al., *Tetrahedron* **2012,** *68*, 10130-10144.
123. Plante, A.; Mauran, D.; Carvalho, S. P.; Pagé, J. Y. S. D.; Pellerin, C.; Lebel, O., *J. Phys. Chem. B* **2009,** *113*, 14884-14891.
124. Wang, R.; Pellerin, C.; Lebel, O., *J. Mater. Chem.* **2009,** *19*, 2747-2753.
125. Plante, A.; Palato, S.; Lebel, O.; Soldera, A., *J. Mater. Chem. C* **2013,** *1*, 1037-1042.
126. Molecular Glasses, Inc. http://molecularglasses.com/content/our-company (page consultée le 20 février 2017).
127. Tang, C. W.; VanSlyke, S. A., *Appl. Phys. Lett.* **1987,** *51*, 913-915.
128. Dalal, S. S.; Fakhraai, Z.; Ediger, M. D., *J. Phys. Chem. B* **2013,** *117*, 15415-15425.
129. Dalal, S. S.; Walters, D. M.; Lyubimov, I.; de Pablo, J. J.; Ediger, M. D., *Proc. Natl. Acad. Sci. USA* **2015,** *112*, 4227-4232.
130. Chen, Y.; Zhang, W.; Yu, L., *J. Phys. Chem. B* **2016,** *120*, 8007-8015.
131. Gujral, A.; O'Hara, K. A.; Toney, M. F.; Chabinyc, M. L.; Ediger, M. D., *Chem. Mater.* **2015,** *27*, 3341-3348.
132. Tylinski, M.; Chua, Y. Z.; Beasley, M. S.; Schick, C.; Ediger, M. D., *J. Chem. Phys.* **2016,** *145*, 174506.
133. Yokoyama, D.; Setoguchi, Y.; Sakaguchi, A.; Suzuki, M.; Adachi, C., *Adv. Funct. Mater.* **2010,** *20*, 386-391.
134. Zhang, W.; Brian, C. W.; Yu, L., *J. Phys. Chem. B* **2015,** *119*, 5071-5078.
135. Zhang, W.; Yu, L., *Macromolecules* **2016,** *49*, 731-735.
136. Snell, K. E.; Hou, R.; Ishow, E.; Lagugné-Labarthet, F., *Langmuir* **2015,** *31*, 7296-7305.
137. Bennani, O. R.; Al-Hujran, T. A.; Nunzi, J.-M.; Sabat, R. G.; Lebel, O., *New J. Chem.* **2015,** *39*, 9162-9170.
138. Kirby, R.; Sabat, R. G.; Nunzi, J.-M.; Lebel, O., *J. Mater. Chem. C* **2014,** *2*, 841-847.
139. Umezawa, H.; Nunzi, J.-M.; Lebel, O.; Sabat, R. G., *Langmuir* **2016,** *32*, 5646-5652.

140. Umezawa, H.; Jackson, M.; Lebel, O.; Nunzi, J.-M.; Sabat, R. G., *Opt. Mater.* **2016,** *60*, 258-263.
141. Bandara, H. M. D.; Burdette, S. C., *Chem. Soc. Rev.* **2012,** *41*, 1809-1825.
142. Kumar, G. S.; Neckers, D. C., *Chem. Rev.* **1989,** *89*, 1915-1925.
143. Gore, P. H.; Wheeler, O. H., *J. Org. Chem.* **1961,** *26*, 3295-3298.
144. Qiu, Y.; Antony, L. W.; de Pablo, J. J.; Ediger, M. D., *J. Am. Chem. Soc.* **2016,** *138*, 11282-9.
145. Baroncini, M., et al., *Nat. Chem.* **2015,** *7*, 634-40.
146. Natansohn, A.; Rochon, P., *Chem. Rev.* **2002,** *102*, 4139-4176.
147. Hurduc, N.; Donose, B. C.; Rocha, L.; Ibanescu, C.; Scutaru, D., *RSC Adv.* **2016,** *6*, 27087-27093.
148. Fang, G. J.; Maclennan, J. E.; Yi, Y.; Glaser, M. A.; Farrow, M.; Korblova, E.; Walba, D. M.; Furtak, T. E.; Clark, N. A., *Nat. Commun.* **2013,** *4*, 1521.
149. Bedrov, D.; Hooper, J. B.; Glaser, M. A.; Clark, N. A., *Langmuir* **2016,** *32*, 4004-4015.
150. Seki, T., *J. Mater. Chem. C* **2016,** *4*, 7895-7910.
151. Saphiannikova, M.; Toshchevikov, V., *J. Soc. Inf. Disp.* **2015,** *23*, 146-153.
152. Liang, Y.; Mauran, D.; Prud'homme, R. E.; Pellerin, C., *Appl. Spectrosc.* **2008,** *62*, 941-947.
153. Rochon, P.; Batalla, E.; Natansohn, A., *Appl. Phys. Lett.* **1995,** *66*, 136-138.
154. Kim, D. Y.; Tripathy, S. K.; Li, L.; Kumar, J., *Appl. Phys. Lett.* **1995,** *66*, 1166-1168.
155. Gombert, A.; Rose, K.; Heinzel, A.; Horbelt, W.; Zanke, C.; Bläsi, B.; Wittwer, V., *Sol. Energ. Mat. Sol. Cells* **1998,** *54*, 333-342.
156. Kang, J.-W.; Kim, M.-J.; Kim, J.-P.; Yoo, S.-J.; Lee, J.-S.; Kim, D. Y.; Kim, J.-J., *Appl. Phys. Lett.* **2003,** *82*, 3823-3825.
157. Kravchenko, A.; Shevchenko, A.; Ovchinnikov, V.; Priimagi, A.; Kaivola, M., *Adv. Mater.* **2011,** *23*, 4174-4177.
158. Yager, K. G.; Barrett, C. J., Amorphous Azobenzene Polymers for Light-Induced Surface Patterning. In *Smart Light-Responsive Materials*, Zhao, Y.; Ikeda, T., Eds. John Wiley & Sons, Inc.: Hoboken, NJ, 2008; pp 145-175.

# Chapitre 2: Heads vs. tails: a double-sided study of the influence of substituents on glass-forming ability and stability of aminotriazine molecular glasses*

## 2.1 Abstract


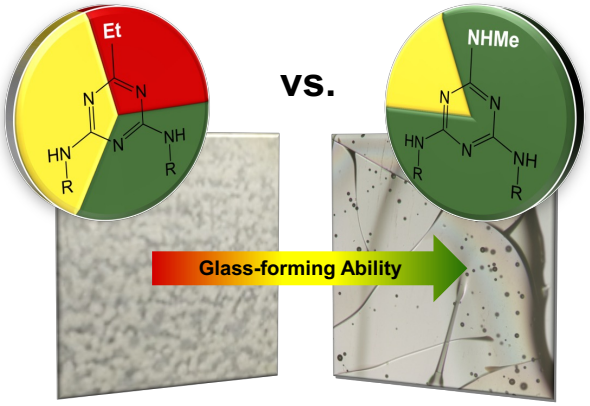


Mexylaminotriazine derivatives are known to spontaneously form long-lived glassy phases. The role played by various structural elements on their glass formation has been studied, but the effect of substituting both arylamino substituents remains largely unknown. A library of 4,6-bis(arylamino)- or 4,6-bis(alkylamino)-1,3,5-triazine derivatives with a methylamino or ethyl substituent in the 2-position were synthesized, and their glass-forming properties were studied. While the 3,5-disubstituted aryl motif proved to be the best among those studied for promoting glass formation, glass-forming ability and stability were found to be in large part influenced by the "headgroup" at the 2-position of the triazine ring, with dramatic differences in glass-forming behavior observed from one headgroup to the other.


## 2.2 Introduction

The ability of organic or inorganic compounds to adopt a glassy phase, as opposed to more ordered crystalline phases, is commonly associated with inorganic glasses (e.g. $SiO_2$) or polymers, which are ubiquitously used in a wide variety of materials.[1] Small molecules are also capable of adopting a glassy state under certain extreme conditions, such as rapid cooling from the melt, freeze-drying and spray-drying, causing the molecules to solidify at a rate quicker than

---

* Publié en tant qu'article dans *New Journal of Chemistry*: Laventure, A.; Soldera, A.; Pellerin, C.; Lebel, O. *New J. Chem.* **2013**, *37*, 3881-3889. O.L. a procédé à la synthèse des composés et à leur caractérisation de base.

their rate of crystallization.[2] However, it has already been shown that some compounds can readily form glassy states under ambient conditions without such treatments, if they present some of the following "typical" features: a globular and irregular shape, a poor packing, a structure with few elements of symmetry, the capability to adopt multiple conformations, and the formation of weak and non-specific interactions with neighboring molecules.[3,4] These compounds, called molecular glasses or amorphous molecular materials, are prized for various applications ranging from opto-electronics[5-7] to nanolithography,[8-10] nanopatterning, and amorphous drug formulations.[11-14] Unlike polymers, small molecules offer the advantages of being easier to purify, characterize and process, which are counterbalanced by their higher (often undesirable) propensity to crystallize upon heating or prolonged standing.[15-17]

The correlation between a compound's molecular structure, its propensity to form glasses, its glass transition temperature ($T_g$), and its mechanical properties remains poorly understood.[18] This is exacerbated by the fact that the very nature of the glass transition itself is equally misunderstood.[1,2,15] As a result, molecular glass design relies heavily on trial and error assisted by some structural guidelines.[18] Molecular glasses must be designed to possess structures that impede crystallization: features that promote and direct crystallization must be avoided at all costs.

Mexylaminotriazines have revealed themselves as a stimulating class of glass-forming compounds from both fundamental and applied standpoints.[19] In opposition to "conventional" molecular glasses, mexylaminotriazines are relatively rigid, symmetrical, and they can self-assemble by hydrogen bonding in a predictable fashion.[20-22] Their molecular structures can be easily tuned to display a wide range of $T_g$ and physical properties.[23,24] For instance, it is possible to design glasses incorporating functionality such as chromophores, as was demonstrated with tetraphenylporphyrin.[25] Because of these characteristics, mexylaminotriazines constitute an extremely appealing model to gain a better understanding of the glassy state and how certain structures can access it with a higher propensity. Furthermore, the presence of hydrogen bonding results in very high stability of the glassy phase, which we define in this paper as the kinetic

resistance of the glass to crystallization, thus paving the way for simple and well-defined strategies for designing high-performance glasses for practical applications.

In previous work, the role of the "headgroup" at the 2-position has been studied and was shown to have a significant impact on both glass-forming ability and $T_g$, with most derivatives readily forming glasses.[23] It was also shown that replacing one of the two mexylamino "tail" groups with various arylamino or cycloalkylamino substituents resulted in retention of glass-forming ability and stability.[24] The effect of substituting both mexylamino groups, on the other hand, has not been documented yet, and while there have been other bis(arylamino)-1,3,5-triazine derivatives reported in the literature,[26] their glass-forming properties have not been probed in detail.

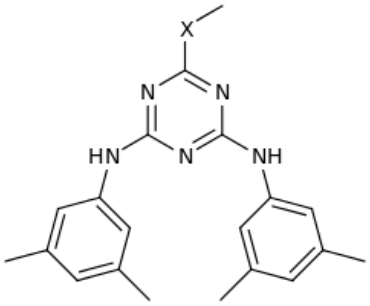


**1a:** X = NH
**1b:** X = $CH_2$

The present study thus aims to monitor the impact of aryl group structure on glass-forming ability (GFA), glass stability (GS) and $T_g$ for the diaminotriazine skeleton. To accomplish so, a library of diaminotriazine derivatives bearing various aryl and alkyl groups were synthesized, and their thermal properties were characterized. The effect of the headgroup was also taken into account, by synthesizing two series of compounds, one with a methylamino headgroup, which has been shown to result in extremely stable glasses, and one with an ethyl headgroup, which is known to yield marginally stable glasses, as exemplified by bis(mexylamino) parent compounds **1a-b**.[19,23] Unexpectedly, the headgroup proved to have a tremendous impact on glass-forming properties, with most ancillary amino groups studied showing radically different behavior from one headgroup to the other. Most compounds from the methylamino series readily formed stable glasses, even under slow cooling conditions. In contrast, several ethyl-substituted derivatives crystallized upon slow cooling and almost all of them crystallized upon heating. Glass-forming ability thus stems from the structures of the headgroup and the amino groups acting in concert to frustrate crystallization; however, the results with the ethyl-substituted series have pinpointed the 3,5- substitution pattern to be the best for promoting glass formation.

## 2.3 Results and discussion

### 2.3.1 Synthesis

Derivatives with two identical aryl groups **2** and **4** (individual structures are listed in Table 2.1) were synthesized in 60-94% yields from the respective 4,6-dichloro-1,3,5-triazine precursors and excess (2.2 equiv) anilines in refluxing THF or dioxane (Scheme 2.1). The reaction did not require the presence of a base to occur. Typically, yields were higher and reaction times were shorter with the weakly electron-donating ethyl chain as headgroup. For the methylamino headgroup, the reaction with ortho-substituted anilines required longer reaction times (3 days) to reach completion, while bulkier 2,6-disubstituted anilines required the reaction to be run in refluxing dioxane for both headgroups.

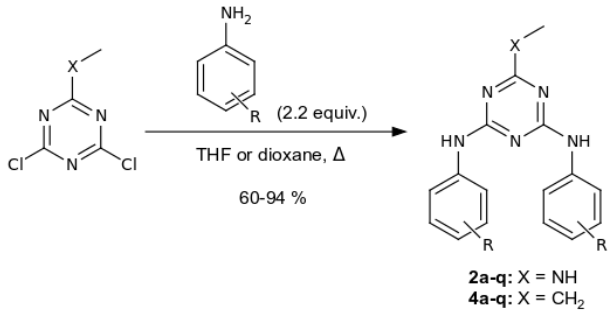


**Scheme 2.1.** Synthesis of compounds **2a-q** and **4a-q**.

Typically, only an extraction with aqueous acid was required to remove the excess aniline. For anilines with lower solubility in acidic aqueous media (3,5-dibromoaniline, 3,5-diiodoaniline and 3,5-di-tert-butylaniline), however, some aniline typically remained, but could be removed by trituration in hot methanol followed by filtration.

Derivatives with alkylamino groups 3 and 5 were synthesized by a similar procedure, by refluxing the respective 4,6-dichloro-1,3,5-triazines with a large excess of amine in THF (Scheme 2.2).

4,6-Di-tert-butylamino-2-methylamino-1,3,5-triazine (5b) could not be synthesized in an acceptable yield by this method; it was instead synthesized from 4,6-di-tert-butylamino-2-chloro-1,3,5-triazine and aqueous methylamine in refluxing THF (Scheme 2.3).

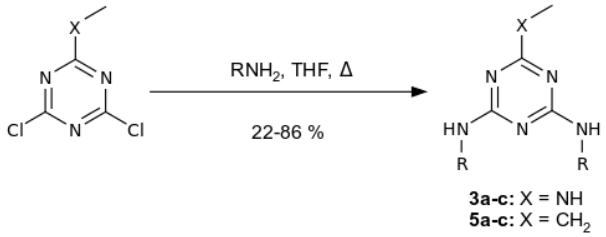


**Scheme 2.2**. Synthesis of compounds **3a/c** and **5a-c**.

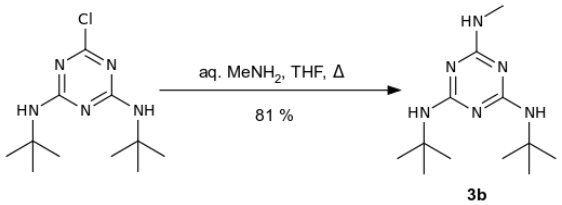


**Scheme 2.3**. Synthesis of compound **3b**.

As with other glass-forming aminotriazines, solvents, and especially THF and dioxane, are difficult to remove completely, and require melting the compounds under vacuum to obtain completely dry samples.

For compounds **2-3** with a methylamino headgroup, $^{1}$H NMR spectra recorded at ambient temperature typically showed broad ortho signals and two distinct signals for both ArN-H protons, which is a consequence of hindered rotation of the strongly conjugated methylamino group, and which has already been documented in our previous work.[24] This problem could be solved by recording the spectra at 90 $^{o}$C, which resulted in sharp, well-defined signals. $^{13}$C NMR spectra often also showed some split peaks for aromatic signals, and sometimes for the triazine carbon atoms bonded to the ArNH groups. On the other hand, compounds **4-5** with freely rotating ethyl headgroups did not show this behavior, with the sole exception of bis(3,4,5-trimethoxyphenylamino) derivative **4p**.

## 2.3.2 Thermal properties

### 2.3.2.1 Classification of compounds

The thermal behavior of compounds **1-5** was studied by differential scanning calorimetry (DSC). Different cooling rates from 0.5 to 100 °C/min were used to generate a glassy phase.

The glass transition temperatures of the compounds, reported in Table 2.1, were then determined from the second heating cycle, using a 5 °C/min rate. Data are compiled so that a comparison can be made between compounds substituted with the same ancillary groups (2 x R) but a different headgroup (NHMe or Et). All the compounds bearing a NHMe headgroup present a $T_g$ between 22 and 129 °C, meaning that they all have the ability to form a glass. However, it is not the case for the Et headgroup compounds. Out of 21 compounds, only 15 show a glass transition with a $T_g$ that ranges between 19 and 96 °C, which is systematically lower than the $T_g$ of their NHMe analogue. The remaining six compounds with an Et headgroup (**4b**, **4h**, **4q**, **5a**, **5b** and **5c**) did not show any $T_g$ from -50 °C up to their decomposition temperature even when quenched at 100 °C/min.

The formation of a glassy state depends on the cooling rate applied to an initially amorphous sample (which is equivalent to its molten state).[15] Vitrification occurs when crystallization is circumvented, either by an ineffective nucleation process, or because the crystal growth kinetics is slow compared to the cooling rate. A critical cooling rate ($R_c$) can thus be defined as a threshold value, i.e. the slowest rate at which a compound can be cooled without crystallizing[27] (or, at least in the context of this study, without presenting detectable signs of crystallization by DSC). As a result, the thermal behavior of a compound upon cooling represents its glass-forming ability (GFA). As reported in Table 2.2, four different levels of GFA were established based on the critical cooling rate, from the best glass-formers (level 1) that remain completely amorphous upon cooling at 0.5 °C/min, to the worst (level 4) that are semi-crystalline even on quenching below $T_g$ at 100 °C/min. One should keep in mind that these categories do not stand as absolute ones since their boundaries were set according to the experimental cooling rates used herein. As an example, a compound that crystallizes partially when cooled at 2 °C/min but stays completely amorphous under a 5 °C/min cooling rate was given a GFA level 2. A compound with a GFA level 4 crystallizes partially under a 100 °C/min rate but it may be able to form a completely amorphous phase if cooled at a faster rate than was experimentally accessible. The crystallization was sometimes observed directly upon cooling by the presence of a crystallization exotherm, or was monitored indirectly using the subsequent heating thermogram. If the cold crystallization enthalpy is smaller than the melting enthalpy, one can conclude that the compound had crystallized upon cooling.

**Table 2.1.** Comparison of the glass transition temperature ($T_g$), crystallisation temperature ($T_c$) and melting temperature ($T_m$) of compounds **1-5** with NHMe or Et headgroups. Compounds are classified according to their glass-forming ability (GFA) and their glass stability (GS).

| Ancillary Group 2 x R | NHMe Headgroup | | | | | | Et Headgroup | | | | | |
|---|---|---|---|---|---|---|---|---|---|---|---|---|
| | Compound | $T_g$ °C | $T_c$ °C | $T_m$ °C | GFA | GS | Compound | $T_g$ °C | $T_c$ °C | $T_m$ °C | GFA | GS |
| **3,5-$Me_2C_6H_3$** | **1a** | 94 | - | - | 1 | G | **1b** | 41 | - | 135 | 1 | G |
| **Ph** | **2a** | 56 | 150-160 | 170 | 1 | P | **4a** | 27 | 52 | 162 | 4 | - |
| **2-$MeC_6H_4$** | **2b** | 55 | 128 | 149 | 1 | G | **4b** | - | - | 169 | - | - |
| **3-$MeC_6H_4$** | **2c** | 60 | - | - | 1 | G | **4c** | 19 | 94 | 112 | 1 | P |
| **4-$MeC_6H_4$** | **2d** | 67 | 139 | 169 | 1 | G | **4d** | 35 | 61/109 | 152 | 3 | P |
| **2,3-$Me_2C_6H_3$** | **2e** | 70 | - | - | 1 | G | **4e** | 46 | 73 | 169 | 4 | - |
| **2,4-$Me_2C_6H_3$** | **2f** | 54 | - | 170 | 1 | G | **4f** | 39 | 59/88/114 | 121/158 | 4 | - |
| **2,5-$Me_2C_6H_3$** | **2g** | 66 | - | - | 1 | G | **4g** | 32 | 121 | 136 | 1 | P |
| **2,6-$Me_2C_6H_3$** | **2h** | 89 | - | - | 1 | G | **4h** | - | - | dec. 240 | - | - |
| **3,4-$Me_2C_6H_3$** | **2i** | 71 | - | - | 1 | G | **4i** | 34 | 74/126 | 135/144 | 2 | P |
| **2,4,6-$Me_3C_6H_2$** | **2j** | 83 | 180 | dec. 249 | 1 | G | **4j** | 60 | - | dec. 240 | (1) | G |
| **3,5-$F_2C_6H_3$** | **2k** | 54 | 84 | 182/191 | 3 | P | **4k** | 25 | 69 | 153 | 2 | P |
| **3,5-$Cl_2C_6H_3$** | **2l** | 83 | 135/195 | 190/212 | 3 | P | **4l** | 52 | 109 | 169 | 3 | P |
| **3,5-$Br_2C_6H_3$** | **2m** | 94 | - | - | 1 | G | **4m** | 66 | 135-140 | 191 | 3 | P |
| **3,5-$I_2C_6H_3$** | **2n** | 128 | - | - | 1 | G | **4n** | 96 | 166 | 196 | 1 | G |
| **3,5-$(OMe)_2C_6H_3$** | **2o** | 65 | - | - | 1 | G | **4o** | 35 | 108 | 126 | 1 | G |
| **3,4,5-$(OMe)_3C_6H_2$** | **2p** | 94 | - | - | 1 | G | **4p** | 63 | 117 | 186 | 1 | G |
| **3,5-$(tBu)_2C_6H_3$** | **2q** | 129 | 173 | 234 | 3 | P | **4q** | - | - | 215 | - | - |
| **iPr** | **3a** | 22 | - | - | 1 | G | **5a** | - | 45 | dec. 120 | - | - |
| **tBu** | **3b** | 39 | 91 | dec. 145 | (1) | G | **5b** | - | 40 | dec. 140 | - | - |
| **Cy** | **3c** | 58 | 130 | 160 | 3 | P | **5c** | - | 105 | dec. 197 | - | - |

dec.: decomposition occurs before the compound reaches its melting point

(1): compound could not be completely melt but did show crystallization upon cooling or heating

G: good glass stability; P: poor glass stability

**Table 2.2.** Description of the glass-forming ability (GFA) levels.

| | GFA Levels | Critical cooling rate ($R_c$) °C/min |
|---|---|---|
| Best glass-former | 1 | $R_c < 0.5$ |
| ↓ | 2 | $2 \leq R_c < 5$ |
| | 3 | $5 \leq R_c < 100$ |
| Worst glass-former | 4 | $R_c \geq 100$ |

No compound had its critical cooling rate ($R_c$) between 0.5 and 2 °C/min so no GFA level is defined in that range.

In addition to the GFA, the thermal behavior of the initially glassy sample upon heating allows evaluating its kinetic glass stability* (GS) through its kinetic resistance to cold crystallization.[28] The GS was characterized by determining whether or not the compound showed an exothermic crystallization peak upon heating. Again, this categorization (good, poor or no GS) is relative to the applied heating rate, which was set at 5 °C/min. The slower or faster kinetics of this molecular reorganization hence determine whether the compound crystallizes or not when exposed to a particular heating rate.[1] This GS attribution can help infer the resistance to crystallization of a molecular glass over time under different conditions, in particular to determine if it would likely form a long-lived species.

The results of the GFA and GS classifications are presented in Table 2.1 and enable to compare the influence of the structure of the headgroup and the ancillary groups. No GFA level was attributed for samples that did not form a glassy phase in the range of temperatures studied. The thermal behaviors corresponding to different GFA levels and GS are exemplified by representative DSC traces in Figure 2.1. Figure 2.1a (compound **1b**) represents the thermal behavior of compounds with GFA levels 1 or 2 and good GS: only a glass transition is observed upon cooling above their critical cooling rate, and no crystallization is observed upon heating. No compound with GFA levels 3 or 4 showed good GS, which is not surprising since their $R_c$ was larger than the 5 °C/min heating rate. Compound **4g** (Figure 2.1b) is representative of samples with GFA levels 1, 2 or 3 that do not resist to crystallization (poor GS). A completely

* In this context, the term “stability” does not refer to "thermodynamic stability" since, by definition, a glass is metastable and reverts towards its thermodynamic equilibrium state as soon as it is generated.

amorphous glass is produced after cooling above $R_c$, but it crystallizes (and usually melts, as shown by the endothermic peak on the DSC trace) upon heating. The behavior of a compound that is assigned a GFA level 4 is exemplified by compound **4m** in Figure 2.1c. It crystallizes upon cooling (an enlargement of the crystallization region is shown in the insert) and crystallizes upon heating, but still undergoes a glass transition upon cooling and heating. The concept of glass stability loses its sense for such samples since the cold crystallization kinetics is enhanced by the presence of crystals generated during the cooling ramp. This type of sample is thus considered semi-crystalline and stands as an example of mediocre glass-formers. Finally, Figure 2.1d (compound **4b**) is representative of compounds that are not glass-formers (no GFA level is assigned) over the covered range of cooling rates. No glass transition is observed either on cooling or subsequent heating. Only an exothermic crystallization peak is observed in cooling and an endothermic melting peak upon heating.

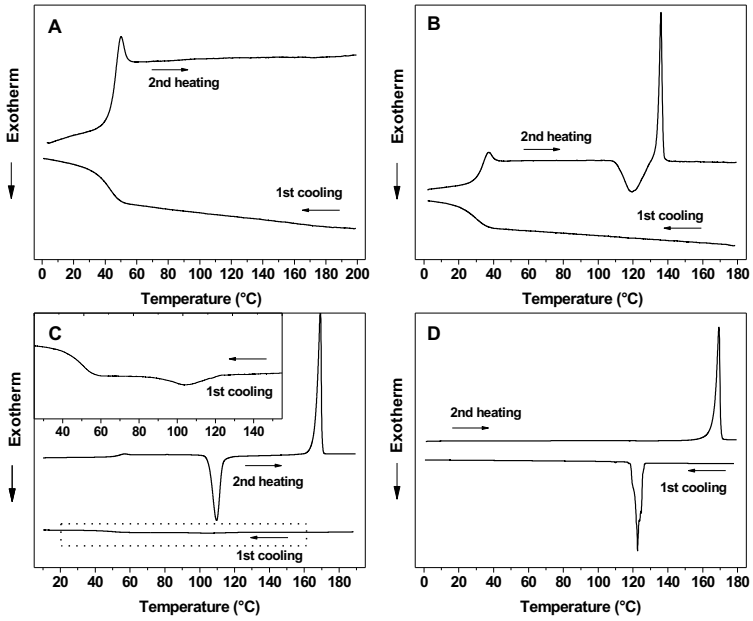


**Figure 2.1.** Representative DSC traces of (A) compounds with GFA level 1 and good GS (compound **1b**); (B) compounds with GFA level 1 and poor GS (compound **4g**); (C) compounds that crystallize upon cooling (compound **4m**) and (D) compounds that do not form a glass upon cooling (compound **4b**). All traces were obtained using a 5 °C/min cooling or heating rate. Samples were first cooled from the melt state and then heated.

A schematic representation of the established classification is shown in Figure 2.2, where the $T_g$ of the compounds is represented as a function of their GFA level. Compounds with NHMe and Et headgroups are represented by filled and open symbols, respectively. Moreover, different symbols are used to distinguish four types of ancillary groups: alkylaryl, haloaryl, alkoxyaryl and alkyl ancillary groups. This diagram helps to draw conclusions concerning the relative influence of the structure of the headgroup and the ancillary group on GFA, GS and $T_g$ of compounds.

#### 2.3.2.2. Influence of the headgroup

The main difference between the two headgroups resides in the fact that the methylamino (NHMe) function can readily form intermolecular hydrogen bonds, as opposed to the ethyl (Et) one. Moreover, the methylamino group is strongly conjugated with the triazine ring, resulting in hindered rotation compared to the freely rotating ethyl group. This results in an obvious trend: almost all NHMe compounds present a better GFA than their Et analogues (the only exception is compound **2k** with a GFA level 3 while its Et equivalent **4k** has a GFA level 2). This tendency is consistent with the behavior of some of dibenzoyl *N*-alkyl ethylene diamine organic glass-formers synthesized by Karis and coworkers, where the combination of hindered rotation isomerism and intermolecular hydrogen bonding helped to prevent the nucleation process.[29] In fact, hydrogen bonds have already been identified as key interactions that frustrate crystallization.[20] The NHMe headgroup contributes to the formation of hydrogen bonded aggregates that pack poorly in addition to the ancillary amino groups.[22] These aggregates are preserved even after the compound has undergone its glass transition, making more difficult the reorganization of the amorphous phase into its crystalline form over cooling.[21] In other words, aggregates contribute to thwart crystallization: one can thus expect that the more aggregates are maintained through hydrogen bonding in the liquid state, the better the GFA will be. For instance, Figure 2.2 shows that more than three quarters of the NHMe compounds (filled symbols) were assigned a GFA level 1, as compared to only one third of the Et headgroup ones (open symbols). This result is expected, considering the numerous systems involving hydrogen bonds that are commonly used in food products or pharmaceutical materials (e.g. sugars, such as trehalose or sucrose) for their efficient glass-forming ability.[11]

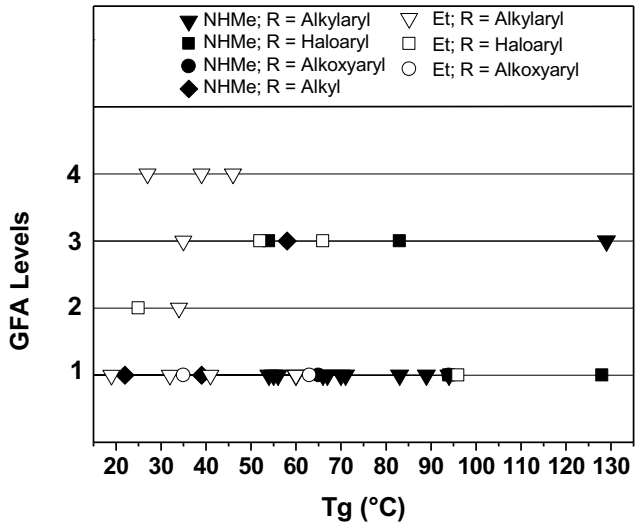


**Figure 2.2.** Classification of compounds according to their glass-forming ability (GFA) levels.

The remaining NHMe compounds (4 out of 21) are all classified in GFA level 3. This required tenfold increase in cooling rate clearly makes the GFA level 1 compounds stand out from the others, proving their excellent capability to generate a glassy phase. In contrast, GFA levels 2, 3 and 4 are found among the Et headgroup ones, pointing out to the fact this headgroup does not promote GFA with the same propensity as the NHMe functional group can. If fewer aggregates are formed and preserved above $T_g$, molecules are less constrained to reorganize in their crystalline form during cooling, thus leading to a semi-crystalline sample. Taken to the extreme, this situation leads to completely crystalline samples, which is the case for 6 Et compounds. Compound **4b** has crystallized under cooling and melted during heating, without a discernible glass transition in the studied range of cooling rates. As for the other ones (compounds **4h**, **4q**, **5a**, **5b** and **5c**), no transition at all were recorded during the second and third DSC scans. Visual evidence suggested that these samples were crystalline (opaque powders compared to glassy samples having a vitreous aspect) but could not be melt before their decomposition. Their presumed crystalline state was confirmed by X-ray diffraction (not shown).

A better GFA helps to prevent crystallization upon cooling, but also generally improves the GS. The only compounds that have resisted to cold crystallization were classified in GFA level 1. As expected, compounds with GFA levels 2 and 3 did not resist to crystallization (no

GS could be attributed to GFA level 4 compounds since they were not completely amorphous after cooling). However, a GFA level 1 does not guarantee a good GS: compounds **2a**, **4c** and **4g**, which are assigned a GFA level 1, show a poor GS. Considering the fact that NHMe compounds were mostly associated with the GFA level 1 category, it is expected that they present better GS than their Et analogues. Out of the 21 NHMe compounds, 16 resisted to crystallization when a 5 °C/min heating ramp was applied, as compared to only 5 for the Et compounds, confirming the expected trend. The structure of the headgroup strongly influences the GFA, which in turn has an impact on the GS of the compound.

The $T_g$ of NHMe headgroup compounds are higher than their Et analogues. Compounds with a NHMe headgroup are mostly found in the right part of Figure 2.2, with $T_g$ higher than 50 °C (except for **3a** and **3b**, 22 °C and 39 °C, respectively); compounds with a Et headgroup are found in the left part of the diagram with $T_g$ below 70 °C (except for compound **4n**, 96 °C). A similar correlation between the $T_g$ values and the presence of hydrogen bonding sites is also observed for disubstituted benzenes, where the $T_g$ of cresol (198 K, di-substituted by one $–CH_3$ and one –OH groups) is much higher than that of xylene (125.5 K, di-substituted by two $–CH_3$ groups).[30] A comparison between the $T_g$ of analogous compounds (bearing the same ancillary group but a different headgroup) is shown in Figure 2.3, where the $T_g$ of Et headgroup compounds are plotted as function of $T_g$ of NHMe headgroup compounds. The dashed line stands as an iso-$T_g$ reference. Glass transition temperatures follow a clear common trend: the $T_g$ of Et headgroup compounds always increases as the $T_g$ of NHMe headgroup does so. However, data points are all below the dashed line. Compounds with Et headgroups systematically present a $T_g$ that is between 5 and 14% lower than that of their NHMe analogue (see Table 2.S1 in Supporting information, where $T_g$ differences are quantitatively reported). The largest differences correspond to the compounds bearing ancillary groups substituted with methyl substituents.

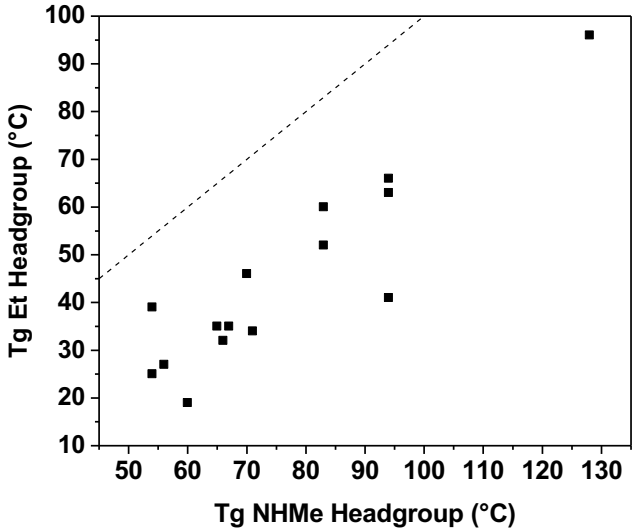


**Figure 2.3.** $T_g$ comparison of analogous compounds bearing the same ancillary groups but a different headgroup. The dashed line represents the iso-$T_g$ curve.

### 2.3.2.3. Influence of the ancillary groups

The aromaticity of the ancillary groups is obviously a structural feature that enhances the GFA of compounds and increases their $T_g$, the latter notably arising due to the rigidity of the aryl moieties.[18] Compounds substituted with alkyl ancillary groups showed a poor glass-forming ability with a much lower $T_g$ than aryl compounds, or even no GFA at all. The result regarding GFA is opposed to the hypothesis that non-planar cyclic alkyl groups, such as cyclohexane ancillary groups, could potentially create more free volume than the planar phenyl ones, as observed in some organic glass-formers composed of an adamantane core, and thus could lead to better glass-forming compounds.[31] In fact, compounds with alkyl ancillary groups could form a glassy phase only if they bore a methylamino headgroup. NHMe compounds **3a** and **3b** stand in the GFA level 1 category while cyclohexylamino derivative **3c** is classified in GFA level 3, presenting a $T_g$ of 22, 39 and 58 °C, respectively. Although the $T_g$ increases with the size of the alkyl ancillary groups (iPr < tBu < Cy), they are still low compared to the $T_g$ of the reference aryl-substituted compound **1a** (94 °C). The Et analogues of these three NHMe alkyl compounds (**5a**, **5b** and **5c**, respectively) did not undergo a glass transition. Since the alkyl ancillary groups cannot establish π-π interactions as aryl-substituted compounds can,[32] the establishment of a disordered network that prevents an efficient packing of molecules is limited. In fact, it should be emphasized that the purpose of using π-electron systems in our compounds is completely

different from that of other glass-formers: while Shirota *et al*, among others, rely on these electron-rich, bulky and sometimes twisted structures (e.g. starbust-shaped or dendritic molecules,[18] triphenylamine derivatives[33-35], spirofluorene units[36]) to avoid strong interactions between molecules, we seek to promote intermolecular interactions using aromatic moieties to favour the formation of a glassy phase.

The structure of the substituents borne by the aryl ancillary group also influences the GFA and the $T_g$ of the compounds. Substituents that participate in hydrogen bonds as acceptors (like methoxy or halide groups) promote GFA more efficiently than alkyl ones. Alkoxyaryl compounds are all found in GFA level 1, haloaryl ones present various degrees of GFA, being assigned to levels 1, 2 and 3, while alkylaryl compounds are distributed throughout all GFA levels. It is suggested that the establishment of a disordered network is favored by the multiple hydrogen bonding possibilities brought by the electronegativity and the polarizability of the substituents. This statement is supported by Naito's work, reporting that molecules having plural hydrogen bonding sites can self-assemble in a network that improves their glass-forming ability.[37]

Within the alkoxyaryl category, a difference could be made between the 3,5-OMe and the 3,4,5-OMe substitution pattern. Regardless of the headgroup, the addition of two methoxy groups leads to a $T_g$ increase of 30 °C. Compounds **2p** and **4p**, bearing six OMe groups, show a higher $T_g$ (94 and 65 °C, respectively) than their tetra-OMe-substituted analogues **2o** and **4o** (63 and 35 °C, respectively). It demonstrates that $T_g$ is not necessarily higher for a better glass-former: compound **4o** is part of the GFA level 1 group, with a $T_g$ as low as 35 °C. Multiple hydrogen bonding possibilities help to maintain aggregates upon cooling, preventing the establishment of a well-ordered structure.

A clear distinction between the haloaryl compounds can also be observed. Unlike the case of the methoxy substituents, the number of halide atoms borne by the ancillary group is the same for each compound. The differences between the GFA and the $T_g$ of these compounds can be linked to the halides' polarizability: I > Br > Cl > F. This trend was also observed by Shirota with haloaryl-substituted triarylamine derivatives.[3] This behavior could be attributed either to the higher volume of larger halides impeding mobility in the solid, or to the halides' capacity to establish non-covalent interactions, which contribute to form aggregates in the liquid state and

maintain them upon cooling, thus preventing crystallization. Independently of the headgroup, the 3,5-I and 3,5-Br substitution patterns present a higher $T_g$ than the reference 3,5-Me compounds (**1a** and **1b**), while the 3,5-Cl and 3,5-F compounds have a lower $T_g$ (except for the Et 3,5-Cl compound **4l**). Analogous haloaryl compounds with NHMe and Et headgroups were assigned the same GFA level, except for the 3,5-F compound (Et derivative **4k** has a GFA level 2 compared to 3 for its NHMe analogue **2k**, but its $T_g$ is lower: 25 °C compared to 54 °C).

No clear trend could be drawn concerning the GFA and alkyl substitution patterns. Referring to Table 2.1 or Figure 2.2, one can see that alkylaryl compounds are found on all levels (1 to 4) and that half of the six compounds that never formed a glassy phase were alkylaryl (**4b**, **4h** and **4q**). This type of substituent does not seem to particularly promote GFA, but it demonstrates once more that the 3,5- substitution pattern is optimal in helping to frustrate crystallization upon cooling,[19] even in the case where the headgroup cannot readily form hydrogen bonds. Et-substituted compound **1b** is 3,5- substituted and is classified as GFA level 1 with high GS, while compound **4h**, substituted with the same number of Me groups but at the 2,6 positions, is unable to generate a glassy phase. If the headgroup readily forms hydrogen bonds (like NHMe), the structure of the ancillary group (and the position of its substituents) does not have a tremendous effect on GFA. On the other hand, if the headgroup cannot form hydrogen bonds easily (like Et), it is the substituents borne by the (aromatic) ancillary group that influence the most the GFA of a compound. This observation can be related to that of Alba-Simionesco and coworkers, in which *meta*-isomers of some disubstituted benzenes undergo supercooling more efficiently than their *ortho*- or *para*-substituted ones.[30] Moreover, it seems that the number of Me alkyl groups influences the $T_g$ of the compounds. For the NHMe headgroup compounds, the average $T_g$ of the mono-Me substitution pattern (e.g. 2-Me) is approximately 10 °C lower compared to the di-Me one (e.g. 2,4-Me), which itself is nearly 10 °C lower than the tri-Me one (2,4,6-Me). This same trend, i.e. the increase of $T_g$ with the number of alkyl groups, is also found for compounds with Et headgroup, but less clearly. Finally, the $T_g$ of compounds **2b**-**2d** and **4c**-**4d** follow the order ortho < meta < para, as was reported in our previous study on unsymmetrically-substituted compounds.[24]

### 2.3.2.4. Influence of ancillary group symmetry

We have studied in a previous study[24] the GFA and $T_g$ of a library of methylaminotriazine derivatives that were substituted with two different ancillary groups: one was always kept as a mexylamino ((3,5-dimethylphenyl)amino) group, while the other was another arylamino or a cycloalkylamino group. These ancillary groups were themselves substituted by different functional groups on distinct positions. In this paper, the two ancillary groups linked to the same methylaminotriazine core of compounds 1a-3c are identical. In the following comparison, these two series of compounds will be referred to as unsymmetrical (two different ancillary groups) and symmetrical (two identical ancillary groups) compounds, keeping in mind that these designations do not relate to the group symmetry formal definitions. The mexylamino motif has already been identified in previous studies[19,23] as an efficient GFA and GS promoting ancillary group. Indeed, almost all unsymmetrical compounds formed a completely amorphous phase when cooled under a 5 °C/min rate and did not crystallize upon heating.[†] A very similar behavior is observed for NHMe-substituted symmetrical compounds. As it can be recalled from Table 2.1, only 4 symmetrical compounds crystallized when cooled at 5 °C/min, which is a cooling rate that allowed the formation of a glassy phase for all the unsymmetrical compounds. It seems that the absence of the mexylamino GFA promoter and the increased molecular symmetry created by the presence of two identical ancillary groups do not have a tremendous impact on the GFA and GS of compounds, even if one of Shirota's empirical guidelines to generate a long-lived molecular glass suggests to avoid symmetry[18] and that a study on butanediol isomers has pinpointed that their glass-forming ability depends on their symmetry, and thus on the location of the hydrogen bonding sites.[38] However, there is no guarantee that analogues of the unsymmetrical series with a different headgroup or in which the mexylamino group was substituted by another arylamino group would show similar GFA or GS.

Observations could also be made regarding the $T_g$ of unsymmetrical and symmetrical compounds. Figure 2.4 shows that the $T_g$ of symmetrical compounds increases more or less linearly as the $T_g$ of unsymmetrical analogue increases, as was the case in Figure 2.3 when

[†] Only the GFA of the 2,4,6-Me substituted arylamino compound (**11**) could not be evaluated, because its decomposition occurred before melting was completed.

comparing the $T_g$ of compounds with NHMe or Et headgroups. Only three data points are above the iso-$T_g$ reference line, leading to the conclusion that the $T_g$ of more than 75% of unsymmetrical compounds is slightly higher than that of their symmetrical analogues. The $T_g$ differences range between 0.3 and 4.9%, with an average difference of about only 1% (see Table 2.S2 in Supporting information for quantitative differences detailed for each compound). It shows that the $T_g$ difference that is due to symmetry of the ancillary groups borne by the methylaminotriazine core is much less important than the effect of the headgroup structure (10% difference), confirming the dominant role played by the headgroup on thermal behavior of the compounds.

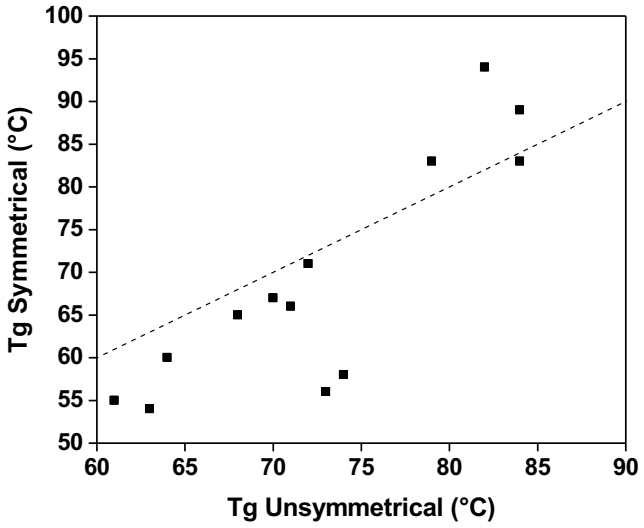


**Figure 2.4.** $T_g$ comparison of unsymmetrical (bearing one mexylamino and one ancillary group R) and symmetrical (two ancillary groups R) analogues. The dashed line represents the iso-$T_g$ curve.

## 2.4 Conclusions

Two series of bis(arylamino)- or bis(alkylamino)-1,3,5-triazine derivatives were synthesized, with either a methylamino or an ethyl headgroup, and their respective glass-forming ability (GFA) and glass stability (GS) were evaluated. It was determined that the headgroup showed a more pronounced impact than the ancillary amino groups for both GFA and GS, with almost all compounds of the methylamino series showing glass formation to some extent, and a majority of compounds showing appreciable GS, while fewer compounds of the

ethyl series showed GFA, and in most cases with a much lower GS than their methylamino counterparts. Among the ancillary groups evaluated, the 3,5-disubstituted aryl motif clearly emerged as the best for promoting glass formation, and substituents capable of interacting via non-covalent interactions typically promoted glass formation to a higher extent than weakly interacting substituents.

## 2.5 Experimental section

### 2.5.1 General

2- Methylamino-4,6-bis(mexylamino)-1,3,5-triazine (**1a**),[19] 2-methylamino-4,6-bis(phenylamino)-1,3,5-triazine (**2a**),[39] 2-methylamino-4,6-bis(isopropylamino)-1,3,5-triazine (**3a**),[40] 2-chloro-4,6-bis(tert-butylamino)-1,3,5-triazine,[41] 2-ethyl-4,6-bis(mexylamino)-1,3,5-triazine (**1b**),[23] 2-ethyl-4,6-bis(isopropylamino)-1,3,5-triazine (**5a**),[42] and 2-ethyl-4,6-bis(cyclohexylamino)-1,3,5-triazine (**5c**)[42] were prepared according to literature procedures. All other reagents and solvents were purchased from commercial sources and used without further purification. All reactions were performed under ambient atmosphere. SiliaFlash P60 grade silica gel and TLC plates were purchased from SiliCycle. $^{1}$H NMR spectra were recorded on a Bruker Avance 400 MHz, a Varian Mercury 300 MHz, or a Varian Inova 600 MHz spectrometer at 298 K or 363 K (as indicated). $^{13}$C NMR spectra were recorded on a Varian Mercury 300 MHz spectrometer at 298 K. FTIR spectra were recorded on a Tensor 27 FT-IR spectrometer (Bruker Optics) equipped with a liquid nitrogen-cooled HgCdTe detector and a MIRacle (Pike Technologies) silicon attenuated total reflection (ATR) accessory. Films were directly cast on the ATR crystal from $CH_2Cl_2$ solution. Decomposition analyses of molecular glasses were obtained using a TGA 2950 or a Q500 thermogravimetric analyzer (TA Instruments) at a heating rate of 10 °C/min under a nitrogen atmosphere. $T_g$, $T_c$ and $T_m$ were recorded by DSC with a TA Instruments Q1000 or Q2000 calorimeter calibrated with indium using a heating rate of 5 °C/min and different cooling rates (0.5, 2, 5 and 100 °C/min) from 20 °C to 200 °C, unless otherwise noted. $T_g$ were reported as the average of the values observed in the second heating scan after an initial cycle of heating and cooling at 5 °C/min.

## 2.5.2 Syntheses

*2-methylamino-4,6-bis(arylamino)-1,3,5-triazine or 2-ethyl-4,6-bis(arylamino)-1,3,5-triazine derivatives*

To a round-bottomed flask equipped with a magnetic stirrer and a water-jacketed condenser were added either 4,6-dichloro-2-methylamino-1,3,5-triazine or 4,6-dichloro-2-ethyl-1,3,5-triazine (1.00 mmol) and the corresponding aniline (2.20 mmol) in THF (10 mL). The mixture was then heated to reflux for 18 h (unless otherwise indicated), after which 1M aqueous HCl and $CH_2Cl_2$ were added. Both layers were separated, then the organic layer was extracted with 1M aqueous NaOH, dried over $Na_2SO_4$, filtered, and the volatiles were thoroughly evaporated under reduced pressure. In cases where traces of the aniline remained (monitored by TLC using 10 % AcOEt/$CH_2Cl_2$), the crude product was triturated in hot methanol then filtered and washed with methanol.

Yields, thermal and spectral data for each individual compound are reported in Supporting Information.

*2-Methylamino-4,6-bis(tert-butylamino)-1,3,5-triazine (3b)*

2-chloro-4,6-bis(tert-butylamino)-1,3,5-triazine[41] (0.306 g, 1.19 mmol) was dissolved in THF (10 mL) in a round-bottomed flask equipped with a magnetic stirrer and a water-jacketed condenser. Aqueous methylamine (40 wt%, 5 mL), was added, then the mixture was refluxed for 18 h. After allowing the mixture to cool down to room temperature, $CH_2Cl_2$ and 1M aq. HCl were added, and both layers were separated. The organic layer was washed with aq. $NaHCO_3$, then recovered, dried over $Na_2SO_4$, filtered, and the volatiles were evaporated under reduced pressure. The crude product was recrystallized from hexanes to yield, after drying, 0.244 g compound **3b** (0.970 mmol, 81 %). $T_g$ 39 °C, $T_c$ 91 °C, $T_{dec}$ 145 °C; FTIR (ATR/$CH_2Cl_2$) 3435, 3273, 2962, 2930, 1565, 1501, 1450, 1398, 1359, 1247, 1209, 1152, 1106, 1033, 974, 922, 814, 739, 704 $cm^{-1}$; $^1H$ NMR (300 MHz, $CDCl_3$, 298 K) δ 4.86 (br s, 3H), 2.85 (d, $^3J$ = 4.1 Hz, 3H), 1.39 (s, 18H) ppm; $^{13}C$ NMR (75 MHz, $CDCl_3$) δ 165.9, 165.2, 50.5, 29.3, 27.4 ppm; HRMS (ESI, $MH^+$) calcd. for $C_{12}H_{25}N_6$ *m/e*: 253.2135, found: 253.2138.

*2-Methylamino-4,6-bis(cyclohexylamino)-1,3,5-triazine (3c)*

4,6-dichloro-2-methylamino-1,3,5-triazine (0.179 g, 1.00 mmol) was dissolved in THF (15 mL) in a round-bottomed flask equipped with a magnetic stirrer and a water-jacketed condenser. Cyclohexylamine (2 mL), was added, then the mixture was refluxed for 18 h. After allowing the mixture to cool down to room temperature, $CH_2Cl_2$ and 1M aq. HCl were added, and both layers were separated. The organic layer was washed with aq. $NaHCO_3$, then recovered, dried over $Na_2SO_4$, filtered, and the volatiles were thoroughly evaporated under reduced pressure to yield 0.224 g compound **3c** (0.736 mmol, 74 %). $T_g$ 58 °C, $T_c$ 130 °C, $T_m$ 160 °C; FTIR (ATR/$CH_2Cl_2$) 3266, 3165, 2928, 2857, 1566, 1503, 1464, 1449, 1414, 1398, 1360, 1348, 1295, 1258, 1169, 1132, 1108, 1059, 1027, 973, 890, 845, 813, 737 $cm^{-1}$; $^1H$ NMR (300 MHz, $CDCl_3$, 298 K) δ 4.95 (br s, 1H), 4.88 (br s, 2H), 3.78 (br s, 2H), 2.89 (d, $^3J$ = 4.1 Hz, 3H), 1.97 (m, 4H), 1.69 (m, 4H), 1.57 (m, 2H), 1.33 (m, 4H), 1.16 (m, 6H) ppm; $^1H$ NMR (400 MHz, DMSO-$d_6$, 363 K) δ 5.92 (s, 1H), 5.74 (s, 2H), 3.70 (m, 2H), 2.74 (d, $^3J$ = 4.8 Hz, 3H), 1.87 (m, 4H), 1.69 (m, 4H), 1.56 (m, 2H), 1.24 (m, 10H) ppm; $^{13}C$ NMR (75 MHz, $CDCl_3$) δ 166.2, 164.9, 49.0, 33.3, 27.5, 25.7, 24.9 ppm; HRMS (ESI, $MH^+$) calcd. for $C_{16}H_{29}N_6$ *m/e*: 305.2448, found: 305.2452.

*2.5.2.4 2-Ethyl-4,6-bis(tert-butylamino)-1,3,5-triazine (5b)*

4,6-Dichloro-2-ethyl-1,3,5-triazine (0.178 g, 1.00 mmol) was dissolved in THF (10 mL) in a round-bottomed flask equipped with a magnetic stirrer and a water-jacketed condenser. *tert*-Butylamine (10 mL), was added, then the mixture was refluxed for 3 days. After allowing the mixture to cool down to room temperature, $CH_2Cl_2$ and 1M aq. HCl were added, and both layers were separated. The organic layer was washed with aq. $NaHCO_3$, then recovered, dried over $Na_2SO_4$, filtered, and the volatiles were thoroughly evaporated under reduced pressure to yield 0.216 g compound **5b** (0.859 mmol, 86 %). $T_c$ 40 °C, $T_{dec}$ 140 °C; FTIR (ATR/$CH_2Cl_2$) 3436, 3277, 3147, 2965, 2933, 2878, 1564, 1502, 1452, 1436, 1361, 1305, 1234, 1137, 1061, 1036, 986, 921, 825 $cm^{-1}$; $^1H$ NMR (300 MHz, $CDCl_3$, 298 K) δ 5.43 (s, 2H), 2.43 (m, 2H), 1.43 (s, 18H), 1.21 (t, $^3J$ = 7.6 Hz, 3H) ppm; $^{13}C$ NMR (75 MHz, $CDCl_3$) δ 176.8, 164.0, 51.0, 31.3, 29.1, 11.4 ppm; HRMS (ESI, $MNa^+$) calcd. for $C_{13}H_{25}NaN_5$ *m/e*: 274.2002, found: 274.2007.

## 2.6 Acknowledgements

The authors thank the Academic Research Programme (ARP) from RMC and the Fonds de Recherche du Québec – Nature et Technologies (FRQNT) for funding. AL thanks the Natural Sciences and Engineering Research Council of Canada (NSERC) for undergraduate and graduate scholarships. The authors also acknowledge René Gagnon from Université de Sherbrooke for mass spectrometry and Alexandre Arnold from Université du Québec à Montréal for high-temperature NMR experiments.

## 2.7 References

1. Biroli, G.; Garrahan, J. P., *J. Chem. Phys.* **2013,** *138*, 12A301.
2. Angell, C. A., *Science* **1995,** *267*, 1924-1935.
3. Shirota, Y., *J. Mater. Chem.* **2000,** *10*, 1-25.
4. Strohriegl, P.; Grazulevicius, J. V., *Adv. Mater.* **2002,** *14*, 1439-1452.
5. Grazulevicius, J. V., *Polym. Adv. Technol.* **2006,** *17*, 694-696.
6. Shirota, Y.; Kageyama, H., *Chem. Rev.* **2007,** *107*, 953-1010.
7. Lygaitis, R.; Getautis, V.; Grazulevicius, J. V., *Chem.Soc. Rev.* **2008,** *37*, 770-788.
8. De Silva, A.; Felix, N. M.; Ober, C. K., *Adv. Mater.* **2008,** *20*, 3355-3361.
9. Tanaka, M.; Rastogi, A.; Kudo, H.; Watanabe, D.; Nishikubo, T.; Ober, C. K., *J. Mater. Chem.* **2009,** *19*, 4622-4626.
10. Bauer, W.-A. C.; Neuber, C.; Ober, C. K.; Schmidt, H.-W., *Adv. Mater.* **2011,** *23*, 5404-5408.
11. Hancock, B. C.; Zografi, G., *J. Pharm. Sci.* **1997,** *86*, 1-12.
12. Yu, L., *Adv. Drug Deliv. Rev.* **2001,** *48*, 27-42.
13. Gao, P., *Mol. Pharmaceutics* **2008,** *5*, 903-904.
14. Kawakami, K., *J. Pharm. Sci.* **2009,** *98*, 2875-2885.
15. Ediger, M. D.; Angell, C. A.; Nagel, S. R., *J. Phys. Chem.* **1996,** *100*, 13200-13212.
16. Baird, J. A.; Olayo-Valles, R.; Rinaldi, C.; Taylor, L. S., *J. Pharm. Sci.* **2010,** *99*, 154-168.
17. Baird, J. A.; Santiago-Quinonez, D.; Rinaldi, C.; Taylor, L. S., *Pharm. Res.* **2012,** *29*, 271-284.

18. Shirota, Y., *J. Mater. Chem.* **2005,** *15*, 75-93.
19. Lebel, O.; Maris, T.; Perron, M. E.; Demers, E.; Wuest, J. D., *J. Am. Chem. Soc.* **2006,** *128*, 10372-10373.
20. Wang, R. Y.; Pellerin, C.; Lebel, O., *J. Mater. Chem.* **2009,** *19*, 2747-2753.
21. Plante, A.; Mauran, D.; Carvalho, S. P.; Page, J.; Pellerin, C.; Lebel, O., *J. Phys. Chem. B* **2009,** *113*, 14884-14891.
22. Plante, A.; Palato, S.; Lebel, O.; Soldera, A., *J. Mater. Chem. C* **2013,** *1*, 1037-1042.
23. Wuest, J. D.; Lebel, O., *Tetrahedron* **2009,** *65*, 7393-7402.
24. Eren, R. N.; Plante, A.; Meunier, A.; Laventure, A.; Huang, Y. S.; Briard, J. G.; Creber, K. J.; Pellerin, C.; Soldera, A.; Lebel, O., *Tetrahedron* **2012,** *68*, 10130-10144.
25. Meunier, A.; Lebel, O., *Org. Lett.* **2010,** *12*, 1896-1899.
26. Over 20 000 compounds containing bis(phenylamino)-1,3,5-triazine skeleton have been reported so far, for example: Zerkowski, J. A.; Seto, C. T.; Wierda, D. A.; Whitesides, G. M., *J. Am. Chem. Soc.* **1990,** *112*, 9025-9026.
27. Lu, Z. P.; Liu, C. T., *Acta Mater.* **2002,** *50*, 3501-3512.
28. Nascimento, M. L. F.; Souza, L. A.; Ferreira, E. B.; Zanotto, E. D., *J. Non-Cryst. Solids* **2005,** *351*, 3296-3308.
29. Karis, T. E.; Kim, S. J.; Gendler, P. L.; Cheng, Y. Y., *J. Non-Cryst. Solids* **1995,** *191*, 293-303.
30. Alba-Simionesco, C.; Fan, J.; Angell, C. A., *J. Chem. Phys.* **1999,** *110*, 5262-5272.
31. Chen, S. H.; Mastrangelo, J. C.; Shi, H. Q.; Bashirhashemi, A.; Li, J. C.; Gelber, N., *Macromolecules* **1995,** *28*, 7775-7778.
32. Kim, T. D.; Kang, J. W.; Luo, J. D.; Jang, S. H.; Ka, J. W.; Tucker, N.; Benedict, J. B.; Dalton, L. R.; Gray, T.; Overney, R. M.; Park, D. H.; Herman, W. N.; Jen, A. K. Y., *J. Am. Chem. Soc.* **2007,** *129*, 488-489.
33. Kim, M. J.; Seo, E. M.; Vak, D.; Kim, D. Y., *Chem. Mater.* **2003,** *15*, 4021-4027.
34. Komino, T.; Nomura, H.; Yahiro, M.; Adachi, C., *Chem. Phys. Lett.* **2013,** *563*, 70-75.
35. Cekaviciute, M.; Simokaitiene, J.; Jankauskas, V.; Raisys, S.; Kazlauskas, K.; Jursenas, S.; Grazulevicius, J. V., *J. Phys. Chem. C* **2013,** *117*, 7973-7980.
36. Sonntag, M.; Kreger, K.; Hanft, D.; Strohriegl, P.; Setayesh, S.; de Leeuw, D., *Chem. Mater.* **2005,** *17*, 3031-3039.

37. Naito, K., *Chem. Mater.* **1994,** *6*, 2343-2350.

38. Maria, T. R.; Lopes Jesus, A. J.; Eusébio, M. E., *J. Therm. Anal. Calorim.* **2010,** *100*, 385-390.

39. Matsui, K.; Hagiwara, K.; Soeda, Y., *Yuki Gosei Kagaku Kyokaishi* **1960,** *18*, 184-189.

40. Raillard, S.; Krebber, A.; Chen, Y.; Ness, J. E.; Bermudez, E.; Trinidad, R.; Fullem, R.; Davis, C.; Welch, M.; Seffernick, J.; Wackett, L. P.; Stemmer, W. P. C.; Minshull, J., *Chem. Biol.* **2001,** *8*, 891-898.

41. Zerkowski, J. A.; Whitesides, G. M., *J. Am. Chem. Soc.* **1994,** *116*, 4298-4304.

42. Irikura, T.; Abe, Y.; Okamura, K.; Higo, K.; Maeda, A.; Morinaga, F.; Shirai, G.; Hatae, S., *J. Med. Chem.* **1970,** *13*, 1081-1089.

## 2.8 Supporting information

### Spectral data for compounds 2b-q and 4a-q

*Voir* Annexe I. Les spectres RMN peuvent être consultés au http://www.rsc.org/suppdata/nj/c3/c3nj00709j/c3nj00709j.pdf

### Additional thermal analyses for compounds 1-5

**Table 2.S1.** $T_g$ comparison between compounds bearing NHMe and Et headgroups

| 22. x R | NHMe headgroup | | Et headgroup | | Tg Comparison | |
|---|---|---|---|---|---|---|
| | Compound | $T_g$ °C | Compound | $T_g$ °C | Difference °C | Difference % |
| **3,5-$Me_2C_6H_3$** | 1a | 94 | 1b | 41 | 53 | 14 |
| **Ph** | 2a | 56 | 4a | 27 | 29 | 9 |
| **3-$MeC_6H_4$** | 2c | 60 | 4c | 19 | 41 | 12 |
| **4-$MeC_6H_4$** | 2d | 67 | 4d | 35 | 32 | 9 |
| **2,3-$Me_2C_6H_3$** | 2e | 70 | 4e | 46 | 24 | 7 |
| **2,4-$Me_2C_6H_3$** | 2f | 54 | 4f | 39 | 15 | 5 |
| **2,5-$Me_2C_6H_3$** | 2g | 66 | 4g | 32 | 34 | 10 |
| **3,4-$Me_2C_6H_3$** | 2i | 71 | 4i | 34 | 37 | 11 |
| **2,4,6-$Me_3C_6H_2$** | 2j | 83 | 4j | 60 | 23 | 6 |
| **3,5-$F_2C_6H_3$** | 2k | 54 | 4k | 25 | 29 | 9 |
| **3,5-$Cl_2C_6H_3$** | 2l | 83 | 4l | 52 | 31 | 9 |
| **3,5-$Br_2C_6H_3$** | 2m | 94 | 4m | 66 | 28 | 8 |
| **3,5-$I_2C_6H_3$** | 2n | 128 | 4n | 96 | 32 | 8 |
| **3,5-$(OMe)_2C_6H_3$** | 2o | 65 | 4o | 35 | 30 | 9 |
| **3,4,5-$(OMe)_3C_6H_2$** | 2p | 94 | 4p | 63 | 31 | 8 |

**Table 2.S2.** $T_g$ comparison between compounds bearing one (unsymmetrical and two (symmetrical) ancillary groups R.

| R | Unsymmetrical[1] 1 x R | | Symmetrical 2 x R | | $T_g$ Comparison | |
|---|---|---|---|---|---|---|
| | Compound | $T_g$ °C | Compound | $T_g$ °C | Difference °C | Difference % |
| **Ph** | 3 | 73 | 2a | 56 | 17 | 4.9 |
| **2-$MeC_6H_4$** | 4 | 61 | 2b | 55 | 6 | 1.8 |
| **3-$MeC_6H_4$** | 5 | 64 | 2c | 60 | 4 | 1.2 |
| **4-$MeC_6H_4$** | 6 | 70 | 2d | 67 | 3 | 0.9 |
| **2,4-$Me_2C_6H_3$** | 7 | 63 | 2f | 54 | 9 | 2.7 |
| **2,5-$Me_2C_6H_3$** | 8 | 71 | 2g | 66 | 5 | 1.5 |
| **2,6-$Me_2C_6H_3$** | 9 | 84 | 2h | 89 | -5 | -1.4 |
| **3,4-$Me_2C_6H_3$** | 10 | 72 | 2i | 71 | 1 | 0.3 |
| **2,4,6-$Me_3C_6H_2$** | 11 | 79 | 2j | 83 | -4 | -1.1 |
| **3,5-$Cl_2C_6H_3$** | 18 | 84 | 2l | 83 | 1 | 0.3 |
| **3,5-$(OMe)_2C_6H_3$** | 27 | 68 | 2o | 65 | 3 | 0.9 |
| **3,4,5-$(OMe)_3C_6H_2$** | 28 | 82 | 2p | 94 | -12 | -3.4 |
| **Cy** | 42 | 74 | 3c | 58 | 16 | 4.6 |

*Reference*

1. Eren, R. N.; Plante, A.; Meunier, A.; Laventure, A.; Huang, Y. S.; Briard, J. G.; Creber, K. J.; Pellerin, C.; Soldera, A.; Lebel, O., *Tetrahedron* **2012,** *68*, 10130-10144.

# Chapitre 3: Unraveling the interplay between hydrogen bonding and rotational energy barrier to fine-tune the properties of triazine molecular glasses*

## 3.1 Abstract


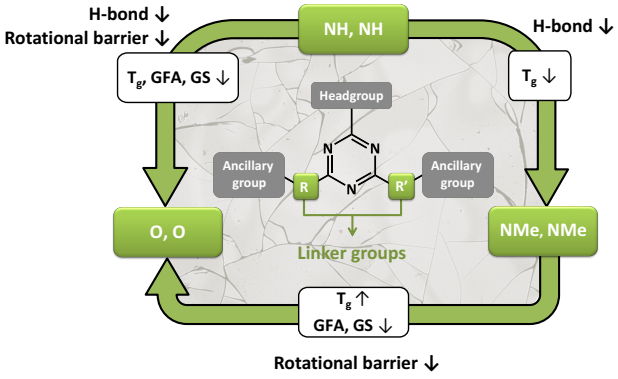


Mexylaminotriazine derivatives form molecular glasses with outstanding glass-forming ability (GFA), high resistance to crystallization (glass kinetic stability, GS), and a glass transition temperature ($T_g$) above room temperature that can be conveniently modulated by selection of the headgroup and ancillary groups. A common feature of all these compounds is their secondary amino linkers, suggesting that they play a critical role in their GFA and GS for reasons that remain unclear because they can simultaneously form hydrogen (H) bonds and lead to a high interconversion energy barrier between different rotamers. To investigate independently and better control the influence of H bonding capability and rotational energy barrier on $T_g$, GFA and GS, a library of twelve analogous molecules was synthesized with different combinations of NH, NMe and O linkers. Differential scanning calorimetry (DSC) revealed that these compounds form, with a single exception, kinetically stable glasses with $T_g$ values spanning a very broad range from -25 to 94 °C. While variable temperature infrared spectroscopy combined to chemometrics reveals that, on average, around 60% of the NH groups are still H-bonded as high as 40 °C above $T_g$, critical cooling rates obtained by DSC clearly show that molecules without H-bond donating linkers also present an


* Publié en tant qu'article dans *Physical Chemistry Chemical Physics*: Laventure, A.; De Grandpré, G.; Soldera, A.; Lebel, O.; Pellerin, C. *Phys. Chem. Chem. Phys.* **2016**, *18*, 1681-1692. G.D.G. a procédé aux calculs des barrières énergétiques de rotation. O.L. a procédé à la synthèse des composés et à leur caractérisation de base.

outstanding GFA, meaning that H bonding plays a dominant role in controlling $T_g$ but is not required to prevent crystallization. It is a high interconversion energy barrier, provoking a distribution of rotamers, that most efficiently promotes both GFA and resistance to crystallization. These new insights pave the way to more efficient glass engineering by extending the possible range of accessible $T_g$, allowing in particular the preparation of homologous glass-formers with high GS at ambient temperature in either the viscous or vitreous state.

## 3.2 Introduction

Organic glasses, by opposition to crystals, are amorphous materials that lack periodic order.[1] They possess various properties such as macroscopic homogeneity, transparency, better solubility and compositional flexibility, among others, that can be advantageously exploited in a wide array of (bio)materials applications. These organic amorphous materials can be prepared using either polymers or small molecules. The latter, also named molecular glasses, offer the advantages of being isomolecular and easier to purify than polymers, but they generally necessitate more extreme processing conditions to impede crystallization and they tend to crystallize faster over time, thus losing their advantageous properties. To cope with these issues, molecular glasses showing both an excellent glass-forming ability (GFA) and a high kinetic stability (glass stability, GS, *i.e.* resistance to crystallization) are therefore sought, particularly in the context of the rapid expansion of the organic electronics field and the need to optimize excipients in pharmaceutical products, two domains requiring materials that readily form long-lived amorphous phases.[2,3] Unveiling the intimate link between molecular structure and these properties is thus of particular interest. Although the synthesis and characterization of libraries of compounds with natural poor packing and slow crystallization kinetics is one of the keys to unravel the challenging task of efficient glass design, limited work has been conducted on homologous series of organic compounds. In an attempt to relate the molecular properties and the bulk behavior of amorphous materials, different groups have studied the kinetics and the thermodynamics of glass formation in xylenes[4] and trisnaphtylbenzene isomers,[5] and more recently, in libraries of stilbenes[6] and trisarylbenzene analogues.[7]

While previous studies have usually focused on glass-forming molecules that can only interact by weak van der Waals interactions, Lebel and co-workers have introduced in 2006 a series of bis(mexyl)aminotriazine derivatives with outstanding GFA[8] that are capable of hydrogen bonding, a stronger intermolecular interaction that usually promotes crystallization and is widely used in crystal engineering to create predictably ordered and well-packed structures.[9,10] Over the last decade, more than 100 glass-forming triazine derivatives have been synthesized and characterized, successfully demonstrating that regularly-shaped and symmetrical compounds that can participate in hydrogen bonds can also readily form amorphous phases. Moreover, these aminotriazine compounds, shown in Scheme 3.1 (bearing two mexyl[†] ancillary groups), challenge the predictions of Wicker *et al*. based on a machine learning approach, which place them at the border of the crystalline and amorphous states.[11] These counterintuitive features make aminotriazine derivatives an interesting model system to deepen our understanding of the glassy phase and of the molecular parameters leading to a good GFA. They also stand out as a model system for experimental convenience: i) the vitreous phase of most of these compounds is kinetically stable for a relatively long time, limiting nucleation and growth of crystals during measurements (several of these compounds even resist crystallization in their supercooled liquid state for over 18 months upon annealing and even under shear stress);[12] ii) selection of the headgroup and ancillary groups enables tuning their glass transition temperature ($T_g$) values over a wide temperature range from 19 to 131 °C; and iii) their excellent GFA allows applying a slow cooling rate, thus enabling *in situ* characterization using techniques with relatively low temporal resolution.

The role of the headgroup and the ancillary groups of these molecules has been extensively studied previously.[13,14] In contrast, little is known about the influence of the groups linking the triazine core to the ancillary groups (R and R' linkers in Scheme 3.1) on the GFA, GS and $T_g$ of these compounds. Indeed, secondary amines (NH) have been employed almost systematically as linkers until now; their H-bond donor character and/or their high rotational energy barrier may thus be critical in explaining the excellent GFA and high $T_g$ for the numerous analogues synthesized so far. Indeed, studies of the headgroup structure have revealed that both

[†] mexyl = 3,5-diphenyl

hydrogen bonding and a high rotational barrier, along with steric bulk, promote glass formation and modulate $T_g$,[15,16] but it is yet unclear how the interplay between these three parameters influences glass formation and $T_g$ for the ancillary group linkers. In the only attempt so far, substituting both NH groups by oxygen atoms has resulted in crystallization within less than 24 hours at ambient temperature.[8] This high propensity to crystallize was assumed to be a consequence of the absence of self-assembly by hydrogen bonding,[8] but it could also be due to a lower rotational barrier for the aryloxy groups, which are less strongly conjugated to the triazine ring than arylamino groups and can thus rearrange more easily to an ordered packing.[16] It is thus crucial to undertake a more systematic study of the impact of the ancillary linkers on GFA, GS and $T_g$ to determine the contribution of each molecular parameter to these properties. Furthermore, being able to retain the excellent GFA and resistance to crystallization without using NH groups as linkers would give access to materials with a lower $T_g$ range while retaining the demonstrated synthetic flexibility of these triazine derivatives, allowing their functionalization with different headgroups and ancillary groups, and thus opening the door to new exciting functional materials being in their viscous state at ambient temperature.

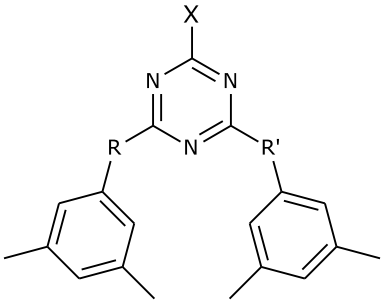


**Headgroup:** X = NHMe or OMe
**Linker:** R, R' = NH, NMe or O

**Scheme 3.1.** Chemical structure of the studied compounds.‡

In this work, the impact of the linkers on glass formation is probed systematically by synthesizing and characterizing a new library of 12 compounds featuring three different linkers: NH, NMe and O. The elimination of the H-bond donor capability (*vs.* the reference compound

‡ Marvin was used for drawing, displaying and characterizing chemical structures, substructures and reactions (Schemes 3.1; 3.3-3.5 and II.S1), Marvin 6.0.0, 2013, ChemAxon (http://www.chemaxon.com).

with R = R' = NH) by replacing the NH linkers either by the isosteric but more freely rotating O group, or by the isoelectronic and sterically hindered NMe group revealed that H-bonding interactions at the linker location do not stand as a requirement for the spontaneous formation of long-lived glasses, but rather shows that a high rotational barrier is necessary to prevent crystallization. On the other hand, decreasing the number of hydrogen-bonding groups resulted in a sharp decrease of $T_g$, leading to kinetically stable glasses with $T_g$ values as low as -25 °C. Combining variable-temperature infrared (IR) spectroscopy and chemometrics analyses revealed quantitative relationships between the $T_g$ and the average number of bonded NH groups at $T_g$ and the enthalpy of H-bond formation. Relations between $T_g$ and GFA were also found for glass-formers with linkers that cannot lead to H-bond and are rationalized by taking into account both the rotational energy barrier around the linker and the nature of the intermolecular interactions involved. These structure-properties relationships provide valuable insight towards establishing unified guidelines for the engineering of stable functional glasses with tunable thermal properties.

## 3.3 Results and discussion

The compounds studied herein (Scheme 3.1) all share the same triazine core and bis(3,5-dimethylphenyl) ancillary groups. By exploiting all the combinations of available linkers (NH, NMe and O) and headgroups (NHMe or OMe), the library is composed of two series of six compounds for each headgroup. Scheme 3.2 highlights that this group of linkers enables a systematic investigation of the influence of hydrogen bonding, rotational energy barrier, and steric bulk separately.

Indeed, both the O and NMe linkers cannot donate hydrogen bonds, as opposed to the NH linker. On the other hand, the NMe linkers are expected to present a high rotational energy barrier similar to that of the NH linkers, due to electron delocalization with the triazine ring, while it should be lower for the O linkers. Finally, the NH and O linkers are isosteric, while the NMe linker is bulkier. More specifically, in the sequence NH,NH → NH,O → O,O, shown on the left side of Scheme 3.2, the H-bonding possibility decreases while retaining a similar steric hindrance but lowering the rotational energy barrier. Changing the linkers from NH,NH to NH,NMe to NMe,NMe also provides a gradual decrease of the number of H-bond donors

without affecting much the rotational barrier but this time combined with an increase in the steric hindrance. Finally, the sequence NMe,NMe → NMe,O → O,O completes the cycle, allowing the comparison of non H-bonded linkers with a larger or smaller steric hindrance and, as shown below, rotational energy barrier.

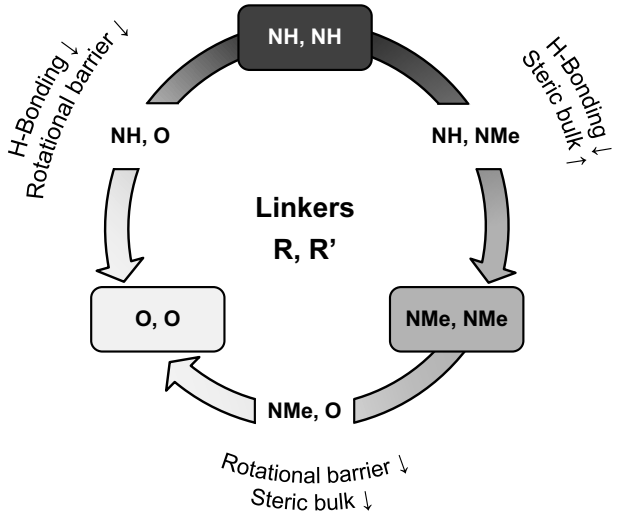


**Scheme 3.2.** Systematic investigation of the linker groups.

## 3.3.1 Synthesis

The reference compounds **1** and **2** with two NH linkers and a NHMe and a OMe headgroup, respectively, were synthesized according to literature procedures, as well as the cyanurate **3** with two O linkers and a OMe headgroup.[8]

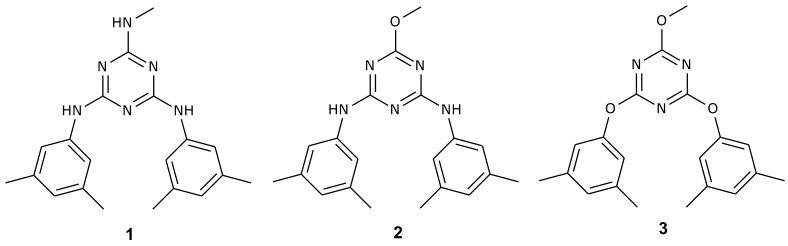


Mexyloxytriazine derivatives **4-6** were prepared in 47-74 % yield from the corresponding chlorotriazine derivatives and 3,5-dimethylphenol in the presence of $K_2CO_3$ in refluxing dioxane (Scheme 3.3), in a procedure similar to the one used to synthesize cyanurate **3**.[8] The products could be conveniently purified by dissolving in dichloromethane followed by

washing with aqueous NaOH to remove the excess of 3,5-dimethylphenol and salts, any triazine impurities generated during the reaction being insoluble in dichloromethane. N-Methylmexylaminotriazine derivatives with a NHMe headgroup **7-8** were synthesized in 48-77 % yield from the corresponding chlorotriazines with a slight excess of N,3,5-trimethylaniline in refluxing dioxane (Scheme 3.4). Removal of the excess of N,3,5-trimethylaniline by aqueous acid washing followed by neutralization gave pure compounds **7-8**.

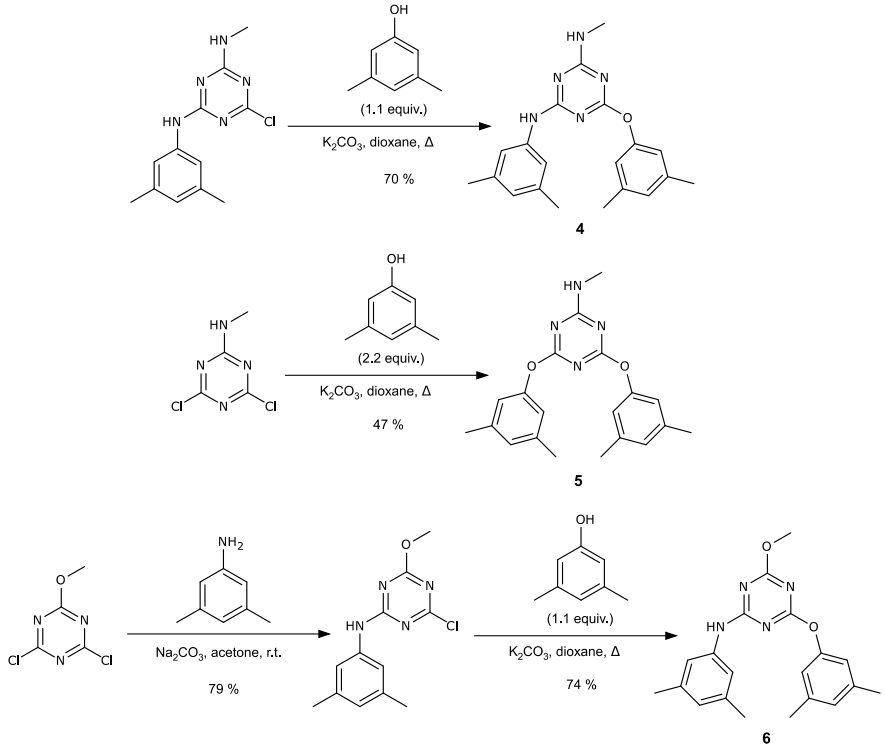


**Scheme 3.3.** Syntheses of compounds **4-6**.

However, for compounds with a OMe headgroup, this route proved unsuccessful as the methoxy group hydrolyzed during the reaction. Instead, methoxy-substituted N-methylated compounds **9-12** were synthesized from their NH analogues by methylation with sodium hydride and iodomethane in DMF (Scheme 3.5). Bis-mexylaminotriazine **2** could be converted to either mono-N-methyl derivative **9** or di-N-methyl analogue **10** depending on the conditions of the reaction. For compound **10**, conversion silica pad, while mono-N-methyl derivatives **9**, **11** and **12** could all be purified by recrystallization from hot hexanes. Interestingly, for compound **11**, the methylation was regioselective to the mexylamino group, and the NHMe headgroup did not impact the outcome of the reaction in a significant fashion.

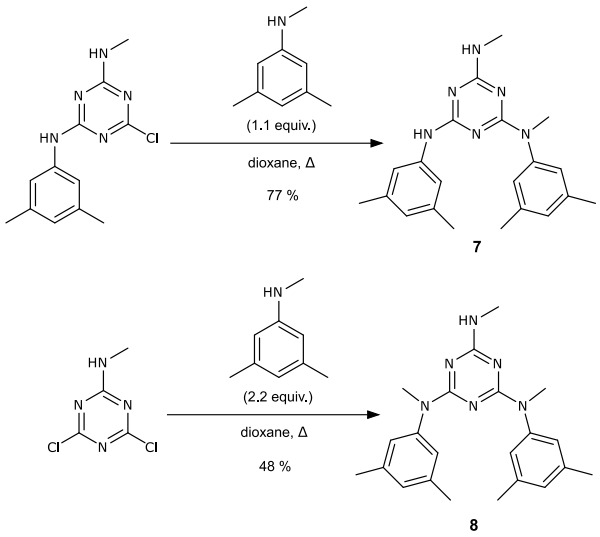


**Scheme 3.4.** Syntheses of compounds **7-8**.

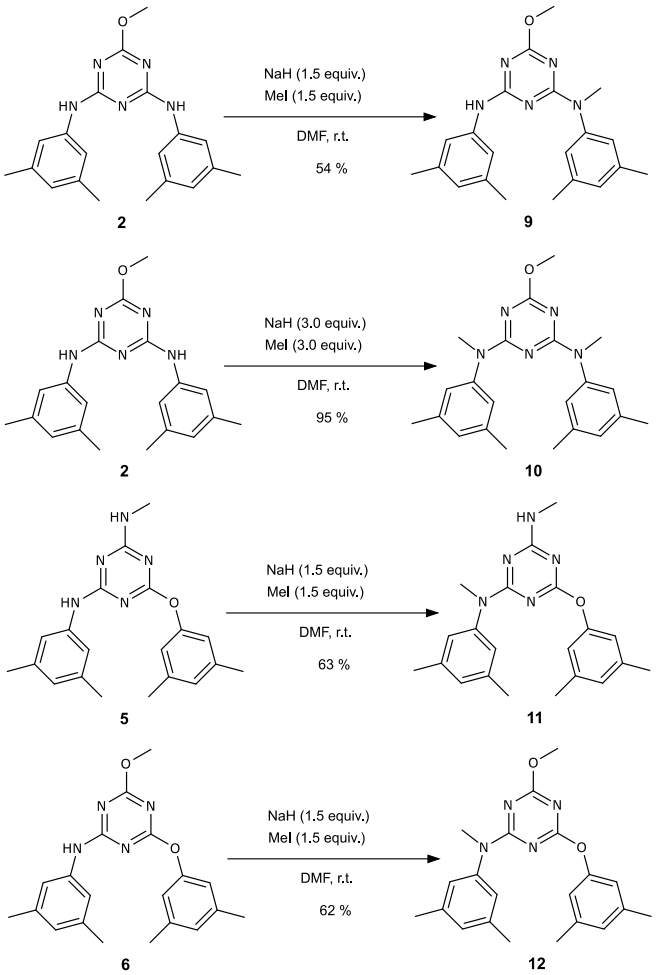


**Scheme 3.5.** Syntheses of compounds **9-12**.

### 3.3.2 Thermal properties

Differential scanning calorimetry (DSC) revealed that eleven out of the twelve compounds studied herein present an outstanding GFA, being completely amorphous (within DSC detection limit) after cooling from the melted state as slowly as 0.5 °C/min. The only exception is compound NHMe/O,O (**5**) (from this point, to simplify the referencing, compound identification numbers will be preceded by X/R,R', where X is the headgroup and R,R' are the linkers) whose critical cooling rate, *i.e.* the slowest rate at which a molecule can be cooled without presenting any traces of crystallization, is faster than 100 °C/min. This increase in critical cooling rate by at least a factor of 200 was not observed for compounds substituted with a OMe headgroup and for another library of compounds with phenyl ancillary groups instead of mexyl groups (see Supplementary Information and Scheme II.S1 for synthetic procedures and Figure 3.S1 for $T_g$), reinforcing the conclusion that the behavior of NHMe/O,O compound **5** is an isolated case. These results show for the first time that H-bonds are, in fact, not necessary to prepare molecular glasses with excellent GFA from triazine derivatives.

Figure 3.1 shows that the linkers play an extremely important role on the thermal properties of the molecules, their $T_g$ spanning from -25 to 94 °C (also see Table 3.S1 in SI). Indeed, classifying the $T_g$ values in ascending order clearly shows that the sequence of linker pairs follows the same order for the series with NHMe (in blue) and OMe (in orange) headgroups. Compounds featuring the NHMe headgroup always present a higher $T_g$ than their OMe analogues. On average, this difference is 27 °C, which is close to the previously observed 29 °C average difference between analogues with NHMe and ethyl (Et) headgroups.[14] This difference in $T_g$ is expected since the NHMe group is a H-bond donor and is strongly conjugated to the triazine core, thus increasing the strength of intermolecular interactions and hindering its rotation compared to the OMe and Et groups. Interestingly, substituting a NH linker for an O or a NMe lowers $T_g$ by the same magnitude, with an average of 31 °C, showing the large impact of the H-bond donating character of the linkers on $T_g$. The series of phenyl-substituted compounds (*vide supra*, Figure II.SI) present $T_g$ values very similar to those of their mexyl-substituted analogues, confirming the important role of the linkers on $T_g$. Two additional qualitative trends can be observed in Figure 3.1. First, $T_g$ increases with the number of NH groups (NMe,NMe < NH,NMe < NH,NH and O,O < NH,O < NH,NH) as previously reported

by Naito[17] and van der Sman[18] for glassy H-bonded systems. Second, and more surprisingly, O linkers lead to higher $T_g$ values than NMe linkers (NMe,NMe < NMe,O < O,O) despite their weaker conjugation to the triazine ring, possibly due to their smaller size (the sterically hindered NMe linkers can obstruct hydrogen bonding with the triazine N atoms for compounds with the NHMe headgroup) or dipolar interactions.

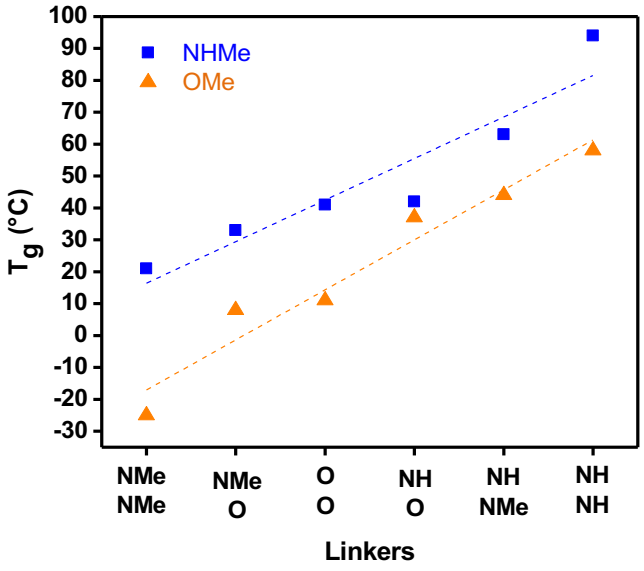


**Figure 3.1**. $T_g$ of the compounds with the NHMe (blue) or OMe (orange) headgroup and different linkers.

Linker groups also influence the kinetic glass stability of the compounds. Indeed, cold crystallization was observed by DSC for compounds OMe/O,O (**3**), NHMe/O,O (**5**), NHMe/NH,O (**4**), NHMe/NMe,O (**11**) and OMe/NH,NMe (**9**) (see Table 3.S1 in SI). In fact, the only compounds containing a O linker that did not show any crystallization by DSC are OMe/NH,O derivative **6** and its OMe/NMe,O analogue **12**, though both compounds crystallized over two weeks on standing at ambient temperature. In sharp contrast, OMe/NMe,NMe derivative **10**, which shows the lowest $T_g$ value in the series, is kinetically stable at ambient temperature, which is close to 50 °C above its $T_g$, for more than a year. In comparison, its analogue OMe/NH,NH (**2**) crystallizes within three days upon annealing at 50 °C above its $T_g$. These features make the compounds with NMe linkers extremely competitive compared to other low $T_g$ molecular glasses: in contrast to them, no long alkyl chain[19] or silyl ether[20] groups need

to be introduced in their structure to impede crystallization. This represents a step forward in the study of homologous glass-formers, limiting the need to take into account the influence of supplementary structures introduced to extend the range of $T_g$.

### 3.3.3 IR spectroscopic characterization of H-bonded glasses

IR spectroscopy is a technique of choice to investigate hydrogen bonding *in situ* during cooling because of its chemical selectivity and its sensitivity to the environment and changes in interactions.[21] For instance, Tang *et al.* have correlated the NH stretching frequency to the hydrogen bonding strength and patterns in analogous amorphous pharmaceutical compounds.[22] Others working on organic OH-containing glass-former systems (sugars, 2-biphenylmethanol) have monitored *in situ* the frequency shift of the "bonded" and the "free" OH vibrations as a function of temperature and observed a break of slope at $T_g$, revealing that the rate of H-bond formation changes between the viscous and glassy states.[23,24] Series of temperature-controlled IR spectra were thus recorded upon cooling at 2 °C/min for the compounds with at least one NH group with the exception of NHMe/O,O (**5**) since its critical cooling rate is too fast (> 100 °C/min) to allow IR measurements with sufficient signal-to-noise ratio without inducing partial crystallization. Figure 3.2 shows a representative example for NHMe/NH,NH compound 1 ($T_g$ = 94 °C), displaying the mid-IR spectral region corresponding to the "free" and "bonded" NH (around 3407 and 3280 $cm^{-1}$, respectively) and the aromatic and aliphatic CH (3050-2850 $cm^{-1}$) stretching vibrations. It should be noted that the "free" and "bonded" labels are used for simplicity and should be understood as NH groups "strongly" and "weakly" H-bonded, respectively. Upon cooling from 130 to 40 °C, the principal changes occur in the NH stretching region as pinpointed by the arrows: the absorbance of the band corresponding to the "free" NH species decreases while that of the "bonded" NH species increases, meaning that a larger fraction of the NH groups are strongly H-bonded in the glassy state than in the viscous state.

In the past, we have observed changes in the relative amounts of "bonded" and "free" NH groups for triazine derivatives that resulted in a break in slope at $T_g$ when plotting the absorbance ratio as a function of temperature. This conclusion was based on relative or semi-quantitative analysis, at best. Here, we aim to obtain for the first time quantitative information on the H-bonded species during the vitrification of triazine derivatives and to relate it to their

macroscopic properties, such as their $T_g$ and enthalpy of H-bond formation. Chemometrics analysis is an appealing method in this context since traditional univariate analysis is not sufficient to obtain an absolute fraction of H-bonds because the "free" and the "bonded" NH stretching bands (besides the Fermi resonance band)[25] are broad and overlapped, making difficult their band fitting or direct integration. This statistical tool processes the data in a multivariate fashion to capture only the significant changes contained in the input variables, simplifying the extraction of the desired information.[26] A self-modeling multivariate curve resolution (MCR) approach was chosen, the Self-Modeling Mixture Analysis (SMMA), because it requires no prior knowledge of the species quantified (spectra for the pure "free" and "bonded" species are not necessary).[27,28] For instance, this approach was successfully used to study quantitatively the H-bond breaking dynamics of water upon heating.[29-31] A linear combination of pure "free" and "bonded" spectra, generated by the algorithm, is then used to reconstruct the experimental spectra and to evaluate the fraction of each species. Such analysis provides a good picture of the behavior of H-bonds upon thermal changes, even though it consists in a simplified model of the more realistic distribution of bond strengths within the material.[32]

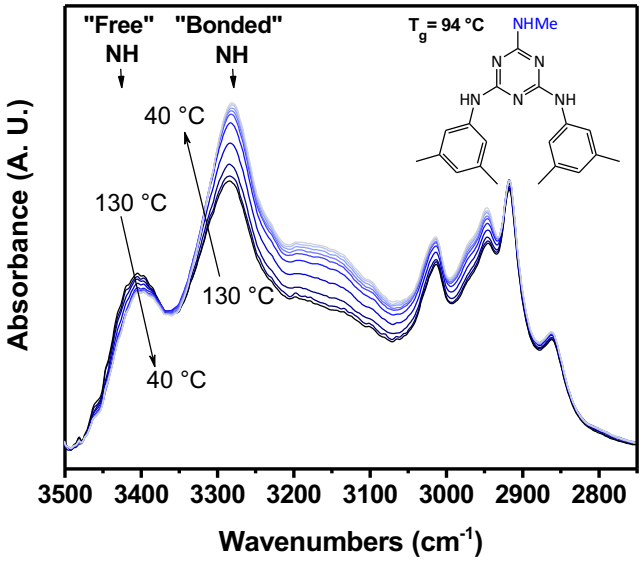


**Figure 3.2.** Infrared spectra of the NHMe/NH,NH compound **1** (shown in the inset) recorded upon cooling highlighting the variation of the "free" and "bonded" NH bands with temperature.

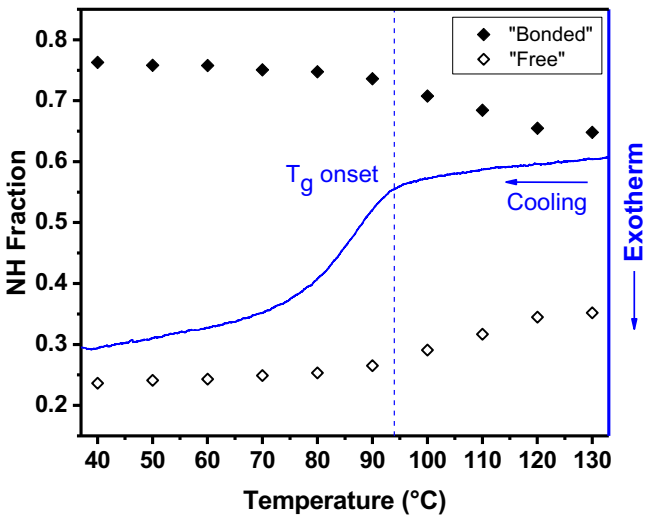


**Figure 3.3.** Evolution of the "free" and the "bonded" NH fractions (black, left Y axis) with temperature during cooling at 2 °C/min for NHMe/NH,NH compound **1**. A DSC trace recorded at the same rate is superimposed (blue, right Y axis).

The results of the calculations (details on the mathematical process can be found in the SI in Figures 3.S2 and 3.S3) for NHMe/NH,NH derivative **1** are shown in Figure 3.3, where the "bonded" and "free" NH fractions (left black Y axis) are plotted as a function of temperature (data were recorded during cooling). At temperatures above $T_g$, in the viscous state, approximately 65% of the NH groups are "bonded" and 35% are "free". Upon cooling below $T_g$, the percentage of "bonded" NH increases to reach 75%, leaving only 25% of "free" NH groups in the glassy state. In both curves, a change of slope can be observed around 95 °C, which corresponds to the $T_g$ of the compound (94 °C), clearly showing that the glass transition occurs upon cooling when the fraction of H-bonded NH groups almost stops increasing. To reinforce this correspondence, a DSC scan recorded upon cooling at 2 °C/min (same rate as used to record the IR spectra) is superimposed on Figure 3.3 to allow comparing the H-bonding and the bulk relaxation dynamics of the sample. An excellent agreement is observed between the spectroscopic $T_g$ and the onset of the DSC $T_g$, suggesting that the compound becomes more and more viscous as the temperature is lowered and tends to jam while undergoing glass transition when a sufficient amount of H-bonds is formed. Once in the glassy state, the mobility is severely reduced, limiting the formation of additional H-bonds and explaining the quasi-plateau observed

below $T_g$. The fact that 65% of the NH groups are still strongly H-bonded in the viscous state for NHMe/NH,NH compound **1** (the other compounds show similar fractions, between 55 and 75% at $T_g$ + 40 °C, see Table 3.S2 in SI), is well in line with our previous suggestion, based on qualitative results,[14,15,33] that the presence of H-bonds holding together the molecules above $T_g$ thwarts crystallization upon cooling by preventing their reorganization into a crystalline lattice in the supercooled liquid.

Even though the type of H-bonded pattern (aggregates or network) found in H-bonded samples and the number of molecules involved in such structures are still sources of debate in the literature, interesting comparisons between the fractions obtained here and in other studies can be made. The large amount of "bonded" NH groups observed above $T_g$ is not surprising considering that it has been estimated by IR spectroscopy that 26% of NH groups were still bonded in Nylon-6,6 above its melting point.[34] Moreover, in their IR study of alcohols, Barlow *et al.* have raised the idea that the fraction of H-bonded species must reach a value lying between 0.6 and 0.7 to allow the formation of aggregates (composed of chains or ring structures) in the liquid or supercritical state.[35] This threshold is close to the "bonded" NH fraction observed in our system at the $T_g$ onset, when the system dynamics radically slows down. Moreover, the simulation work done by Harvey *et al.* on glassy imidazole oligomers,[36] probably the system closest to ours considering the possibility of NH···N interactions, led to fractions of H-bonded species both above and below $T_g$ that correlate well with the values reported here, from 0.6 in the viscous state to 0.85 in the glassy phase (for equivalent temperatures relative to $T_g$)[37] indicating that SMMA provides reliable results and, most importantly, that the phenomena are more general than for the library we have studied.

To investigate if there is a quantitative relation between the fraction of "bonded" NH and the $T_g$ of the compounds, we have multiplied the fraction of "bonded" NH calculated at the $T_g$ of each compound by their respective number of NH groups. The results plotted in Figure 3.4A show that $T_g$ does indeed increase monotonically with the number of H-bonded NH groups per molecule for both the NHMe and OMe headgroup series, as highlighted by the blue and orange dotted lines, respectively. The compounds for which the number of H-bonded NH groups could not be measured by IR spectroscopy are also shown in Figure 3.4A. For the compounds of the OMe series that do not bear NH linkers, it is clear that no H-bonds are present. For

NHMe/O,O derivative 5 (crossed symbol), whose critical cooling rate was too fast for IR measurements, it is assumed that the average number of bonded NH groups is the same as for compound NHMe/NMe,NMe (**8**). In both cases, the data are in good agreement with the linear fits of $T_g$ with the average number of "bonded" NH, supporting the validity of the calculations and the generality of the observed behavior. These observations are in good agreement with the work of van der Sman, where the $T_g$ of carbohydrate derivatives was directly proportional to the number of available hydroxyl groups,[18] and also with the hypothesis made by Kaminski *et al.*[38] that H-bonds can increase the effective molecular weight of a compound, thus increasing its $T_g$.

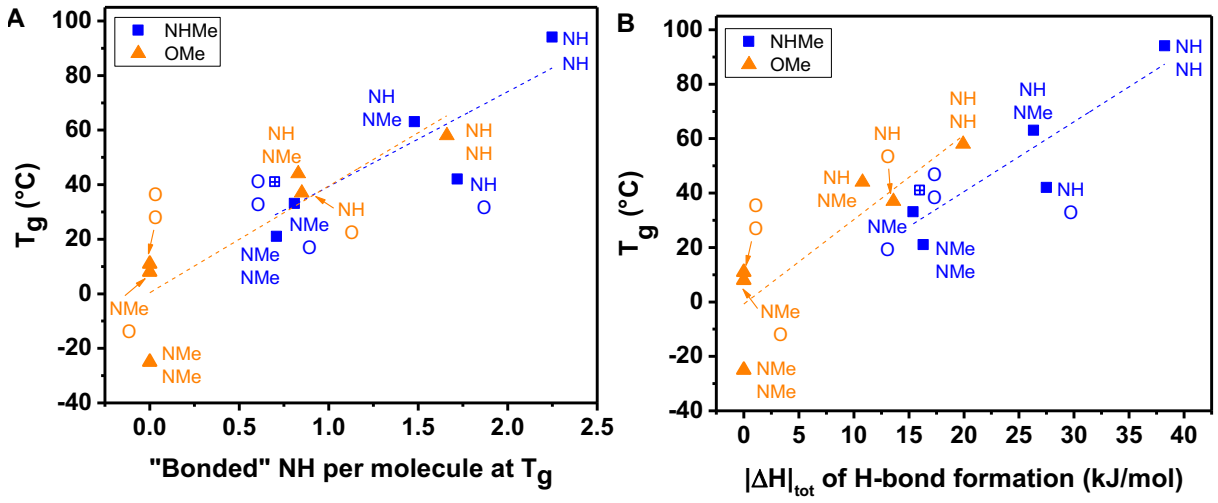


**Figure 3.4.** A) Evolution of $T_g$ with the average number of "bonded" NH per molecule at $T_g$ and B) evolution of $T_g$ with the calculated absolute value of enthalpy ($|\Delta H|_{tot}$) of H-bond formation per molecule. The blue and orange dashed lines indicate the relationship between the variables for the NHMe and OMe headgroups, respectively. A crossed symbol is used for NHMe/O,O compound **5** since its average number of bonded NH groups and $|\Delta H|_{tot}$ of H-bond formation were assumed to be identical to those of NHMe/NMe,NMe compound **8**.

One should keep in mind that not only the number of intermolecular interactions influences the $T_g$; the strength of these interactions must also be taken into account to explain the differences in $T_g$ values.[39] To investigate this relationship, the enthalpy of H-bond formation was calculated using the fractions of "free" and "bonded" NH found above $T_g$, where a

thermodynamic equilibrium takes place as expressed by equation 3.1,[32] giving rise to the equilibrium constant of equation 3.2. Data below $T_g$ cannot be used since the compounds do not reach equilibrium in the glassy state. Using the van't Hoff equation (3.3), the ΔH of H-bond formation can then be calculated. The linear fit for NHMe/NH,NH compound 1 is shown as a representative example in Figure 3.S4, where the slope leads to an absolute enthalpy value of 17 kJ/mol.

$$free\ \text{NH} \rightleftharpoons bonded\ \text{NH} \tag{3.1}$$

$$K_{eq} = \frac{Bonded\ \ NH}{Free\ \ NH} \tag{3.2}$$

$$lnK_{eq} = \frac{-\Delta H}{RT} + \frac{\Delta S}{R} \tag{3.3}$$

Similar values are calculated for the other compounds (see Table 3.S3 in SI) with an average of 15 kJ/mol. These enthalpies are in good agreement with the values reported for the formation of individual hydrogen bonds: NH···N and NH···O are classified at the border between "weak" and "strong" intermolecular interactions[9] with association energies of approximately 16 kJ/mol.[40] The total enthalpy per molecule ($|\Delta H|_{tot}$) can then be obtained by multiplying the average number of "bonded" NH at $T_g$ by the |ΔH| of H-bond formation calculated for each compound. For NHMe/NH,NH compound 1, the calculated $|\Delta H|_{tot}$ is 38 kJ/mol and is comparable to the value of 37 kJ/mol reported by Pawlus *et al.* for amorphous adonitol sugar bearing 3.5 effective OH groups.[41] The $T_g$ of the compounds are plotted as a function of $|\Delta H|_{tot}$ in Figure 3.4B. The value of $T_g$ increases with enthalpy, confirming that it depends not only on the number of H-bonds but also on their strength. As in Figure 3.4A, the non H-bonded compounds and the NHMe/O,O derivative **5** (crossed symbol) were added to the plot considering $|\Delta H|_{tot} = 0$ and the $|\Delta H|_{tot}$ of the NHMe/NMe,NMe compound **8**, respectively, to confirm the trend observed. However, it must be understood that while the triazine nitrogen atoms are the strongest electron donors present and thus the most prevalent H-bond acceptors, a variety of NH···Y interactions are possible (Y = nitrogen or oxygen atom from another headgroup, from a linker, and from the triazine ring, without excluding possible weaker NH···π interactions with the mexyl or triazine rings) meaning that the calculated enthalpy of H-bond formation represents an average of all possibilities.[42-44]

Another striking observation in Figure 3.4B is that for a similar enthalpy of H-bond formation per molecule, $T_g$ is systematically higher for compounds with the OMe than the NHMe headgroup. This suggests that, in absence of H-bonds, other interactions take over and can also enable a good GFA. The comparison of Figure 3.4A and 3.4B emphasizes this hypothesis: the OMe/NH,NH compound 2 has a similar average number (1.4-1.7) of "bonded" NH at $T_g$ as its NHMe/NH,NMe (1) and NHMe/NH,O (4) analogues that also contain two NH groups, but its $|\Delta H|_{tot}$ of H-bond formation is almost 25% lower. The same observation can be made by comparing the OMe and Et headgroup with two NH linkers. As mentioned in the Thermal properties section, while these compounds present, on average, the same $T_g$ and have the same average number of bonded NH per molecule at $T_g$, *i.e.* 1.7 (the same chemometrics procedure was applied for the Et/NH,NH compound, not shown), the Et compound has a $|\Delta H|_{tot}$ that is 27% higher than the OMe one. This illustrates that a compound can present a higher $T_g$ even if its $|\Delta H|_{tot}$ of H-bonds formation is lower, reinforcing the idea that H-bonds are not mandatory to achieve a glass-former design presenting a good GFA and a convenient $T_g$ for devices used at or above room temperature.

### 3.3.4 Calculation of rotational energy barrier of non H-bonded linkers

The non H-bonded glass-formers with OMe headgroup and O and NMe linkers present, as expected, a lower $T_g$ than their H-bonded analogues, but they nevertheless possess a very good GFA. They can thus bring further fundamental insights on the impact on $T_g$ and GFA of the rotation of the ancillary groups, which is closely related to the conformational flexibility that has been reported to be a parameter influencing the GFA.[45-47] *Ab initio* calculations were conducted to estimate the activation energy required for rotating bonds between the linkers R or R' and the triazine core, as illustrated in the inset of Figure 3.5. These simulations reveal that the O linkers have a much lower rotational energy barrier (20 kJ/mol) than the NMe linkers (54 kJ/mol). Figure 3.5 shows a monotonic $T_g$ decrease as the rotational energy barrier increases. As shown in previous studies, establishing a direct link between $T_g$ and the rotational energy barrier is not straightforward and molecular dynamics simulations involving an assembly of molecules should be employed to specifically unveil the microscopic origin of variations of $T_g$, GFA, and GS.[16] Nevertheless, calculations on one molecule can lead to plausible interpretation. A lower rotational energy barrier would allow the mexyl groups to adapt better to their

environment above $T_g$, and thus to form more π-π interactions that lead to jamming at higher temperature, therefore leading to a higher $T_g$. A similar argument can be used for crystallization and can help explaining the much worse GFA of the NHMe/O,O compound **5** compared to all the other glasses. This compound needs a very rapid cooling rate, faster than 100 °C/min to prevent crystallization, while all its analogues yield a glass at cooling rates lower than 0.5 °C/min. In fact, both compounds with O,O linkers (with NHMe or OMe headgroup) present a poor resistance to crystallization, both on standing at ambient temperature and upon heating, and their crystallization temperature (Table 3.S1) is 20 °C lower than for the other compounds of this library. These behaviors can be attributed to a faster sampling of different rotameric states by the mexyl groups allowing them to find the most thermodynamically stable one. In contrast, the much higher interconversion energy barrier of the NMe (or NH) linkers tends to favor the coexistence of multiple conformers, thereby preventing the molecules from organizing into an ordered crystalline structure.

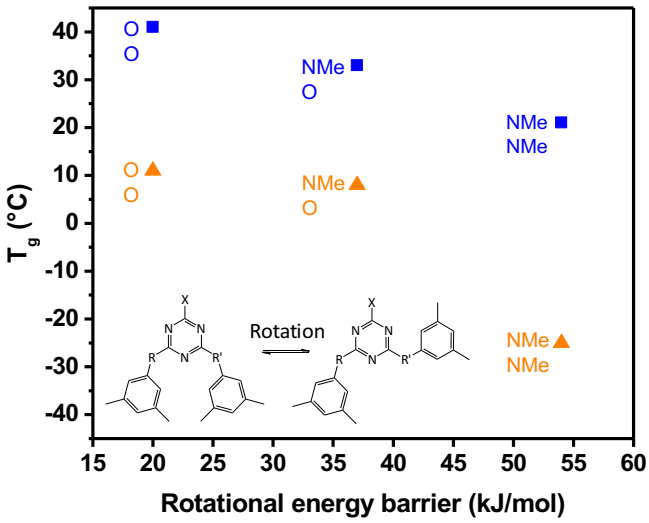


**Figure 3.5.** Relation between the $T_g$ and the calculated rotational energy barrier for the non H-bonded linkers. The inset shows the rotation of the ancillary group for which the energy barrier is simulated.

These observations are consistent with the results for the compounds with a NHMe headgroup bearing non-H bonded linkers: they also show a higher $T_g$ with O linkers than with NMe linkers for this series. In this case, the lower rotational barrier that is believed to lead to an

easier formation of π-π interactions may also be combined to the better accessibility (lower steric hindrance) of the O linkers to accept an H-bond from the NH of the headgroup, or even to dipolar interactions between O linkers due to their additional lone pair of electrons compared to NMe linkers. For instance, it has been shown that strong intramolecular and weaker intermolecular O···O interactions are partly responsible for the planarity and face-to-face stacking in the single crystal structure of 2,6-dinitrophenol.[48] Such interactions could partly explain why compounds bearing O linkers show higher $T_g$ than their NMe analogues even if their rotational barrier is lower.

## 3.4 Conclusions

This investigation of a homologous series of 12 glass-forming triazine derivatives bearing NH, NMe and O linkers provided new insights on the influence of H-bonding and interconversion energy barrier on the glass transition, glass-forming ability and glass kinetic stability. These compounds with excellent glass-forming ability (critical cooling rate lower than 0.5 °C/min for 11 compounds) present a $T_g$ ranging from -25 to 94 °C, revealing the dramatic importance of delicate molecular modifications on glass properties. Variable-temperature infrared spectroscopy and chemometrics analysis were combined to monitor quantitatively for the first time H-bonding upon the vitrification of triazine derivatives. They revealed a monotonic increase of $T_g$ with the average number of bonded NH groups at $T_g$ and with the enthalpy of H-bond formation per molecule. The rotational energy barriers of the non H-bonded linkers were calculated and, as expected, indicated that the rotation of NMe linkers is significantly more hindered than that of O linkers. In spite of this, the $T_g$ of compounds bearing O linkers was systematically higher than for those with NMe linkers, and their resistance to crystallization was lower. These observations lead to several conclusions that reinforce our understanding of the glass-forming behavior of this family of materials. In contrast to previous assertions, the presence of H-bonding groups contributes to glass formation (more than the half of the NH groups are still H-bonded even at 40 °C above their $T_g$) and to increasing $T_g$ but is not necessary for glass formation. The existence and kinetic accessibility of multiple conformations of similar energies with hindered equilibria due to high rotational barriers is likely a more important contributor to glass-forming ability. For these reasons, headgroups or linkers that rotate more

easily lead to a decrease in resistance to crystallization (worse kinetic stability). Finally, the presence of hydrogen bonds, by raising $T_g$, hinders crystallization of the compound at ambient temperature, but actually promotes crystallization upon annealing above $T_g$. The lessons learned through the present study point towards NMe linkers as structural elements enabling to design glasses with low $T_g$ values with long-term kinetic stability above their $T_g$. Such glasses show promise for applications involving materials in their viscous state, where few small molecules show a both an excellent glass-forming ability and high enough resistance to crystallization to be viable candidates.

## 3.5 Experimental section

### 3.5.1 General

2-Methylamino-4,6-dichloro-1,3,5-triazine,[8] 2-methoxy-4,6-dichloro-1,3,5-triazine,[49] 2-methylamino-4-mexylamino-6-chloro-1,3,5-triazine,[13] 2-methylamino-4,6-bis(mexylamino)-1,3,5-triazine (1),[8] 2-methoxy-4,6-bis(mexylamino)-1,3,5-triazine (2),[8] 2-methoxy-4,6-bis(3,5-dimethylphenoxy)-1,3,5-triazine (3),[8] 2-methoxy-4,6-bis(phenylamino)-1,3,5-triazine (13),[50] 2-chloro-4,6-bis(N-methylphenylamino)-1,3,5-triazine,[51] 2-(phenylamino)-4,6-dichloro-1,3,5-triazine,[52] and N,3,5-trimethylaniline[53] were prepared according to literature procedures. All other reagents and solvents were purchased from commercial sources and used without further purification. All reactions were performed under ambient atmosphere. SiliaFlash P60 grade silica gel and TLC plates were purchased from SiliCycle.

$^1$H NMR spectra were recorded on a Bruker Avance 400 MHz or a Varian Mercury 300 MHz at 298 K or 363 K (as indicated). $^{13}$C NMR spectra were recorded on a Varian Mercury 300 MHz spectrometer at 298 K. FT-IR spectra were recorded on a Tensor 27 FT-IR spectrometer (Bruker Optics) equipped with a liquid nitrogen-cooled HgCdTe detector and a MIRacle (Pike Technologies) silicon attenuated total reflection (ATR) accessory as films directly cast on the ATR crystal from $CH_2Cl_2$ solution. Decomposition analyses of molecular glasses were obtained using a TGA 2950 thermogravimetric analyzer (TA Instruments) at a heating rate of 10 °C/min under a nitrogen atmosphere. The glass transition, crystallization and melting temperatures ($T_g$, $T_c$ and $T_m$, respectively) were recorded by DSC with a PerkinElmer

DSC 8500 calorimeter calibrated with indium using a heating rate of 10 °C/min. $T_g$ values are reported as the average of the values observed in heating after an initial cycle of heating and cooling at 10 °C/min.

### 3.5.2 Variable-temperature infrared spectroscopy

Solutions of NH-substituted compounds in $CH_2Cl_2$ were spin-coated with a Headway Research EC-101 apparatus at 4000 rpm during 30 s on ZnSe windows. Variable-temperature transmission spectra were recorded, with a resolution of 4 $cm^{-1}$, using a Vertex 70 FT-IR spectrometer (Bruker Optics) equipped with a DTGS detector and a FTIR600 heating stage equipped with a T95 LinkPad temperature controller (Linkam Scientific Intruments). Samples were first heated to the highest temperature that did not induce dewetting or cold crystallization of the film, followed by a 3 min isotherm. Samples were then cooled down using a cooling rate of 2 °C/min and 100 scans were averaged for measuring each spectrum at each 10 °C. Background single beam spectra were recorded for each temperature. Principal component analysis and SMMA analysis were carried out using the PCA and the Purity algorithms, respectively, available in PLS_Toolbox (Eigenvector Research). Prior to these analyses, spectra were preprocessed using the baseline correction and the normalization area options.

### 3.5.3 Calculation methodology

Calculations were carried out using the Density Functional Theory approach using B3LYP as the functional with the 6-31g(d,p) basis set in the Gaussian 09 © environment.[54] The *scan* keyword was used. To determine the potential energy barrier, a scan of the dihedral angle associated with the bond between the linker and the mexyl group, was undertaken. It consists in constraining this angle to a specific value. It is then incremented by steps of 10° between 0 and 180°. At each step, the geometry of the rest of the molecule is optimized in order to reach a minimum in energy. The rotational potential energy barrier corresponds to the energy that needs to be crossed to go from one state of minimum energy to the other (both minimum energy states are equal in energy).

### 3.5.4 Syntheses

*Voir* Annexe II.

## 3.6 Acknowledgements

The authors thank the Academic Research Programme (ARP) from RMC and the Fonds de Recherche du Québec – Nature et Technologies (FRQNT) for funding. AL thanks the Natural Sciences and Engineering Research Council (NSERC) of Canada for a Vanier graduate scholarship. The authors are also grateful to Dr. René Gagnon (Université de Sherbrooke) for mass spectrometry analysis and Dominic Lauzon (Université de Montréal) for executing some of the variable-temperature FT-IR measurements. Computations were made on the supercomputer Mammouth from Université de Sherbrooke, managed by Calcul Québec and Compute Canada.

## 3.7 References

1. Ediger, M. D.; Angell, C. A.; Nagel, S. R., *J. Phys. Chem.* **1996,** *100*, 13200-13212.
2. Kulkarni, A. P.; Tonzola, C. J.; Babel, A.; Jenekhe, S. A., *Chem. Mater.* **2004,** *16*, 4556-4573.
3. Hancock, B. C.; Zografi, G., *J. Pharm. Sci.* **1997,** *86*, 1-12.
4. Alba, C.; Busse, L. E.; List, D. J.; Angell, C. A., *J. Chem. Phys.* **1990,** *92*, 617-624.
5. Whitaker, C. M.; McMahon, R. J., *J. Phys. Chem.* **1996,** *100*, 1081-1090.
6. Ping, W.; Paraska, D.; Baker, R.; Harrowell, P.; Angell, C. A., *J. Phys. Chem. B* **2011,** *115*, 4696-4702.
7. Liu, T.; Cheng, K.; Salami-Ranjbaran, E.; Gao, F.; Glor, E. C.; Li, M.; Walsh, P. J.; Fakhraai, Z., *Soft Matter* **2015,** *11*, 7558-7566.
8. Lebel, O.; Maris, T.; Perron, M.-È.; Demers, E.; Wuest, J. D., *J. Am. Chem. Soc.* **2006,** *128*, 10372-10373.
9. Desiraju, G. R., *Acc. Chem. Res.* **2002,** *35*, 565-573.
10. Wuest, J. D., *Chem. Commun.* **2005,** 5830-5837.
11. Wicker, J. G. P.; Cooper, R. I., *CrystEngComm* **2015,** *17*, 1927-1934.

12. Carvalho, S. P.; Wang, R.; Wang, H.; Ball, B.; Lebel, O., *Cryst. Growth Des.* **2010,** *10*, 2734-2745.
13. Eren, R. N., et al., *Tetrahedron* **2012,** *68*, 10130-10144.
14. Laventure, A.; Soldera, A.; Pellerin, C.; Lebel, O., *New J. Chem.* **2013,** *37*, 3881-3889.
15. Plante, A.; Mauran, D.; Carvalho, S. P.; Pagé, J. Y. S. D.; Pellerin, C.; Lebel, O., *J. Phys. Chem. B* **2009,** *113*, 14884-14891.
16. Plante, A.; Palato, S.; Lebel, O.; Soldera, A., *J. Mater. Chem. C* **2013,** *1*, 1037-1042.
17. Naito, K., *Chem. Mater.* **1994,** *6*, 2343-2350.
18. van der Sman, R. G., *J. Phys. Chem. B* **2013,** *117*, 16303-13.
19. Zhang, L.; Xu, S.; Yang, Z.; Cao, S., *Mater. Chem. Phys.* **2011,** *126*, 804-810.
20. Kamino, B. A.; Castrucci, J.; Bender, T. P., *Silicon* **2011,** *3*, 125-137.
21. Risen Jr, W. M., *J. Non-Cryst. Solids* **1985,** *76*, 97-108.
22. Tang, X.; Pikal, M.; Taylor, L., *Pharm. Res.* **2002,** *19*, 477-483.
23. Imamura, K.; Sakaura, K.; Ohyama, K.-i.; Fukushima, A.; Imanaka, H.; Sakiyama, T.; Nakanishi, K., *J. Phys. Chem. B* **2006,** *110*, 15094-15099.
24. Baran, J.; Davydova, N. A.; Pietraszko, A., *J. Mol. Struct.* **2005,** *744–747*, 301-305.
25. Costard, R.; Greve, C.; Fidder, H.; Nibbering, E. T., *J. Phys. Chem. B* **2015,** *119*, 2711-25.
26. Gemperline, P., *Practical Guide To Chemometrics*. 2nd ed.; CRC Press: Boca Raton, 2006.
27. Windig, W.; Guilment, J., *Anal. Chem.* **1991,** *63*, 1425-1432.
28. Windig, W.; Stephenson, D. A., *Anal. Chem.* **1992,** *64*, 2735-2742.
29. Libnau, F. O.; Toft, J.; Christy, A. A.; Kvalheim, O. M., *J. Am. Chem. Soc.* **1994,** *116*, 8311-8316.
30. Segtnan, V. H.; Šašić, Š.; Isaksson, T.; Ozaki, Y., *Anal. Chem.* **2001,** *73*, 3153-3161.
31. Šašić, S.; Segtnan, V. H.; Ozaki, Y., *J. Phys. Chem. A* **2002,** *106*, 760-766.
32. Angell, C. A.; Rodgers, V., *J. Chem. Phys.* **1984,** *80*, 6245-6252.
33. Wang, R.; Pellerin, C.; Lebel, O., *J. Mater. Chem.* **2009,** *19*, 2747-2753.
34. Garcia, D.; Starkweather, H., Jr., Hydrogen Bonding in Nylon 66 and Model Compounds. In *Fourier Transform Infrared Characterization of Polymers*, Ishida, H., Ed. Springer US: 1987; Vol. 36, pp 213-230.

35. Barlow, S. J.; Bondarenko, G. V.; Gorbaty, Y. E.; Yamaguchi, T.; Poliakoff, M., *J. Phys. Chem. A* **2002,** *106*, 10452-10460.
36. Harvey, J. A.; Auerbach, S. M., *J. Phys. Chem. B* **2014,** *118*, 7609-7617.
37. Harvey, J. A.; Basak, D.; Venkataraman, D.; Auerbach, S. M., *Mol. Phys.* **2012,** *110*, 957-966.
38. Kaminski, K., et al., *Macromolecules* **2013,** *46*, 1973-1980.
39. Angell, C. A.; Alba-Simionesco, C.; Fan, J.; Green, J. L., Hydrogen Bonding and the Fragility of Supercooled Liquids and Biopolymers. In *Hydrogen Bond Networks*, Bellissent-Funel, M.-C.; Dore, J., Eds. Springer Netherlands: 1994; Vol. 435, pp 3-22.
40. Steiner, T., *Angew. Chem. Int. Ed.* **2002,** *41*, 48-76.
41. Pawlus, S.; Grzybowski, A.; Paluch, M.; Wlodarczyk, P., *Phys. Rev. E* **2012,** *85*, 052501.
42. Vaupel, S.; Brutschy, B.; Tarakeshwar, P.; Kim, K. S., *J. Am. Chem. Soc.* **2006,** *128*, 5416-5426.
43. Bloom, J. W. G.; Raju, R. K.; Wheeler, S. E., *J. Chem. Theory Comput.* **2012,** *8*, 3167-3174.
44. Wheeler, S. E.; Bloom, J. W., *J. Phys. Chem. A* **2014,** *118*, 6133-47.
45. Mahlin, D.; Ponnambalam, S.; Heidarian Höckerfelt, M.; Bergström, C. A. S., *Mol. Pharm.* **2011,** *8*, 498-506.
46. Yu, L.; Reutzel-Edens, S. M.; Mitchell, C. A., *Org. Process Res. Dev.* **2000,** *4*, 396-402.
47. Karis, T. E.; Kim, S. J.; Gendler, P. L.; Cheng, Y. Y., *J. Non-Cryst. Solids* **1995,** *191*, 293-303.
48. Cenedese, S.; Zhurov, V. V.; Pinkerton, A. A., *Cryst. Growth Des.* **2015,** *15*, 875-883.
49. Tanaka, T.; Noguchi, M.; Watanabe, K.; Misawa, T.; Ishihara, M.; Kobayashi, A.; Shoda, S.-i., *Org. Biomol. Chem.* **2010,** *8*, 5126-5132.
50. Dudley, J. R.; Thurston, J. T.; Schaefer, F. C.; Holm-Hansen, D.; Hull, C. J.; Adams, P., *J. Am. Chem. Soc.* **1951,** *73*, 2986-2990.
51. Kober, E.; Rätz, R., *J. Org. Chem.* **1962,** *27*, 2509-2514.
52. Matsuno, T.; Kato, M.; Tsuchida, Y.; Takahashi, M.; Yaguchi, S.; Terada, S., *Chem. Pharm. Bull.* **1997,** *45*, 291-296.
53. Fusco, R.; Sannicolo, F., *J. Org. Chem.* **1982,** *47*, 1691-1696.

54. Frisch, M. J.; Trucks, G. W.; Schlegel, H. B.; Scuseria, G. E.; Robb, M. A.; Cheeseman, J. R.; Zakrzewski, V. G.; Montgomery, J. J. A.; Stratmann, R. E.; Burant, J. C.; Dapprich, S.; Millam, J. M.; Daniels, A. D.; Kudin, K. N.; Strain, M. C.; Farkas, O.; Tomasi, J.; Barone, V.; Cossi, M.; Cammi, R.; Mennucci, B.; Pomelli, C.; Adamo, C.; Clifford, S.; Ochterski, J.; Petersson, G. A.; Ayala, P. Y.; Cui, Q.; Morokuma, K.; Malick, D. K.; Rabuck, A. D.; Raghavachari, K.; Foresman, J. B.; Cioslowski, J.; Ortiz, J. V.; Stefanov, B. B.; Liu, G.; Liashenko, A.; Piskorz, P.; Komaromi, I.; Gomperts, R.; Martin, R. L.; Fox, D. J.; Keith, T.; Al-Laham, M. A.; Peng, C. Y.; Nanayakkara, A.; Challacombe, M. W.; Gill, P. M.; Johnson, B.; Chen, W.; Wong, M. W.; Andres, J. L., Gonzalez, C.; Head-Gordon, M.; Replogle, E. S.; Pople, J. A. Gaussian 98, Revision A.6, Gaussian, Inc., Pittsburgh PA, 1998.

## 3.8 Supporting information

### Synthesis of compounds 13-15 and NMR spectra of compounds

*Voir* Annexe II. Les spectres RMN peuvent être consultés au http://www.rsc.org/suppdata/c5/cp/c5cp06630a/c5cp06630a1.pdf

### Characterization

**Table 3.S1.** Comparison of the glass transition temperature ($T_g$), crystallisation temperature ($T_c$) and melting temperature ($T_m$) of compounds **1-12**.

| Linkers | Headgroup | | | | | | | |
|---|---|---|---|---|---|---|---|---|
| | NHMe | | | | OMe | | | |
| | | $T_g$ (°C) | $T_c$ (°C) | $T_m$ (°C) | | $T_g$ (°C) | $T_c$ (°C) | $T_m$ (°C) |
| NH, NH | **1** | 94 | - | - | **2** | 58 | - | 168 |
| O,O | **5** | 41 | 58, 100 | 180 | **3** | 11 | 98 | 129 |
| NH, O | **4** | 42 | 122 | 178 | **6** | 37 | - | - |
| NH, NMe | **7** | 63 | - | - | **9** | 44 | 126 | 148 |
| NMe, NMe | **8** | 21 | - | - | **10** | -25 | - | - |
| NMe, O | **11** | 33 | 126 | 152 | **12** | 8 | - | 129 |

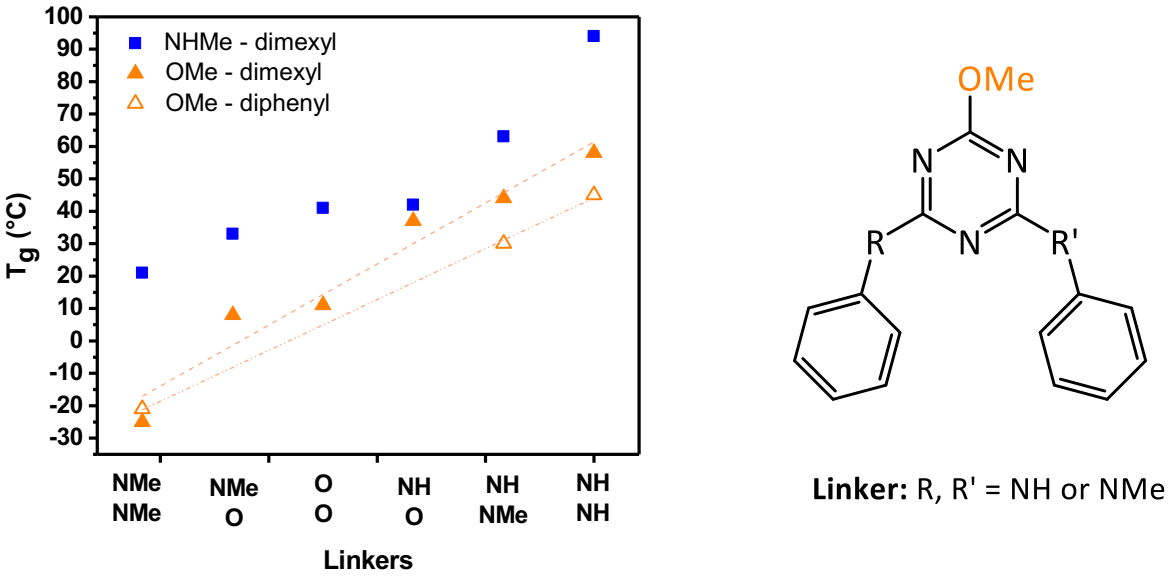


**Figure 3.S1.** Evolution of $T_g$ according to their headgroup and linkers. Compounds bearing an OMe headgroup and diphenyl moieties as shown on the right (dashed-dotted line, shown at the right of the figure and represented by open symbols) follow the trend of the dimexyl (dashed line) for the OMe headgroup series of compounds.

*Chemometrics processing of the spectra*

From the experimental spectral input data, the algorithm first defines the pure variables (the wavenumbers that present the highest ratio of standard deviation to the mean)[2] to enable the calculation of the pure component spectra, *i.e.* the spectra that would be equivalent to a totally "free" NH species and a totally "bonded" NH species in our case (see Figure 3.S2). These two spectra can then be used in a linear combination to reproduce the experimental spectral input data. Principal component analysis (PCA) was conducted prior to the SMMA and revealed that, for all compounds, two components account for 97 to 99% of the variance of the experimental spectral input data, meaning that our system can be reasonably well described using solely the "free" and "bonded" components.[2,3,4]

Figure 3.S3 compares the original (experimental) and the reconstructed data. In all cases, the calculated relative root sum of square difference (rrssq, which calculates the difference

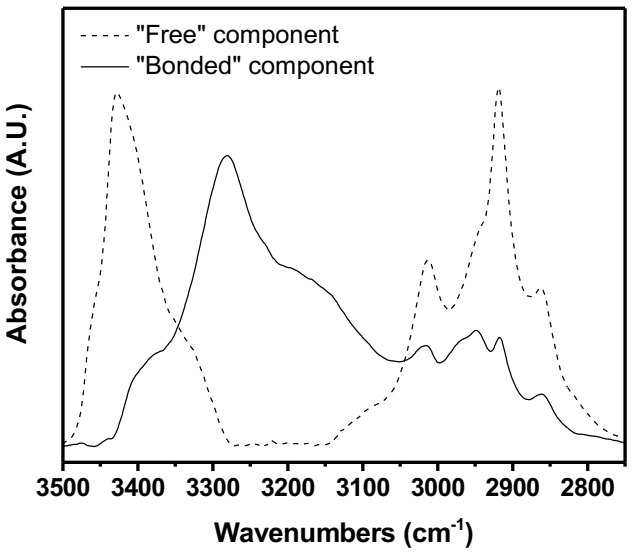


**Figure 3.S2.** Pure components spectra corresponding to the "free" NH species and the "bonded" NH species extracted from the variable-temperature IR spectra of the NHMe/NH,NH compound **1**.

between the two data sets) lies between 0.003 and 0.015, indicating an excellent agreement between the two sets of spectra and confirming the uselessness of considering a third component to describe the system. Indeed, the intensity of the residuals is two orders of magnitude lower than the intensity of the original spectra. Sometimes, residuals show what could be considered as structured data, where a derivative-shaped band showed in between the "free" and the "bonded" bands (around 3325 $cm^{-1}$ for the NHMe/NH,NH compound **1**, see the right panel of Figure 3.S3). A similar third component was observed in other H-bonded systems and defined as the intermediate case between the two species by Šašić *et al*., among others.[2] In the present case, and in the cases reported in the literature, this component does not contribute significantly to the data, accounting for less than 1% of the original spectra. A two-component representation was thus chosen as a suitable model for the systems (without ruling out the existence of a minor third species in the real system). The fractions of each species displayed in Figure 3.3 of the main text correspond to the multiplying factor needed to reconstruct the spectral data from the two corresponding pure component spectra. It must be emphasized that we do not claim that these fractions, although absolute (versus relative), stand as the "real" numbers. Indeed, Dupuy *et al.* have demonstrated that quantification with this SMMA method leads to a relative error of

10%.[5] However, we believe that the comparison of this quantification is still meaningful because the data processing was done identically for all compounds.

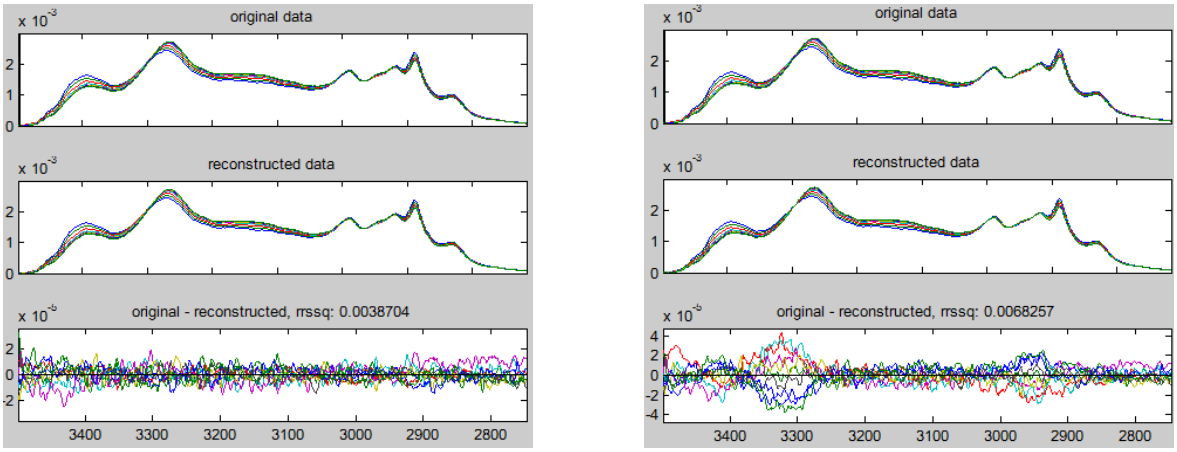


**Figure 3.S3.** Reconstructed original spectra of NHMe/NH,NH compound **1** for two independent samples using two pure component spectra. In the left panel, no evidence of a residual component is found while a small contribution, larger at extreme temperatures, is found around 3325 $cm^{-1}$ in the right panel.

**Table 3.S2.** Average fraction of bonded NH (± standard deviation for three measurements) at different temperatures for the compounds studied by variable-temperature IR spectroscopy.

| Linkers | Headgroup | | | | | | | |
|---|---|---|---|---|---|---|---|---|
| | NHMe | | | | OMe | | | |
| | | $T_g - 20$ | $T_g$ | $T_g + 40$ | | $T_g - 20$ | $T_g$ | $T_g + 40$ |
| NH, NH | **1** | 0.77 ± 0.02 | 0.74 ± 0.01 | 0.66 ± 0.01 | **2** | 0.85 ± 0.01 | 0.83 ± 0.01 | 0.76 ± 0.01 |
| O, O | **5** | - | - | - | **3** | - | - | - |
| NH, O | **4** | - | 0.86 ± 0.01 | 0.79 ± 0.02 | **6** | - | 0.85 ± 0.01 | 0.75 ± 0.01 |
| NH, NMe | **7** | 0.77 ± 0.02 | 0.73 ± 0.02 | 0.60 ± 0.03 | **9** | - | 0.8 ± 0.1 | 0.72 ± 0.1 |
| NMe, NMe | **8** | 0.73 ± 0.02 | 0.71 ± 0.01 | 0.55 ± 0.02 | **10** | - | - | - |
| NMe, O | **11** | - | 0.81 ± 0.02 | 0.67 ± 0.01 | **12** | - | - | - |

*Calculation of the enthalpy of H-bond formation*

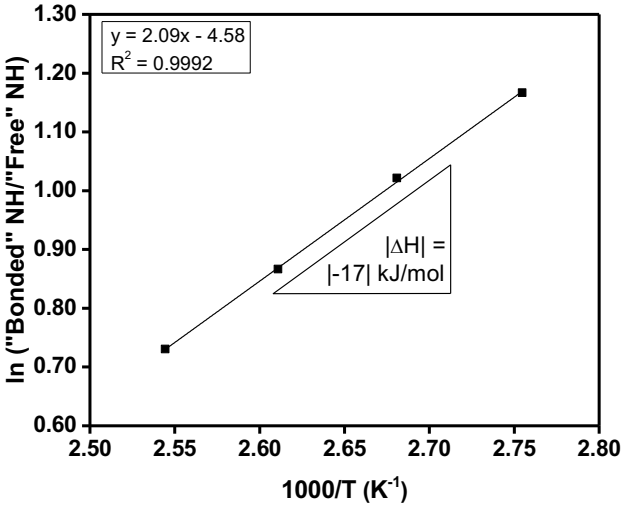


**Figure 3.S4.** Construction of the van't Hoff plot from the "bonded" and "free" NH fractions of the NHMe/NH,NH (**1**). The value of the slope gives access to the ΔH of H-bonds formation.

**Table 3.S3.** Enthalpy of H-bond formation (± standard deviation for three measurements) for the compounds studied by variable-temperature IR spectroscopy.

| Linkers | Headgroup | | | |
|---|---|---|---|---|
| | NHMe | | OMe | |
| | kJ/mol | | kJ/mol | |
| NH, NH | **1** | 17 ± 2 | **2** | 12 ± 1 |
| O,O | **5** | - | **3** | - |
| NH, O | **4** | 16 ± 1 | **6** | 16 ± 1 |
| NH, NMe | **7** | 17.8 ± 0.4 | **9** | 13 ± 2 |
| NMe, NMe | **8** | 23 ± 2 | **10** | - |
| NMe, O | **11** | 19 ± 2 | **12** | - |

*References*


1. Lebel, O., Maris, T., Perron, M.-È., Demers, E., Wuest, J. D. *J. Am. Chem. Soc.* **2006,** *128*, 10372.
2. Šašić, S., Segtnan, V. H., Ozaki, Y. *J. Phys. Chem. A* **2002,** *106*, 760.
3. Libnau, F. O., Toft, J., Christy, A. A., Kvalheim, O. M. *J. Am. Chem. Soc.* **1994,** *116*, 8311.
4. Segtnan, V. H., Šašić, Š., Isaksson, T., Ozaki, Y. *Anal. Chem.* **2001,** *73*, 3153.
5. Dupuy, N., Batonneau, Y. *Anal. Chim. Acta* **2003,** *495*, 205.

# Chapitre 4: Glass versus crystal: a balancing act between competing intermolecular interactions*

## 4.1 Abstract


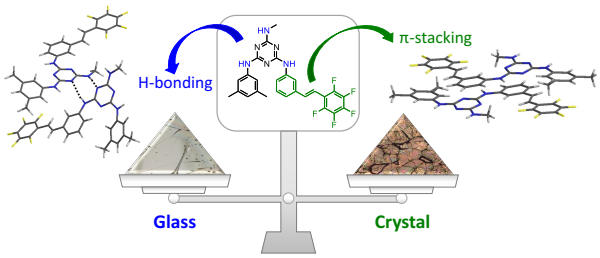


Hydrogen (H) bonds can be used either for crystal engineering or for designing compounds capable of forming very stable glassy phases. Herein, a second type of directional noncovalent interaction, π-π stacking, is introduced to establish the interplay between both types of interactions on crystal and glass formation. For this purpose, two mexyla-minotriazine derivatives incorporating 2,3,4,5,6-pentafluorostilbene groups (with or without a H-bond donor at the 2 position of the triazine) and their nonfluorinated analogues were synthesized to compare their glass-forming and crystallization properties. Although all four compounds showed glass-forming ability, only the fluorinated compounds showed crystallization with kinetics strongly affected by the presence or absence of the H-bond donor group. X-ray diffraction of the pentafluorostilbene-containing derivatives revealed an extended π-π stacking interaction different from that of 2,3,4,5,6-pentafluorostilbene. These results, combined with infrared spectroscopy measurements suggest that π-π stacking promotes crystallization, whereas hydrogen bonding impedes it due to the higher conformational constraints imposed by π-π stacking, thereby decreasing the degrees of liberty and the possibilities for secondary interactions with other molecules.


## 4.2 Introduction

Molecular glasses, or molecular amorphous materials, are small organic molecules that can readily form glassy phases and remain indefinitely amorphous under ambient conditions.[1-7]

---

* Publié en tant qu'article dans *Crystal Growth & Design*: Laventure, A.; Maris, T.; Pellerin, C.; Lebel, O. *Cryst. Growth Des.* **2017**, doi 10.1021/acs.cgd.6b01567. T.M. a résolu les structures cristallines. O.L. a procédé à la synthèse des composés, à leur caractérisation de base et au calcul des surfaces de van der Waals.

Although these properties are shared with inorganic glasses (e.g. $SiO_2$) and polymers, molecular glasses are unique among amorphous materials because their discrete, monodisperse chemical structures provide several advantages such as an easier purification and characterization, more reproducible processing conditions, and more homogeneous behavior between different samples and within the same sample. Although there are disadvantages associated with small molecules, including lower yield stress and mechanical resistance, their principal limitation is their propensity to crystallize over time, as the glassy state is metastable.[1-3]

Just as structural guidelines have been identified to promote and influence the crystallization of organic compounds, certain structural elements are known to combat crystallization, both in terms of their effects on the propensity to form glasses under mild processing conditions (glass-forming ability, GFA) and on the kinetic resistance to crystallization (glass stability, GS). Irregular molecular shapes, nonplanarity, the presence of flexible groups, and conformational ambiguity have emerged as structural features that promote glass formation, as opposed to crystallization.[4-6, 8-9] The design of molecular glasses with improved resistance to crystallization has led to their use in a wide range of practical applications, ranging from photonics,[10-12] optoelectronics[4-6] and nanolithography,[13-14] to formulations for amorphous drugs.[15-16]

Although strong and directional intermolecular interactions have long been associated with crystallization and are a well-known tool for engineering crystals, the presence of hydrogen (H) bonds does not necessarily prevent compounds from forming glasses, as evidenced by mexylaminotriazine derivatives.[17-20] This class of compounds has demonstrated strong GFA, often remaining completely amorphous under cooling from the melt at rates as low as 0.05 °C/min, and high to extreme GS, even at temperatures above their glass transition temperature ($T_g$), depending on the triazine substituents. It was recently shown that the principal factor contributing to glass formation is the presence of conformers of similar energy with high interconversion barriers, thereby resulting in similar populations of different conformers and in suboptimal packing.[21-22] Nevertheless, the presence of hydrogen bonds substantially increases the $T_g$ of molecular glasses compared to analogous compounds that cannot H-bond, therefore limiting molecular mobility and contributing to higher glass stability in the vitreous state. Furthermore, H-bonds remain present in the material even at temperatures well above $T_g$, though

the degree of H-bonding decreases with temperature, thus providing molecular cohesion in the viscous state that contributes to a high glass-forming ability.[22-23]

It is currently not known if other types of noncovalent interactions can provide a similar GFA and GS behavior in molecular glasses. Moreover, when two different types of such interactions are present, the outcome of their interplay is unclear: it may enhance glass formation by increasing the probability of kinetic trapping in multiple conformational and aggregation states that prevent efficient regular packing, or it may promote crystallization if the additional interaction rather favors the adoption of a specific conformation and/or local-scale packing that is closer to the equilibrium state in the energy landscape.

The present study therefore aims to study the effect of the simultaneous presence of two orthogonal strong intermolecular interactions on glass formation in mexylaminotriazine derivatives. Among available noncovalent interactions, electrostatic interactions often interfere with hydrogen bonds, whereas long alkyl chains associated with van der Waals interactions may result in $T_g$ values that are under ambient temperature, thereby limiting their usefulness for most practical applications.[18] On the other hand, donor-acceptor aromatic interactions, commonly referred to as π-π stacking,[24] is a type of noncovalent interaction that is widely studied[25] because of its implication in various domains ranging from supramolecular chemistry to chemical biology (e.g. DNA and protein tertiary structures).[26-27] Its interplay with hydrogen bonding is still being explored, but the combination of both interactions has been successfully exploited to design specific supramolecular structures, such as synthetic molecular strands,[28] in addition to being revealed as an efficient strategy for enhancing the performance of solar cells[29] and preparing luminescence-switching solids.[30] Aromatic moieties capable of π-π stacking can be easily introduced as substituents on the mexylaminotriazine core. As it is a weaker interaction than H-bonding, it is crucial to introduce groups that will enhance π-π stacking strength in order to study the effect of two competing intermolecular interactions on the crystallization/vitrification behavior of molecular compounds. For this purpose, the benzene-perfluorobenzene couple is a prime model because it is a well-known case of strong and directional π-π stacking that has been used as supramolecular synthons in crystal engineering.[31] The case of 2,3,4,5,6-pentafluorostilbene, where molecules stack in columns with alternating fluorinated and nonfluorinated groups, is one example, among others, where this pattern is

used.[32-33] It has been notably exploited to prepare supramolecular nanofibers and hydrogels,[34] and used in liquid crystals, polymeric materials,[35] and nonlinear optical amorphous molecular materials.[36-38]

Herein, two mexylaminotriazine derivatives incorporating a 2,3,4,5,6-pentafluorostilbene moiety, one with a H-bond donor as the headgroup (2 position of the triazine) and the other without, and their two nonfluorinated analogues, were synthesized and studied. The fluorinated derivatives proved capable of glass formation but they crystallized upon heating, whereas their nonfluorinated analogues remained in the glassy state indefinitely. X-ray diffraction of single crystals of the fluorinated derivatives revealed that, unlike 2,3,4,5,6-pentafluorostilbene, these molecules form extended π-π stacking interactions involving the stilbene moieties along with the triazine and mexyl rings. Infrared spectroscopy (IR) measurements showed that hydrogen bonding in the amorphous material impedes crystallization whereas the π-π stacking interactions favor crystallization. The outcome for the different derivatives is explained on the one hand by the competition between the molecular disorder induced by multiple H-bonds that tend to kinetically trap in the glassy state the nonfluorinated compounds in multiple disordered conformations and on the other hand by the higher degree of conformational homogeneity and local packing enabled by the π-π stacking of pentafluorostilbene derivatives that promotes their crystallization.

## 4.3 Results and discussion

### 4.3.1 Synthesis

The most straightforward strategy to synthesize mexylaminotriazine derivatives incorporating stilbene groups involves reacting 2-methylamino-4-mexylamino-6-[(3-formylphenyl)amino]-1,3,5-triazine **1a**, which has already been reported in the literature,[19] and analogue **1b**, by a Wittig reaction with the corresponding benzyltriphenylphosphonium salts in the presence of NaH in DMF (Scheme 4.1).[39]

Target stilbenes **2a**, **2b**, **3a** and **3b** (also referred to subsequently as NHMe/Ph, $NMe_2$/Ph, NHMe/$F_5$Ph, and $NMe_2$/$F_5$Ph, respectively) were thus accessed in one synthetic step and in 48-74 % yields after purification on silica. Whereas fluorinated analogues NHMe/$F_5$Ph **3a** and

$NMe_2/F_5Ph$ **3b** were obtained exclusively as the *E* isomer owing to the electron-withdrawing character of the 2,3,4,5,6-pentafluorophenyl groups, parent compounds NHMe/Ph **2a** and $NMe_2$/Ph **2b** were obtained as *E*/*Z* mixtures. Compound **2a** could only be enriched to a 3:1 *E*/*Z* ratio by flash chromatography because of the highly polar nature of the compound, whereas attempts to enrich the *E* isomer by chemical methods ($I_2$-mediated isomerization for example) resulted in the formation of undesirable side products. On the other hand, compound $NMe_2$/Ph **2b** gave a 1:1 mixture of isomers that could be partially separated by chromatography using 7:3 hexanes/ethyl acetate as eluent, thereby allowing a small sample of pure *E* isomer to be obtained that could be studied.

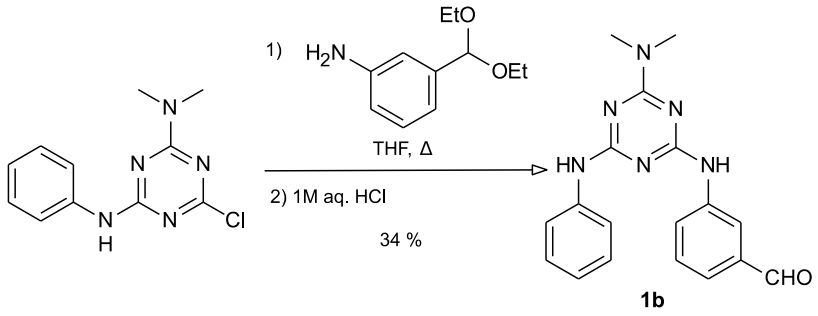


**1a:** R = H, R' = Me
**1b:** R = Me, R' = H

**2a:** R = H, R' = Me, Ar = Ph, X = Cl (E/Z)
**2b:** R = Me, R' = H, Ar = Ph, X = Cl (E/Z)
**3a:** R = H, R' = Me, Ar = $F_5$Ph, X = Br (E)
**3b:** R = Me, R' = H, Ar = $F_5$Ph, X = Br (E)

**Scheme 4.1.** Synthesis of compounds **2a-b** and **3a-b**.

Both precursors **1a** and **1b** were used to better discriminate between the effects of the presence of the pentafluorophenyl group and H-bonding on glass-forming ability. In compounds **1b**, **2b**, and **3b**, the methylamino headgroup and mexylamino group, which are both known as being excellent at promoting glass formation, are replaced by dimethylamino and phenylamino

groups, respectively, which were previously shown to give rise to mediocre GFA and poor GS.[18-19]

### 4.3.2 Thermal properties

Differential scanning calorimetry (DSC) was used to evaluate the thermal properties of stilbene derivatives **2a** and **2b** and their fluorinated analogues **3a** and **3b**. Their glass transition temperature ($T_g$) values and critical cooling rate ($R_c$), i.e., the slowest rate at which a compound can be cooled from the melt without showing detectable crystallization signs by DSC, are listed in Table 4.1 (representative DSC scans are shown in Figure S1). As expected, both stilbene derivatives bearing a H-bond donating methylamino headgroup, NHMe/Ph **2a** and NHMe/$F_5$Ph **3a**, readily form glasses even upon extremely slow cooling ($R_c$ < 0.05 ºC/min). They are kinetically stable at ambient temperature and do not crystallize upon heating at a rate of 10 ºC/min. Surprisingly, both compounds show the same $T_g$ at 78 ºC. The presence of a pentafluorophenyl ring in compound **3a** does not result in a higher $T_g$ despite the stronger aromatic interactions, which leads to the conclusion that the π-π interactions are not dominant over the H-bonding when this compound is in its amorphous state. The $T_g$ of these two compounds is lower than that of the bis(mexylamino) parent compound (94 ºC) but similar to those of other closely similar triazine analogues.[19]

**Table 4.1.** Glass transition temperature ($T_g$) and critical cooling rate ($R_c$) of compounds **2a-b** and **3a-b.**

| Compound | Headgroup/Stilbene | $T_g$ (ºC) | $R_c$ (ºC/min) |
|---|---|---|---|
| **2a** | NHMe/Ph | 78 | < 0.05 |
| **2b** | $NMe_2$/Ph | 50 | < 0.05 |
| **3a** | NHMe/$F_5$Ph | 78 | < 0.05 |
| **3b** | $NMe_2$/$F_5$Ph | 67 | 10 < $R_c$ < 50 |

In contrast to compounds **2a** and **3a**, DSC measurements revealed fundamental differences in the thermal behavior of compounds $NMe_2$/Ph **2b** and $NMe_2$/$F_5$Ph **3b**. Despite its headgroup and ancillary groups known to induce poor GFA, stilbene derivative $NMe_2$/Ph **2b** proved capable of forming glasses even when cooled as slowly ($R_c$ < 0.05 ºC/min) as its H-

bonded analogue **2a** with a lower $T_g$ value of 50 ºC and without signs of crystallization upon heating. Because the sample used contained only the *E* isomer, this lower $T_g$ value compared to its NHMe/Ph **2a** counterpart cannot be attributed to an *E*/*Z* mixture but rather mainly to the headgroup's lack of H-bond donating capability, which we have previously shown to be the most influential group on thermal properties and also to the presence of the phenyl ancillary groups expected to decrease the $T_g$ of 20 ºC compared to mexyl groups.[19] On the other hand, the perfluorinated analogue $NMe_2/F_5Ph$ **3b** only resists crystallization when cooled at rates higher than 10 ºC/min, more than 2 orders of magnitude faster than the other compounds, and undergoes cold crystallization above its $T_g$ of 67 ºC. This $T_g$ value is intermediate between those of the H-bonded compounds (78 ºC) and of its nonfluorinated analogue (50 ºC). It is lower than for **3a** because of the incapability of the headgroup to establish H-bonds and the less bulky ancillary group (phenyl instead of mexyl). It is however 17 °C higher than for **2b** because the presence of the perfluorophenyl moiety favors stronger aromatic interactions in comparison with the nonfluorinated one. Thus, both types of strong noncovalent interactions can contribute to increasing the $T_g$ of molecular glasses when crystallization is avoided. The cold-crystallization behavior observed in the DSC heating scans of compound **3b** suggests that stronger aromatic interactions involving pentafluorophenyl groups in the viscous sample favor crystallization at slow cooling rates. As will be shown below, they impose a more rigid organization between molecules that promotes the regular packing found in crystals.

### 4.3.3 Hydrogen bonding changes upon cooling from the melt

To further investigate the respective influences of H-bonding and aromatic interactions on glass-forming ability, we used variable-temperature infrared (IR) spectroscopy to study the four compounds in situ during their cooling process (2 ºC/min) from the melted state. Indeed, we have shown in a recent study that tracking the changes occurring in the mid-IR NH stretching region and applying chemometrics analysis provide quantitative insight on the evolution of H-bonding (average number of interactions and their enthalpy of formation) during the vitrification phenomenon.[22] Figure 4.1 displays the evolution with temperature of the "free" (3430-3400 $cm^{-1}$) and the "bonded" (3270-3280 $cm^{-1}$) NH stretching bands for the four compounds. Upon cooling compounds NHMe/Ph **2a** and $NHMe/F_5Ph$ **3a** from 200 ºC (red) down to 40 ºC (blue) (Figure 4.1a and 4.1c, respectively), the absorbance of the "free" band decreases as the

absorbance of the "bonded" band increases. This shows that the number of strong H-bonds increases as the compounds (initially in their viscous state) vitrify. This behavior is consistent with other mexylaminotriazine molecular glasses for which a larger average number of strong H-bonds was also found in the vitreous phase.[22] The average number of strongly bonded NH per molecule increases, when cooling from 200 to 40 ºC, from 1.2 to 2.1 for compound NHMe/Ph **2a** and from 1.4 to 2.3 for compound NHMe/$F_5$Ph **3a**. The values at $T_g$ (78 ºC) are very similar for both compounds, 2.0 and 2.2, which is consistent with their identical $T_g$ values. These values are slightly lower than for the bis(mexylamino) parent compound (2.3 at its $T_g$ of 94 °C), and thus in agreement with the trend we have previously demonstrated where $T_g$ increases with the average number of strongly bonded NH groups (headgroup and linkers) per molecule at $T_g$.[22]

In contrast with compounds with the NHMe headgroup, panels b and d in Figure 4.1 show that the absorbance of both "free" and "bonded" bands increases for compounds $NMe_2$/Ph **2b** and $NMe_2$/$F_5$Ph **3b** upon cooling. The increase of the "free" band is slight for $NMe_2$/Ph **2b** but is much more important in the case of fluorinated compound **3b** with the band becoming much narrower than for any other compound. Because its critical cooling rate is much higher than 2 ºC/min, it should be emphasized that this compound undergoes partial crystallization upon cooling, by opposition to vitrification for the other compounds (see DSC curves shown in Figure 4.S1b). Moreover, the spectrum recorded at 200 ºC already shows evidence of crystallinity because its melting point is 202 ºC. Unfortunately, the shape of the "free" bands complicates the chemometrics analyses, making it difficult to evaluate with reliability the average number of bonded NH groups of these compounds. However, it is clear that for compound **3b**, the absorbance of the "free" NH band is larger than the "bonded" one after cooling to 40 ºC. This relative proportion has not been observed previously in either the vitreous or the crystalline state of any analogous compounds. To confirm that the presence of this large fraction of "free" NH groups is characteristic of the crystalline state of compound $NMe_2$/$F_5$Ph **3b**, we measured variable-temperature IR spectra upon heating a completely amorphous sample

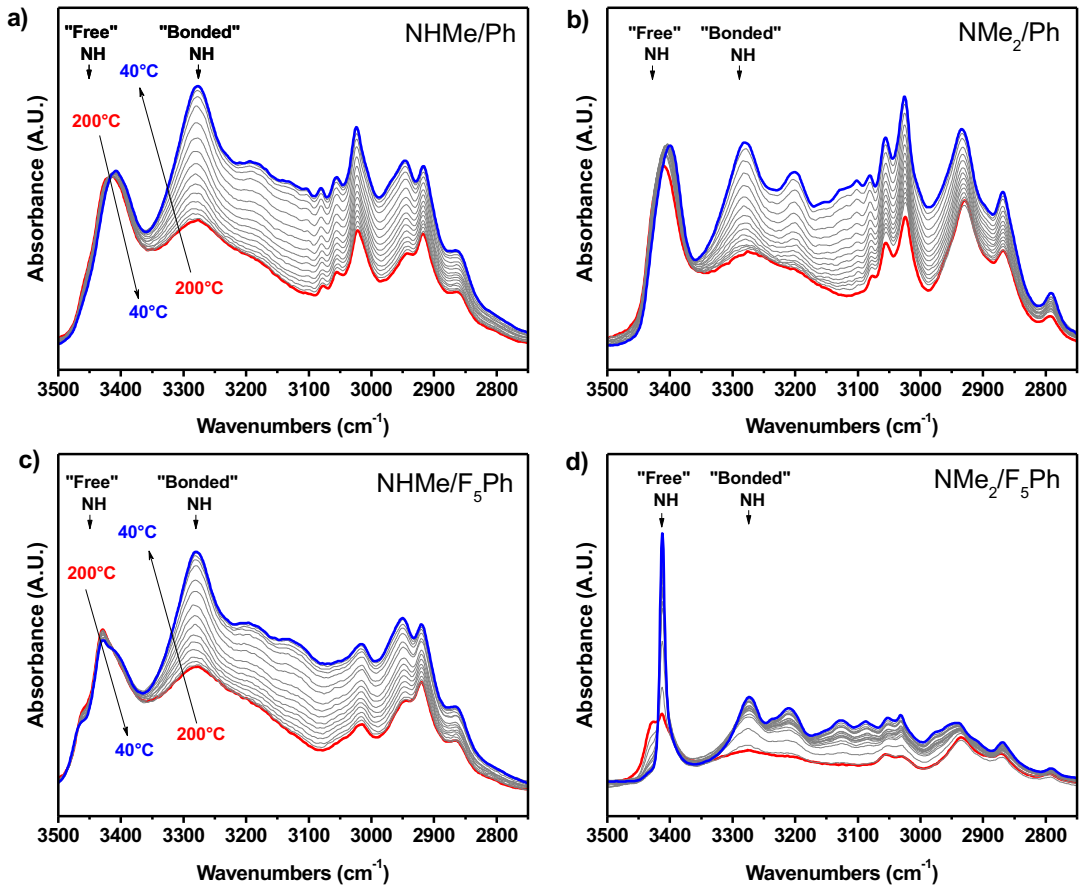


**Figure 4.1.** Variable-temperature IR spectra of compounds a) NHMe/Ph **2a**, b) $NMe_2$/Ph **2b**, c) NHMe/$F_5$Ph **3a** and d) $NMe_2$/$F_5$Ph **3b** recorded with a cooling rate of 2 °C/min.

(obtained by quenching melted **3b** much faster than its $R_c$ using liquid nitrogen) because DSC heating scans show that it undergoes cold crystallization. Figure 4.S2 displays the series of spectra recorded from 40 ºC (blue) in the amorphous state up to 120 ºC (red) in the crystalline state. At 40 ºC, the "free" NH band is broad, and as the temperature increases and the compound undergoes its glass transition, its absorbance starts to increase while that of the "bonded" NH band decreases, the expected behavior for an amorphous compound.

The "free" NH band then becomes narrower during the cold crystallization process. The spectrum of the quenched sample at 40 °C is similar to those of the other compounds recorded in the vitreous state, indicating that the fraction of "bonded" NH groups is higher in the glassy sample, whereas the spectrum in the cold-crystallized state is qualitatively very similar to the

spectrum at 40 °C in Figure 4.1d, which supports the fact that a larger amount of "free" NH is present in the crystalline state than in the glassy state. These observations imply that the crystallization of $NMe_2/F_5Ph$ **3b** requires the disruption of at least some of the H-bonds present in the amorphous state and that it must therefore be accompanied by the formation of another interaction than H-bonding, shown in the next section to be the aromatic interaction involving the pentafluorophenyl group.

### 4.3.4 Crystal structures of compounds NHMe/$F_5$Ph 3a and $NMe_2/F_5Ph$ 3b

Although pentafluorostilbene derivative $NMe_2/F_5Ph$ **3b** could be easily crystallized from $DMSO/CH_2Cl_2$, single crystals of NHMe/$F_5$Ph **3a** suitable for X-ray diffraction could be grown directly by thermal annealing at 150 ºC during 24 h even if it readily forms stable glasses. In contrast, all attempts to crystallize nonfluorinated analogues NHMe/Ph **2a** and $NMe_2$/Ph **2b** proved unsuccessful, instead yielding amorphous precipitates.

Compound $NMe_2/F_5Ph$ **3b** crystallized in the triclinic P-1 space group with two molecules per unit cell. Figure 4.2a shows that both arylamino substituents point toward different directions with all four aromatic rings roughly coplanar and with the stilbene moiety oriented toward the headgroup rather than away from the rest of the molecule, giving the molecule a more compact Z-like shape (additional views are provided in Figure 4.S3). The pentafluorostyryl group of the stilbene moiety is disordered over two positions, though this does not significantly change the general shape of the molecules. This orientational disorder is caused by the pedal motion of the two benzyl moieties around the alkene bond and is often encountered in stilbene molecular structures.[40] Unfortunately, it crystallized with two guest DMSO molecules with 30 % of the crystal volume accessible to guests. An extended H-bonded network was not found in the crystal structure of compound $NMe_2/F_5Ph$ **3b**. The molecules rather hydrogen bond with DMSO molecules (Figure 4.2a), arguably because the bulky dimethylamino headgroup hinders the formation of strong hydrogen bonds. For instance, it has been shown that a smaller headgroup, OMe, allows the formation of H-bonds between the NH linkers and the nitrogen atoms of the triazine in the crystalline structure of an analogous molecular glass.[41] An attempt was made to eliminate these residual DMSO molecules in the single crystals of **3b** used for the crystallographic analysis by drying them under vacuum. Although the resulting crystals

were not suitable for a single crystal structure determination, IR spectra were recorded before and after the DMSO removal procedure (Figure 4.S4a). The spectrum of crystalline **3b** containing DMSO molecules does not show any clear "free" NH band, which is consistent with the crystal structure of Figure 4.2a where both NH groups from the linkers are H-bonded to DMSO. Removal of DMSO under vacuum yields a spectrum with a strong and narrow "free" NH band very similar to that of the crystalline sample obtained by cooling the melt. These results lead to the conclusion that, despite the presence of DMSO molecules, almost identical interactions are found in the single crystal and in the crystals obtained by cooling, ensuring that the comparisons made between the crystals of the two fluorinated compounds NHMe/$F_5$Ph **3a** and $NMe_2$/$F_5$Ph **3b** are reliable.

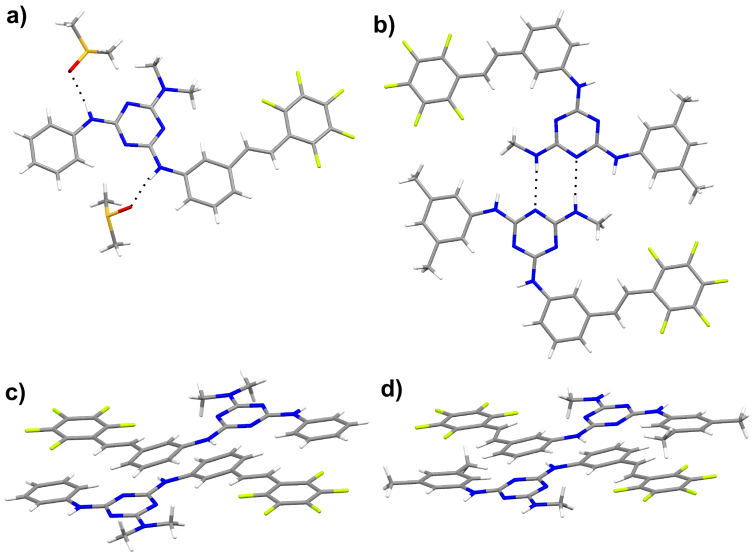


**Figure 4.2.** View of intermolecular interactions in the crystal structures of compounds NHMe/$F_5$Ph **3a** and $NMe_2$/$F_5$Ph **3b**. a) Hydrogen bonding with DMSO molecules of compound $NMe_2$/$F_5$Ph **3b**, b) H-bonded dimer of compound **3a**, c) π-stacked dimer of compound **3b**, d) π-stacked dimer of compound **3a**. Only one of two disordered positions for the stilbene group of compound **3b** is shown. The other position can be found in Figure 4.S3d.

Compound NHMe/$F_5$Ph **3a** also crystallized in the triclinic space group P-1 with two molecules per unit cell. The conformation of individual molecules is similar to that for

$NMe_2/F_5Ph$ **3b** (Figure 4.2b, additional views can be found in Figure 4.S5), with the methyl group of the NHMe headgroup oriented toward the stilbene group, thereby exposing the other face of the triazine ring to facilitate H-bonding with neighboring molecules. Unlike analogue **3b**, no disorder was observed for the stilbene moieties. This absence of orientational disorder in the stilbene molecular structure could be explained by the presence of H-bonds creating a higher energy barrier for the pedal motion, which hinders the conformational interconversion.[40] Compound $NHMe/F_5Ph$ **3a** crystallized in a close-packed structure with no space accessible for guest molecules with a Kitaigorodskii packing index of 71.4 % (calculated using the CALC VOID routine of PLATON),[42] which is significantly higher than the "usual" value for small organic molecules (65 %).[43] In contrast, previously published values for related mexylaminotriazine derivatives ranged from 60 to 65 %.[41] Unlike $NMe_2/F_5Ph$ **3b**, molecules of compound $NHMe/F_5Ph$ **3a** form H-bonded dimers between the NHMe headgroups and the triazine rings as shown in Figure 4.2b, where the stilbene and linker NH groups are not involved at all in the H-bonded pattern.

Although 2,3,4,5,6-pentafluorostilbene (abbreviated as $F_5$-stilbene from hereon) is known to crystallize in extended π-stacked columns with alternating phenyl and pentafluophenyl groups (Figure 4.S6), the crystal structures of compounds $NHMe/F_5Ph$ **3a** and $NMe_2/F_5Ph$ **3b** show a wholly different motif of aromatic interactions between the pentafluorostilbene moieties. Instead, **3a** and **3b** molecules form discrete dimers through extended π-π stacking where the mexyl ring and the stilbene alkene, which are both electron-rich, interact with the electron-deficient pentafluorophenyl and triazine rings, respectively (Figure 4.2c and d). For compound **3a**, closest centroid-centroid distances of 3.73 and 3.60 Å were observed with shift distances of 1.54 and 1.25 Å, respectively. For compound **3b**, slightly longer distances of 3.88 and 3.89 Å with shift distances of 1.67 and 1.81 Å were observed, likely a consequence of the more hindered dimethylamino headgroup.

A comparison of the IR spectra of the single crystal and amorphous states of compounds $NHMe/F_5Ph$ **3a** and $NMe_2/F_5Ph$ **3b** reveals differences in the intermolecular interactions present. Figure 4.3a shows for both compounds in the amorphous state (solid lines) a broad "bonded" NH band that is larger than the "free" band, whereas the "free" band is more intense in the crystalline state (dotted lines). This result validates that the NH of the linker groups of

compounds **3a** and **3b** partially H-bond in the amorphous state, although they do not in the crystalline structure (Figure 4.2) and thus impede the crystallization process. In both cases, the "free" NH bands in the crystalline state are narrower than in the amorphous state, indicating that the molecular environment of the "free" NH is much more specific in the crystalline state than in the amorphous sample presenting an inhomogeneous distribution of molecular environments and interaction strengths. It should be noted that the presence of two "free" NH bands for NHMe/$F_5$Ph **3a** may be due to the splitting of degenerated modes or intermolecularly coupled modes often encountered in vibrational spectra of crystals.[44]

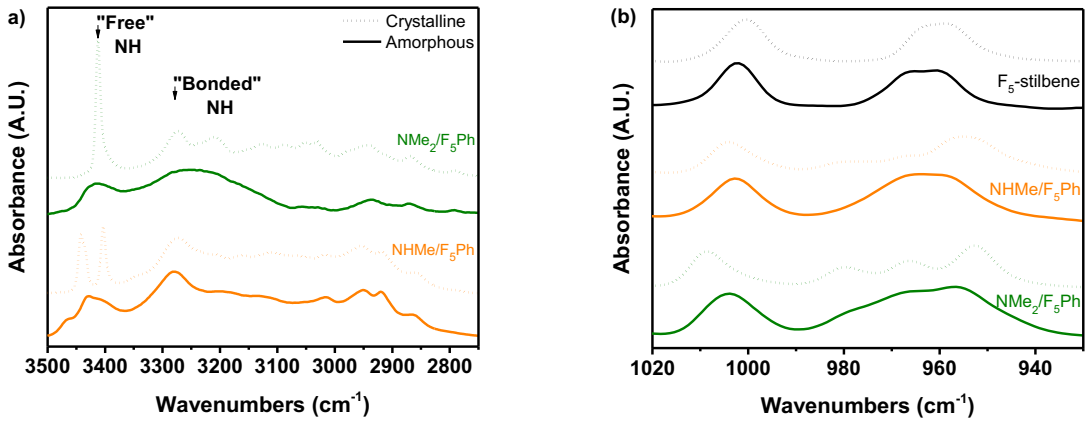


**Figure 4.3.** IR spectra showing the a) NH and b) CF stretching regions of compounds NHMe/$F_5$Ph **3a** (orange) and $NMe_2$/$F_5$Ph **3b** (green) in their crystalline (dotted line) and noncrystalline (solid line) states. The spectra of 2,3,4,5,6-pentafluorostilbene in the crystalline state and in solution (benzene-$d_6$) are also shown (black) for the CF stretching region.

The CF stretching regions, which can provide information on the aromatic interactions present,[45] also show differences between the crystalline and amorphous states and also with the spectra of $F_5$-stilbene itself (Figure 4.3b). The spectra of the crystalline (dotted lines) compounds **3a** and **3b** both show a series of three bands at 980, 966, and 953 $cm^{-1}$ (these bands are also retrieved in single crystals of $NMe_2$/$F_5$Ph **3b** after the DMSO removal procedure, see Figure 4.S4b) consistent with their similar π-stacking pattern in Figure 4.2c and d. This band pattern is not found in the single crystals of $F_5$-stilbene, which only presents a band with a maximum at 960 $cm^{-1}$ and crystallizes with a different π-stacking pattern (Figure 4.S6). Interestingly, the

spectra observed in the noncrystalline state (solid lines) of $F_5$-stilbene and NHMe/$F_5$Ph **3a** are similar, featuring a band at 1002 $cm^{-1}$ and a band with components at 966 and 960 $cm^{-1}$, evidencing that the molecular environment of the fluorinated ring is similar for these compounds. The spectrum of the amorphous $NMe_2$/$F_5$Ph **3b** also shows a band at 1002 $cm^{-1}$ but in contrast with the other compounds, it contains a lower wavenumber band with three components that corresponds to that observed in the crystalline state (it is broader in the amorphous sample because of the lack of long-range order). This result clearly reveals that the molecular environment of the pentafluorophenyl ring is already perturbed by aromatic interactions even if crystallization was prevented by the competing H-bonding interactions of the NH linkers, as observed in Figure 4.3a. The presence of these three band components in the amorphous sample indicates that π-π stacking interactions are more efficient in compound **3b** than in **3a** and explains the difference in their critical cooling rate. This result makes sense because in the headgroup of compound **3b**, the H is substituted by an additional methyl group. With the loss of a H-bond donor coupled with the additional steric bulk of the methyl group, compound **3b** is less efficient to establish H-bonds that kinetically impede the formation of π stacks in the viscous state above $T_g$. The π-π stacking can thus form and create a molecular environment analogous to that found in the crystalline structure, thereby driving crystallization and explaining the fast critical cooling rate needed to obtain compound **3b** in its glassy state. Contrastingly, compound **3a**, whose NHMe headgroup efficiently H-bonds and hinders the formation of π stacks, readily forms glasses upon slow cooling.

### 4.3.5 Competition of the interactions

To rationalize the observed stacking of the pentafluorostilbene moieties and the H-bonded interactions in the crystalline structures, the geometries of an individual molecule of compounds **2a**, **2b**, **3a** and **3b** were optimized using DFT calculations (B3LYP/6-311G(d,p)). One possible explanation emerges by looking at the coefficients of the HOMO (Figure 4.4a) and LUMO (Figure 4.4b) frontier orbitals of compound NHMe/$F_5$Ph **3a** (the HOMO and LUMO orbitals of compound **3b** are identical to those of compound **3a** and are shown in Figure 4.S7a). The HOMO orbital is mostly located on the electron-rich mexyl group, while the LUMO is located on the stilbene moiety, in contrast to nonfluorinated derivatives NHMe/Ph **2a** and $NMe_2$/Ph **2b**, where both the HOMO and LUMO are located on the stilbene moiety (Figure

4.S7b and c). In the π-π stacked dimer shown above in Figure 4.2d, the respective HOMO and LUMO orbitals of each molecule thus show significant overlay. This specific packing geometry thus seems to arise at least partly from the interaction between frontier orbitals in addition to the electrostatic interactions between electron-rich and poor moieties.

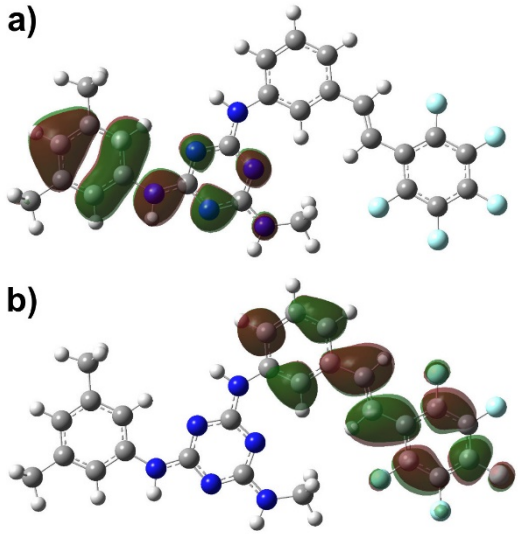


**Figure 4.4.** View of the frontier a) HOMO and b) LUMO orbitals of compound NHMe/$F_5$Ph **3a** calculated by DFT (B3LYP/6-311G(d,p)) with Gaussian 09 software.

The relative propensities of the compounds studied to crystallize and the IR data suggest that the π-π stacking interaction formed by compounds **3a** and **3b**, although different from the one in $F_5$-stilbene, is the driving force for the crystallization and for the crystalline packing of these derivatives. The H-bonding enthalpy measured experimentally[22] for the NHMe/$F_5$Ph **3a** compound in the viscous state using IR spectroscopy is -39 kJ/mol molecule$^{-1}$ (an identical value was determined for compound NHMe/Ph **2a**), which corresponds to -13 kJ/mol for each individual H bond. Despite the fact that the π-π stacking arrangement for the dimers in Figure 4.2c and d is different from the classical aryl-perfluoroaryl interaction, these H-bond interaction values can be comparable to the association energy reported between benzene and hexafluorobenzene in its sandwich complex form, which is -20 kJ/mol.[46]. Both types of noncovalent interactions therefore seem able to compete in the viscous state, with π-π stacking promoting crystallization (by limiting conformational flexibility) and the hydrogen bonding

frustrating crystallization (by promoting the formation of different conformers), which is in agreement with previous studies.[29, 47] Indeed, in this family of compounds,[22] the primary factor responsible for impeding crystallization was revealed to be the presence of multiple conformers with similar energies and high interconversion barriers, and hydrogen bonding was shown to contribute as a kinetic trap by providing additional cohesion between molecules in both the viscous and vitreous states.[22-23]

Both types of interactions are moderately strong and are both likely to form reversibly above $T_g$. Moreover, both interactions are weaker than the energy barrier for the rotation of the NHR groups around the triazine ring.[22, 48-49] It is therefore unlikely that the relative strengths of these two particular types of interactions account for their impact on crystallization kinetics. A more likely explanation would thus involve the shape of the aggregates and their respective ability to pack efficiently. Indeed, for the molecules of compounds **3a** and **3b** to crystallize from the viscous state, two barriers must be overcome: 1) as there is a higher density of hydrogen bonds in the amorphous phase than in the crystal, any superfluous hydrogen bonds must be broken during crystallization (an enthalpic barrier), and 2) the molecules must adopt the required conformation for π-π stacking (an entropic barrier). As the molecules involved in the π-π stacking interact in an extended face-to-face fashion, stricter conformational constraints are imposed on the molecules and a higher portion of the van der Waals surface of each molecule (52.0 $Å^2$ per molecule, 10.6 %, as determined from the crystal structure) is involved in the interaction. These constraints in turn lead to a more rigid structure, less conformational freedom, closer packing, and both less available space for forming secondary weak interactions with other neighboring molecules and less variety of such interactions. In contrast, the molecules hydrogen bond in a lateral fashion; therefore, the portion of the surface shared by the two molecules is minimal (9.4 $Å^2$ per molecule, 1.9 %). Although the hydrogen-bonded dimer in the crystal structure is planar, molecules that hydrogen bond in the amorphous state are more likely to be twisted, and it is also possible that molecules form a single hydrogen bond with a neighbor rather than a pair as shown in Figure 4.2b, therefore decreasing even more the shared van der Waals surface. This leaves more surface available for interacting with other molecules through interactions that are less directional and more ambiguous, providing more conformational degrees of liberty and decreasing the probability that both molecules will exist in the same

conformation and giving rise to aggregates with awkward shapes that cannot pack in an optimal fashion.

Because nonfluorinated derivatives NHMe/Ph **2a** and $NMe_2$/Ph **2b** could not be crystallized, it is impossible to clearly determine how the stilbene moieties would interact in the crystalline state. Stilbene itself crystallizes in a zipperlike pattern with each molecule forming two types of edge-to-face π-π stacking interactions with four neighboring molecules.[40] Unlike the face-to-face π-π stacking involving the pentafluorinated rings, these interactions are much weaker individually. Furthermore, in each of these interactions, an average of 2.4 $Å^2$ of the van der Waals surface per molecule is shared (1.1 % of the total surface), which is significantly lower than for the extended π-π stacking interaction of compounds **3a** and **3b** or that of $F_5$-stilbene itself (20.6 $Å^2$ per molecule, 8.0 %). As a result, the stilbene moieties are expected to interact in a less directional and homogeneous fashion, and not to compete significantly with the stronger hydrogen bonds. This would explain why compounds **2a** and **2b** completely failed to crystallize.

## 4.4 Conclusion

Herein, the impact of the interplay between two types of intermolecular interactions, hydrogen bonding and π-π stacking, on crystallization and glass-forming ability was studied by comparing two pairs of mexylaminotriazine derivatives containing 2,3,4,5,6-pentafluorostilbene moieties, a supramolecular synthon known for forming face-to-face π-π stacking, with their nonfluorinated analogues. Each pair included one derivative containing an easily accessible H-bond donor group and one derivative without it. Although all four compounds studied showed the ability to form glasses, both pentafluorostilbene derivatives showed crystallization with varying crystallization kinetics, whereas the nonfluorinated derivatives could not be successfully crystallized. The crystal structures of both pentafluorostilbene analogues were determined by X-ray crystallography and showed an extended π-π stacking interaction involving all four aromatic rings (different from the stacking observed in 2,3,4,5,6-pentafluorostilbene) and less hydrogen bonding than in the amorphous state. Hydrogen bonding and π-π stacking thus act in competition in the amorphous material with π-π stacking promoting crystallization and hydrogen bonding impeding it. It is concluded

that this behavior is due to the constraints imposed on the molecules by the interactions: π-π stacking interactions involve a significant fraction of the van der Waals surface of the molecules and require the molecules to adopt a specific conformation, whereas hydrogen bonds form laterally and involve a small portion of the surface, thereby offering more conformational freedom to the molecules and allowing a higher variety of secondary interactions. This study also highlights the effect of substituent groups on balancing the relative importance of available interactions. In the present case, substituting a NH for a NMe group simultaneously decreased the formation of H bonds by providing one less H-bond donor and increasing steric bulk, resulting instead in the formation of a competing π-π stacking interaction, even in the amorphous state. These findings provide valuable insights for both the crystal and glass engineering of molecular materials.

## 4.5 Experimental section

### 4.5.1 General

2-Methylamino-4-mexylamino-6-[(3-formylphenyl)amino]-1,3,5-triazine (**1a**),[19] 2-dimethylamino-4-phenylamino-6-dichloro-1,3,5-triazine,[50] and 2,3,4,5,6-pentafluorobenzyltriphenylphosphonium bromide[39] were prepared according to literature procedures. All other reagents and solvents were purchased from commercial sources and used without further purification. All reactions were performed under an ambient atmosphere. SiliaFlash P60 grade silica gel and TLC plates were purchased from SiliCycle. $^{1}$H NMR spectra were recorded on a Bruker Avance 400 MHz or a Varian Mercury 300 MHz spectrometer at 298 or 363 K (as indicated). $^{13}$C NMR spectra were recorded on a Varian Mercury 300 MHz spectrometer at 298 K. $^{19}$F NMR spectra were recorded on a Bruker Avance 400 MHz spectrometer at 298 K. Decomposition analyses of molecular glasses were obtained using a TGA 2950 thermogravimetric analyzer (TA Instruments) at a heating rate of 10 °C/min under a nitrogen atmosphere. Transition temperatures (glass transition temperature $T_g$, crystallization temperature $T_c$ and melting temperature $T_m$) were recorded by DSC with a PerkinElmer DSC 8500 calorimeter calibrated with indium using a heating rate of 10 °C/min. $T_g$ were reported after an initial cycle of heating and ballistic cooling and as the average of the values observed in heating. Critical cooling rates ($R_c$) were determined by cooling the melted compounds at

different rates, from fast (100 °C/min) to slow (0.05 °C/min) until the compounds showed any sign of crystallization (either crystallization exotherm upon cooling or a residual enthalpy of melting upon heating in cases where cold crystallization followed by melting was observed). IR spectra were recorded on a Tensor 27 FT-IR spectrometer (Bruker Optics) equipped with a liquid nitrogen-cooled HgCdTe detector. For ambient temperature measurements, films (unless otherwise noted) were directly cast from $CH_2Cl_2$ solutions on the silicon crystal of a MIRacle (Pike Technologies) attenuated total reflection (ATR) accessory. The spectrum of crystalline $F_5$-stilbene was recorded using a VariGATR (Harrick Scientific) accessory. For variable-temperature spectroscopy, a Golden Gate (Specac) diamond ATR accessory was used. Samples were directly deposited on the ATR crystal, heated to 200 °C followed by a 3 min isotherm and then cooled at a rate of 2 °C/min. Single beam spectra were recorded at each 5 °C by averaging 100 scans with a 4 $cm^{-1}$ resolution. Background spectra were recorded for each temperature. The average number of H-bonded NH groups per molecule and the total enthalpy of H-bond formation were computed from the variable-temperature spectra recorded above $T_g$ using a principal component analysis and SMMA procedure as previously reported by Laventure et al.[22] The geometries of compounds **2a**, **2b**, **3a** and **3b** were optimized and their HOMO and LUMO orbitals were calculated using the Gaussian 09 software with the B3LYP functional and the 6-311G(d,p) basis set.

*Voir* Annexe III pour la procédure relative à la synthèse des composés.

### 4.5.2 Crystal structure determination

Crystals of compound NHMe/$F_5$Ph **3a** were prepared by annealing the melted compound at 150 °C for 24 h and single crystals of **3b** were crystallized from DMSO/$CH_2Cl_2$. For each compound, a suitable crystal was selected and mounted on a cryoloop on a Bruker Venture Metaljet diffractometer. The crystal was kept at 100 K (**3a**) and 110 K (**3b**) during data collection. Using Olex2,[51] the structure was solved with the XT[52] structure solution program using intrinsic phasing and refined with the XL[53] refinement package using least squares minimization. In the case of **3b**, the crystal was two-components twins with refined fractions of 0.9567(7) and 0.0433(7).

### 4.5.3 Crystal data

Compound NHMe/$F_5$Ph **3a** $C_{26}H_{21}F_5N_6$ (M =512.49 g/mol): triclinic, space group P-1 (no. 2), $a$ = 8.0372(7) Å, $b$ = 9.8143(8) Å, $c$ = 14.9100(12) Å, $\alpha$ = 87.061(5)°, $\beta$ = 76.319(5)°, $\gamma$ = 84.542(5)°, V = 1137.04(17) Å$^3$, Z = 2, T = 100 K, μ(GaKα) = 0.662 mm$^{-1}$, $D_{calc}$ = 1.497 g/cm$^3$, 37272 reflections measured (5.31° ≤ 2Θ ≤ 121.608°), 5245 unique ($R_{int}$ = 0.0635, $R_{sigma}$ = 0.0372) which were used in all calculations. The final $R_1$ was 0.0550 (I > 2σ(I)) and $wR_2$ was 0.1614 (all data).

Compound $NMe_2$/$F_5$Ph **3b** $C_{29}H_{31}F_5N_6O_2S_2$ (M =654.72 g/mol): triclinic, space group P-1 (no. 2), $a$ = 7.9866(3) Å, $b$ = 11.0761(4) Å, $c$ = 17.2150(6) Å, $\alpha$ = 90.6702(17)°, $\beta$ = 99.6908(17)°, $\gamma$ = 99.0590(17)°, V = 1481.25(9) Å$^3$, Z = 2, T = 110 K, μ(GaKα) = 1.461 mm$^{-1}$, $D_{calc}$ = 1.468 g/cm$^3$, 6736 reflections measured (4.534° ≤ 2Θ ≤ 121.306°), 6736 unique ($R_{int}$ = 0.0412, $R_{sigma}$ = 0.0352) which were used in all calculations. The final $R_1$ was 0.0563 (I > 2σ(I)) and $wR_2$ was 0.1537 (all data).

## 4.6 Acknowledgments

AL thanks the Natural Sciences and Engineering Research Council (NSERC) of Canada for a Vanier graduate scholarship. The authors are also grateful to Dr. René Gagnon (Université de Sherbrooke) for mass spectrometry analysis, and to WestGrid and Compute Canada for access to the supercomputer Grex for the DFT calculations.

## 4.7 References

1. Angell, C. A., *Science* **1995,** *267*, 1924-1935.
2. Ediger, M. D.; Angell, C. A.; Nagel, S. R., *J. Phys. Chem.* **1996,** *100*, 13200-13212.
3. Berthier, L.; Ediger, M. D., *Phys. Today* **2016,** *69*, 40-46.
4. Shirota, Y., *J. Mater. Chem.* **2000,** *10*, 1-25.
5. Shirota, Y., *J. Mater. Chem.* **2005,** *15*, 75-93.
6. Shirota, Y.; Kageyama, H., *Chem. Rev.* **2007,** *107*, 953-1010.
7. Lygaitis, R.; Getautis, V.; Grazulevicius, J. V., *Chem. Soc. Rev.* **2008,** *37*, 770-788.
8. Ping, W.; Paraska, D.; Baker, R.; Harrowell, P.; Angell, C. A., *J. Phys. Chem. B* **2011,** *115*, 4696-4702.

9. Liu, T.; Cheng, K.; Salami-Ranjbaran, E.; Gao, F.; Glor, E. C.; Li, M.; Walsh, P. J.; Fakhraai, Z., *Soft Matter* **2015,** *11*, 7558-7566.
10. Ishow, E.; Lebon, B.; He, Y.; Wang, X.; Bouteiller, L.; Galmiche, L.; Nakatani, K., *Chem. Mater.* **2006,** *18*, 1261-1267.
11. Nakano, H.; Takahashi, T.; Kadota, T.; Shirota, Y., *Adv. Mater.* **2002,** *14*, 1157-1160.
12. Traskovskis, K.; Mihailovs, I.; Tokmakovs, A.; Jurgis, A.; Kokars, V.; Rutkis, M., *J. Mater. Chem.* **2012,** *22*, 11268-11276.
13. Yoshiiwa, M.; Kageyama, H.; Shirota, Y.; Wakaya, F.; Gamo, K.; Takai, M., *Appl. Phys. Lett.* **1996,** *69*, 2605-2607.
14. Kadota, T.; Kageyama, H.; Wakaya, F.; Garno, K.; Shirota, Y., *Chem. Lett.* **2004,** *33*, 706-707.
15. Yu, L., *Adv. Drug. Deliv. Rev.* **2001,** *48*, 27-42.
16. Gao, P., *Mol. Pharm,* **2008,** *5*, 903-904.
17. Lebel, O.; Maris, T.; Perron, M.-È.; Demers, E.; Wuest, J. D., *J. Am. Chem. Soc.* **2006,** *128*, 10372-10373.
18. Wuest, J. D.; Lebel, O., *Tetrahedron* **2009,** *65*, 7393-7402.
19. Eren, R. N., et al., *Tetrahedron* **2012,** *68*, 10130-10144.
20. Laventure, A.; Soldera, A.; Pellerin, C.; Lebel, O., *New J. Chem.* **2013,** *37*, 3881-3889.
21. Damasceno, P. F.; Engel, M.; Glotzer, S. C., *Science* **2012,** *337*, 453-457.
22. Laventure, A.; De Grandpré, G.; Soldera, A.; Lebel, O.; Pellerin, C., *Phys. Chem. Chem. Phys.* **2016,** *18*, 1681-1692.
23. Plante, A.; Mauran, D.; Carvalho, S. P.; Pagé, J. Y. S. D.; Pellerin, C.; Lebel, O., *J. Phys. Chem. B* **2009,** *113*, 14884-14891.
24. Martinez, C. R.; Iverson, B. L., *Chem. Sci.* **2012,** *3*, 2191-2201.
25. Wheeler, S. E.; Bloom, J. W. G., *J. Phys. Chem. A* **2014,** *118*, 6133-6147.
26. Mignon, P.; Loverix, S.; Steyaert, J.; Geerlings, P., *Nucleic Acids Res.* **2005,** *33*, 1779-1789.
27. Saenger, W., Forces Stabilizing Associations Between Bases: Hydrogen Bonding and Base Stacking. In *Principles of Nucleic Acid Structure*, Springer New York: New York, NY, 1984; pp 116-158.

28. Berl, V.; Huc, I.; Khoury, R. G.; Krische, M. J.; Lehn, J.-M., *Nature* **2000,** *407*, 720-723.
29. Aytun, T.; Barreda, L.; Ruiz-Carretero, A.; Lehrman, J. A.; Stupp, S. I., *Chem. Mater.* **2015,** *27*, 1201-1209.
30. Yuan, M. S., et al., *Chem. Mater.* **2014,** *26*, 2467-2477.
31. Patrick, C. R.; Prosser, G. S., *Nature* **1960,** *187*, 1021-1021.
32. Coates, G. W.; Dunn, A. R.; Henling, L. M.; Ziller, J. W.; Lobkovsky, E. B.; Grubbs, R. H., *J. Am. Chem. Soc.* **1998,** *120*, 3641-3649.
33. Reichenbacher, K.; Suss, H. I.; Hulliger, J., *Chem. Soc. Rev.* **2005,** *34*, 22-30.
34. Hsu, S.-M.; Lin, Y.-C.; Chang, J.-W.; Liu, Y.-H.; Lin, H.-C., *Angew. Chem. Int. Ed.* **2014,** *53*, 1921-1927.
35. Weck, M.; Dunn, A. R.; Matsumoto, K.; Coates, G. W.; Lobkovsky, E. B.; Grubbs, R. H., *Angew. Chem. Int. Ed.* **1999,** *38*, 2741-2745.
36. Gray, T.; Kim, T. D.; Knorr, D. B.; Luo, J. D.; Jen, A. K. Y.; Overney, R. M., *Nano Lett.* **2008,** *8*, 754-759.
37. Kim, T.-D., et al., *J. Am. Chem. Soc.* **2007,** *129*, 488-489.
38. Zhou, X. H., et al., *Adv. Mater.* **2009,** *21*, 1976-1981.
39. Clément, S., et al., *J. Org. Chem.* **2010,** *75*, 1561-1568.
40. Harada, J.; Ogawa, K., *J. Am. Chem. Soc.* **2001,** *123*, 10884-10888.
41. Wang, R.; Pellerin, C.; Lebel, O., *J. Mater. Chem.* **2009,** *19*, 2747-2753.
42. Spek, A., *J. Appl. Crystallogr.* **2003,** *36*, 7-13.
43. Kitaigorodskii, A. I., *Molecular Crystals and Molecules*. Academic Press: New York, 1973.
44. Chalmers, J. M., Mid-Infrared Spectroscopy of the Condensed Phase. In *Handbook of Vibrational Spectroscopy*, Chalmers, J. M.; Griffiths, P. R., Eds. John Wiley & Sons, Ltd: Chichester, 2002; Vol. 1, p 128.
45. Meić, Z.; Güsten, H., *Spectrochim. Acta, Part A* **1980,** *36*, 1021-1027.
46. Tsuzuki, S.; Uchimaru, T.; Mikami, M., *J. Phys. Chem. A* **2006,** *110*, 2027-2033.
47. Seth, S. K.; Sarkar, D.; Kar, T., *CrystEngComm* **2011,** *13*, 4528-4535.

48. Hyengoyan, A. P.; Mamyan, S. S.; Gomktsyan, T. A.; Hambardzumyan, E. N.; Vorskanyan, A. S.; Eliazyan, K. A.; Pivazyan, V. A.; Dovlatyan, V. V., *Chem. Heterocycl. Compd.* **2005,** *41*, 1059-1061.
49. Plante, A.; Palato, S.; Lebel, O.; Soldera, A., *J. Mater. Chem. C* **2013,** *1*, 1037-1042.
50. Eaton, D. C. L., Boris N. DE2051521, 1971.
51. Dolomanov, O. V.; Bourhis, L. J.; Gildea, R. J.; Howard, J. A. K.; Puschmann, H., *J. Appl. Crystallogr.* **2009,** *42*, 339-341.
52. Sheldrick, G., *Acta Crystallogr. Sect. C: Cryst. Struct. Commun.* **2015,** *71*, 3-8.
53. Sheldrick, G., *Acta Crystallogr. Sect. A: Found. Crystallogr.* **2008,** *64*, 112-122.

## 4.8 Supporting information

### Synthesis of stilbene derivatives 2b and 3a-3b

*Voir* Annexe III. Les spectres RMN peuvent être consultés au http://pubs.acs.org/doi/suppl/10.1021/acs.cgd.6b01567/suppl_file/cg6b01567_si_001.pdf

### Characterization

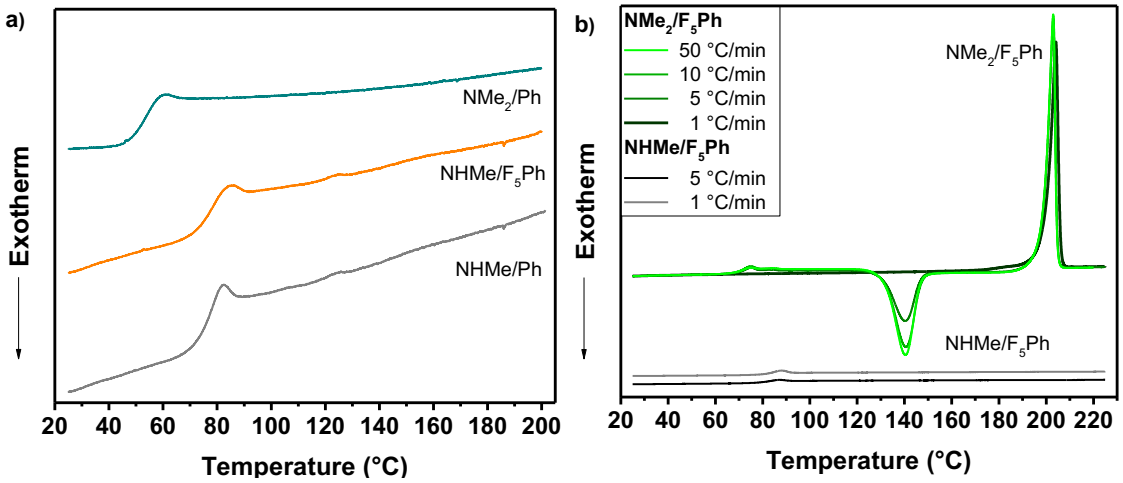


**Figure 4.S1.** Differential scanning calorimetry heating scans at 10 °C/min following a cooling scan at a) 10 °C/min for compounds **2a-b** NHMe/Ph and $NMe_2$/Ph and **3a** NHMe/$F_5$Ph and at b) different cooling rates mentioned in the inset for $NMe_2$/$F_5$Ph **3b** and NHMe/$F_5$Ph **3a**. The critical cooling rate of **3b** is between 50 °C/min and 10 °C/min since these scans present a residual melting enthalpy ($\Delta H_{melting} - \Delta H_{crystallization}$) of 0 J/g (completely amorphous) and 4 J/g (partially crystallized), respectively. These residual melting enthalpies correspond to approximate degrees of crystallinity of 0% and 4%, respectively. The degree of crystallinity increases with further decrease of the cooling rate: 30% for 5 °C/min and essentially 100% for 1 °C/min (as indicated by the absence of a $T_g$ or cold crystallization peak). Heating scans following cooling ramps at 5 and 1 °C/min are also shown for compound NHMe/$F_5$Ph **3a** to show that it remains completely amorphous, while **3b** shows evidence of crystallinity, at the cooling rate used in the variable-temperature IR experiments (2 °C/min).

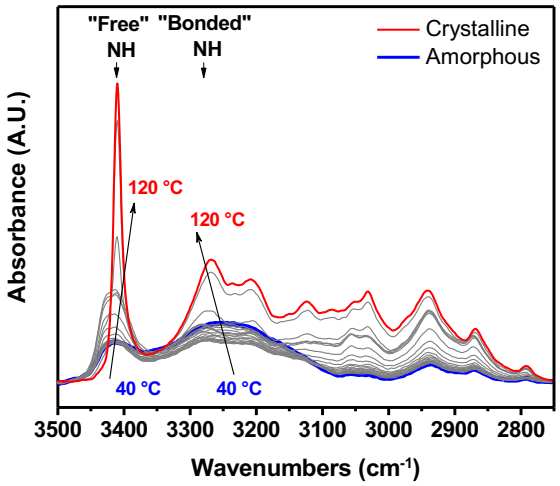


**Figure 4.S2.** Variable-temperature IR spectra of compound $NMe_2/F_5Ph$ **3b** recorded from an amorphous sample (quenched from the melt using liquid nitrogen) with a heating rate of 2 °C/min to highlight the cold crystallization observed for this compound. The cold crystallization occurs at a lower temperature than the one observed in the DSC heating scan (10 °C/min) since the heating rate used in the IR experiment is lower.

## Additional Crystal Structure Data for Compound $NMe_2/F_5Ph$ 3b

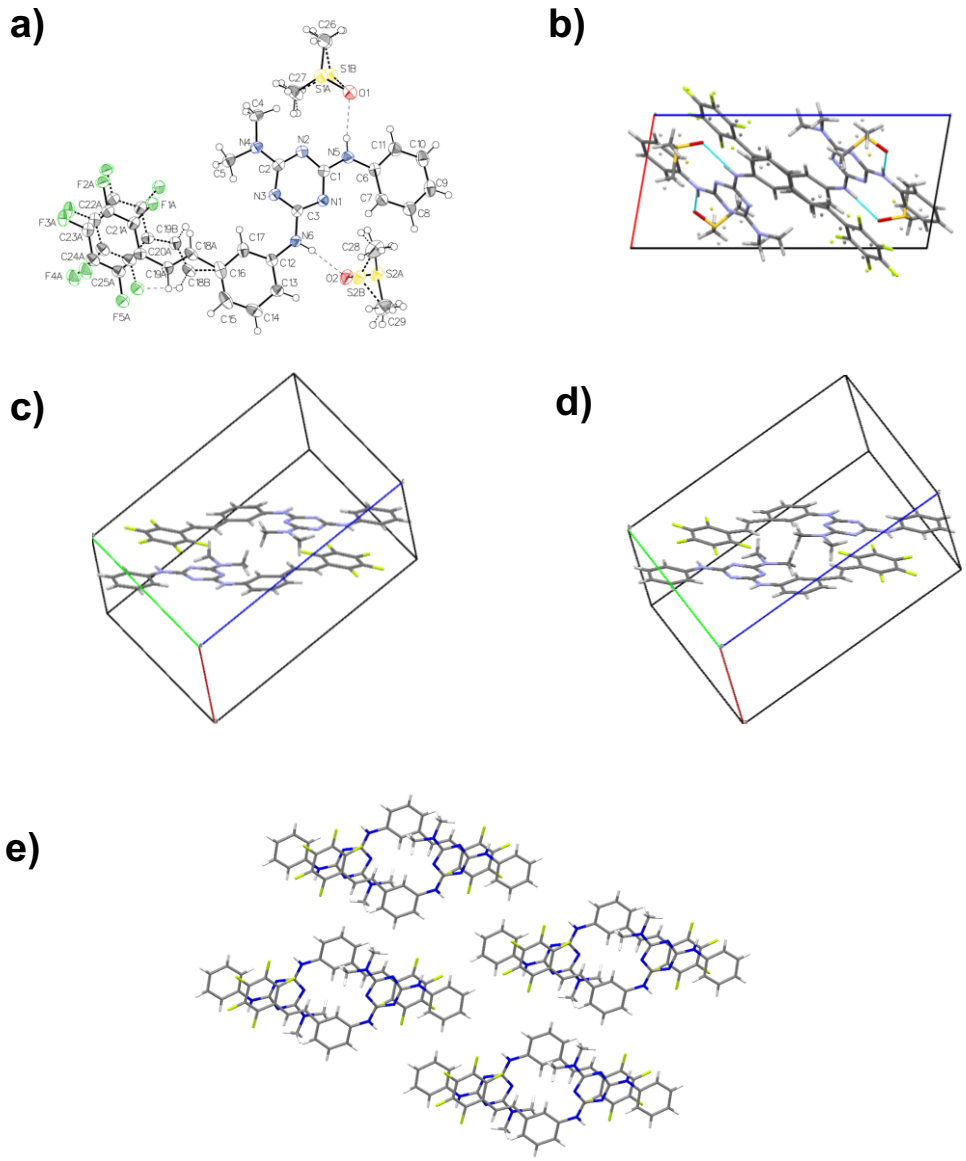


**Figure 4.S3.** Additional Crystal Structure Data for Compound $NMe_2/F_5Ph$ **3b**. a) ORTEP view of the compound **3b** with the numbering scheme adopted. Ellipsoids are drawn at 50% probability level. Hydrogen atoms are represented by spheres of arbitrary size. b) Unit cell packing along the *b* axis highlighting the H-bonds between the DMSO molecules and the NH linkers of the compounds. Resulting unit cell packing without the DMSO molecules of c) one of the disordered pentafluorostilbene orientation and d) the other disordered pentafluorostilbene orientation. e) Extended packing for one of the pentafluorostilbene orientation (presented in Figure 4.S3c).

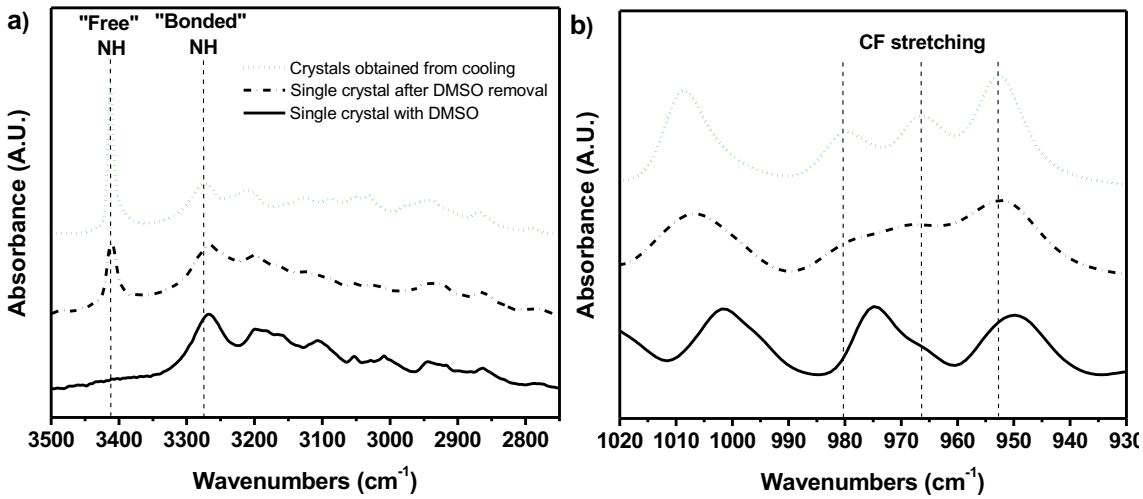


**Figure 4.S4.** IR spectra of the a) NH stretching region and the b) CF stretching region of compound $NMe_2/F_5Ph$ **3b**. Removal of the DMSO molecules (1 week under vacuum) from the single crystals tends to show the same bands as the crystals obtained from cooling a melted sample.

## Additional Crystal Structure Data for Compound $NHMe/F_5Ph$ 3a

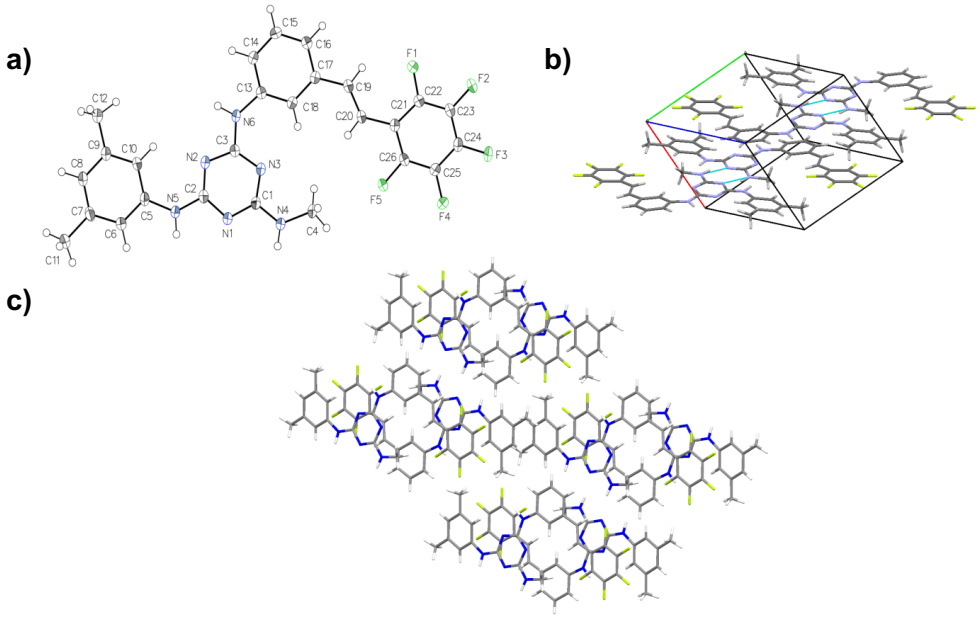


**Figure 4.S5.** Additional Crystal Structure Data for Compound $NHMe/F_5Ph$ **3a**. a) ORTEP view of the compound $NHMe/F_5Ph$ **3a** with the numbering adopted. Ellipsoids are drawn at 50% probability level. Hydrogen atoms are represented by spheres of arbitrary size. b) Corresponding packing diagram. c) Extended packing.

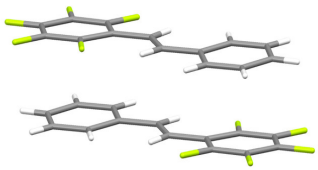

**Figure 4.S6.** View of the π-stacked dimer in the crystal structure of 2,3,4,5,6-pentafluorostilbene ($F_5$-stilbene) compound.

**a)**

**b)**

**c)**

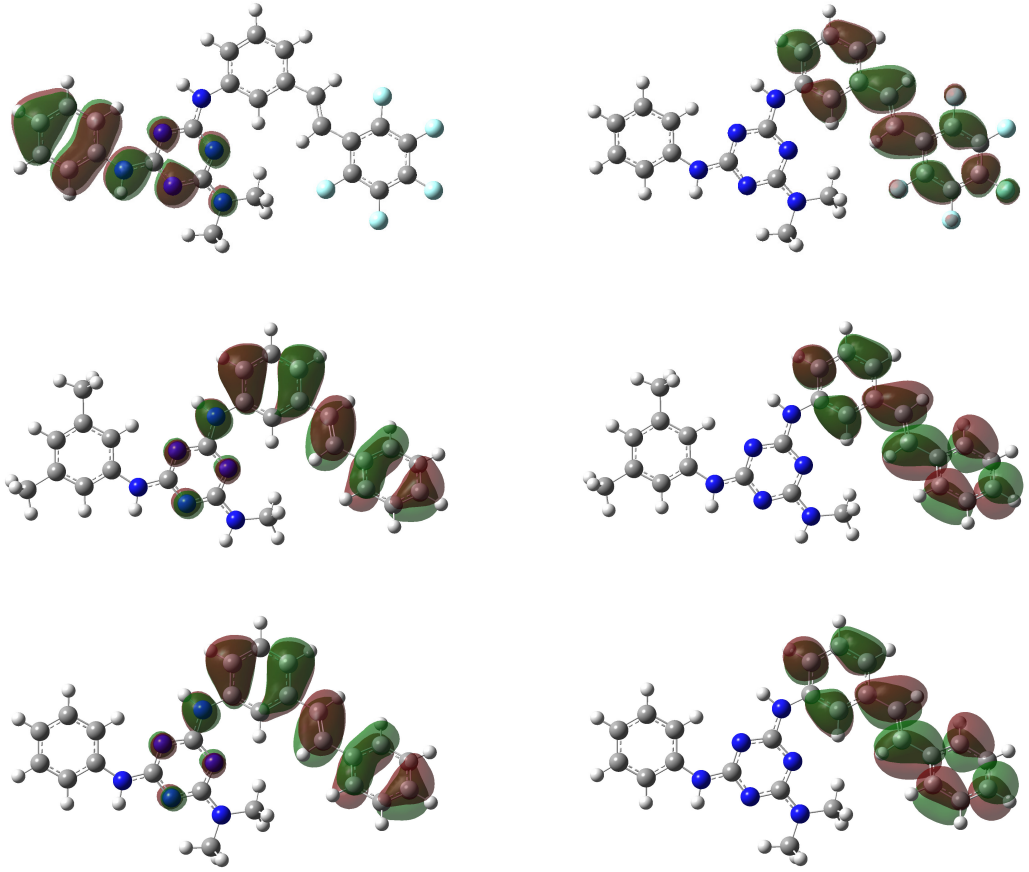

**Figure 4.S7.** View of the frontier orbitals calculated by DFT (B3LYP/6-311G(d,p)) with the Gaussian 09 software. HOMO and LUMO orbitals for compound a) $NMe_2/F_5Ph$ **3b**, b) NHMe/Ph **2a**, and c) $NMe_2$/Ph **2b**.

*Reference*


1. Coates, G. W.; Dunn, A. R.; Henling, L. M.; Ziller, J. W.; Lobkovsky, E. B.; Grubbs, R. H., *J. Am. Chem. Soc.* **1998**, *120*, 3641-3649.

# Chapitre 5: Influence of hydrogen bonding on the kinetic stability of vapor-deposited glasses of triazine derivatives*

## 5.1 Abstract


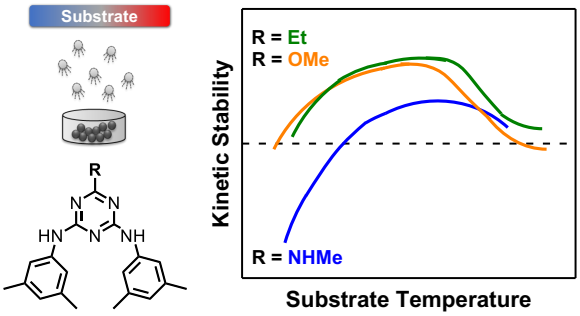


It has recently been established that physical vapor deposition (PVD) can produce organic glasses with enhanced kinetic stability, high density, and anisotropic packing, with the substrate temperature during deposition ($T_{substrate}$) as the key control parameter. The influence of hydrogen bonding on the formation of PVD glasses has not been fully explored. Herein, we use a high-throughput preparation method to vapor-deposit three triazine derivatives over a wide range of $T_{substrate}$, from 0.69 to 1.08$T_g$, where $T_g$ is the glass transition temperature. These model systems are structural analogues containing a functional group with different H-bonding capabilities at the 2-position of a triazine ring: 1) NHMe (1) 2-methylamino-4,6-bis(3,5-dimethyl-phenylamino)-1,3,5-triazine (NHMe) (H-bond donor), 2) OMe (2) 2-methoxy-4,6-bis(3,5-dimethylphenylamino)-1,3,5-triazine (OMe) (H-bond acceptor), and 3) Et (3) 2-ethyl-4,6-bis(3,5-dimethyl-phenylamino)-1,3,5-triazine (Et) (none). Using spectroscopic ellipsometry, we find that the Et and OMe compounds form PVD glasses with relatively high kinetic stability, with the transformation time (scaled by the α-relaxation time) on the order of $10^3$, comparable to other highly stable glasses formed by PVD. In contrast, PVD glasses of NHMe are only slightly more stable than the corresponding liquid-cooled glass. Using IR spectroscopy, we find that both the supercooled liquid and the PVD glasses of the NHMe derivative show a higher average number of bonded NH per molecule than that in the other two compounds. These results suggest that H-


---

* Publié en tant qu'article dans *Journal of Physical Chemistry B*: Laventure, A.; Gujral, A.; Lebel, O.; Pellerin, C.; Ediger, M.D. *J. Phys. Chem. B* **2017**, *121*, 2350-2358. A.G. a effectué les mesures de diffraction des rayons X. O.L. a procédé à la synthèse des composés.

bonds hinder the formation of stable glasses, perhaps by limiting the surface mobility. Interestingly, despite this difference in kinetic stability, all three compounds show properties typically observed in highly stable glasses prepared by PVD, including a higher density and anisotropic molecular packing (as characterized by IR and wide-angle X-ray scattering).

## 5.2 Introduction

Physical vapor deposition (PVD) of organic molecules somewhat below the glass transition temperature ($T_g$) can produce glasses with enhanced properties that are relevant for promising organic electronic and optoelectronic technologies.[1-4] These as-deposited glasses exhibit enhanced kinetic stability, low enthalpy, high density, and anisotropic packing.[1-2, 4-16] These properties can be controlled by the temperature of the substrate during deposition ($T_{substrate}$). One indication of the high kinetic stability of these glasses is that when annealed above $T_g$, a much longer time is required for them to transform into the supercooled liquid in comparison to that required for a liquid-cooled glass of the same material.[17-20] For several systems, it has been shown that high kinetic stability correlates reasonably with glass density.[5, 18, 21] The mechanism underlying the formation of stable PVD glasses is thought to be related to enhanced surface mobility.[1, 22-23] Indeed, experimental and computational results agree qualitatively and have led to the conclusion that vapor deposition at $T_{substrate}$ somewhat below $T_g$ enables the molecules to have enough mobility to explore the energy landscape and find a packing configuration that is low in energy, before they are buried by further deposition.[24-25] The lower-energy packing arrangements found in this process also have higher activation energy barriers for rearrangements, which lead to the higher kinetic stability of the as-deposited glasses.

Not all organic molecules form stable glasses when vapor-deposited,[26-30] and in particular, reports of stable glasses of H-bonded compounds are uncommon. Vapor deposition of glycerol leads to the formation of a liquid with properties distinct from those of the ordinary supercooled liquid, but it does not appear that glasses with high kinetic stability are formed.[28-29] Similarly, although PVD of water has been reported many times, the formation of stable water glasses has not been reported.[27] Tylinski *et al.* recently vapor-deposited six hydroxyl (OH)-containing molecules and characterized the kinetic stability of the resulting glasses. Five out of six compounds yielded glasses with low to medium kinetic stability, and only benzyl alcohol

presented a stability comparable to that of previously vapor-deposited glasses of non-H-bonded compounds.[30] These results indicate that the hydroxyl functional group impedes, in many cases, the formation of high kinetic stability glasses. Recent work by Yu and co-workers provides a qualitative explanation for the effect of H-bonding on stable glass formation.[31] Measurements on a series of polyols capable of extensive H-bonding showed much smaller surface diffusion coefficients at $T_g$ in comparison to molecules without H-bonds. This and other recent results by Yu and co-workers[23, 31-33] are consistent with the view that H-bonding in molecules containing OH groups limits surface mobility near $T_g$. Without surface mobility, molecules cannot find low-energy packing arrangements during deposition; thus stable glasses cannot be formed.

To further explore the influence of H-bonding on the stability of PVD glasses, we study here a series of three triazine derivatives that are substituted with amino (NH) groups. The NH group allows an interesting comparison with OH-containing molecules. H-bonds established by NH groups are generally weaker than those established by OH groups,[34] and as a result, NH-containing molecules would be expected to be more likely to form glasses with high kinetic stability. Vapor deposition of molecules containing NH groups has been reported previously, but these studies do not allow the impact of the NH group on kinetic stability to be assessed.[35-36] The model system used in this work (see Scheme 5.1) offers the possibility of a systematic study as the three molecules are structural analogues: they possess the same core and only the headgroup (2-position of the triazine ring) is modified. The headgroups studied herein present different H-bonding capabilities: $NHCH_3$ (NHMe; H-bond donor), $OCH_3$ (OMe; H-bond acceptor), and $CH_2CH_3$ (Et; no H-bond capability). The headgroup was chosen for systematic modification because it is the most accessible for intermolecular interactions and is the most influential group with respect to the thermal properties of these compounds.[37-38] In addition, as these compounds are all glasses at ambient temperature and possess an excellent resistance to crystallization,[39] they are an ideal system for *ex situ* characterization of glass properties. Thus, high-throughput spectroscopic ellipsometry, IR spectroscopy and wide-angle X-ray scattering (WAXS) can be used to assess the kinetic stability, density, isothermal transformation time, and anisotropy of the as-deposited glasses. Moreover, a method combining chemometrics and IR enabling the quantification of H-bonds has been developed for these triazine derivatives,[38]

which allows investigation of the correlation between glass stability and the H-bonding capability.

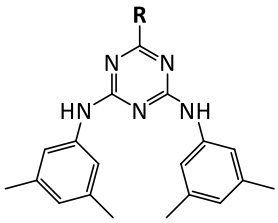


| R | Name | $T_g$ (K) |
|---|---|---|
| $CH_2CH_3$ | Et | 314 |
| $OCH_3$ | OMe | 330 |
| $NHCH_3$ | NHMe | 360 |

**Scheme 5.1.** Chemical structure, abbreviated name and glass transition temperature ($T_g$) of the three triazine derivatives studied.

We find that PVD glasses of the Et- and OMe-substituted triazine derivatives show high kinetic stability. The time required for the most stable glasses to transform into the supercooled liquid during isothermal annealing is of the order of $10^3$ when scaled by the α-relaxation time. In contrast, PVD glasses of the NHMe-substituted compound are only slightly more stable than its liquid-cooled glass. Using IR, we find that both the supercooled liquid and the PVD glasses of the NHMe derivative show a higher average number of bonded NH per molecule than that in the two other compounds. These results indicate that extensive H-bonding involving NH groups hinders the formation of stable glasses; this extends the conclusion of previous work[30] on OH-containing molecules. Despite the observed differences in kinetic stability, all three triazine compounds show some properties that are usually observed only in highly stable glasses. Spectroscopic ellipsometry indicates their higher density, whereas IR and WAXS experiments revealed anisotropy of the molecular orientation and structure, showing that the triazine ring has a tendency to orient parallel to the substrate at low $T_{substrate}$.

## 5.3 Experimental methods

### 5.3.1 Sample preparation

2-Methylamino-4,6-bis(3,5-dimethyl-phenylamino)-1,3,5-triazine (NHMe),[40] 2-methoxy-4,6-bis(3,5-dimethyl-phenylamino)-1,3,5-triazine (OMe)[40] and 2-ethyl-4,6-bis(3,5-

dimethyl-phenylamino)-1,3,5-triazine (Et)[39] were synthesized according to literature procedures. Glassy films were prepared by PVD using a custom-built vacuum chamber at pressures of $10^{-7}$ torr. Double-sided polished silicon wafers (Virginia Semiconductors) were used as substrates. The substrate was held in the chamber by a temperature-gradient stage that has been previously described.[5] This enables the simultaneous deposition of a variety of glasses at different $T_{substrate}$ values. A quartz crystal microbalance (Sycon) was used to ensure a constant deposition rate. The true rate of deposition (0.25 ± 0.03 nm/s) was determined by dividing the final film thickness (determined by ellipsometry) by the time required to complete the deposition. At least two gradient samples were prepared for each of the three compounds, and data from all samples are shown in Figures 5.2, 5.3, 5.6, and 5.7.

### 5.3.2 Spectroscopic ellipsometry

A J. A. Woollam M-2000U spectroscopic ellipsometer with a focused spot size of 0.6 mm was used. A custom-built stage was used as previously described for temperature control.[5] Data within the 500 – 1000 nm wavelength range were modeled using a uniaxial anisotropic Cauchy model. Measurements at a single incidence angle were used during temperature-ramping experiments. Otherwise, three incident angles were used in all measurements to provide more precise characterization.

### 5.3.3 IR

Transmission IR spectra were obtained with a Bruker Tensor 27 spectrometer equipped with a liquid-nitrogen-cooled mercury cadmium telluride detector and a custom-built sample holder previously described.[41] Spectra were acquired at normal incidence by averaging 100 scans of the samples at a resolution of 4 $cm^{-1}$ and using a blank double-polished wafer for the background scans. Measurements of the thermally transformed samples were used as the isotropic reference spectra. Equation 1 was used for the calculations of the triazine ring orientation order parameter, $S_z$:

$$S_z = 1 - \frac{A}{A_0} \qquad \text{(Equation 1)}$$

Here $A$ and $A_0$ are the absorbances of the 810 $cm^{-1}$ band in the spectra of the as-deposited and liquid-cooled glasses, respectively. $A$ was observed to be independent of the incident

polarization, consistent with uniaxial anisotropy. Calculations of the average number of bonded NH per molecule were done following a previously described chemometrics procedure.[38]

### 5.3.4 WAXS

Two-dimensional asymmetric X-ray scattering patterns were obtained on a Bruker D8 Discover diffractometer equipped with a 50 W Cu Kα source and a Vantec500 detector. The temperature-gradient samples (as described above) were measured at various positions along the sample, corresponding to unique substrate temperatures. The spot size is 2 mm, leading to a measurement with substrate temperature resolution of about 5 K. The incident angle, $\theta = 4^{\circ}$, was chosen to meet the Bragg condition of the anisotropic diffraction peak. For the comparison shown below, we integrated the scattering intensities of the anisotropic peak and amorphous haloes for the various glasses. The anisotropic peak was integrated along $2\theta$ from 4.5 to 5.5˚, whereas the amorphous halo was integrated along $2\theta$ from 12.8 to 32.0˚. For both features, we integrated azimuthally from -35 to 35˚ (where 0˚ is along the out-of-plane scattering vector).

## 5.4 Results

### 5.4.1 High-throughput preparation of PVD glasses and ellipsometric characterization

Scheme 5.1 shows the chemical structure of the three triazine derivatives utilized in this study. The core (triazine), the linkers (NH) and the ancillary groups (3,5-dimethyl-phenyl) are the same for the three compounds, which allows us to isolate the influence of the headgroup (R). Three different headgroups were chosen for their increasing capability of participating in H-bonding interactions. A color-code is also assigned to each headgroup for clarity: $NHCH_3$ (abbreviated as NHMe, in blue; H-bond donor), $OCH_3$ (OMe, in orange; H-bond acceptor) and $CH_2CH_3$ (Et, in green; no H-bond capability). The $T_g$ values listed in the table of Scheme 5.1 were measured by ellipsometry while cooling the supercooled liquid at 1 K/min (after the transformation of the corresponding as-deposited glass). $T_g$ ranges from 314 K (Et) to 330 K (OMe) and 360 K (NHMe). (One of the NHMe derivative temperature-gradient samples indicated a $T_g$ of 358 K and results from this sample were scaled accordingly.) The fact that the

$T_g$ values are all above ambient temperature enables high-throughput *ex situ* characterization of the different glasses obtained by the temperature-gradient deposition with spectroscopic ellipsometry, IR and WAXS.

Using the temperature-gradient stage described in the Experimental Methods section, glasses of the three triazine derivatives were vapor-deposited at $T_{substrate}$ ranging from 0.69 to 1.08 $T_g$. Figure 5.1 shows representative spectroscopic ellipsometry experiments for glasses prepared from each compound. The thickness changes observed by ellipsometry are plotted as a function of the ramping temperature ($T_{ramping}$), scaled by the $T_g$ of each liquid-cooled glass. In each case, upon heating at 1 K/min, the thickness of the as-deposited glass increases abruptly as it transforms into its supercooled liquid. The temperature at which the transformation begins ($T_{onset}$) is indicated for one of the data sets. After each sample reached the supercooled liquid state, it was cooled at 1 K/min, forming the liquid-cooled glass at $T_g$. All three as-deposited samples are thinner than their corresponding liquid-cooled glasses, which indicates higher density.[42] The Et and OMe samples show almost the same fractional thickness changes as a function of $T_{ramping}/T_g$. NHMe follows a similar trend, but its thickness change is smaller, indicating that its relative density is lower than that of the Et and OMe glasses. The three as-deposited glasses displayed in Figure 5.1 have $T_{onset}$ values higher than the $T_g$ of the corresponding liquid-cooled glass. The Et and OMe compounds having the higher values of $T_{onset}/T_g$ and thus have higher kinetic stabilities relative to their liquid-cooled glasses. The results for the Et and OMe compounds are qualitatively similar to those for other highly stable glasses.[1, 6]

The densities of the vapor-deposited glasses relative to those of the liquid-cooled glasses ($\Delta\rho$) are shown in Figure 5.2 as a function of $T_{substrate}/T_g$. The three compounds follow similar trends, where the maximum density is found at $T_{substrate}/T_g$ values between 0.75 and 0.85, and is about 1.2 % higher than that of the corresponding liquid-cooled glass. At $T_{substrate}/T_g \geq 1$, the density is near that of the liquid-cooled glass; a value of $\Delta\rho = 0$ is consistent with the view that deposition yields the equilibrium supercooled liquid.

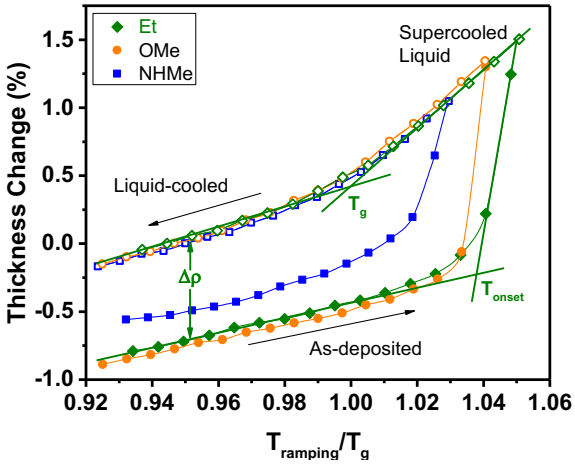


**Figure 5.1.** Thickness changes for ~350 nm films of PVD glasses of the three triazine derivatives measured by ellipsometry, as a function of the ramping temperature ($T_{ramping}$) scaled to $T_g$. These samples were vapor-deposited at $T_{substrate} = 0.90T_g$ (Et and NHMe) and $0.91T_g$ (OMe). During the first heating (1 K/min), the as-deposited glass starts to transform into the supercooled liquid at $T_{onset}$. The supercooled liquid was then cooled at 1 K/min with the liquid-cooled glass forming at $T_g$.

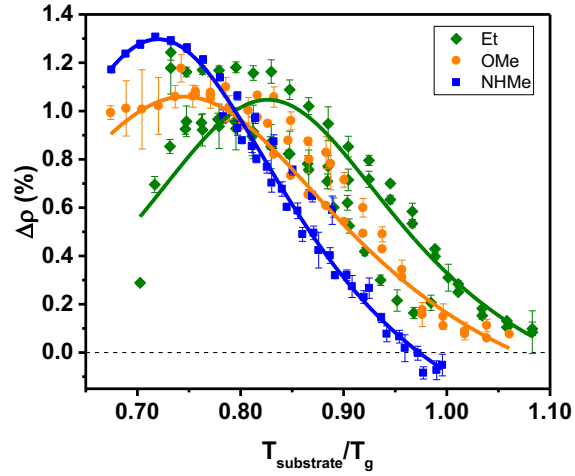


**Figure 5.2.** Relative densities (Δρ) of vapor-deposited glasses of the three triazine derivatives as a function of the substrate temperature during deposition, scaled to $T_g$ for each compound. The density of the as-deposited glass is calculated relative to the density of a glass prepared by cooling the liquid at 1 K/min. The lines are guides to the eye. The error bars correspond to the standard deviation calculated for 5 independent spots measured on the same sample.

### 5.4.2 Kinetic stability

Figure 5.3 presents the onset temperature for transformation into the supercooled liquid ($T_{onset}$), a measure of kinetic stability,[1] for all of the PVD glasses of the three triazine derivatives. These $T_{onset}$ values are scaled by the $T_g$ of the compound and plotted as a function of $T_{substrate}$ scaled by $T_g$. Values of $T_{onset}/T_g$ greater than 1 mean that the as-deposited glass has a greater kinetic stability than that of the corresponding liquid-cooled glass and values lower than 1 mean that the as-deposited glass is less stable than the corresponding liquid-cooled glass. The Et and OMe derivatives show maximum $T_{onset}/T_g$ values that are very similar (1.03, at $T_{substrate}/T_g \sim 0.85$) whereas the NHMe derivative shows a smaller maximum (1.01, at $T_{substrate}/T_g \sim 0.90$). Whereas the Et and OMe samples show enhanced kinetic stability over almost the entire temperature range probed, the NHMe derivative produces unstable glasses at a lower substrate temperature. The lower maximal $T_{onset}/T_g$ value and a significant region of unstable glasses both indicate that PVD is less able to increase the kinetic stability of the glasses of the NHMe derivative, in comparison to that of the Et and OMe derivatives.

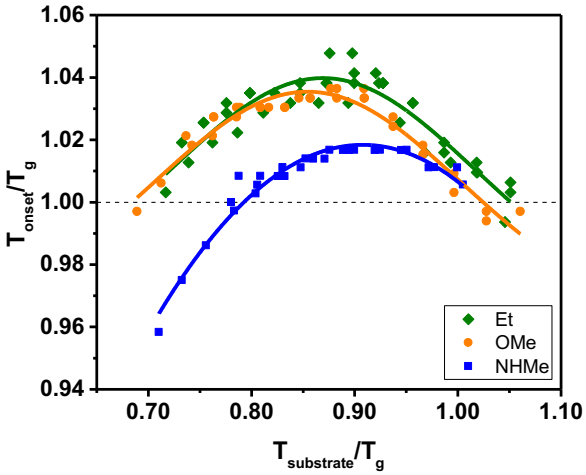


**Figure 5.3.** Comparison of the onset temperature for transformation into the supercooled liquid ($T_{onset}$) for three triazine derivatives during heating of the as-deposited glasses, as a function of the substrate temperature during deposition. Higher $T_{onset}$ values indicate greater kinetic stability. The lines are guides to the eye.

Isothermal annealing experiments were conducted on the most stable as-deposited glasses of each of the three compounds to more accurately characterize their kinetic stability.

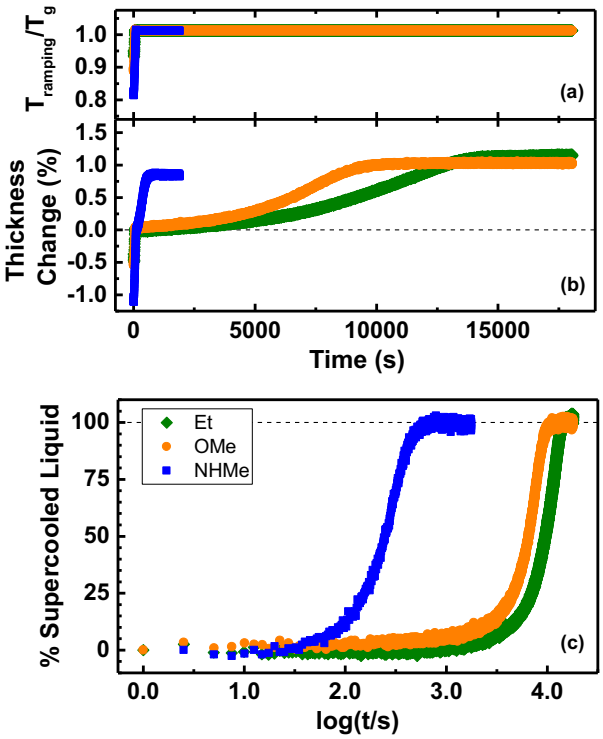


**Figure 5.4.** Isothermal transformation of the as-deposited glasses of the three triazine derivatives, as measured by ellipsometry. (a) Temperature profile used for the isothermal transformation experiment. (b) Thickness changes as a function of time. The glasses chosen for this experiment were deposited at $T_{substrate}/T_g$ values near their maximal kinetic stability. For each system, the isothermal transformation experiment was performed at $T_g + 4$ K ($\approx 1.01T_g$). (c) Fraction of the sample that has transformed into the supercooled liquid as a function of logarithmic time, using the data from panel b. Glasses of the NHMe compound show substantially lower kinetic stability than that of glasses of the other two systems.

The samples were deposited at similar relative deposition temperatures corresponding to $T_{substrate} = 0.92T_g$ for Et, at 0.90 $T_g$ for OMe and at $0.91T_g$ for NHMe and were prepared with similar thicknesses (ca. 350 nm). The temperature profile used for these isothermal annealing experiments is shown in Figure 5.4a. The annealing temperature was $T_g + 4$ K ($\approx 1.01$ $T_g$) for all three compounds. The thickness changes during the annealing process were followed by ellipsometry and are displayed in Figure 5.4b; for this plot, the reference state is the thickness of the sample when the annealing temperature was first reached. All three samples become

thicker with annealing time as they isothermally transform into the supercooled liquid. However, the time required to transform into the supercooled liquid, that is, to reach a plateau in Figure 5.4b, follows this descending order: Et, OMe and NHMe. These data were used to plot the transformation as a function of logarithmic time in Figure 5.4c; time zero corresponds to the time when the annealing temperature is first reached. The vertical axis, the fraction of the sample with the molar volume of the supercooled liquid, was calculated by normalizing to the total increase in thickness.[30] As a longer transformation time is associated with increased kinetic stability, these results clearly demonstrate that the Et and OMe glasses have a similarly high kinetic stability relative to that of their liquid-cooled glasses. In comparison, the NHMe glass has a transformation time that is roughly 1.5 orders of magnitude smaller, indicating that the PVD was less successful in increasing the kinetic stability. These results are qualitatively consistent with the results presented in Figure 5.3.

### 5.4.3 Hydrogen-bonding

IR was used to probe the H-bonding in glasses of all three as-deposited compounds. Figure 5.5 displays a representative set of IR spectra recorded for glasses of the OMe derivative vapor-deposited at a range of $T_{substrate}$ values. The left part of the figure shows the "free" (3400 $cm^{-1}$) and the "bonded" (3285 $cm^{-1}$) NH stretching bands. In reality, more than two categories of H-bonds exist, but only two are used herein for clarity. As $T_{substrate}$ increases from 0.69 $T_g$ (black) up to 0.91 $T_g$ (orange), the absorbance of the "free" band decreases as the absorbance of the "bonded" band increases, indicating that the number of strong H-bonds somewhat increases. The "free" NH band also slightly shifts to the right upon increasing $T_{substrate}$, meaning that these weak interactions strengthen at higher $T_{substrate}$. The changes in absorbance may be used in combination with chemometrics analyses published previously[38] to quantify the average number of bonded NH per molecule as a function of $T_{substrate}/T_g$. These numbers, along with those calculated for the liquid-cooled glasses (1.65 for Et and OMe and 2.3 for NHMe), can be found in Figure 5.S1 in Supporting information (SI). As shown in Figure 5.S1, to a first approximation, hydrogen bonding in the PVD glasses is similar to that in the corresponding liquid-cooled glass. As discussed below, these numbers can test a possible link between the number of H-bond interactions and the ability to form glasses with high kinetic stability.

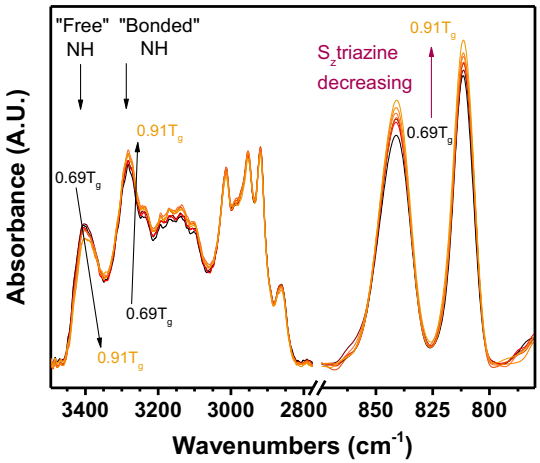


**Figure 5.5.** IR spectra of OMe glasses deposited at selected substrate temperatures between 0.69 (black) and 0.91 $T_g$ (orange). The NH stretching region (3500-3100 $cm^{-1}$) with "free" and "bonded" NH bands is shown. The absorbance of the "free" NH stretching band decreases, whereas the absorbance of the "bonded" NH band increases when the deposition temperature is increased from $0.69T_g$ to $0.91T_g$. These changes in absorbance are used to calculate the average number of bonded NH per molecule. The triazine deformation band (810 $cm^{-1}$) is also presented; the average orientation of the triazine ring can be obtained from this band.

### 5.4.4 Anisotropy of molecular orientation and structure

IR is also useful to evaluate the molecular orientation of the triazine moiety of the three compounds as a function of $T_{substrate}$. The right part of Figure 5.5 shows two bands (841 and 810 $cm^{-1}$) associated with out-of-plane deformation modes of the triazine ring in the OMe compound. As $T_{substrate}$ is increased from 0.69 $T_g$ (black) to 0.91 $T_g$ (orange), the absorbance of these bands increases. A high absorbance corresponds to a more perpendicular orientation of the triazine ring relative to the substrate. The changes of absorbance at 810 $cm^{-1}$ were used to calculate the orientation order parameter $S_z$ that characterizes the orientation of the transition dipole for the 810 $cm^{-1}$ absorption using Equation 1.

The orientation order parameter $S_z$ for the triazine moiety in the as-deposited glasses of the three compounds is shown in Figure 5.6 as a function of $T_{substrate}/T_g$. In detail, $S_z = (3\langle\cos^2\theta\rangle - 1)/2$, where $\theta$ is the angle between the surface normal and the transition dipole for the 810 $cm^{-1}$ absorption. The transition dipole is normal to the triazine ring and is represented by the circled dot in the triazine moiety (in fuchsia) in the inset to Figure 5.6.

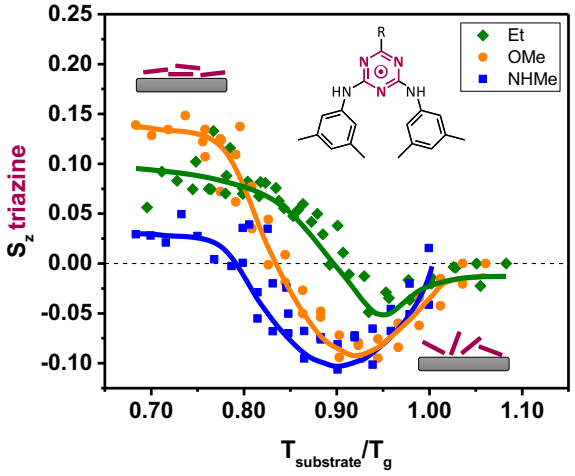


**Figure 5.6.** Comparison of the orientation order parameter $S_z$ for the triazine ring for the three compounds as a function of substrate temperature during deposition. $S_z$ characterizes the average orientation of the transition dipole that is perpendicular to the plane of the triazine represented as a circled dot, in the inset at the top right corner. As shown by the schematic illustrations, triazine units tend to orient somewhat parallel to the substrate when compounds are deposited at low substrate temperatures. Near $T_{substrate} = 0.92\ T_g$, triazine units tend to orient somewhat perpendicular to the substrate. The lines are guides to the eye.

Two cartoons representing a simplified visualization of the triazine ring orientation at low and high $T_{substrate}/T_g$ are also included as insets. The $S_z$ values for all three compounds exhibit similar trends. At low $T_{substrate}$, the $S_z$ value is positive, which means that the triazine ring has some tendency to be parallel to the substrate. The maximum values are between 0.15 (for OMe) and 0.025 (for NHMe); for reference, the maximum $S_z$ value is 1 (triazine ring perfectly parallel to the substrate). At higher values of $T_{substrate}/T_g$, $S_z$ values as low as -0.10 are observed; the minimum possible value is -0.5 (triazine ring perfectly perpendicular to the substrate). For $T_{substrate}/T_g \geq 1$, the $S_z$ values are near to 0, which is expected as the as-deposited glass should be equivalent to the (isotropic) liquid-cooled glass.

WAXS measurements were performed on PVD glasses of the three compounds to evaluate their structural anisotropy. The inset of Figure 5.7 shows a representative 2D WAXS pattern of an Et glass deposited at $T_{substrate} = 0.87T_g$, near its maximal kinetic stability. The scattering pattern shows an out-of-plane anisotropic peak at $q \sim 0.5$ Å$^{-1}$ and an amorphous halo

at q ~ 1.4 $Å^{-1}$. Although the amorphous halo is also found in liquid-cooled glasses, the out-of-plane 0.5 $Å^{-1}$ scattering feature is unique to the PVD glasses and corresponds to a periodic electron density modulation with a length scale of a little over 1 nm along the substrate normal. As this is approximately the size of the molecules under investigation, the presence of the anisotropic peak is evidence of molecular layers propagating along the substrate normal. The strength of the peak is reflective of the extent of ordering. To compare the relative strengths of the peaks of various glasses, the integrated intensities of the anisotropic peaks are normalized against the integrated intensity of the amorphous haloes at 1.4 $Å^{-1}$, similar to a previously reported protocol.[43] This intensity ratio is plotted in Figure 5.7 as a function of $T_{substrate}/T_g$. The highest scattering ratio is observed at $T_{substrate} \sim 0.85T_g$ for all three triazine derivatives. From its maximal value, the integrated scattering ratio decreases as $T_{substrate}$ increases and tends toward 0 at $T_{substrate}/T_g \geq 1$. This behavior is in agreement with our expectation that deposition above $T_g$ results in the (isotropic) supercooled liquid.

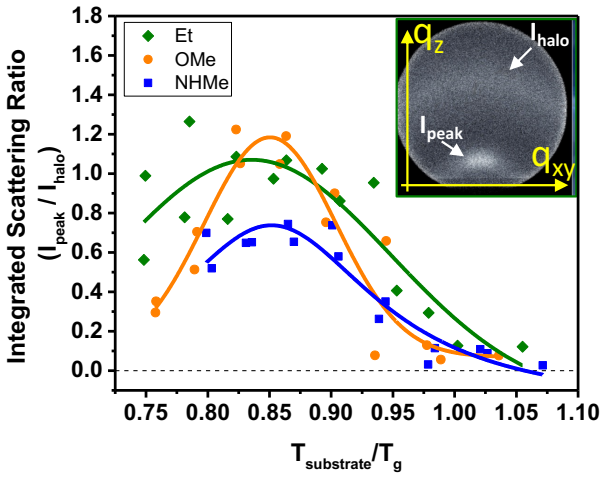


**Figure 5.7.** Anisotropic packing in PVD glasses of triazine compounds, as indicated by WAXS. The inset shows the 2D WAXS pattern measured for the PVD glass of Et deposited at $T_{substrate}/T_g$ = 0.87 and identifies the low q peak and the amorphous halo. The ratio of the integrated scattering intensities for the low q peak and the amorphous halo is presented as a function of the substrate temperature during deposition. The lines are guides to the eye.

## 5.5 Discussion

### 5.5.1 Kinetic stability: comparison to other PVD glasses

Isothermal annealing transformation times measured for PVD glasses of the three triazine compounds provide clear quantitative insights about kinetic stability. Although the transformation time depends strongly on the annealing temperature, the ratio of the transformation time to the α-relaxation time of the supercooled liquid is a much weaker function of temperature and thus allows a better comparison to other PVD glasses.[15, 17-18] The annealing experiments shown in Figure 5.4 were conducted at $T_g$ + 4 K. For all three compounds, the α-relaxation time at this temperature can be estimated to be $10^{0.8\pm0.3}$ s by assuming a value of 100 s at the differential scanning calorimetry $T_g$ and a fragility value, m, in the range of 80-120. Whereas Figure 5.4c shows that glasses of the Et and OMe compounds show similar transformation times, on the order of $10^3$ $\tau_\alpha$, NHMe presents a transformation time that is about 1.5 orders of magnitude smaller. For reference, a liquid-cooled glass that is annealed just above $T_g$ is expected to have a transformation time of $\sim 1$ $\tau_\alpha$.

Relative to $\tau_\alpha$, the transformation times for glasses of the Et and OMe compounds are somewhat smaller than the largest transformation times reported for PVD glasses of organic molecules. For instance, under similar conditions, the transformation times for glasses of 1,3-bis-(1-naphthyl)-5-(2-naphthyl)benzene (α,α,β-TNB)[17], N,N'-bis(3-methylphenyl)-N,N'-diphenylbenzidine (TPD),[18] and indomethacin (IMC)[18] are all $\sim 10^4$ $\tau_\alpha$. The NHMe transformation time is significantly lower than that of its Et and OMe analogues. Its transformation time on the order of $10^{1.5}$ $\tau_\alpha$ is closer to that of the PVD glasses of ethanol, which falls in the range of moderate kinetic stability.[30]

The values of $T_{onset}/T_g$ shown in Figure 5.3 are consistent with these conclusions. The maximal values reached by the Et and OMe compounds are slightly lower than the values reached by other organic compounds such as IMC, TPD, N,N'di(1-naphthyl)-N,N'-diphenyl-(1,1'-biphenyl)-4,4'-diamine (NPB) and 1-4-di[4-(N,N'-diphenyl)amino]styryl-benzene (DSA-Ph) that are between 1.04 and 1.06.[6] The maximal value of $T_{onset}/T_g$ =1.01 that the NHMe compound presents is much lower than these values, which confirms that PVD is less successful at increasing the kinetic stability beyond that of the liquid-cooled glass. A similarly low maximal

value of $T_{onset}/T_g$ was reported very recently for a series of hydroxyl-containing organic compounds.[30] Another similarity between glasses of the NHMe compound and those of many hydroxyl-containing compounds is the production of PVD glasses that are less stable than the liquid-cooled glass when deposition occurs at $T_{substrate}$ below 0.79 $T_g$.

### 5.5.2 Influence of hydrogen-bonding capability on ability to form stable glasses

To test a possible link between H-bonding capability and the ability to form PVD glasses of high kinetic stability, we make use of the quantification of H-bonding provided by the IR measurements in Figure 5.5. The average numbers of bonded NH per molecule calculated for the liquid-cooled glasses and the as-deposited glasses are compiled in Figure 5.S1. Over the entire $T_{substrate}$ range that is probed, the average number of bonded NH per molecule is higher for the as-deposited NHMe glasses than for the Et and OMe glasses. The average number of bonded NH per molecule for PVD glasses of NHMe is about 2.3, whereas for the Et and OMe glasses the average is roughly 1.6.[38] As the enthalpies of formation for H-bonds are, on average, equivalent for these specific compounds (roughly -15 kJ/mol),[38] comparing the average number of bonded NH per molecule is a sufficient measure of the importance of the H-bond network. Hence, we conclude that more extensive H-bond interactions are found in the NHMe compound than in Et and OMe. This conclusion is also supported by the higher $T_g$ value for the liquid-cooled glass of the NHMe compound. As discussed in the Introduction, it has been suggested that H-bonding may interfere with the formation of stable glasses, possibly, because it limits the surface diffusion.[30-31, 33] The results for the three triazine derivatives are consistent with this view, in that the most H-bonded system is also the least capable of forming glasses with high kinetic stability.

We now attempt to understand the kinetic stability of PVD glasses of the triazine compounds in light of the results for previously studied organic molecules. The molecules that form the most kinetically stable glasses by PVD have no capability for H-bonding (such α,α,β-TNB[17] and TPD[18]) or only modest H-bonding (IMC).[42] If H-bonding interferes with stable glass formation, then it makes sense that PVD glasses of the triazine compounds are not as stable as those of α,α,β-TNB and TPD. On the other hand, as the H-bonds formed by the NH group are

generally weaker than those formed by OH, it makes sense that the triazine derivatives form glasses with a generally higher kinetic stability than do the alcohols that have been studied up to this point.[30] Clearly this analysis could be improved by using a method of assessing the importance of H-bonding that could be uniformly applied to all organic molecules.

Yu and co-workers have provided a mechanism by which H-bonding might limit surface mobility (and thus stable glass formation) and it is interesting to examine systems containing NH bonds in this light. For systems without H-bonding, a molecule at the free surface might be free of approximately half of the interactions that limit its mobility in the bulk and thus exhibit substantial surface mobility.[44-45] For systems with H-bonding networks, it is likely that the surface will restructure to preserve a large fraction of the H-bonds; in this case, a molecule at the free surface would still be strongly interacting with the bulk and thus exhibit only modestly enhanced surface mobility. For alcohols, Tylinski *et al.* argued that the Debye relaxation might be interpreted as evidence for a substantial H-bonding network.[30] The Debye relaxation occurs at much longer time scales than those for the reorientation of individual molecules and involves long-lived H-bonding structures.[46] Combined dielectric spectroscopy measurements and shear-mechanical tests revealed that an amine-substituted compound, 2-ethyl-1-hexylamine, possesses a relaxation mode that is analogous to the Debye mode found in its hydroxyl analogue, 2-ethyl-1-hexanol, but lower in intensity.[47] This mode indicates that the NH groups can form network structures in the supercooled liquid that influence the liquid structure and dynamics, even if the NH interactions are not as strong as the corresponding OH interactions. Thus, it is certainly plausible that NH-containing molecules such as the NHMe triazine derivative can also form network structures that would considerably limit surface mobility. It would be interesting to test for the presence of the Debye relaxation in the supercooled liquids of these triazine compounds.

### 5.5.3 Density and anisotropy: comparison to other PVD glasses

Although the kinetic stability of the PVD glasses of the three triazine derivatives can be easily rationalized in light of previous results, this is not the case for the density measurements. Despite their substantial differences in kinetic stability, all three compounds show features typically observed in highly stable PVD glasses, such as high density and considerable anisotropy of molecular orientation and structure. For instance, glasses of the triazine

derivatives have densities ~1.2 % higher than those of the corresponding liquid-cooled glasses for $T_{substrate}$ between 0.75 and 0.85 $T_g$ (Figure 5.2). These relative densities are very similar to the ones reported previously for highly stable glasses such as α,α,β-TNB,[48] TPD,[6] and IMC[5], which show density increases between 1.0 and 1.4 % in the same $T_{substrate}/T_g$ range. For these highly stable systems, a strong correlation was reported between density and kinetic stability.[5, 18, 21] On the basis of this previous work, we would expect that the NHMe compounds would exhibit a more modest density increase than that shown in Figure 5.2. Although we do not have a good explanation for the combination of high density and modest kinetic stability exhibited by some PVD glasses of the NHMe compound, we will offer one speculative idea. Work exploring the temperature and pressure dependence of dynamics in supercooled liquids has led to the conclusion that systems with strong H-bonding have dynamics in which temperature (rather than density) is the dominant control variable.[49] Although this observation would not explain why PVD glasses of the NHMe derivative have such high density, it does suggest that high density would not necessarily result in high kinetic stability.

Previous work on PVD glasses has shown a connection between anisotropic molecular orientation and surface mobility, and we briefly comment on the results shown in Figure 5.6 for the three triazine compounds in light of that work. For a series of rodlike molecules, it was argued that molecular orientation in the glass results from partial equilibration of molecules near the glass surface during deposition.[6, 41] Organic molecules at the equilibrium liquid/vapor interface generally would be expected to exhibit anisotropic molecular orientation and this orientation can be trapped into a glass during deposition. Although this previous work provides no specific prediction for the orientation of PVD glasses of the triazine derivatives, it does suggest that systems with different surface mobilities should exhibit different anisotropies. Therefore, the similar trends for molecular orientation as a function of $T_{substrate}/T_g$ for the three molecules are surprising given that we have argued that the surface mobility of the NHMe system is likely substantially lower (to account for its lower kinetic stability).

WAXS characterization of PVD glasses of the three triazine derivatives shows evidence for anisotropic scattering that is qualitatively similar to that observed for PVD glasses of other organic molecules. Glasses deposited at $T_{substrate}$ lower than the $T_g$ of the compounds all show a broad low q peak around 0.5 $Å^{-1}$ (see Figure 5.7 inset) that has been associated with a tendency

toward molecular layering in other stable PVD glasses such as TNB isomers[17] ($q \sim 0.5$ Å$^{-1}$) and IMC[43] ($q \sim 0.6$ Å$^{-1}$). Qualitatively similar features have been observed in computer simulations of PVD glasses of trehalose.[50] We emphasize that the observed scattering for these triazine compounds is not related to a crystalline packing since the samples do not show other indications of crystallization, for example, these glasses become liquids when heated above $T_g$ even though they are far below their melting points. Instead, we interpret the low q scattering peak as an indicator of an anisotropic amorphous packing. The integrated scattering ratio of the compounds presented in Figure 5.7 as a function of $T_{substrate}/T_g$ shows that the as-deposited glasses of the OMe and Et compounds present a maximal tendency to layering when deposited at $T_{substrate} \sim 0.85\ T_g$. These results make sense assuming that the kind of organization measured by X-ray is partly accomplished by surface mobility. Indeed, results from Figure 5.7 are consistent with those of kinetic stability (Figure 5.3), in that the NHMe compound exhibits lower-intensity anisotropic peaks and the maximum intensity of this peak is observed at higher values of $T_{substrate}/T_g$.

## 5.6 Conclusion

We have used a high-throughput preparation method to vapor-deposit a series of triazine derivatives that possess different H-bonding capabilities in order to assess systematically the impact of H-bonding on the formation of stable glasses by PVD. Spectroscopic ellipsometry measurements revealed that the Et and OMe compounds formed glasses with high kinetic stability evidenced by their high values of $T_{onset}/T_g$ and their long transformation times on the order of $10^3\ \tau_\alpha$, which is only slightly lower than that for the most stable vapor-deposited organic glasses. PVD glasses of the NHMe analogue exhibited lower kinetic stability although they were still substantially more stable than the corresponding liquid-cooled glass. A possible link between the kinetic stability and the extent of H-bonding was tested by quantifying the average number of bonded NH groups per molecule using IR. The NHMe compound showed a higher number of bonded NH groups per molecule in its supercooled liquid state and in its PVD glasses, suggesting that numerous H-bonds hinder the formation of stable glasses, possibly by lowering the surface mobility of the compound. This suggestion is consistent with the previous work by Yu and co-workers.[31] Despite these differences in kinetic stability, PVD glasses of all three

triazine compounds showed higher density and also showed anisotropy of molecular orientation and structure. The high densities of PVD glasses of the NHMe compound were surprising given their lower kinetic stability. The connection between density and kinetic stability has been a topic of current interest[5, 18, 21] and deserves further attention.

This study adds three triazine derivatives to the set of vapor-deposited organic compounds with H-bonding capability and complements a very recently published study of PVD glasses of six alcohols.[30] The new results are consistent with the alcohol work in that the triazine compound that exhibited the greatest degree of hydrogen bonding also produced PVD glasses of the lowest kinetic stability. In addition, the triazines as a group produced PVD glasses of greater kinetic stability than the alcohols, an observation that we attribute to the NH hydrogen bonds being weaker on average than OH hydrogen bonds. All of these observations are consistent with the idea that H-bonding interferes with stable glass formation by lowering the surface mobility. It would be of interest to conduct surface diffusion experiments on these triazine compounds to directly test our inference that the NHMe compound has the lowest surface mobility.

## 5.7 Acknowledgments

This work was supported by the U.S. Department of Energy, Office of Science, Basic Energy Sciences, under Award DE-SC0002161. A.L. thanks the Natural Sciences and Engineering Research Council of Canada (NSERC) for a Michael Smith Foreign Study Supplement and a Vanier graduate scholarship. The authors gratefully acknowledge use of instrumentation supported by NSF through the University of Wisconsin – Madison MRSEC (DMR-1121288). We also thank Jaritza Gómez, Travis Powell, Michael Tylinski and Diane Walters for helpful discussions.

## 5.8 References

1. Swallen, S. F.; Kearns, K. L.; Mapes, M. K.; Kim, Y. S.; McMahon, R. J.; Ediger, M. D.; Wu, T.; Yu, L.; Satija, S., *Science* **2007,** *315*, 353-356.
2. Yokoyama, D., *J. Mater. Chem.* **2011,** *21*, 19187-19202.
3. Selvakumar, N.; Barshilia, H. C., *Sol. Energ. Mat. Sol. Cells* **2012,** *98*, 1-23.

4. Kearns, K. L., et al. In *Molecular Orientation, Thermal Behavior and Density of Electron and Hole Transport Layers and the Implication on Device Performance for OLEDs*, 2014; pp 91830F-91830F-12.
5. Dalal, S. S.; Fakhraai, Z.; Ediger, M. D., *J. Phys. Chem. B* **2013,** *117*, 15415-15425.
6. Dalal, S. S.; Walters, D. M.; Lyubimov, I.; de Pablo, J. J.; Ediger, M. D., *Proc. Natl. Acad. Sci. USA* **2015,** *112*, 4227-4232.
7. Whitaker, K. R.; Tylinski, M.; Ahrenberg, M.; Schick, C.; Ediger, M. D., *J. Chem. Phys.* **2015,** *143*, 084511.
8. Gujral, A.; O'Hara, K. A.; Toney, M. F.; Chabinyc, M. L.; Ediger, M. D., *Chem. Mater.* **2015,** *27*, 3341-3348.
9. Ramos, S. L. L. M.; Oguni, M.; Ishii, K.; Nakayama, H., *J. Phys. Chem. B* **2011,** *115*, 14327-14332.
10. L. M. Ramos, S. L.; Chigira, A. K.; Oguni, M., *J. Phys. Chem. B* **2015,** *119*, 4076-4083.
11. Ishii, K.; Nakayama, H., *Phys. Chem. Chem. Phys.* **2014,** *16*, 12073-12092.
12. Rodríguez-Tinoco, C.; Gonzalez-Silveira, M.; Rafols-Ribe, J.; Lopeandia, A. F.; Rodriguez-Viejo, J., *Phys. Chem. Chem. Phys.* **2015,** *17*, 31195-31201.
13. Rodríguez-Tinoco, C.; Gonzalez-Silveira, M.; Ràfols-Ribé, J.; Garcia, G.; Rodríguez-Viejo, J., *J. Non-Cryst. Solids* **2015,** *407*, 256-261.
14. Zheng, Y.-Q., et al., *Nanotechnology* **2015,** *26*, 405202.
15. Rodríguez-Tinoco, C.; Gonzalez-Silveira, M.; Ràfols-Ribé, J.; Lopeandía, A. F.; Clavaguera-Mora, M. T.; Rodríguez-Viejo, J., *J. Phys. Chem. B* **2014,** *118*, 10795-10801.
16. Liu, T., et al., *J. Chem. Phys.* **2015,** *143*, 084506.
17. Dawson, K.; Kopff, L. a.; Zhu, L.; McMahon, R. J.; Yu, L.; Richert, R.; Ediger, M. D., *J. Chem. Phys.* **2012,** *136*, 094505.
18. Walters, D. M.; Richert, R.; Ediger, M. D., *J. Chem. Phys.* **2015,** *142*, 134504.
19. Chua, Y. Z.; Ahrenberg, M.; Tylinski, M.; Ediger, M. D.; Schick, C., *J. Chem. Phys.* **2015,** *142*, 054506.
20. León-Gutierrez, E.; Garcia, G.; Clavaguera-Mora, M. T.; Rodríguez-Viejo, J., *Thermochim Acta* **2009,** *492*, 51-54.

21. Rodríguez-Tinoco, C.; González-Silveira, M.; Barrio, M.; Lloveras, P.; Tamarit, J. L.; Garden, J. L.; Rodríguez-Viejo, J., *Sci. Rep.* **2016,** *6*, 34296.
22. Yu, L., *Adv. Drug Deliv. Rev.* **2016,** *100*, 3-9.
23. Brian, C. W.; Yu, L., *J. Phys. Chem. A* **2013,** *117*, 13303-13309.
24. Lyubimov, I.; Antony, L.; Walters, D. M.; Rodney, D.; Ediger, M. D.; de Pablo, J. J., *J. Chem. Phys.* **2015,** *143*, 094502.
25. Mangalara, J. H.; Marvin, M. D.; Simmons, D. S., *J. Phys. Chem. B* **2016,** *120*, 4861-4865.
26. Souda, R., *J. Phys. Chem. B* **2010,** *114*, 11127-11132.
27. Sepúlveda, A.; Leon-Gutierrez, E.; Gonzalez-Silveira, M.; Rodríguez-Tinoco, C.; Clavaguera-Mora, M. T.; Rodríguez-Viejo, J., *J. Chem. Phys.* **2012,** *137*, 244506.
28. Capponi, S.; Napolitano, S.; Wübbenhorst, M., *Nat. Commun.* **2012,** *3*, 1233.
29. Kasina, A.; Putzeys, T.; Wübbenhorst, M., *J. Chem. Phys.* **2015,** *143*, 244504.
30. Tylinski, M.; Chua, Y. Z.; Beasley, M. S.; Schick, C.; Ediger, M. D., *J. Chem. Phys.* **2016,** *145*, 174506.
31. Chen, Y.; Zhang, W.; Yu, L., *J. Phys. Chem. B* **2016,** *120*, 8007-8015.
32. Zhang, W.; Brian, C.; Yu, L., *J. Phys. Chem. B* **2015,** *119*, 5071-5078.
33. Zhang, W.; Yu, L., *Macromolecules* **2016,** *49*, 731-735.
34. Desiraju, G. R., *Acc. Chem. Res.* **2002,** *35*, 565-573.
35. Naito, K.; Sakurai, M.; Egusa, S., *J. Phys. Chem. A* **1997,** *101*, 2350-2357.
36. Zhu, L.; Yu, L., *Chem. Phys. Lett.* **2010,** *499*, 62-65.
37. Laventure, A.; Soldera, A.; Pellerin, C.; Lebel, O., *New J. Chem.* **2013,** *37*, 3881-3889.
38. Laventure, A.; De Grandpré, G.; Soldera, A.; Lebel, O.; Pellerin, C., *Phys. Chem. Chem. Phys.* **2016,** *18*, 1681-1692.
39. Wuest, J. D.; Lebel, O., *Tetrahedron* **2009,** *65*, 7393-7402.
40. Lebel, O.; Maris, T.; Perron, M.-È.; Demers, E.; Wuest, J. D., *J. Am. Chem. Soc.* **2006,** *128*, 10372-10373.
41. Jiang, J.; Walters, D. M.; Zhou, D.; Ediger, M. D., *Soft Matter* **2016,** *12*, 3265-3270.
42. Dalal, S. S.; Ediger, M. D., *J. Phys. Chem. Lett.* **2012,** *3*, 1229-1233.
43. Dawson, K. J.; Zhu, L.; Yu, L.; Ediger, M. D., *J. Phys. Chem. B* **2011,** *115*, 455-463.
44. Stevenson, J. D.; Wolynes, P. G., *J. Chem. Phys.* **2008,** *129*, 234514.

45. Mirigian, S.; Schweizer, K. S., *J. Chem. Phys.* **2014,** *140*, 194506.
46. Böhmer, R.; Gainaru, C.; Richert, R., *Phys. Rep.* **2014,** *545*, 125-195.
47. Adrjanowicz, K.; Jakobsen, B.; Hecksher, T.; Kaminski, K.; Dulski, M.; Paluch, M.; Niss, K., *J. Chem. Phys.* **2015,** *143*, 181102.
48. Dalal, S. S.; Sepúlveda, A.; Pribil, G. K.; Fakhraai, Z.; Ediger, M. D., *J. Chem. Phys.* **2012,** *136*, 204501.
49. Roland, C. M.; Hensel-Bielowka, S.; Paluch, M.; Casalini, R., *Rep. Prog. Phys.* **2005,** *68*, 1405-1478.
50. Singh, S.; de Pablo, J. J., *J. Chem. Phys.* **2011,** *134*, 194903.

## 5.9 Supporting information

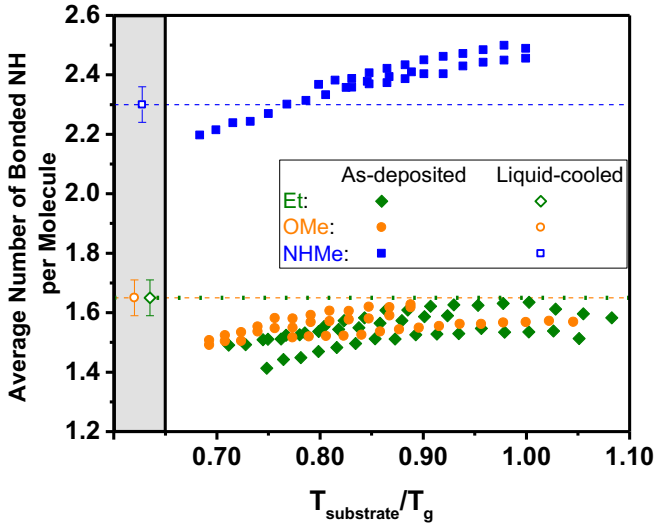


**Figure 5.S1.** Average number of bonded NH per molecule (measured at room temperature) in PVD glasses as a function of the substrate temperature during deposition, normalized by $T_g$ of each compound. The grey left panel shows the average number of bonded NH per molecule (also measured at room temperature) for the liquid-cooled glasses, with their standard deviations, as previously published.[1] A dashed line has been used to represent this average number in the right panel.

*Reference*

1. Laventure, A.; De Grandpré, G.; Soldera, A.; Lebel, O.; Pellerin, C. *Phys. Chem. Chem. Phys.* **2016**, *18*, 1681-1692.

# Chapitre 6: Submolecular plasticization induced by photons in azobenzene materials*

## 6.1 Abstract


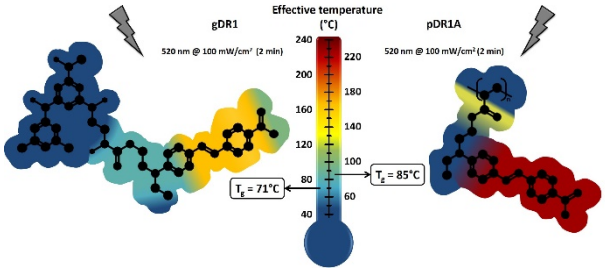


We demonstrate experimentally for the first time that the illumination of azobenzene derivatives leads to changes in molecular environment similar to those observed on heating but that are highly heterogeneous at the submolecular scale. This localized photoplasticization, which can be associated with a free volume gradient, helps to understand the puzzling phenomenon of photoinduced macroscopic material flow and photoexpansion upon illumination far below the glass transition temperature ($T_g$). The findings stem from the correlation of infrared (IR) spectral band shifts measured upon illumination with those measured at controlled temperatures for two amorphous DR1-functionalized azo derivatives, a polymer, pDR1A, and a molecular glass, gDR1. This new approach reveals that IR spectroscopy can be used as an efficient label-free molecular-scale thermometer that allows the assignment of an effective temperature ($T_{eff}$) to each moiety in these compounds when irradiated. While no band shift is observed upon illumination for the vibrational modes assigned to backbone moieties of pDR1A and gDR1 and a small band shift is found for the spacer moiety, dramatic band shifts are recorded for the azo moiety, corresponding to an increase in $T_{eff}$ of up to nearly 200 °C and a molecular environment that is equivalent to thermal heating well above the bulk $T_g$ of the material. An irradiated azo-containing material thus combines characteristic properties of amorphous materials both below and above its bulk $T_g$. The direct measurement of $T_{eff}$ is a powerful probe of the local environment at the submolecular scale, paving the way toward better rationalization of


---

* Publié en tant qu'article dans *Journal of the American Chemical Society*: Vapaavuori, J.[§]; Laventure, A.[§]; Bazuin, C. G.; Lebel, O.; Pellerin, C., *J. Am. Chem. Soc.* **2015**, *137*, 13510-13517. [§] = contribution égale. J.V. a réalisé les mesures liées au pDR1A et co-rédigé le manuscrit. O.L. a procédé à la synthèse du gDR1.

photoexpansion and the athermal malleability of azo-containing materials upon illumination below their $T_g$.

## 6.2 Introduction

The repetitive photoisomerization of azobenzene derivatives, either covalently bonded or doped in glassy materials, can lead to photoinduced motion observable on macroscopic scales. This phenomenon has been exploited for the all-optical fabrication of nano- and microstructured surfaces,[1-2] for the tridimensional ordering of microphase-separated block copolymer structures,[3] as well as for the imaging of plasmonic structures.[4-5] However, a deeper understanding of the fundamentals governing this process is still required to fully take advantage of it. Indeed, how light can render glassy materials malleable at temperatures far below their bulk glass transition temperature ($T_g$), often as much as 100 K, is currently one of the most puzzling questions in the materials science community. At such temperatures, the large-scale segmental motions of polymers are normally very slow or essentially frozen.[6]

Multiple approaches to address this paradox have been proposed, and there is an intensive debate about whether photoinduced motion is caused by a decrease of certain mechanical properties upon irradiation itself,[7-8] often referred to as photosoftening or photofluidization, or whether the photoinduced orientation of the azo units can create stresses large enough to reshape materials in the glassy state.[9] The discussion is complicated by difficulties in the direct comparison of different methods used for measuring (bulk) mechanical properties and by ambiguity in what the terms "photosoftening" and "photofluidization" actually mean. They are sometimes understood metaphorically for describing softening that does not necessarily lead to a fluid-like state, and sometimes more literally to indicate the transformation of the material into a fluid-like state comparable to heating it above its bulk $T_g$ into the viscoelastic flow region in the case of amorphous materials. The photoinduced melting of star-shaped azobenzene tetramers was recently demonstrated at ambient temperature, showing that isothermal light-powered fluidization of a crystal is possible.[10] For these reasons, building a unified and comprehensive picture of the state existing in azo-containing materials under illumination is rather challenging.

It is well established that the photoisomerization of azobenzenes requires greater volume than that occupied by either the (static) *trans* or *cis* isomers, thus generating additional free volume.[11-15] In particular, ellipsometry and neutron reflectometry studies have shown that irradiation leads to photoexpansion of the poly(Disperse Red 1 acrylate) (pDR1A) homopolymer at ambient temperature (around 60 °C below the bulk $T_g$ for a molecular weight of ~5000 g/mol).[16-17] A pressure gradient resulting from different amounts of free volume created under an interference illumination pattern was also suggested as the driving force for all-optical surface patterning leading to the formation of surface relief gratings (SRGs),[18] although this view was criticized for not being able to account for the polarization dependence of SRG formation.[1] A similar photomechanical effect can be used to photoinduce bending of free-standing films due to the gradually diminishing light intensity in an absorbing material.[19]

There have been several attempts to directly observe photoinduced mechanical changes in azomaterials. Karageorgiev *et al.* conducted AFM-based indentation measurements and demonstrated a light-induced decrease in viscosity by many orders of magnitude as well as anisotropic polymer flow.[20] In support of this, Hurduc *et al.* observed the flow of actinic filaments on polysiloxane-based azopolymers under illumination of 488 nm light through fluorescence microscopy.[21] In this case, the photofluidization was strongly material dependent and was observed for cyano-tailed azobenzene side chains but not for $NO_2$- and H-tailed groups, which might be related to the higher capability of the former to promote a liquid crystalline mesophase. Fang *et al.* studied photofluidization from the viewpoint of relaxation dynamics and reported that, in dense self-assembled azo-containing monolayers under illumination by linearly polarized 514 nm light, only a few molecules are transiently heated to a temperature as high as 800 K, far above the $T_g$ of most organic materials, whereas the overall material temperature increases by less than 1 K.[22] Finally, molecular simulations by Teboul *et al.* gave evidence of dynamic heterogeneities in glassy azo-containing materials.[15, 23]

Herein, we probe the athermal malleability phenomenon from a molecular point of view, in contrast to a macroscopic point of view, by exploiting the selectivity of infrared spectroscopy (IR) with *in-situ* temperature control and illumination of the materials. We thereby show experimental evidence for the first time that the repeated photoisomerization of azobenzenes induces changes in their molecular environment that are similar to those observed on bulk

heating but that are heterogeneously distributed within individual molecules or molecular segments. We do this using two amorphous azomaterials, namely the pDR1A homopolymer and a DR1-containing mexylaminotriazine molecular glass,[24] gDR1 (a small organic molecule that readily forms an amorphous phase without requiring extreme processing conditions). Correlating the positions of IR bands associated with different molecular moieties under illumination of unpolarized 520 nm light with their positions at controlled temperatures leads to the concept of an effective temperature, $T_{eff}$, as an indicator of the local molecular environment under illumination. This novel label-free IR method allows observing a submolecular $T_{eff}$ gradient under illumination that, in the case of pDR1A**,** is as large as 200 °C between the azo moiety and the backbone and that can be associated with a free volume gradient**.** Combined with the photo-orientation ability of azo moieties, this observation offers a plausible origin for photoinduced motion in azomaterials below their glass transition temperature.

## 6.3 Experimental section

Solutions of pDR1A (Sigma-Aldrich, MW = 5000 g/mol) and gDR1 (synthesized according to literature procedures[24]) in $CHCl_3$ and $CH_2Cl_2$, respectively, were cast on the single reflection diamond element of a Heated Golden Gate (Specac) attenuated total reflection (ATR) accessory. Spectra were recorded using a Tensor 27 FT-IR spectrometer (Bruker Optics) equipped with a liquid nitrogen-cooled MCT detector. The samples were first heated to 140 °C followed by an isotherm of 3 min. Spectra were recorded during a cooling ramp at 2 °C/min by averaging 100 scans with a 4 $cm^{-1}$ resolution. Background scans were recorded for each sample temperature. After performing these heating and cooling cycles, which at the same time remove the thermal history of the materials, the samples were irradiated using a LED source (Prizmatix FC5Multichannel LED) at 520 nm with an irradiance of 10, 45, or 100 $mW/cm^2$. Three repetitive cycles of 2 min darkness followed by 2 min irradiation were performed to confirm the repeatability of the photoinduced band shifts. An irradiance of 100 $mW/cm^2$ was used to compare the spectroscopic $T_g$ of samples upon cooling in the presence or absence of illumination. Band positions were determined using the OPUS 6.0 software (Bruker Optics) from the center of gravity of the top 50% of the bands. This procedure provides band positions with an uncertainty better than 0.01 $cm^{-1}$ and thus enables following small band shifts with

temperature or under illumination.[25] A nonphotoisomerizing control sample was prepared by dispersing 5 wt% of Nile Red (Sigma-Aldrich) in poly(methyl methacrylate) (PMMA, MW = 35000 g/mol, Scientific Polymer Products). Films were cast from a $CHCl_3$ solution and studied by IR spectroscopy as a function of illumination and temperature as described above.

UV-visible spectra were recorded on films spin-coated on microscope glass slides from the same sample stock solutions using an Ocean Optics 2000+ fiber-coupled spectrometer and a DH-mini light source. Films were annealed at 140 °C for 30 min and cooled slowly to ambient temperature to remove thermal history and ensure comparability with IR samples. Clean glass slides were used as a reference. Differential scanning calorimetry analyses were conducted with a PerkinElmer DSC 8500 calorimeter, calibrated with indium, using a heating rate of 10 °C/min. The $T_g$'s were determined, after an initial cycle of heating and cooling at 10 °C/min, as the average half-height of the heat capacity jump in the second and third heating scans.

## 6.4 Results and discussion

The materials selected for this study, a polymer (pDR1A) and a molecular glass (gDR1) presented in Figure 6.1, are both derivatives of Disperse Red 1 (DR1), one of the most exploited azobenzene derivatives in photorelated studies because its push-pull character leads to rapid *trans-cis-trans* cycles upon illumination in the blue-green part of the visible spectrum. These materials form surface relief gratings (SRGs) efficiently under illumination of a light interference pattern at ambient temperature, well below their $T_g$.[18, 24, 26] To distinguish the behavior of the different chemical groups in these molecules, a color code is used throughout this article, where red refers to the azo moiety, gray to the spacer, and blue to the backbone parts of the molecules.

Figure 6.1 also shows that the UV-visible absorbance spectra of thin films of pDR1A and gDR1 are comparable both in terms of close absorption maxima (445 and 463 nm, respectively) and in terms of the asymmetric shape of the absorption band related to enhanced dipole-dipole interactions between adjacent DR1 units in the solid state.[27] Irradiation with unpolarized light at 520 nm results in photostationary states consisting primarily of *trans* isomers, with less than 5% and 10% of *cis* isomers for gDR1 and pDR1A, respectively, due to the fact that the illumination wavelength falls within the relatively broad range absorbed by both

*trans* and *cis* isomers of DR1 (thus driving both *trans-cis* and *cis-trans* photoisomerization reactions)[28] and that the thermal relaxation lifetime of DR1-type chromophores is on the order of seconds.[29] In addition to enabling efficient photoinduced mass transport, this photostationary state with a low *cis*-isomer concentration facilitates correlating the IR spectroscopy results upon illumination and at controlled temperature because complications due to the presence of bands of the *cis* isomers in the spectra under illumination are mainly avoided.

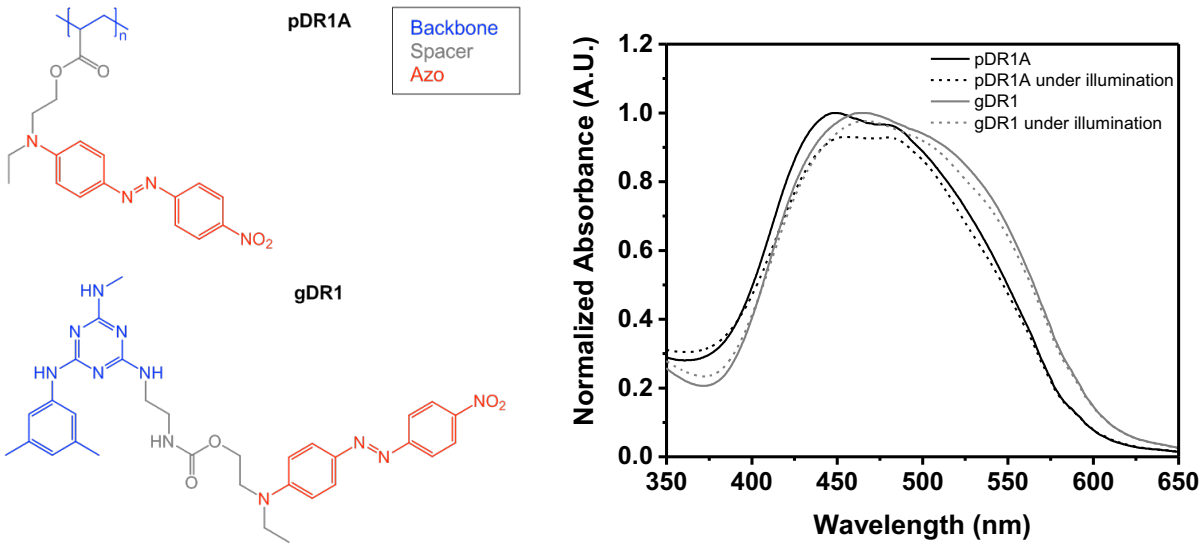


**Figure 6.1.** Molecular structure and UV-visible absorbance spectra of pDR1A and gDR1 before (plain lines) and under (dotted lines) irradiation. A color scheme highlights the azobenzene (red), spacer (gray) and backbone (blue) moieties of the molecules.

We use IR spectroscopy as a powerful label-free probe to investigate how photoisomerization influences the azo materials on a molecular level because the position, shape and width of IR bands all depend on the molecular environment of the absorbing chemical groups of the compound under study.[25, 30] The IR spectra of the compounds investigated here are presented in Figure 6.2. The assignments of the bands of importance for this study are collected in Table 6.S1 (Supporting Information).[31-33] To determine how photoisomerization affects different parts of the molecules, bands that are associated primarily with the azo (red), spacer (gray) and backbone (blue) moieties are color-coded as shown in Figure 6.1. Great care

was taken to avoid overlapped bands due to vibrational modes involving multiple parts of the molecules.

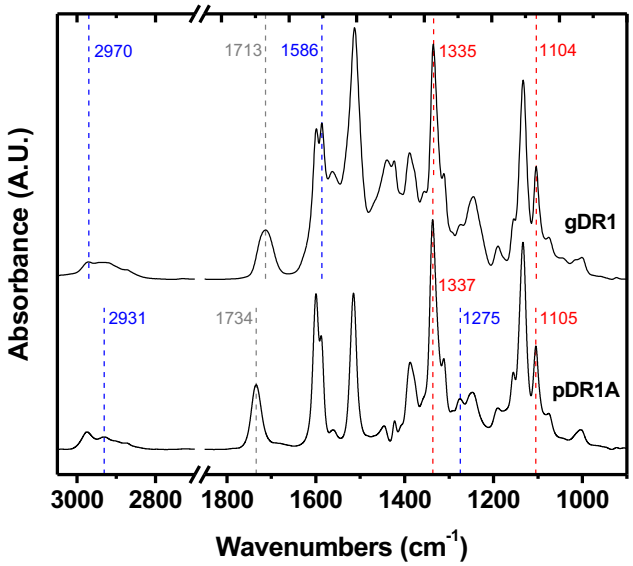


**Figure 6.2.** IR spectra of pDR1A and gDR1 showing selected vibrational modes associated with the azo (red), spacer (gray) and back-bone (blue) moieties of the molecules.

Figure 6.3 shows the observed band shifts (with reference to the position of the band at 40 °C without illumination) for representative functional groups from the backbone, spacer and azo moieties of gDR1 and for the azo group of pDR1A (results for the spacer and backbone of pDR1A are given in Figure 6.S1 of the SI) as the sample is cooled from 140 °C, which is well above the $T_g$ (data colored according the code of Figure 6.1, bottom X axis), and when cyclic illumination is applied at a constant temperature of 40 °C (data in green, top X axis). A gradual band shift is clearly observed when the temperature of the sample is changed. The evolution of band position as a function of temperature often allows determining phase transition temperatures because it reflects the perturbation of the molecular environment. First-order phase transitions, such as a melting event, can be observed spectroscopically as an abrupt change in band position at the transition temperature,[34-35] similar to the jumps observed when measuring the specific volume or the enthalpy.[6] Since the glass transition of amorphous materials is a pseudo-second order transition, a change of slope is expected at the transition temperature.[6, 36-38] Indeed, a change of slope upon cooling gDR1 is clearly observable in Figure 6.3B and 6.3C

at 71 °C, a temperature that corresponds to its bulk $T_g$[39] as determined by differential scanning calorimetry (DSC). A similar change of slope upon cooling is observed at 85 °C for pDR1A in Figure 6.3D,

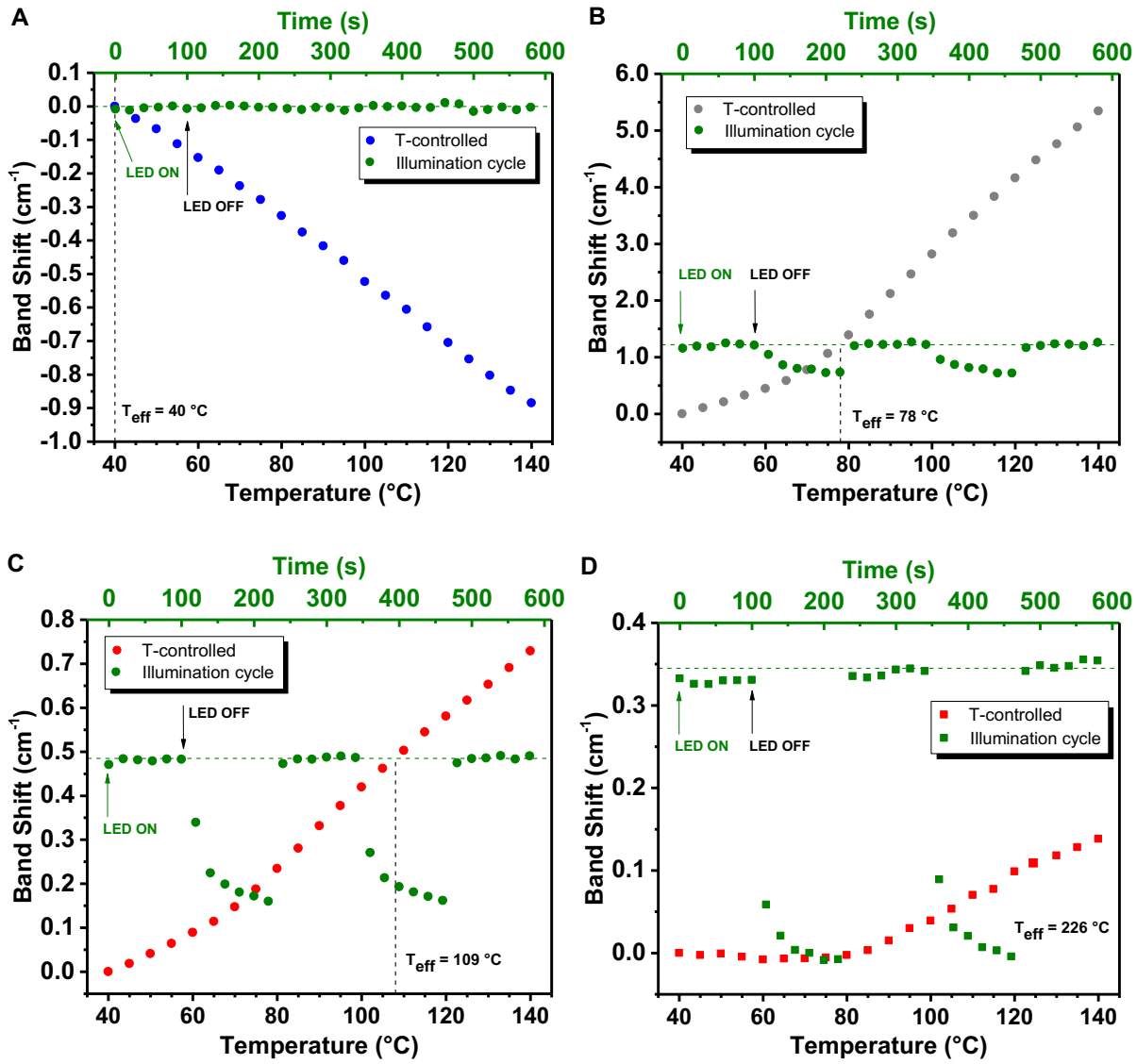


**Figure 6.3.** Procedure for determining the effective temperature ($T_{eff}$) of the chemical groups by comparison of the IR band shifts under illumination cycles at 40 °C (green) and in the dark during temperature (T)-controlled ramps (see text for details). Examples are shown for the gDR1 A) backbone (1586 $cm^{-1}$ triazine ring stretching), B) spacer (1713 $cm^{-1}$ C=O stretching) and C) azo (1335 $cm^{-1}$ $NO_2$ symmetric stretching) bands and for the pDR1A D) azo (1337 $cm^{-1}$ $NO_2$ symmetric stretching) band.

which similarly corresponds to its bulk $T_g$ value determined by DSC. The positions of the selected IR bands are thus indicators of the molecular environment of the moieties involved. It should be noted here that, as will be shown in Figures 6.4 and 6.S2, the spectroscopic $T_g$ of gDR1 and pDR1A are not affected under the illumination conditions applied.

When the samples are irradiated with 520 nm light, a clear shift is observed for the bands associated with the azo and spacer moieties even though the bulk temperature of the sample remains fixed at 40 °C. The repeatability of the photoinduced band shifts, clearly observable in Figure 6.3B-D during consecutive cycles of 120 s of illumination (LED on) followed by 120 s of relaxation in darkness (LED off) (data in green, top X axis), indicates that the transient modification of the molecular environment upon photoisomerization is repeatable, as previously shown in photoexpansion studies of pDR1A by Barrett and co-workers using ellipsometry measurements.[16-17] When the thermally induced and photoinduced band shifts are compared, the most striking observations are that they systematically evolve in the same direction and that the amplitude of the photoinduced band shifts increases with increasing proximity of the chemical group to the azo moiety. More specifically, as compared to the effect of raising the bulk sample temperature, no significant band shift is observed under illumination for the backbone (Figure 6.3A), a relatively small shift is observed for the spacer (Figure 6.3B) and a much larger relative shift occurs for the azo (Figure 6.3C). Similar observations for pDR1A are shown in Figures 6.3D and S1. In this case, the photoinduced band shift for the azo moiety (Figure 6.3D) is even more than twice the band shift recorded upon heating from 40 to 140 °C.

These observations legitimately raise the question of whether illumination decreases the bulk $T_g$ of the materials. To verify this, $T_g$'s were determined spectroscopically using IR band shifts measured under the conditions of interest. Figure 6.4 displays the band shift of gDR1 as a function of temperature during cooling ramps under irradiation (data with green edges) and without irradiation (data without green edges) for the carbonyl stretching (1713 $cm^{-1}$, in gray) and $NO_2$ symmetric stretching (1335 $cm^{-1}$, in red) bands. Both experimental conditions lead to an identical $T_g$ of 71 °C for gDR1 and of 85 °C for pDR1A (see Figure 6.S2 in SI), in exact agreement with the values obtained for bulk samples by DSC using a 10 °C/min heating ramp. These results unambiguously show that the overall spectroscopic $T_g$ of the materials is unaffected by photoisomerization upon illumination under the conditions used, and are in

accordance with the results of Fang *et al*. showing no significant illumination-related temperature increase in their material despite their observation of an uneven distribution of heated molecular environments.[22] This conclusion is reinforced by the fact that the backbone moieties for both samples show no measurable photoinduced band shift, indicating that their molecular environment is identical with and without illumination, thereby preventing isotropic flow of the bulk sample upon illumination.

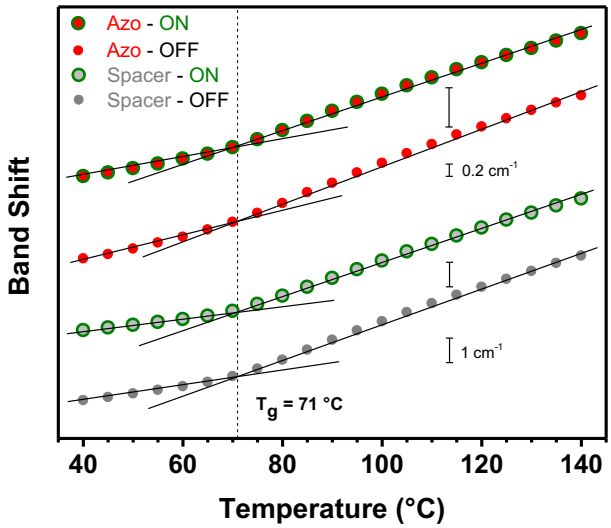


**Figure 6.4.** Evolution of the band shifts (gray: spacer C=O stretching; red: azo $NO_2$ symmetric stretching) of gDR1 on cooling without ("OFF") and with ("ON") illumination at 520 nm using an irradiance of 100 mW/cm$^2$. The change in slope corresponds to the $T_g$ of the material as determined by DSC.

The specific position of an IR absorption band depends on the force constant and the reduced mass of its associated vibrating dipole. The band shifts observed as a function of temperature and under illumination are therefore due to the concomitant evolution of several aspects affecting the local molecular environment of the absorbing groups, including the strength of intermolecular interactions, the local conformation, and the level of stress acting on the bonds.[25, 30] The fact that the band shifts observed in Figures 6.3 and 6.S1 (as well as for the other bands studied but not shown) systematically occur in the same direction when increasing the temperature and when illuminating the sample, strongly suggests that they share the same

molecular origin. The most plausible common origin is the generation of additional free volume in the sample, which would provoke the observed band shifts by decreasing the strength of local intermolecular interactions (by increasing the average molecular distance) and by enabling more freedom to explore the molecular conformational space. Indeed, it is known from photoexpansion studies that repeated *trans-cis-trans* cycling introduces free volume under illumination,[11, 16-17, 40] and that heating amorphous materials also increases their free volume (note that the band shifts observed in Figures 6.3 and 6.4 are very similar to the temperature dependence of specific volume).[6, 38]

A possible alternative interpretation is that the apparent local heating is due to heat dissipation from nonradiative transitions in the chromophore. To rule this out, a sample analogous to pDR1A structurally and spectrally but that does not photoisomerize was prepared by dispersing Nile Red in PMMA. This blend absorbs strongly at the excitation wavelength of 520 nm (its absorption maximum is at 528 nm; see Figure 6.S3A) and presents IR bands that are well isolated for Nile Red and relatively well isolated for PMMA (Figure 6.S3B). Figure 6.S4 shows clear shifts of these bands, along with a change in slope at the PMMA $T_g$ for some bands, upon physically heating the sample, which is very similar to the behavior in gDR1 and pDR1A. In contrast, there is no significant shift for any of these bands under irradiation (Figure 6.S4). Even though the number density of absorbing molecules in this Nile Red / PMMA blend is lower than in gDR1 or pDR1A, the lack of photoinduced shift for the Nile Red bands indicates that local heating due to dissipation of the photon energy does not contribute significantly to the observed band shifts for DR1-containing systems. This result is in agreement with the recently observed athermal photoinduced melting of azobenzene crystals.[10] Furthermore, it confirms the importance of photoisomerization in the observed spectral changes described above and supports the interpretation that free volume plays an important role in the behavior of gDR1 and pDR1A under illumination.

In this context, the similarity of the band shifts observed under illumination and upon heating observed in Figure 6.3 reveal for the first time that illuminating a material capable of photoisomerization induces changes in the molecular environment that are heterogeneously distributed along a single molecule (gDR1) or polymer repeat unit (pDR1A). Since the azo moiety is the group that directly interacts with light, undergoing repeated *trans-cis-trans*

isomerization, the local increase in free volume under illumination is greatest around the azo groups and diminishes with molecular distance from this group, while the glass and the polymer backbone environments are essentially unaffected. In contrast, the increase in free volume introduced by heating the sample is more or less uniformly distributed at the molecular level, leading to band shifts for all of the moieties, azo, spacer and backbone.

These results indicate that certain parts of the molecules experience a local environment under illumination that is analogous to that found at temperatures above, even far above, the $T_g$ of the material while the bulk temperature remains unaffected. This gives rise to the concept that IR can be used as a submolecular "thermometer". Indeed, correlating the photoinduced band shift with the bulk temperature that gives the same band shift allows the determination of a photoinduced "effective temperature", $T_{eff}$, independently for each molecular moiety that is being probed. In other words, we use $T_{eff}$ as an indicator to describe the temperature to which the material must be heated to reproduce the band position (and thus the molecular environment) that is observed under irradiation. It must be stressed, however, that $T_{eff}$ should not be taken literally as the physical temperature of a chemical group. It should also be noted that the amplitude of the band shift with (bulk) temperature is different for each band, and thus the effect of irradiation must be considered in relative terms with respect to the effect of temperature. As an example, Figure 6.3B shows that the C=O band of gDR1 is at the same position under illumination (indicated by the green dashed line) and when heated to 78 °C (highlighted by the black dashed line). Its effective temperature under illumination is therefore 78 °C. (It is of interest to mention that illumination for 120 s is long enough to reach a plateau in the band position for gDR1 but that a slight increase in band shift is observed between cycles for pDR1A, suggesting that reaching a plateau $T_{eff}$ requires a longer illumination time for this polymer.) After the light is switched off, the band positions, and thus $T_{eff}$, gradually return toward the bulk temperature of 40 °C. For some functional groups (Figure 6.3B and 6.3C), a much longer recovery time than 120 s is needed to return to the initial state, which must be related to the movement of glassy matrices that are known to be relatively slow at temperatures below $T_g$ and is a topic for a future study.

The effective temperatures achieved under illumination with an irradiance of 100 $mW/cm^2$ were determined for all of the bands investigated as illustrated in Figure 6.3 and were

highly reproducible from sample to sample. They are reported in Figure 6.5 in graphical form (top), where the filled and open symbols represent $T_{eff}$'s that are above and below the bulk $T_g$ of

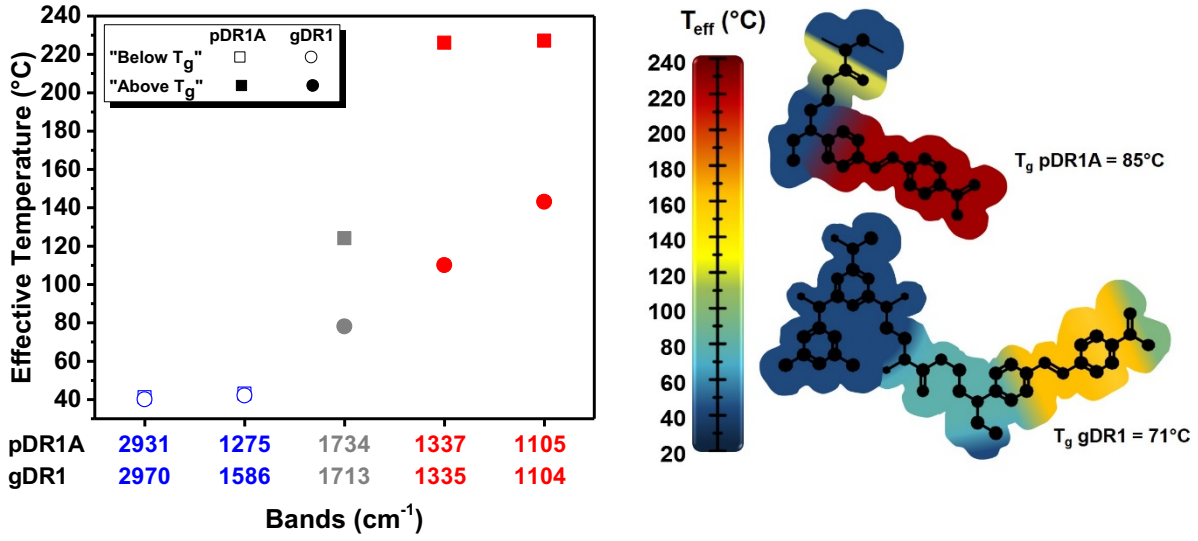


**Figure 6.5. Left**: Effective temperatures ($T_{eff}$) of pDR1A (squares) and gDR1 (circles) bands at 40 °C under irradiation at 520 nm (100 mW/cm$^2$). Blue refers to the backbone bands, grey the spacer bands and red the azo bands. Open and filled symbols indicate a $T_{eff}$ below and above the bulk $T_g$, respectively. **Right**: Molecular representation of $T_{eff}$ according to the color-coded scale.

the material, respectively, and in a color-coded molecular representation (bottom). When the band shifts upon illumination exceed those observed as a function of temperature, such as for the $NO_2$ vibration of pDR1A (see Figure 6.3D), the curve of the band shift as a function of temperature is extrapolated linearly. The behavior of the azo moiety (in red) under illumination is particularly striking. For the symmetric $NO_2$ vibration at about 1336 cm$^{-1}$, the effective temperature under illumination reaches 226 °C (160% higher than the temperature at which the illumination experiment was conducted, i.e. 40 °C) for pDR1A and 109 °C (120% higher than the bulk temperature) for gDR1. These enormous increases in $T_{eff}$ for the azobenzene moiety are confirmed by the corresponding values of 227 and 143 °C, respectively, obtained for the azobenzene aromatic ring deformation band at about 1105 cm$^{-1}$. Thus, the vibrational modes located near the azo chemical function, which, according to current understanding,[41] undergoes either rotation, inversion, concerted inversion or inversion-assisted rotation upon

photoisomerization, feel a molecular environment that, in terms of effective temperature, is equivalent to heating well above the bulk $T_g$ of the materials.

In sharp contrast to the azobenzene bands, the effective temperature upon illumination of the backbone bands remains identical to the bulk temperature, within experimental uncertainty, and is thus more than 30 °C below the bulk $T_g$ in both materials. The C=O groups in the spacers, in gray, present an intermediate behavior, with $T_{eff}$'s of 124 and 78 °C for pDR1A and gDR1, respectively, which are higher than the experimental isothermal 40 °C, but much less than for the azo groups. They are also higher than the bulk $T_g$ but by only 7 °C for gDR1. These values of $T_{eff}$ indicate that the local environment of the C=O groups is influenced even if they are relatively far from the photoisomerizing azo groups.

Since photoinduced mass transport during SRG patterning is reported to depend on the incident irradiance,[18, 24] the impact of illumination intensity on the effective temperature of the different molecular groups was also studied. As shown by Figure 6.6, the effective temperatures are intensity-dependent except for the backbones that do not show any discernible increase in $T_{eff}$ even at the highest intensity investigated (100 mW/cm$^2$). For the azobenzene and spacer groups, the increase in $T_{eff}$ as a function of intensity is not linear but seems to tend toward saturation. This observation is in line with the nonlinear increase in SRG diffraction efficiency as a function of irradiance.[24] It is also consistent with molecular dynamics simulations predicting saturation of the diffusion coefficient of a glass-forming host when a guest azobenzene undergoes high frequency photoisomerization at high intensities.[14] Moreover, the overall effective temperatures are systematically lower, at all irradiances, for gDR1 than for pDR1A. This difference could originate from the hydrogen-bonded network formed by these molecules.[42-43] As shown in Figure 6.S5, these noncovalent interactions remain intact upon illumination, providing still more evidence that cooperative motions of repeat units (for polymers) or complete molecules (for molecular glasses) are not directly affected by photoisomerization. The hydrogen bonds in gDR1 appear to restrict the mobility of the chemical groups, and thus the extent of the photoinduced changes in molecular environment, to a greater extent than the van der Waals interactions among pDR1A side chains.

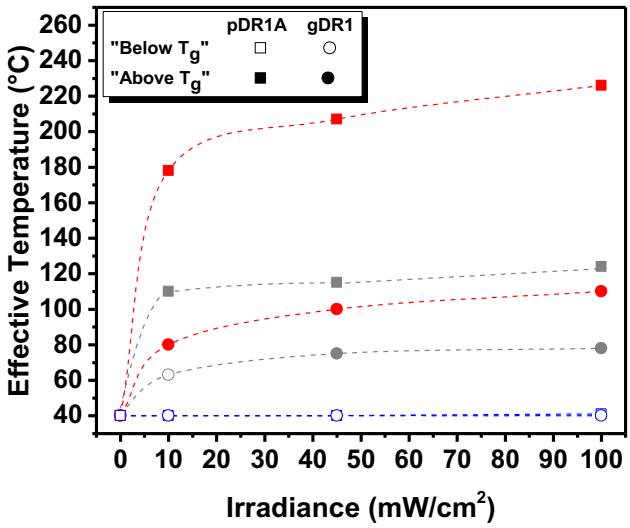


**Figure 6.6.** Influence of the 520 nm irradiance on the effective temperature of bands associated with the backbone (blue), spacer (gray) and azo (red) moieties of pDR1A and gDR1 (the $NO_2$ symmetric stretching was chosen as the representative band for the azo moiety). Dashed lines are guides to the eye.

The inhomogeneous distribution of effective temperature under irradiation can be mapped on the structures of gDR1 and pDR1A according to a color-coded scale, as shown in Figure 6.5 (bottom). It illustrates the creation of submolecular areas with higher mobility (higher $T_{eff}$), as previously hypothesized to explain the photoinduced diffusion and modification of mechanical properties in azomaterials.[14-15, 22-23] Thus, amorphous azo-containing materials under illumination present the properties of both glassy (backbone) and fluid-like (spacer and azo moieties) materials below their bulk $T_g$. This combination of characteristics generated in the "photomobile" state of azo-containing materials is in agreement with simulations by Accary and Teboul that suggested the appearance of soft regions around photoisomerizing azobenzenes dispersed in a more viscous glassy material.[14]

It is noteworthy that these results were obtained for bulk three-dimensional thin films and thus complement the results of Fang *et al.*[22] and Hurduc *et al.*[21], who studied similar phenomena (although not at the submolecular scale) in self-assembled monolayers and at the surface of the material, respectively, where the diffusion rate is already orders of magnitude

faster than in the bulk, making it more difficult to clearly dissociate photoinduced fluidity from the intrinsic fluidity of the materials.[44]

The significance of this experimental demonstration of a heterogeneous generation of photoinduced free volume around specific molecular moieties, as revealed by their larger relative increase in $T_{eff}$ under illumination, resides in the fact that it helps to account for a wide array of puzzling photoinduced phenomena involving azo-containing materials at scales ranging from molecular to macroscopic. Our experimental results relate to some early conclusions made in the 1990s by Kumar *et al.* on the plasticizing effect of light on azopolymers during SRG writing[45] and also to the creation of free volume upon isomerization of azobenzenes reported by Bauer-Gogonea *et al*.[40] It also supports the very recently reported vaporization of liquid water by Fujiwara and Imura upon photoisomerization of azobenzene-modified anodized alumina filtration membranes:[46] these authors proposed that low density areas, created upon photoisomerization, correspond to low-pressure zones that facilitate the evaporation and transport of water molecules across the membrane. These low-pressure zones could also support the hypothesized worm-like (directional along the main molecular axis) diffusion motion, first proposed by Lefin and Nunzi,[47] and further developed by Juan *et al.* to account for polymer motion both during SRG formation[48] and under nanoplasmonic fields.[8] Based on the results, one can further anticipate that, as long as the photochemistry of the azobenzene group is preserved, increasing the bulkiness of the azobenzene substituent should increase the effective temperature gradient along the molecule and favor phototransport by creating a larger fraction of free volume under irradiation. This hypothesis is consistent with the experimental evidence showing that greater bulkiness of azo groups increases their SRG forming capacity.[49] Moreover, a local increase of free volume near the azo moiety could account more realistically for the modification of the material's mechanical properties, by opposition to a truly fluid-like state reached upon illumination.[20] Indeed, a true liquid-like state must not be reached at any point during photoprocessing; if so, it would lead to the erasure of the light-written pattern due to fast relaxation of the material. In contrast, a submolecular free volume gradient, as suggested in the present work, can account both for light-induced motion and for its temporal stability.

## 6.5 Conclusion

We have shown by IR spectroscopy that the sub-$T_g$ illumination of amorphous azomaterials, both polymers (pDR1A) and molecular glasses (gDR1), provokes changes in local environment that are highly heterogeneous at the submolecular scale. To quantify these relative changes, the concept of an effective temperature ($T_{eff}$) was introduced, corresponding to the bulk temperature to which the chemical group in question must be heated in order to reproduce the IR band shift measured under illumination. The change in local environment of the azo moiety upon photoisomerization corresponds to an increase in $T_{eff}$ of up to nearly 200 °C while, in sharp contrast, the local environment of the backbone does not change at all. On the basis of the similarity of the band shifts upon heating and under illumination, two processes known to introduce additional free volume in amorphous (azo)materials, the results are interpreted as evidence for a submolecular gradient of photoinduced free volume. Meanwhile, the bulk $T_g$ of the materials remains unaffected by illumination, at least up to an intensity of 100 mW/cm$^2$, highlighting that the mechanism leading to the photomobile state, which allows macroscopic motion in azomaterials, is inherently different from the fluidization of the material occurring upon heating above its $T_g$. The experimental observation of a heterogeneous distribution of $T_{eff}$ in individual molecules complements the existing evidence for mechanical property modifications under irradiation and offers a general molecular-level picture for how light enables these photoresponsive materials to move remarkable distances at temperatures well below their $T_g$. The IR method presented here could also be used as a submolecular probe of molecular environment perturbations under the application of various other external stimuli, such as electric or magnetic fields, thus broadening the interest of this label-free approach.

## 6.6 Acknowledgments

This work was supported by grants from the Fonds de Recherche du Québec – Nature et Technologies (FRQNT) and from the Natural Sciences and Engineering Research Council (NSERC) of Canada. JV is grateful to Emil Aaltonen Foundation, Finnish Cultural Foundation, and FRQNT for postdoctoral grants. AL thanks NSERC for a Vanier graduate scholarship.

## 6.7 References


1. Lee, S.; Kang, H. S.; Park, J. K., *Adv. Mater.* **2012,** *24*, 2069-103.
2. Priimagi, A.; Shevchenko, A., *J. Polym. Sci., Part B: Polym. Phys.* **2014,** *52*, 163-182.
3. Morikawa, Y.; Kondo, T.; Nagano, S.; Seki, T., *Chem. Mater.* **2007,** *19*, 1540-1542.
4. Haggui, M.; Dridi, M.; Plain, J.; Marguet, S.; Perez, H.; Schatz, G. C.; Wiederrecht, G. P.; Gray, S. K.; Bachelot, R., *ACS Nano* **2012,** *6*, 1299-307.
5. Hubert, C., et al., *Nano Lett.* **2005,** *5*, 615-9.
6. Cowie, J. M. G.; Arrighi, V., *Polymers: Chemistry and Physics of Modern Materials*. 3rd ed.; Taylor & Francis: Boca Raton, FL, USA, 2007.
7. Ambrosio, A.; Marrucci, L.; Borbone, F.; Roviello, A.; Maddalena, P., *Nat. Commun.* **2012,** *3*, 989.
8. Juan, M. L.; Plain, J.; Bachelot, R.; Royer, P.; Gray, S. K.; Wiederrecht, G. P., *ACS Nano* **2009,** *3*, 1573-9.
9. Saphiannikova, M.; Toschevikov, V.; Ilnytskyi, J., *Nonlinear Optics Quantum Optics* **2009,** *41*, 27-57.
10. Baroncini, M., et al., *Nat. Chem.* **2015,** *7*, 634-40.
11. Singleton, T. A.; Ramsay, K. S.; Barsan, M. M.; Butler, I. S.; Barrett, C. J., *J. Phys. Chem. B* **2012,** *116*, 9860-5.
12. Naito, T.; Horie, K.; Mita, I., *Polymer* **1993,** *34*, 4140-4145.
13. Sekkat, Z.; Kleideiter, G.; Knoll, W., *J. Opt. Soc. Am. B* **2001,** *18*, 1854.
14. Accary, J. B.; Teboul, V., *J. Chem. Phys.* **2013,** *139*, 034501.
15. Teboul, V.; Saiddine, M.; Nunzi, J. M.; Accary, J. B., *J. Chem. Phys.* **2011,** *134*, 114517.
16. Tanchak, O. M.; Barrett, C. J., *Macromolecules* **2005,** *38*, 10566-10570.
17. Yager, K. G.; Tanchak, O. M.; Godbout, C.; Fritzsche, H.; Barrett, C. J., *Macromolecules* **2006,** *39*, 9311-9319.
18. Barrett, C. J.; Natansohn, A. L.; Rochon, P. L., *J. Phys. Chem.* **1996,** *100*, 8836-8842.
19. Yu, Y.; Nakano, M.; Ikeda, T., *Nature* **2003,** *425*, 145.
20. Karageorgiev, P.; Neher, D.; Schulz, B.; Stiller, B.; Pietsch, U.; Giersig, M.; Brehmer, L., *Nat. Mater.* **2005,** *4*, 699-703.

21. Hurduc, N.; Donose, B. C.; Macovei, A.; Paius, C.; Ibanescu, C.; Scutaru, D.; Hamel, M.; Branza-Nichita, N.; Rocha, L., *Soft Matter* **2014,** *10*, 4640-7.
22. Fang, G. J.; Maclennan, J. E.; Yi, Y.; Glaser, M. A.; Farrow, M.; Korblova, E.; Walba, D. M.; Furtak, T. E.; Clark, N. A., *Nat. Commun.* **2013,** *4*, 1521.
23. Teboul, V.; Saiddine, M.; Nunzi, J. M., *Phys. Rev. Lett.* **2009,** *103*, 265701.
24. Kirby, R.; Sabat, R. G.; Nunzi, J. M.; Lebel, O., *J. Mater. Chem. C* **2014,** *2*, 841-847.
25. Griffiths, P. R.; De Haseth, J. A., *Fourier Transform Infrared Spectrometry*. 2nd ed.; John Wiley & Sons: Hoboken, NJ, 2007.
26. Rochon, P.; Batalla, E.; Natansohn, A., *Appl. Phys. Lett.* **1995,** *66*, 136-138.
27. Brown, D.; Natansohn, A.; Rochon, P., *Macromolecules* **1995,** *28*, 6116-6123.
28. Loucif-Saibi, R.; Nakatani, K.; Delaire, J. A.; Dumont, M.; Sekkat, Z., *Chem. Mater.* **1993,** *5*, 229-236.
29. Barrett, C.; Natansohn, A.; Rochon, P., *Macromolecules* **1994,** *27*, 4781-4786.
30. Chalmers, J. M., Mid-infrared Spectroscopy of the Condensed Phase. In *Handbook of Vibrational Spectroscopy*, Griffiths, P. R.; Chalmers, J. M., Eds. John Wiley & Sons: Chichester, 2001; pp 128-140.
31. Buffeteau, T.; Lagugné Labarthet, F.; Pézolet, M.; Sourisseau, C., *Macromolecules* **1998,** *31*, 7312-7320.
32. Buffeteau, T.; Pézolet, M., *Appl. Spectrosc.* **1996,** *50*, 948-955.
33. Labarthet, F. L.; Freiberg, S.; Pellerin, C.; Pézolet, M.; Natansohn, A.; Rochon, P., *Macromolecules* **2000,** *33*, 6815-6823.
34. Dluhy, R. A.; Mendelsohn, R.; Casal, H. L.; Mantsch, H. H., *Biochemistry* **1983,** *22*, 1170-1177.
35. Nabet, A.; Auger, M.; Pézolet, M., *Appl. Spectrosc.* **2000,** *54*, 948-955.
36. Tashiro, K.; Yoshioka, A., *Macromolecules* **2002,** *35*, 410-414.
37. Wolkers, W. F.; Oldenhof, H.; Alberda, M.; Hoekstra, F. A., *Biochim. Biophys. Acta* **1998,** *1379*, 83-96.
38. Ferry, J. D., *Viscoelastic Properties of Polymers*. 3rd ed.; John Wiley & Sons: New York, NY, 1980.
39. Hannon, M. J.; Koenig, J. L., *J. Polym. Sci. Part A-2-Polym. Phys.* **1969,** *7*, 1085-&.

40. Bauer-Gogonea, S.; Bauer, S.; Wirges, W.; Gerhard-Multhaupt, R., *J. Appl. Phys.* **1994,** *76*, 2627.
41. Bandara, H. M.; Burdette, S. C., *Chem. Soc. Rev.* **2012,** *41*, 1809-25.
42. Wang, R. Y.; Pellerin, C.; Lebel, O., *J. Mater. Chem.* **2009,** *19*, 2747-2753.
43. Laventure, A.; Soldera, A.; Pellerin, C.; Lebel, O., *New J. Chem.* **2013,** *37*, 3881-3889.
44. Zhu, L.; Brian, C. W.; Swallen, S. F.; Straus, P. T.; Ediger, M. D.; Yu, L., *Phys. Rev. Lett.* **2011,** *106*, 256103.
45. Kumar, J.; Li, L.; Jiang, X. L.; Kim, D. Y.; Lee, T. S.; Tripathy, S., *Appl. Phys. Lett.* **1998,** *72*, 2096-2098.
46. Fujiwara, M.; Imura, T., *ACS Nano* **2015,** *9*, 5705-12.
47. Lefin, P.; Fiorini, C.; Nunzi, J.-M., *Pure Appl. Opt.* **1998,** *7*, 71-82.
48. Juan, M. L.; Plain, J.; Bachelot, R.; Royer, P.; Gray, S. K.; Wiederrecht, G. P., *Appl. Phys. Lett.* **2008,** *93*, 153304.
49. Goulet-Hanssens, A.; Corkery, T. C.; Priimagi, A.; Barrett, C. J., *J. Mater. Chem. C* **2014,** *2*, 7505-7512.

## 6.8 Supporting information

**Table 6.S1.** Assignment of the pDR1A and gDR1 vibrational modes studied.

| | **pDR1A** | | **gDR1** | | **Reference** |
|---|---|---|---|---|---|
| | **Band ($cm^{-1}$)** | **Assignment** | **Band ($cm^{-1}$)** | **Assignment** | |
| **Backbone** | 2931 | $CH_2$ asymmetric stretching* | 2970 | $CH_3$ (aromatic) stretching | 1 |
| | 1275 | CH twisting | 1586 | Triazine ring stretching | 1 |
| **Spacer** | 1734 | C=O stretching | 1713 | C=O stretching | 2, 3 |
| **Azo** | 1337 | $NO_2$ symmetric stretching | 1335 | $NO_2$ symmetric stretching | 1, 3 |
| | 1105 | Ring deformation | 1104 | Ring deformation | 4 |

* May contain a contribution from the $CH_2$ groups from the spacer.

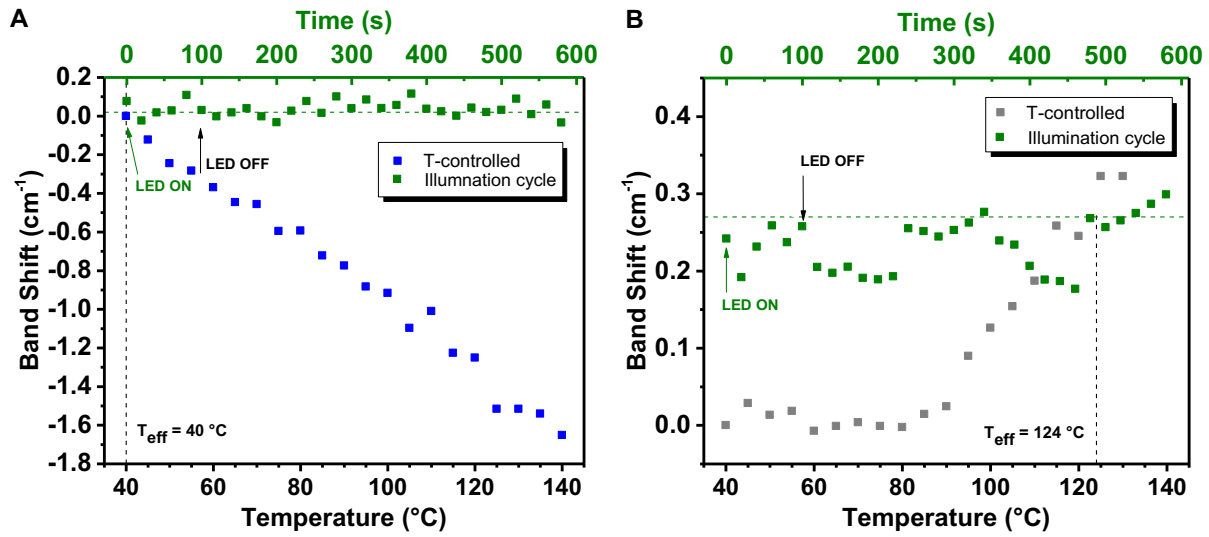


**Figure 6.S1.** Procedure for determining the effective temperature ($T_{eff}$) of chemical groups by comparison of the IR band shifts under illumination cycles at 40 °C (green) and in the dark during temperature (T)-controlled ramps (see text for details). Shown here for **pDR1A** bands for A) the backbone (1275 $cm^{-1}$ CH twisting) and B) the spacer (1714 $cm^{-1}$ C=O stretching).

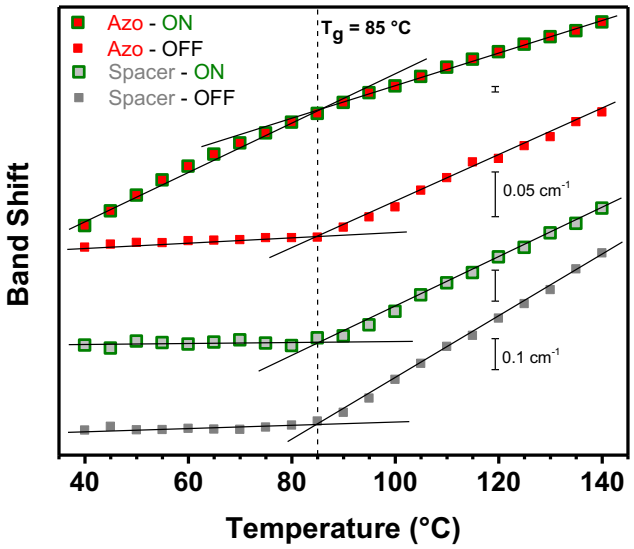


**Figure 6.S2.** Band shifts (grey: spacer C=O stretching; red: azo $NO_2$ symmetric stretching) of **pDR1A** as a function of temperature on cooling without and under illumination (symbols without and with green edges, respectively) at 520 nm using an irradiance of 100 $mW/cm^2$. The change in slope corresponds to the $T_g$ of the material as determined by DSC.

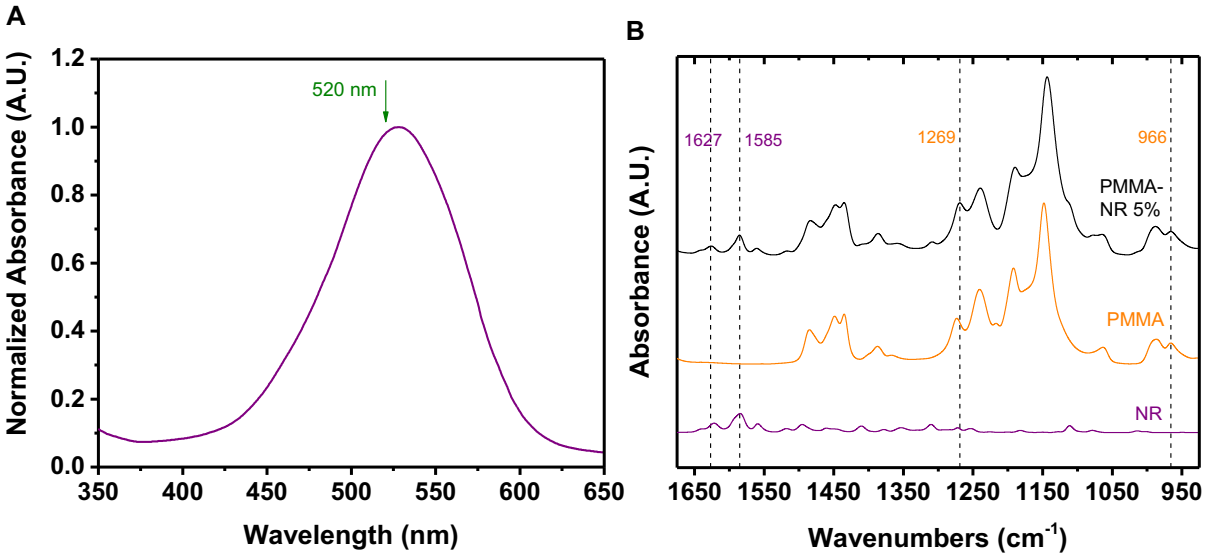


**Figure 6.S3.** A) UV-visible absorption spectrum of a thin film of 5 wt% Nile Red dispersed in PMMA. B) IR spectra of PMMA, Nile Red (NR), and 5 wt% Nile Red in PMMA drop-cast from $CHCl_3$ showing the selected vibrational modes for IR studies.

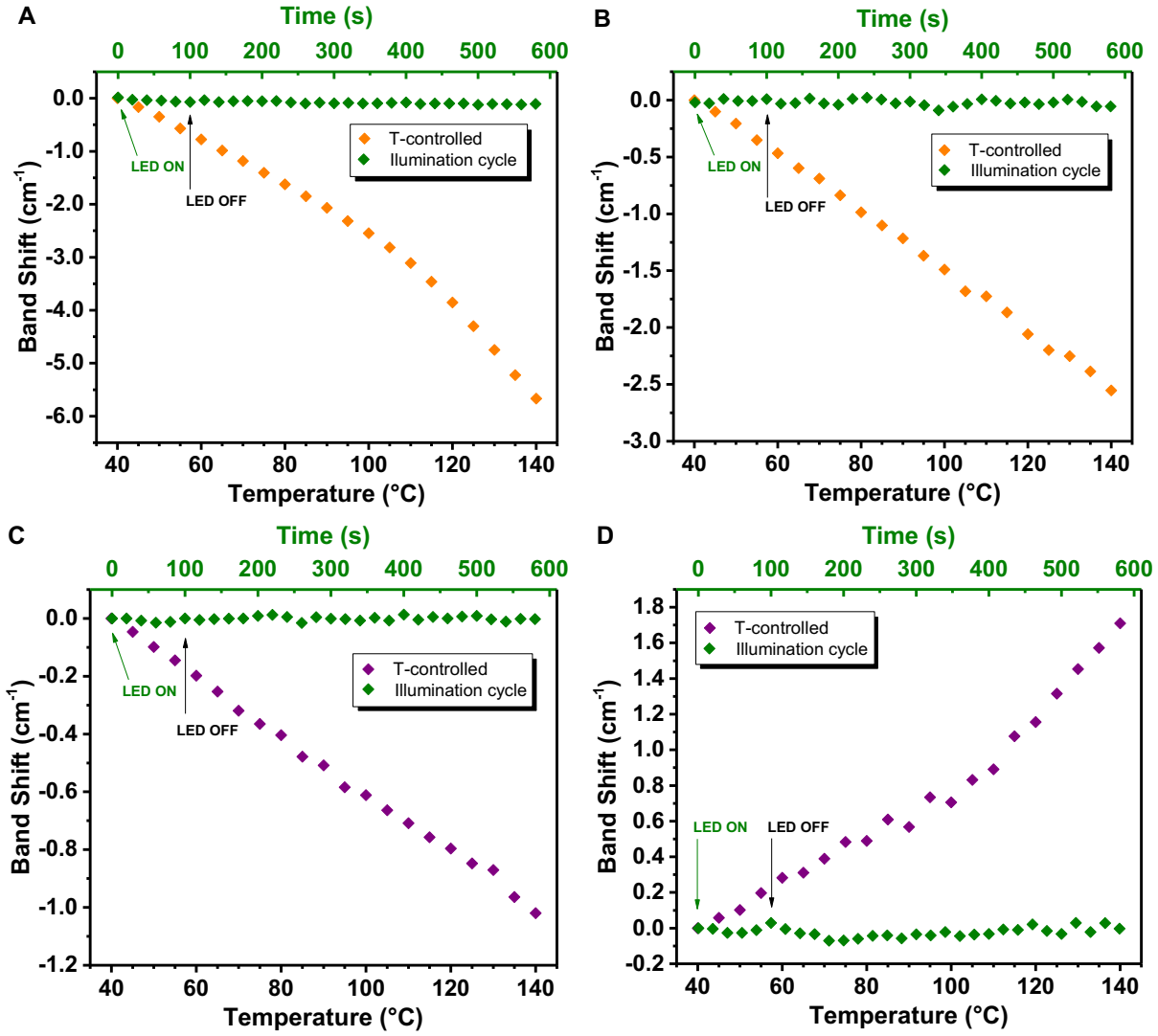


**Figure 6.S4.** IR band shifts under illumination cycles at 40 $^{o}$C (green) and in the dark during temperature (T)-controlled ramps for the 5 wt% Nile Red in PMMA. Examples are shown for PMMA bands (orange) at A) 1268 cm$^{-1}$ and B) 966 cm$^{-1}$, and Nile Red bands (violet) at C) 1586 cm$^{-1}$ and D) 1627 cm$^{-1}$.

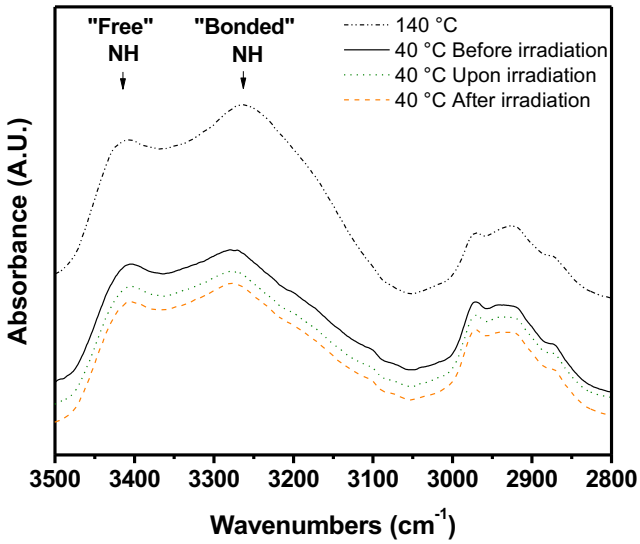


**Figure 6.S5.** Comparison of the NH stretching region of **gDR1** upon heating, and before, under and after irradiation at 520 nm (100 mW/cm$^2$). No significant difference is observed under irradiation, in contrast to when the temperature is changed, suggesting that azo photoisomerization does not change the H-bonded state of **gDR1**.

*References*


1. Socrates, G., *Infrared and Raman Characteristic Group Frequencies: Tables and Charts*. 3rd ed.; John Wiley & Sons: Chichester, England, 2004.
2. Buffeteau, T.; Pézolet, M., *Appl. Spectrosc.* **1996,** *50*, 948-955.
3. Buffeteau, T.; Lagugné Labarthet, F.; Pézolet, M.; Sourisseau, C., *Macromolecules* **1998,** *31*, 7312-7320.
4. Labarthet, F. L.; Freiberg, S.; Pellerin, C.; Pézolet, M.; Natansohn, A.; Rochon, P., *Macromolecules* **2000,** *33*, 6815-6823.

# Chapitre 7: Photoactive/passive molecular glass blends: an efficient strategy to optimize azomaterials for surface relief grating inscription*

## 7.1 Abstract


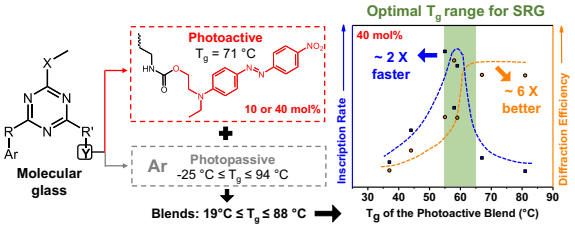


Irradiation of azomaterials causes various photophysical and photomechanical effects that can be exploited for the preparation of functional materials such as surface relief gratings (SRGs). Herein, we develop and apply an efficient strategy to optimize the SRG inscription process by decoupling, for the first time, the important effects of the azo content and glass transition temperature ($T_g$). We prepare blends of a photoactive molecular glass functionalized with the azo Disperse Red 1 (gDR1) with a series of analogous photopassive molecular glasses. Blends with 10 and 40 mol% of gDR1 are completely miscible, present very similar optical properties, and cover a wide range of $T_g$ from below to well above ambient temperature. SRG inscription experiments show that the diffraction efficiency (DE), residual DE and initial inscription rate reach a maximum when $T_g$ is 25-40 °C above ambient temperature for low to high azo content, respectively. Indeed, for a fixed 40 mol% azo content, choosing the optimal $T_g$ enables doubling the SRG inscription rate and increasing DE 6-fold. Moreover, a higher azo content enables higher DE for a similar $T_g$. Spectroscopy measurements indicate that the photo-orientation of DR1 and its thermal stability are maximal with $T_g$ around 70 °C, independent of the azo content. We conclude that the SRG potential of azomaterials depends on their capability to photo-orient but that the matrix rigidity eventually limits the inscription kinetics, leading to an optimal $T_g$ that depends on the azo


---

* Publié en tant qu'article dans *ACS Applied Materials & Interfaces:* Laventure, A.; Bourotte, J.; Vapaavuori, J.; Karperien, L.; Sabat, R.G.; Lebel, O.; Pellerin, C. *ACS Appl. Mater. Interfaces*, **2017**, *9*, 798-808. J.B. a réalisé les manipulations préliminaires; J.V. a exécuté les mesures de spectroscopie UV-visible et PM-IRSAS; L.K. a inscrit les réseaux de diffraction. O.L. a procédé à la synthèse des composés.

content. This study exposes clear material design guidelines to optimize the SRG inscription process and the photoactivity of azomaterials.

## 7.2 Introduction

Azobenzene (azo) derivatives are well-known to undergo repetitive *trans* to *cis* photoisomerizations that lead to photoinduced motion at length scales ranging from molecular to macroscopic. Azo-containing compounds are used in a wide range of applications, from light-controlled artificial molecular machines to photonic devices,[1-3] but the details of their photomechanical response are not yet completely understood. In particular, it is still unclear how their molecular-scale *trans-cis-trans* photoisomerization can be translated into macroscopic motion at temperatures well below the bulk glass transition temperature ($T_g$) where cooperative segmental motion of amorphous materials is extremely slow. This phenomenon, called photomobility, is notably encountered during the inscription of surface relief gratings (SRGs), a process first reported in 1995[4,5] where a polarized light interference pattern creates a topological relief on azo-containing films. Contradictory theories and hypotheses have been proposed to tentatively explain this athermal mass transport, including a decrease of modulus and viscosity under illumination (photofluidization),[6-8] a directional worm-like diffusion motion,[9] a pressure gradient caused by the volume difference between the *trans* and *cis* isomers,[10] and a reorientation approach[11] where the stress created by the photo-orientation of the azo moieties is larger than the yield stress of the material and thus allows its deformation without involving its photosoftening.[12] Some recent experimental[13] and computational[14-16] studies have confirmed that the *trans-cis* isomerization induces changes in the chromophore's molecular environment, either by creating additional free volume and/or by pushing the surrounding molecules in a cage-breaking process, which impacts the material motion potential.

In addition to the above-mentioned works, many efforts have been invested to optimize the SRG formation process by defining the role of different tunable experimental parameters,[17-20] such as the azo content and its molecular structure, the $T_g$ of the matrix and its molecular weight, the thickness of the film, the polarization of the inscribing and probe laser beams, and the inscription temperature. Different systems were studied: azopolymers or amorphous molecular azomaterials where the azo is covalently bonded as a side-chain or is part of the main

chain,[17, 21-22] photopassive polymers doped with azo derivatives,[23] and supramolecular complexes in which azo molecules are bonded in a noncovalent fashion to a photopassive polymer through hydrogen,[24] halogen[25] or ionic bonding[26-27]. While these systems provide useful insight on the SRG process, they do not allow us to clearly disentangle the respective influences of $T_g$ and azo content. Indeed, changing the azo content usually affects the $T_g$ and the molecular weight of the system and, in the case of azopolymers and supramolecular polymer complexes, the entanglement density and chain rigidity. Similarly, tuning the $T_g$ of azomaterials while keeping the azo content fixed necessitates using different host polymer matrices or synthesizing different azopolymers, which inevitably involves variation of the above-mentioned interdependent characteristics and blurs the source of the SRG performance and inscription efficiency. Some trends are already known concerning the effects of azo content and temperature; e.g., using a higher azo content increases diffraction efficiency (DE), while a higher inscription temperature relative to $T_g$ decreases DE, inscription kinetics, and stability of SRGs due to more important thermal relaxation.[21-22, 28-32] Nevertheless, probing the influence of the $T_g$ and azo content parameters individually remains a major challenge.

Lebel and co-workers have recently synthesized a molecular glass functionalized with the azo Disperse Red 1 (DR1), gDR1, and demonstrated that it is an efficient SRG (see Figure 4b in ref 33 for a representative atomic force microscopy image) and nanoscale surface patterning material.[33-35] Such azo-containing molecular glasses, which are small organic molecules that easily form a long-lived amorphous phase (avoiding the risk of azo crystallization), open a new avenue to study independently the impact of $T_g$ and azo content on the photoactivity of azomaterials such as their photoinduced orientation/birefringence and their photomobility. In particular, by blending photoactive gDR1 with a library of its photopassive structural analogues, we are able to tune the $T_g$ of the resulting photoactive blends from below to well above room temperature while keeping the azo content constant. Our approach innovates by presenting several advantages over other systems used to study the temperature dependence of SRG inscription. First, using molecular glasses for the photoactive and passive components eliminates dispersity issues and large differences in molecular weight (and entanglement density in the case of polymers) between the compared materials.[36] Second, it allows tuning the relative inscription temperature more easily than by modifying the experimental temperature, which

requires adding a low pressure chamber on the setup to avoid air turbulence at high temperatures[29] or even water vapor condensation at low temperatures. Third, the same azo chromophore is used in all the experiments, ensuring extremely similar optical properties and photoactivity for all blends, by opposition to systems comparing azo substituents that differ in size and/or electronic properties.[37-38] Finally, the structural similitude between gDR1 and all the photopassive molecular glasses favors similar intermolecular interactions and molecular-level miscibility which are difficult to reproduce with polymer/azopolymer blends and with polymer/azo blends or complexes.

This systematic approach was used to prepare two series of seven amorphous blends containing 10 or 40 mol% of gDR1, respectively, and presenting $T_g$'s from 19 to 88 °C. Our results reveal that a $T_g$ 25-40 °C above ambient temperature is optimal to produce SRGs with the fastest inscription kinetics and with the highest maximal and residual DE. When $T_g$ is below the optimal value, thermal relaxation competes with photoinduced motion and leads to low DE. When $T_g$ is higher than the optimal range, DE values plateau for the 40 mol% blends and decrease for the 10 mol% blends. Time-resolved polarized infrared spectroscopy[39] revealed that this optimal $T_g$ range results from a compromise between (i) the photo-orientation capability of the chromophore, which enables higher saturated DE and is optimal when $T_g$ is 50 °C above ambient temperature, and (ii) the higher resistance to motion of high-$T_g$ matrices, as revealed by the residual orientation values, that limits the SRG inscription kinetics of the system and is especially important at low azo content. Our strategy of blending photoactive and photopassive glasses enabled reaching clear conclusions on the effects of $T_g$ and azo content on the photoactivity of azomaterials that are essential to optimize the SRG inscription process that, to our knowledge, would not have been possible using other approaches.

## 7.3 Experimental section

### 7.3.1 Materials

Compounds gDR1 and g-25 to g94 were synthesized according to literature procedures.[40-42] Blends with 10 and 40 mol% (molar percentages) of gDR1 with compounds g-

25 to g94 (B10%$_{Tg}$ and B40%$_{Tg}$) were prepared by mixing the appropriate volume of their respective stock solutions in $CH_2Cl_2$.

### 7.3.2 Characterization

For differential scanning calorimetry (DSC) analyses, droplets of the blend solutions were directly deposited in DSC pans to generate approximately 2.5 mg samples before letting the solvent evaporate under a fume hood for 3-4 h and then under vacuum for 24 h before closing the pans with their lid. DSC measurements were conducted with a PerkinElmer DSC 8500 calorimeter, calibrated with indium, using a heating rate of 10 °C/min. The $T_g$'s were determined, after an initial cycle of heating and cooling at 10 °C/min, as the average half-height of the heat capacity jump in the second and third heating scans. UV−visible spectra of samples spin-coated on clean glass substrates were recorded with an Ocean Optics USB2000+ spectrophotometer and a DH-mini light source. The minimal *cis* content under irradiation was estimated as the ratio of absorbance of the π-π* band (at 480 nm) of the films after 90 s of illumination with a nonpolarized 520 nm (35 mW/cm$^2$) LED light source (Prizmatix FC5-LED) to the initial absorbance of the band. The thermal relaxation half-life time of the *cis* isomer was determined by recording the absorbance at 480 nm during 300 s after switching off the LED source and fitting the data following the method of Barrett *et al*.[43] which consists of plotting $\ln(A_\infty - A_t)$ as a function of time, where $A_t$ and $A_\infty$ are the absorbance at time t and after relaxation, respectively.

Polarization modulation infrared structural absorption spectroscopy (PM-IRSAS) was used to measure photo-orientation of the DR1 moiety. This technique enables the simultaneous recording of transmission IR spectra polarized parallel (p) and perpendicular (s) to the laser polarization, in addition to their dichroic difference, and therefore provides time-resolved information about the photoinduced orientation *in situ* during the photo-orientation process.[39] Spectra with a 4 cm$^{-1}$ resolution were measured using a Bruker Optics Vertex 70 Fourier transform IR spectrometer coupled to a home-built setup[25] that includes a KRS-5 linear polarizer (Optometrics), a photoelastic modulator (PEM-90 type II/ZS50, Hinds Instruments) to switch the polarization of the IR beam from parallel to perpendicular at 100 kHz, and a liquid nitrogen-cooled photovoltaic mercury−cadmium−telluride (MCT) detector (Kolmar Technologies). A lock-in amplifier (Stanford Research Systems SR830) with a 30 μs time constant and electronic

filters (Frequency Devices 90TP/90IPB) were used to process the experimental signal and record simultaneously the parallel ($A_p$) and perpendicular ($A_s$) polarized IR spectra. The photo-orientation was induced by a 488 nm diode laser (JDSU FCD488-020) with a vertically-polarized output expanded to 7 mm (Thorlabs BE10M-A) to overfill the cross-section area of the IR probe beam. The resulting 18 mW/cm$^2$ beam was incident on the sample at an angle of 20° with respect to the IR probe. The orientation parameter, $<P_2>$, was calculated as $<P_2> = A_p - A_s / (A_p + 2 A_s)$.

### 7.3.3 SRG inscription

To write the SRGs, a Lloyd's mirror interferometer was used to produce the interference pattern from a frequency-doubled diode pumped Nd-$YVO_4$ laser source operating at 532 nm (Coherent Verdi V5), having an approximate irradiance of 230 mW/cm$^2$. The beam passed through a spatial filter, was collimated and then was made circularly polarized with the help of a quarter-wave plate, so that two contra-rotating interfering beams were impinging the sample. This configuration yields an interference pattern on the sample surface with rotating linear polarization orientation and permits maximum molecular orientation.[44] The first-order diffraction efficiency of a nonresonant beam, an *in situ* figure of merit of the efficiency of SRG formation (written at a constant 600 nm pitch for all SRGs in this work), was measured by aligning a Thorlabs low-power diode laser (405 nm) beam in the middle of the half-circle laser interference pattern. The probe laser was initially chopped with a mechanical chopper, and the first-order diffracted signal was attenuated with neutral density filters before being incident on a silicon photodiode. The photodiode signal was then measured with a lock-in amplifier (Stanford Research Systems SR830) and recorded on a computer. The diffraction efficiency (DE) was calculated by dividing the first order diffracted signal by the zeroth transmitted order through the sample.

## 7.4 Results and discussion

### 7.4.1 Thermal and optical properties

The structures of the photoactive azo glass (gDR1) and photopassive compounds (labeled as $gT_g$, where $T_g$ stands for the glass transition temperature of the photopassive glass)

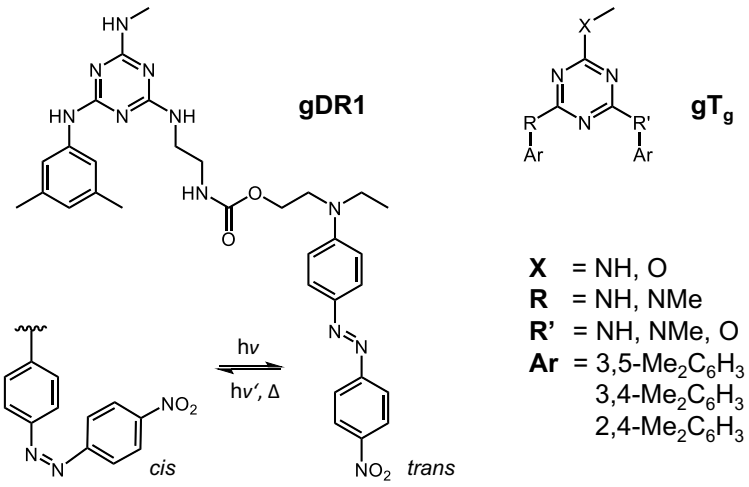


**Scheme 7.1.** Molecular structures of the photoactive (gDR1) and photopassive ($gT_g$) molecular glasses used to prepare the photoactive blends under study.

are shown in Scheme 7.1. The photoisomerization between the *trans* and *cis* isomers of the DR1 moiety is also illustrated. The headgroup (X), the linkers (R and R') on their 1,3,5-triazine core and their ancillary groups (Ar) are listed in Table 7.1 along with their respective glass transition temperatures ($T_g$). These seven photopassive molecular glasses were chosen for their high resistance to crystallization,[42] for their similar chemical structure to gDR1, and for their broad range of $T_g$ (between -25 and 94 °C) that enable preparing photoactive amorphous miscible blends with a $T_g$ from below to well above ambient temperature.

**Table 7.1.** Variable substituents and glass transition temperatures ($T_g$) of the photopassive ($gT_g$) and photoactive (gDR1) molecular glasses used to prepare the photoactive blends under study.

| $gT_g$ | X | R | R' | Ar | $T_g$ (± 1 °C) |
|---|---|---|---|---|---|
| **g94** | NH | NH | NH | 3,5-$Me_2C_6H_3$ | 94 |
| **g70** | NH | NH | NH | 3,4-$Me_2C_6H_3$ | 70 |
| **g54** | NH | NH | NH | 2,4-$Me_2C_6H_3$ | 54 |
| **g37** | O | NH | O | 3,5-$Me_2C_6H_3$ | 37 |
| **g21** | NH | NMe | NMe | 3,5-$Me_2C_6H_3$ | 21 |
| **g8** | O | NMe | O | 3,5-$Me_2C_6H_3$ | 8 |
| **g-25** | O | NMe | NMe | 3,5-$Me_2C_6H_3$ | -25 |
| **gDR1** | - | - | - | - | 71 |

Two series of blends were prepared with 10 or 40 mol% of gDR1 (noted B10% and B40%, respectively). The $T_g$ of these blends, determined using DSC with a scanning rate of 10 °C/min, are shown as a function of the $T_g$ of the photopassive matrix in Figure 7.1 (also listed in Table 7.S1 in Supporting Information (SI)). The $T_g$ of the blends increases smoothly with that of the photopassive glass and varies with blend composition. The $T_g$ of the B40% series blends spans from 37 to 81 °C (labeled as $B40\%_{37}$ to $B40\%_{81}$). Since the B10% blends contain a low fraction of azo, this series allows getting closer to the $T_g$ of the pure matrices, thus extending the accessible temperature range from 19 to 88 °C ($B10\%_{19}$ to $B10\%_{88}$). No crystallization (or melting) was observed in any of the DSC scans, confirming the completely amorphous state of the resulting blends. Furthermore, the presence of a single glass transition with a similar width (15-20 °C) as the pure compounds in the DSC scans of all blends indicates that no phase separation occurs between the photoactive and photopassive molecular glasses, thus ruling out the problems related to dye aggregation.

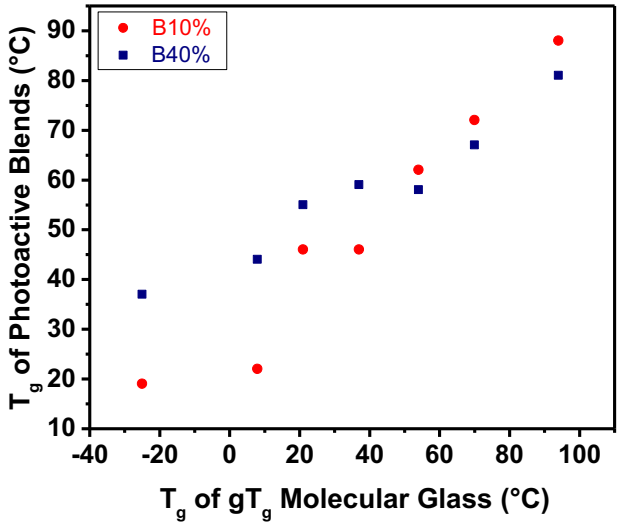


**Figure 7.1.** Evolution of $T_g$ (± 1 °C) of the photoactive B10% and B40% blends as a function of the $T_g$ (± 1 °C) of the photopassive compounds ($gT_g$).

Figure 7.2A shows the UV-visible spectra of spin-coated thin films of gDR1 and of the $B10\%_{19}$, $B10\%_{88}$ and $B40\%_{58}$ blends. The spectra of the blends are all superimposed, leading to the conclusion that their $T_g$ and azo content do not influence their absorption properties, at least in the studied ranges, and demonstrating the advantages of our blending strategy to ease the

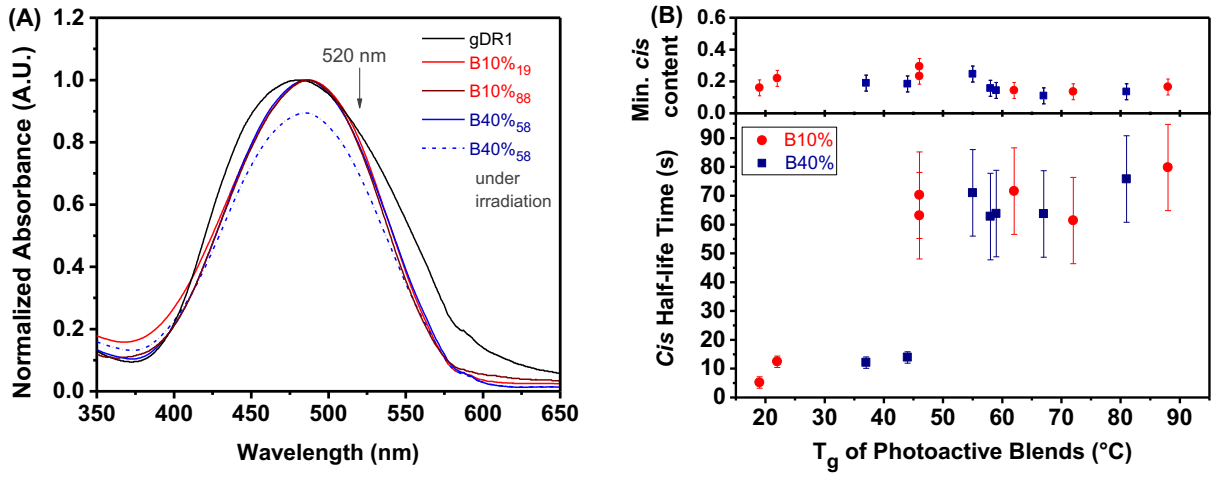


**Figure 7.2.** A) UV-visible spectra of pure gDR1, B10% blends with g94 and g-25 ($B10\%_{88}$, $B10\%_{19}$) and B40% with g54 ($B40\%_{58}$). The spectrum of $B40\%_{58}$ upon irradiation at 520 nm is also shown. B) Top panel: minimal *cis* content of the azo moiety of gDR1 blends as a function of their $T_g$. Bottom panel: *cis* isomer half-life time of the azo moiety of gDR1 blends as a function of the $T_g$ photoactive blends.

comparison between samples. The wavelength of maximal absorbance of the π-π* band is slightly red-shifted for the blends (~487 nm) compared to pure gDR1 (~480 nm) and its width is smaller for the blends, two indications showing that the DR1 chromophores are well isolated from each other in the blends and avoid forming aggregated stacks that lead to excitonic coupling as observed in the spectrum of pure gDR1.[45] As a consequence, these blends enable studying more specifically the impact of $T_g$ and azo content on photoactivity (SRG inscription and photoinduced orientation) since the photoisomerization of the DR1 moiety should not be affected by different degrees of coupling between adjacent chromophores.

Samples were irradiated with an unpolarized 520 nm LED source, followed by thermal relaxation, in order to study the influence of $T_g$ on the minimal *cis* content under photostationary state and on the *cis* half-life time. The spectrum of $B40\%_{58}$ under irradiation is shown as a representative example in Figure 7.2A. The decrease of absorbance of the π-π* band under illumination is attributed to the photoinduced formation of *cis* isomers and is used to estimate the minimal *cis* content under irradiation. When the light is turned off, the absorbance recovers

gradually and allows estimating the *cis* isomer half-life time. These values are plotted as a function of the $T_g$ of the blends in Figure 7.2B. The minimal *cis* content under illumination (upper panel) does not vary significantly with $T_g$ or azo content, with an average of 0.15 ± 0.05 for both B10% and B40% series. This relatively small *cis* isomer content is explained by the fact that the 520 nm irradiation excites both the *trans* π-π* and the *cis* n-π* bands and thus leads to rapid *trans*-*cis*-*trans* isomerization cycles, which is required for efficient SRG inscription.[46] On the other hand, the *cis* half-life time (lower panel) does increase with the $T_g$ of the photoactive blends for both series, starting around 5 s for the lowest $T_g$ blends and increasing suddenly to reach a plateau on the order of 70 s when $T_g$ is around 50 °C or higher. This increase in *cis* half-life time reflects the difference between a viscous and a glassy state, in which the thermal *cis*-*trans* isomerization rate is presumably slowed down because less free volume is available in the material for the transition to occur. Interestingly, this result is in contradiction with the larger rate constant reported by Nakano *et al.*[21] for high $T_g$ amorphous films ($T_g$ = 97 °C, k = 0.020 $min^{-1}$) of azo-containing molecular glasses compared to lower $T_g$ ones ($T_g$ = 27 °C, k = 0.006 $min^{-1}$) when measured at 30 °C. In our case, the capability of the matrix to hydrogen (H)-bond with the *cis* isomer may explain the longer *cis* half-life time. Indeed, the long *cis* lifetimes are observed for the high-$T_g$ blends where the matrix glass contains at least one H-bond donating group while the short lifetimes are observed for the low-$T_g$ blends where the matrix does not contain H-bond donating groups. The fact that the minimal *cis* content under irradiation is similar for all blends indicates that the *cis* isomers cannot accumulate in spite of their longer thermal relaxation lifetime and may be explained by hydrogen bonding of the matrix with the *trans* isomer of DR1.

### 7.4.2 Surface relief grating formation

Figure 7.3 shows the first-order diffraction efficiency (DE) as a function of writing time during the inscription of SRGs at 532 nm (close to the 520 nm irradiation used in the UV-visible experiments) for the B40% (Figure 7.3A) and B10% (Figure 7.3B) series. They will be referred to as the SRG inscription curves. Besides the curve shape *per se*, various information can be extracted from these inscription curves: (1) the DE reached after 100 or 1000 s of illumination, (2) the initial rate of SRG inscription, and (3) the residual DE after the laser is turned off. All of them will be discussed in relation to the $T_g$ of the blends and the azo content.

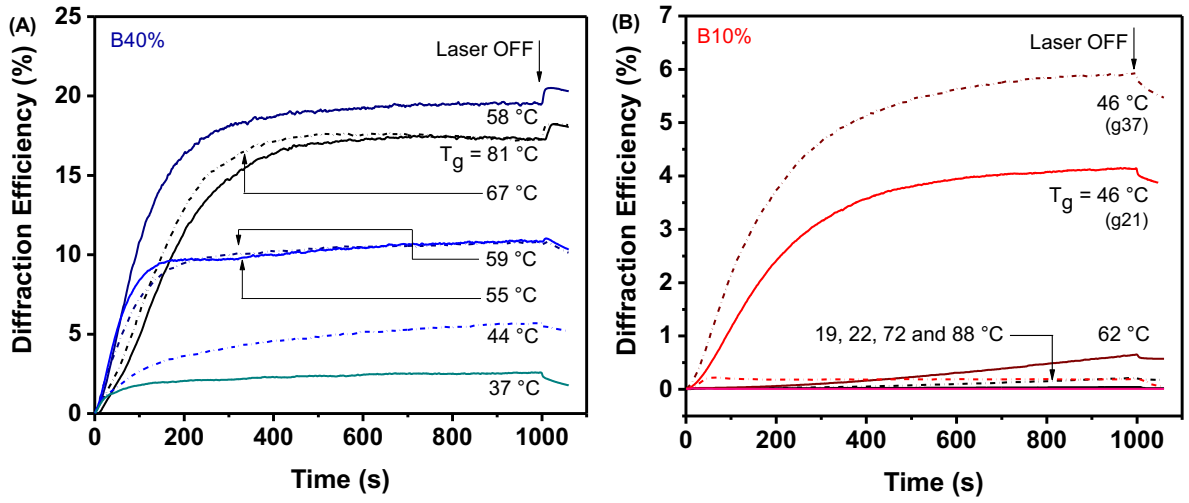


**Figure 7.3.** Diffraction efficiency (DE) as a function of time during the inscription of surface relief gratings for the B40% (A) and B10% (B) blends. Glass transition temperatures ($T_g$) of the photoactive blends are indicated for each inscription curve. Since two samples from the B10% series have the same $T_g$, the photopassive glass used as their matrix is indicated in parentheses below the $T_g$ of the blends. An enlargement of the low DE inscription curves for the B10% samples with $T_g$'s below 46 °C and above 62 °C is shown in Figure 7.S1 in SI.

As shown in Figure 7.3A, the shape of the SRG inscription curves is similar for all the B40% blends. The DE increases rapidly during the first 100 s before slowing down and reaching a pseudoplateau. The filled blue squares in Figure 7.4 represent the DE reached after 1000 s of irradiation ($DE_{1000}$, which is or is close to the maximal DE reached during the inscription) as a function of $T_g$ for the B40% series. The $DE_{1000}$ increases with $T_g$, starting around 2.5 % for the lowest $T_g$ sample $B40\%_{37}$ and reaching a plateau of ~18 % for blends with a $T_g$ higher than 60 °C. In contrast with the B40% series, the SRG inscription curves of the B10% samples do not all present the same shape (Figure 7.3B). Only the two $B10\%_{46}$ samples have inscription curves similar to those of the B40% series and reach high $DE_{1000}$, while the inscription curves of the other B10% samples with both lower and higher $T_g$ are too low to be clearly visible in Figure 7.3B. A close-up provided in Figure 7.S1 of the SI shows that an induction period precedes a slow SRG growth for high $T_g$ blends. In contrast, for lower $T_g$ blends, transient and partially transient (phase and birefringence, respectively) gratings build up rapidly but they are not

followed by the formation of a permanent topological grating; instead, a decrease of DE is observed after a few seconds of irradiation and is followed by a low DE value plateau. A complete erasure (loss of DE) occurs after stopping illumination, confirming that only a transient grating was present. This shape was already reported for experiments conducted at temperatures less than 20 °C below the $T_g$ of azopolymers (pDR1M and pMEA)[29] and for low $T_g$ (15-40 °C) polyazosiloxane[30] and has been attributed to the more important relative contribution of thermal relaxation compared to photoinduced motion.

The $DE_{1000}$ 's for the B10% samples are shown as filled red circles in Figure 7.4. The DE is essentially zero when $T_g$ is below the inscription (ambient) temperature (~0.01 % for $B10\%_{19}$) and is extremely low when $T_g$ is close to the inscription temperature ($0.18 \pm 0.01$ % for $B10\%_{22}$). Such low DE values were reported for SRGs inscribed on low $T_g$ (27 °C) azo molecular glasses.[21] The DE then rapidly increases to reach a maximal value of ~5% at a $T_g$ of 46 °C which, by opposition to the B40% series, is not followed by a plateau at high $T_g$. Instead, an important decrease of DE is observed with further increase in $T_g$, down to approximately 0.04% for the highest $T_g$ sample ($B10\%_{88}$). Such low DE values were also reported for SRGs prepared with high-$T_g$ azopolymer complexes when the azo content was particularly low.[47] Furthermore, the azo content has an important influence on DE when comparing samples with a similar $T_g$, especially for high $T_g$. In particular, the $B10\%_{72}$ sample presents a very low $DE_{1000}$ of $0.21 \pm 0.02$ %, while a much higher $DE_{1000}$ of $17.4 \pm 0.5$ % is reached by $B40\%_{67}$. In fact, an even larger $DE_{1000}$ of around $30.0 \pm 0.7$ % is obtained under the same irradiation conditions for pure gDR1, which can be seen in this comparison as a 100 mol% sample with a very similar $T_g$ of 71 °C (a representative inscription curve is provided in Figure7.S2 of the SI).

Since the DR1 moiety possesses the same optical properties (*vide supra*) in both the B10% and B40% series, it is reasonable to think that a DE value plateauing around 5% could have been reached for the high-$T_g$ B10% samples ($B10\%_{62}$, $B10\%_{72}$, and $B10\%_{88}$) if the inscription time had been long enough. Indeed, the SRG inscription curves for these samples (better seen in Figure7.S1) do not show any sign of saturation after 1000 s of irradiation, in contrast with those of the B40% samples and of the $B10\%_{46}$ samples that reach a quasi-plateau in Figure7.3A and 3B, respectively. This kinetic limitation hypothesis is reinforced by the DE values recorded at 100 s ($DE_{100}$), represented by empty symbols in Figure7.4. For both series, a

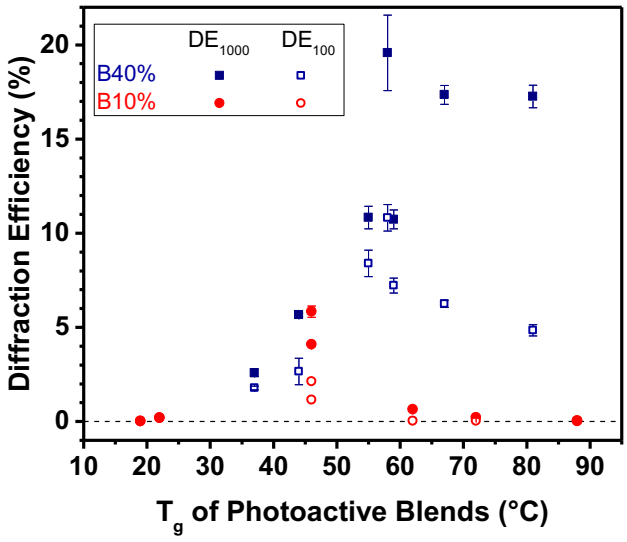


**Figure 7.4.** Diffraction efficiency at 1000 s (filled symbols) and 100 s (empty symbols) for the B10% and B40% blends as a function of their glass transition temperatures ($T_g$).

bell shape is observed with a maximum DE reached at intermediate $T_g$'s, as was observed for the B10% blends after 1000 s. For the B40% series, the maximal $DE_{100}$ occurs at the $T_g$, around 60 °C, that corresponds to the onset of the $DE_{1000}$ plateau. The gap between $DE_{1000}$ and $DE_{100}$ increases above this $T_g$, meaning that a longer time is needed to reach the plateau value for higher $T_g$ samples. A similar gap is also observed for pure gDR1, where the DE is ~11% after 100 s compared to ~30% after 1000 s, which confirms this trend (see Figure7.S2 in SI). For the B10% samples with a $T_g$ close to the inscription temperature, there is no difference between $DE_{1000}$ and $DE_{100}$ because the maximal (very low) attainable DE is reached before 100 s. This behavior is due to the viscous state of the material where any photoinduced motion is effectively compensated by the thermal relaxation. At intermediate $T_g$, the gap between $DE_{1000}$ and $DE_{100}$ is larger, as observed for the B40% samples with high $T_g$ for which the inscription rate is a limiting factor. This observation is consistent with the fact that the shape of the SRG inscription curves of the two intermediate $T_g$ samples is the same as for the B40% samples – the inscription time was long enough to reach a plateau DE. However, in contrast to the high $T_g$ B40% samples, the gap between $DE_{1000}$ and $DE_{100}$ decreases for the highest $T_g$ B10% samples because their very slow inscription kinetics lead to very low DE. To summarize, high-$T_g$ samples have the

potential to reach higher maximal DE values, up to a plateau that depends on the azo content, but their inscription kinetics is increasingly hindered by the increasing viscosity of the matrix, in particular when the azo content is small.

These results suggest that an optimal $T_g$ value exists to optimize both the SRG inscription speed and maximal DE value and that this optimal $T_g$ depends on the azo content. For the B40% series, Figures 7.3A and 7.4 show that this optimal $T_g$ is around 60 °C. For the B10% series with a lower azo fraction, a $T_g$ around 45 °C seems to be optimal to obtain rapidly a maximal DE value, but the fact that the B10%$_{46}$ samples (and those with higher $T_g$) have not reached a DE plateau after 1000 s of inscription suggests that the optimal $T_g$ would be somewhat lower for longer inscription times. The higher optimal $T_g$ for samples with a higher azo content can be rationalized by considering their larger number density of azo undergoing *trans-cis-trans* photoisomerization cycles (by a factor of approximately 4 when comparing the B40% and B10% series since their fraction of *cis* isomers under irradiation is similar in Figure 7.2B). Our previous work[13] has shown that the molecular environment around the DR1 azos undergoing photoisomerization corresponds to an effective temperature much higher than the inscription temperature and even well above the $T_g$ of all the blends studied here. In contrast, the effective temperature of the matrix (or polymer backbone for a DR1-containing azopolymer) was not affected by irradiation, leaving the bulk $T_g$ of the sample unaffected by illumination and preventing viscous flow during SRG inscription. In this context, samples with a larger azo fraction are more capable of perturbing the matrix, either directly by applying more stress on the matrix or by creating a larger relative fraction of free volume that facilitates motion of the matrix by a structural relaxation process. Therefore, samples with a higher azo fraction can perturb matrices with a higher $T_g$, leading to the increase of the optimal $T_g$ from 45 to 60 °C between the B10% and B40% series. Since a higher $T_g$ better prevents isotropic viscous flow of the matrix under illumination (and under dark conditions after SRG writing), the shift of optimal $T_g$ to higher temperatures is accompanied by a higher maximal DE at the plateau for the azo-rich blends. In this context, it is interesting to note that pure gDR1 and pDR1A, one of the most commonly used azopolymers for SRG inscription, both reach maximal DE higher than any of the blends studied here. They possess $T_g$ values of 71 °C and approximately 85 °C (for Mw = 5000 g/mol),[13] respectively, above the optimal $T_g$ of the B40% blends. Since the azo moiety

occupies an increasingly larger fraction in the order of B10% < B40% < gDR1 < pDR1A (when considered as a repeat unit) and assuming that the optimal $T_g$ continues increasing beyond 40% (not linearly since azo-azo interactions affect the photoisomerization efficiency), it can be speculated that the very strong potential for SRG inscription of gDR1 and pDR1A arises from their high azo content combined with a $T_g$ close to the optimal $T_g$ for DR1-containing azomaterials.

The efficiency of the SRG inscription process can also be discussed in terms of the initial rate at which DE develops. Since the diffraction efficiency increases quasilinearly when the irradiation starts for the B40% series, the initial rate can be estimated from the slope of the linear portion of the inscription curves between 10 and 20 s. The analogous analysis cannot be done for the B10% series since the shape of the seven SRG inscription curves is too different.[48] The results in Figure 7.S3A show that the inscription rate (in %/s) first increases with $T_g$, reaches a maximum twice as large as the initial value at $T_g$'s between 55 and 60 °C, and then decreases with further increase of $T_g$. The maximum of the bell corresponds well to the optimal $T_g$ value beyond which the maximal DE of ~18% is achieved. This shape can be rationalized as follows: with a low $T_g$, photoinduced mass transport is efficient, but the rapid thermal relaxation of the matrix compromises the stability of the forming grating, which slows down the overall inscription efficiency and limits the maximum DE attainable. At an intermediate $T_g$ that depends on the azo fraction, an optimal balance is found between these two contributions. This trend from low to intermediate $T_g$ is analogous to the one reported by Veer *et al.* where the SRG inscription rate (and final height) decreased exponentially with increasing experimental temperature[29] (a high temperature corresponding to a low $T_g$ in our case). Finally, when $T_g$ is above the optimal value, thermal relaxation of the matrix may become negligible, but its high viscosity impedes photoinduced mass transport.

It is possible to discuss the inscription rate results from a more fundamental point of view by normalizing the initial slope of the SRG inscription curves by the $DE_{1000}$ reached by their corresponding blends. Figure 7.S3B in SI indicates that the SRG inscription rate (in $s^{-1}$) decreases as $T_g$ increases, which quantitatively confirms the important role of matrix viscosity as discussed qualitatively above. These interpretations are also supported by our previous infrared spectroscopy results showing that under illumination, the molecular environment of the

gDR1 aminotriazine moiety is not modified even when the environment of the azo is highly perturbed by photoisomerization-induced free volume. A very high $T_g$ thus hinders the structural relaxation of the matrix needed to adapt to this photoinduced free volume.

In addition to the azo concentration and $T_g$, the intermolecular interactions present in the material environment also seem to influence the maximal DE. It can be observed in Figure 7.4 that samples B40%$_{58}$ and B40%$_{59}$ show very different saturated DE values of 20 ± 2 % and 10.7 ± 0.5 %, respectively, in spite of their almost identical $T_g$ and azo content. This difference could be due to the presence of three hydrogen (H)-bond donating groups in the headgroup and linkers of the g54 molecular glass composing the photopassive matrix for B40%$_{58}$, compared to only one in g37 which constitutes the photopassive matrix of B40%$_{59}$. The B40%$_{55}$ sample, which has a similar $T_g$ and whose matrix glass (g21) also contains only one NH group, also reaches a DE value of ~11 %. Since we have shown that the presence of numerous NH groups, among others, impacts the thermal properties of molecular glasses,[41-42] H-bonding could promote the matrix motion to adapt to the reorientation of the azo following its photoisomerization cycle, thus leading to higher achievable DE values and providing an additional approach to optimize SRG formation potential of photoactive azo blends.

When the laser is turned off at the end of the SRG inscription process (after 1000 s of illumination), either an increase or a decrease in DE can be observed in Figures 7.3 and S1. To compare quantitatively the temporal stability of the gratings, the residual diffraction efficiency was calculated as the percentage of the DE value recorded 60 s after ceasing the irradiation with respect to $DE_{1000}$. This residual DE value is an indicator of the relative importance of the transient and permanent gratings.[49] When the laser is turned off, the transient gratings disappear and the residual DE will solely be due to the SRG. It is possible that a phase difference between the transient volume gratings and the surface relief grating could explain the decrease or increase in DE after laser irradiation is stopped, depending on whether the gratings diffract in phase or not, respectively.[50] Figure 7.5 shows the complete absence of residual DE (0%) for the samples with a $T_g$ at or below the inscription temperature and its gradual increase up to 90% as $T_g$ increases toward the above-defined optimal values. The residual DE of B10% samples decreases with a further increase in $T_g$ beyond their optimal $T_g$, down to ~45% for B10%$_{88}$. Since these high-$T_g$ blends did not reach a saturated DE plateau in Figure 7.4 because the slow motion of

the matrix reduced the inscription kinetics of the topological grating, this decrease in residual DE can be explained by the lower contribution of the permanent topological grating relative to the transient gratings.

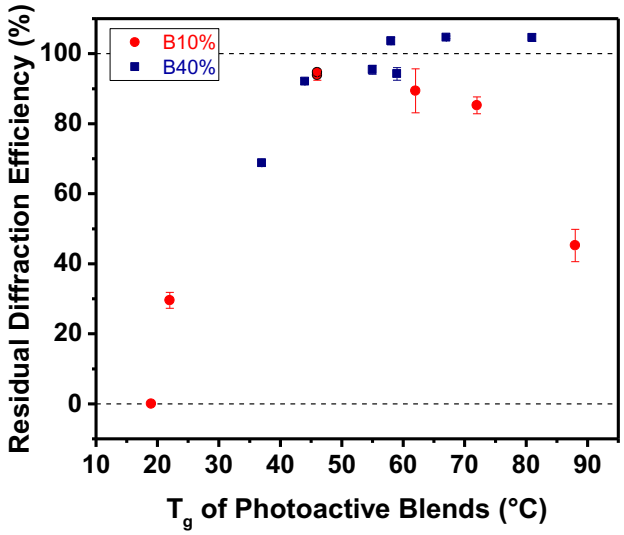


**Figure 7.5.** Residual diffraction efficiency of B10% and B40% as a function of their glass transition temperatures ($T_g$).

Interestingly, three samples ($B40\%_{81}$, $B40\%_{67}$ and $B40\%_{58}$) show an increase in DE when the laser is turned off with residual DE of 104-105%. Two common characteristics of these samples are that their $T_g$ is close to or beyond the optimal $T_g$ (in this case 60 °C) and that their azo content is high enough to reach the DE saturation plateau within the time scale of the inscription experiment. Pure gDR1 also shares these characteristics and shows a residual DE of approximately 135%, the highest value recorded. These observations could be tentatively explained by considering that a high enough orientation level must be achieved in order to promote further alignment of DR1 units or an additional directional motion of the matrix when the irradiation is stopped. As will be shown below, high global orientation level and stability can only be achieved with high azo content and high $T_g$. Previous studies of SRG inscription and photoinduced birefringence on other azomaterials support this suggestion: the amplitude of the DE increase after the laser is turned off decreased at higher experimental temperatures (analogous to a lower $T_g$ here) for a DR1-containing copolymer;[28] lower values of persistent DE

were found for SRGs inscribed on films thinner than 50 nm, which are known to show lower $T_g$ and higher mobility;[49] liquid-crystalline block copolymers, when heated into their smectic phase upon and after irradiation, show an increasing birefringence under dark conditions after irradiation,[51] while supramolecular bisazopolymers behaved similarly only when their doping fraction was higher than 0.5.[52] Another possible explanation for these observations could be the influence of inscription temperature or sample $T_g$ on the phase difference between the transient and surface relief gratings created during the inscription process.[53]

### 7.4.3 Photoinduced orientation

In an attempt to link the observations made about the macroscopic mass transport with the molecular aspects of SRG inscription, PM-IRSAS measurements were conducted to track the photo-orientation of the azo moiety of gDR1 upon illumination. A linearly polarized laser (488 nm, 18 mW/cm$^2$) was used with the goal of approaching the irradiation conditions during SRG inscription, where the contra-rotating interfering beams produce linearly polarized light. Polarized ($A_p$ and $A_s$) and dichroic difference ($\Delta A$) spectra for the B40%$_{67}$ and B40%$_{37}$ blends are shown in Figure 7.S4 in SI. The 1104 cm$^{-1}$ band chosen to quantify the orientation is due to an azobenzene aromatic ring deformation.[13] The $<P_2>$ values calculated using this band are representative of the orientation of the whole chromophore because its transition dipole moment is parallel to the main axis of the DR1 moiety. Figure 7.S5 in SI shows examples of the evolution of the photo-orientation as a function of time for samples B40%$_{37}$ and B40%$_{67}$. The initial $<P_2>$ value is almost 0, which confirms a random orientation before irradiation. When the laser is turned on, the $<P_2>$ values rapidly grow toward negative values because DR1 orients perpendicular to the laser polarization direction (a $<P_2>$ value of -0.5 would indicate a perfect perpendicular orientation). A plateau, labeled $<P_2>_{max}$, is then reached rapidly for samples with low $T_g$ (~20 s) and after a longer irradiation time (but with a larger orientation) for high-$T_g$ samples (~120 s). This six-fold difference in time needed to reach maximal orientation is consistent with the fact that the inscription curves in Figure 7.3 reach their saturation DE faster for low-$T_g$ samples, and with the increasing difference between the $DE_{1000}$ and $DE_{100}$ values observed in Figure 7.4 with increasing $T_g$. A similar observation was made by Barrett *et al.* in their study of a series of $NO_2$-functionalized azopolymers of various spacer length where lower $T_g$ samples (longer spacers) showed larger photoinduced birefringence rate constants.[54] Finally,

when the laser is turned off after 200 s of irradiation, the photo-orientation relaxes rapidly during the first few seconds and then more slowly, essentially plateauing at the end of the 120 s experimental relaxation time frame. The final $<P_2>$ value is called the residual orientation, $<P_2>_{res}$, and informs on the resistance of the material to thermally-induced motion.

Figure 7.6A shows that the photoinduced orientation is almost zero for blends with the lowest $T_g$ and that it gradually increases with $T_g$ (with the exception of the two highest $T_g$ samples). The modest $<P_2>_{max}$ value for low-$T_g$ samples is due to the important contribution of thermal relaxation during irradiation. Accordingly, the DE values recorded for these samples were very low and were not stable after irradiation because only transient gratings could form. A greater photo-orientation (and DE) is observed as $T_g$ increases, reaching a maximum value of approximately -0.09 ± 0.02 for blends with a $T_g$ of 70 °C. However, Figure 7.6A shows that a further increase in $T_g$ is detrimental: a lower photo-orientation is observed for B40%$_{81}$ and B10%$_{88}$. This decreasing orientation is not due to the incapacity of DR1 to undergo photoisomerization since the *cis* content under irradiation is not affected much by a high $T_g$ (Figure 7.2B). It thus appears that the azo moieties mainly return to their original angular distribution after *trans-cis-trans* cycling when the $T_g$ is too high (more than approximately 60 °C above the operating temperature for gDR1), which compromises their capacity to provoke anisotropic motion of the matrix through stress or generation of anisotropic free volume. These results are consistent with the observation of an optimal $T_g$ for SRG inscription where blends with a high $T_g$ showed substantially slower inscription kinetics.

Importantly, the photo-orientation results for the B40% and B10% blends are very similar and indicate that the DR1 orientation is almost independent of azo content for a given $T_g$. This observation is consistent with the very similar optical properties (band position, bandwidth, and minimal fraction of *cis* isomer under irradiation) observed for all blends in Figure 7.2 due to the isolation of the DR1 moieties and is reasonable because $<P_2>$ values are intrinsically normalized per azo. This result contrasts with the lower orientation that we found for azopolymer supramolecular complexes with a higher azo content, which can be explained at least in part by a concomitant change in $T_g$.[25] The trend of Figure 7.6A also reinforces the merit of our photoactive/photopassive glass blending strategy considering that no clear conclusions

could be drawn about the effect of $T_g$ on photoinduced orientation when comparing a series of molecular glasses featuring different chromophores.[37]

Figure 7.6B shows the $<P_2>_{res}$ (%) (calculated as the percentage of $<P_2>_{res}$ with respect to $<P_2>_{max}$) as a function of the $T_g$ of the photoactive blends. These values gradually increase in a sigmoidal-like shape from 0% for the lowest $T_g$ samples, where the rubbery matrix can relax quickly, to a plateau of ~80% for the highest $T_g$ samples because their glassy matrix is highly viscous. As for the $<P_2>_{max}$ values, the trend is not affected by azo content, in this case due to the fact that orientation stability mainly depends on the matrix properties. It is interesting to note that the $<P_2>_{res}$ plateau is reached close to the optimal $T_g$ value (~60 °C) observed in the SRG inscription experiments. However, in contrast with residual DE, $<P_2>_{res}$ seems to be purely temperature-dependent.

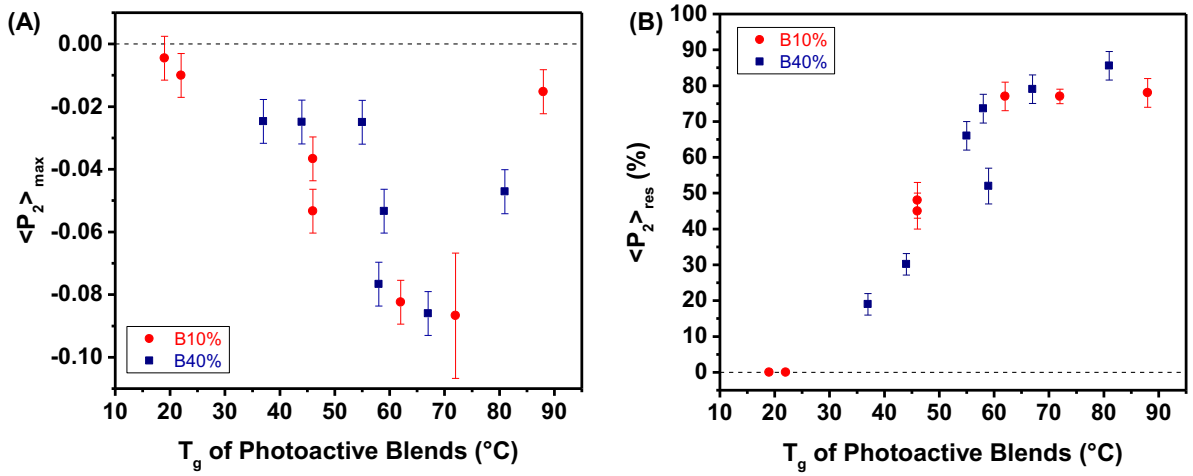


**Figure 7.6.** A) Maximal photo-orientation value ($<P_2>_{max}$) and B) residual photo-orientation percentage value ($<P_2>_{res}$ percentage) of the 1104 $cm^{-1}$ band of the azo moiety of gDR1 as a function of the $T_g$ of the photoactive blends.

An important consequence of the similar DR1 orientation and orientation stability for B40% and B10% samples is that the cumulative orientation generated within the material is about four times larger in B40% samples than in B10% samples with the same $T_g$. This higher global orientation agrees very well with the higher maximal DE reached by the B40% blends (~18% vs. ~5%) and also with the aforementioned requirement of a high azo content for

observing an increase of DE (a residual DE > 100%) after switching off the SRG inscription laser. In this context, it is noteworthy that the $<P_2>_{max}$ value for pure gDR1 is larger (-0.12 ± 0.02) than for any of the blends, which is not surprising because its UV-visible spectrum indicated the existence of interactions between DR1 units, which were absent in the blends, that can favor azo orientation.[55] This larger capability to photo-orient, combined with a larger azo fraction and a similar orientation stability ($<P_2>_{res}$ ~ 65%), help to explain why pure gDR1 formed the SRG with the highest diffraction efficiency (~30%) and with the largest increase in residual DE (~135%) after stopping irradiation.

Our results indicate that molecular orientation and SRG DE are interconnected but that they are not directly proportional since they involve different mechanisms. The photo-orientation and SRG DE both increase with $T_g$ for low to intermediate values, irrespective of the azo content, but the trends in Figures 7.6 and 7.4 are clearly different for $T_g$'s beyond the optimal values, where the B40% samples show a DE plateau and the B10% samples show a decrease in DE. It can be concluded that compounds that are not capable to orient do not have a good SRG potential, either because their $T_g$ is too low or too high, while those that orient do not necessarily lead to high DE values due to the inefficiency of the matrix to take advantage of the *trans-cis-trans* isomerization. In other words, the matrix needs to have an adaptation capability to be pushed anisotropically during the azo isomerization or to adapt to the angular redistribution of the azo moieties, which appears to become the kinetic limiting factor when $T_g$ exceeds the optimal value. This limited adaptability of the matrix manifests itself as large $<P_2>_{res}$ values that translate into slow SRG inscription rates at high $T_g$. This hypothesis implies that the optimal $T_g$ for SRG inscription involves a compromise between reaching the highest possible orientation without exceeding a certain $<P_2>_{res}$ threshold to enable anisotropic matrix motion. In this context, a $<P_2>_{res}$ of 100% would represent an extremely rigid matrix not capable of any adaptation and leading to exceedingly slow inscription kinetics. The results further indicate that it is the cumulative orientation of the chromophores (related to the product of $<P_2>_{max}$ with the azo number density) that is of highest importance for SRG formation, not the orientation level of the individual azo units. This explains why blends or compounds with the same $T_g$ but with a larger relative azo content have a better potential for writing SRG with a high DE, and also

why the optimal $T_g$ for high DE and fast inscription kinetics shifts to higher temperature for systems with higher azo content.

## 7.5 Conclusion

The strategy of mixing photoactive / photopassive molecular glasses allowed us to decouple for the first time the influence of two important yet often interconnected parameters, the $T_g$ and the azo content, on the photoactivity of azomaterials in order to optimize the SRG inscription process. Using this strategy, we prepared miscible photoactive blends with very similar optical properties by mixing 10 or 40 mol% of a photoactive DR1-containing molecular glass with a series of its structural analogues to tune the $T_g$ between 19 and 88 °C without changing the azo content. This advantageous model system revealed that a trade-off between different parameters must be made in order to optimize SRG inscription in terms of diffraction efficiency and inscription kinetics. A high azo content (for a constant $T_g$) and larger photoinduced orientation (generally promoted by a high $T_g$) enable forming SRG with a larger DE; however, a high orientation stability (also encountered with high-$T_g$ materials) reflects a low matrix adaptability that slows down the kinetics of the inscription process. As a consequence, an optimal intermediate $T_g$ enables fast SRG inscription and maximal (saturated) DE. The optimal $T_g$ ranges between ~45 and 60 °C for our amorphous DR1-containing blends and is higher for higher azo content (and probably higher for pure DR1-containing glasses or azopolymers). For samples with a lower $T_g$, the efficient thermal relaxation of the rubbery matrix leads to very low DE and orientation and to limited temporal stability for both. On the other hand, for samples with higher $T_g$, the photo-orientation of the chromophore upon SRG inscription is impeded by the high viscosity of the matrix, which translates into slower kinetics and to lower DE values if the inscription time (or irradiance) is too small to reach saturation.

The results presented herein emphasize the importance of $T_g$ in amorphous systems and offer useful guidelines to optimize the choice and/or the preparation of efficient azomaterials for SRG inscription and possibly for other photoisomerization-enabled processes. Finally, it must be highlighted that the strategy of blending miscible active/passive molecular glasses, applied here to SRG inscription, is not limited to SRG or to light-responsiveness and should be broadly applicable to other types of stimuli-active/passive materials.

## 7.6 Acknowledgements

The authors thank the Fonds de Recherche du Québec – Nature et Technologies (FRQNT, #2012-PR-147034), the Natural Sciences and Engineering Research council of Canada (NSERC, #312493 and #2015-05743) and the Canadian Defence Academy Research Programme (CDARP) from RMC for funding. AL thanks NSERC for a Vanier graduate scholarship. JB thanks Mercator and FAME for foreign study scholarships. JV wishes to thank FRQNT, Finnish Cultural Foundation and the Academy of Finland for postdoctoral grants. LK thanks NSERC for an undergraduate student research award.

## 7.7 References

1. Kundu, P. K.; Klajn, R., *ACS Nano* **2014,** *8*, 11913-11916.
2. Yager, K. G.; Barrett, C. J., Azobenzene Polymers for Photonic Applications. In *Smart Light-Responsive Materials*, Zhao, Y.; Ikeda, T., Eds. John Wiley & Sons, Inc.: 2008; pp 1-46.
3. Seki, T., *J. Mater. Chem. C* **2016,** *4*, 7895-7910.
4. Rochon, P.; Batalla, E.; Natansohn, A., *Appl. Phys. Lett.* **1995,** *66*, 136-138.
5. Kim, D. Y.; Tripathy, S. K.; Li, L.; Kumar, J., *Appl. Phys. Lett.* **1995,** *66*, 1166-1168.
6. Ambrosio, A.; Marrucci, L.; Borbone, F.; Roviello, A.; Maddalena, P., *Nat. Commun.* **2012,** *3*, 989.
7. Hurduc, N.; Donose, B. C.; Macovei, A.; Paius, C.; Ibanescu, C.; Scutaru, D.; Hamel, M.; Branza-Nichita, N.; Rocha, L., *Soft Matter* **2014,** *10*, 4640-4647.
8. Harrison, J. M.; Goldbaum, D.; Corkery, T. C.; Barrett, C. J.; Chromik, R. R., *J. Mater. Chem. C* **2015,** *3*, 995-1003.
9. Lefin, P.; Fiorini, C.; Nunzi, J.-M., *Pure Appl. Opt.* **1998,** *7*, 71-82.
10. Barrett, C. J.; Natansohn, A. L.; Rochon, P. L., *J. Phys. Chem.* **1996,** *100*, 8836-8842.
11. Saphiannikova, M.; Toshchevikov, V., *J. Soc. Inf. Disp.* **2015,** *23*, 146-153.
12. Yadavalli, N. S.; Loebner, S.; Papke, T.; Sava, E.; Hurduc, N.; Santer, S., *Soft Matter* **2016,** *12*, 2593-2603.
13. Vapaavuori, J.; Laventure, A.; Bazuin, C. G.; Lebel, O.; Pellerin, C., *J. Am. Chem. Soc.* **2015,** *137*, 13510-13517.

14. Bedrov, D.; Hooper, J. B.; Glaser, M. A.; Clark, N. A., *Langmuir* **2016,** *32*, 4004-4015.
15. Teboul, V.; Saiddine, M.; Nunzi, J.-M., *Phys. Rev. Lett.* **2009,** *103*, 265701.
16. Teboul, V.; Saiddine, M.; Nunzi, J.-M.; Accary, J.-B., *J. Chem. Phys.* **2011,** *134*, 114517.
17. Natansohn, A.; Rochon, P., *Chem. Rev.* **2002,** *102*, 4139-4176.
18. Stumpe, J.; Kulikovska, O.; Goldenberg, L. M.; Zakrevskyy, Y., Photo-Induced Phenomena in Supramolecular Azobenzene Materials. In *Smart Light-Responsive Materials*, John Wiley & Sons, Inc.: 2008; pp 47-94.
19. Mahimwalla, Z.; Yager, K. G.; Mamiya, J.-i.; Shishido, A.; Priimagi, A.; Barrett, C. J., *Polym. Bull.* **2012,** *69*, 967-1006.
20. Priimagi, A.; Shevchenko, A., *J. Polym. Sci., Part B: Polym. Phys.* **2014,** *52*, 163-182.
21. Nakano, H.; Tanino, T.; Takahashi, T.; Ando, H.; Shirota, Y., *J. Mater. Chem.* **2008,** *18*, 242-246.
22. Börger, V.; Pohle, S.; Kuliskovska, O.; Gharaggozloo-Hubmann, K.; Stumpe, J.; Menzel, H., *Macromol. Symp.* **2009,** *275–276*, 257-265.
23. Yesodha, S. K.; Sadashiva Pillai, C. K.; Tsutsumi, N., *Prog. Polym. Sci.* **2004,** *29*, 45-74.
24. Priimagi, A.; Cattaneo, S.; Ras, R. H. A.; Valkama, S.; Ikkala, O.; Kauranen, M., *Chem. Mater.* **2005,** *17*, 5798-5802.
25. Vapaavuori, J.; Heikkinen, I. T. S.; Dichiarante, V.; Resnati, G.; Metrangolo, P.; Sabat, R. G.; Bazuin, C. G.; Priimagi, A.; Pellerin, C., *Macromolecules* **2015,** *48*, 7535-7542.
26. Zhang, Q.; Wang, X.; Barrett, C. J.; Bazuin, C. G., *Chem. Mater.* **2009,** *21*, 3216-3227.
27. Wang, X.; Vapaavuori, J.; Wang, X. X.; Sabat, R. G.; Pellerin, C.; Bazuin, C. G., *Macromolecules* **2016,** *49*, 4923-4934.
28. Matsui, T.; Yamamoto, S.-i.; Ozaki, M.; Yoshino, K.; Kajzar, F., *J. Appl. Phys.* **2002,** *92*, 6959-6965.
29. Veer, P. U.; Pietsch, U.; Saphiannikova, M., *J. Appl. Phys.* **2009,** *106*, 014909.
30. Luca, A. R.; Moleavin, I.-A.; Hurduc, N.; Hamel, M.; Rocha, L., *Appl. Surf. Sci.* **2014,** *290*, 172-179.
31. Virkki, M.; Tuominen, O.; Kauranen, M.; Priimagi, A., *Opt. Express* **2016,** *24*, 4964-4971.

32. Veer, P. U.; Pietsch, U.; Mueller, A. D., *Appl. Phys. Lett.* **2009,** *94*, 231911.
33. Kirby, R.; Sabat, R. G.; Nunzi, J.-M.; Lebel, O., *J. Mater. Chem. C* **2014,** *2*, 841-847.
34. Bennani, O. R.; Al-Hujran, T. A.; Nunzi, J.-M.; Sabat, R. G.; Lebel, O., *New J. Chem.* **2015,** *39*, 9162-9170.
35. Umezawa, H.; Nunzi, J.-M.; Lebel, O.; Sabat, R. G., *Langmuir* **2016,** *32*, 5646-5652.
36. Ho, M.-S.; Natansohn, A.; Barrett, C.; Rochon, P., *Can. J. Chem.* **1995,** *73*, 1773-1778.
37. Snell, K. E.; Hou, R.; Ishow, E.; Lagugne-Labarthet, F., *Langmuir* **2015,** *31*, 7296-7305.
38. Snell, K. E.; Stéphant, N.; Pansu, R. B.; Audibert, J.-F.; Lagugné-Labarthet, F.; Ishow, E., *Langmuir* **2014,** *30*, 2926-2935.
39. Liang, Y.; Mauran, D.; Prud'homme, R. E.; Pellerin, C., *Appl. Spectrosc.* **2008,** *62*, 941-947.
40. Lebel, O.; Maris, T.; Perron, M.-È.; Demers, E.; Wuest, J. D., *J. Am. Chem. Soc.* **2006,** *128*, 10372-10373.
41. Laventure, A.; Soldera, A.; Pellerin, C.; Lebel, O., *New J. Chem.* **2013,** *37*, 3881-3889.
42. Laventure, A.; De Grandpré, G.; Soldera, A.; Lebel, O.; Pellerin, C., *Phys. Chem. Chem. Phys.* **2016,** *18*, 1681-1692.
43. Barrett, C.; Natansohn, A.; Rochon, P., *Chem. Mater.* **1995,** *7*, 899-903.
44. Lagugné Labarthet, F.; Buffeteau, T.; Sourisseau, C., *J. Phys. Chem. B* **1998,** *102*, 5754-5765.
45. Brown, D.; Natansohn, A.; Rochon, P., *Macromolecules* **1995,** *28*, 6116-6123.
46. Goldenberg, L. M.; Gritsai, Y.; Stumpe, J., *J. Opt.* **2011,** *13*, 075601.
47. Koskela, J. E.; Vapaavuori, J.; Ras, R. H. A.; Priimagi, A., *ACS Macro Lett.* **2014,** *3*, 1196-1200.
48. No reliable portion of the initial DE values could be chosen to estimate their initial SRG inscription rate. However, it is clear from Figure S1 that the same trend as for the B40% series is qualitatively present for the intermediate and high $T_g$ blends and that the SRG inscription rates form a bell shaped curve with respect to $T_g$.
49. Yager, K. G.; Barrett, C. J., *J. Chem. Phys.* **2007,** *126*, 094908.
50. Lagugné Labarthet, F.; Buffeteau, T.; Sourisseau, C., *J. Phys. Chem. B* **1998,** *102*, 2654-2662.
51. del Barrio, J.; Oriol, L.; Alcalá, R.; Sánchez, C., *Macromolecules* **2009,** *42*, 5752-5760.

52. Wu, S.; Duan, S.; Lei, Z.; Su, W.; Zhang, Z.; Wang, K.; Zhang, Q., *J. Mater. Chem.* **2010,** *20*, 5202-5209.

53. Yager, K. G.; Tanchak, O. M.; Godbout, C.; Fritzsche, H.; Barrett, C. J., *Macromolecules* **2006,** *39*, 9311-9319.

54. Barrett, C.; Choudhury, B.; Natansohn, A.; Rochon, P., *Macromolecules* **1998,** *31*, 4845-4851.

55. Apitz, D.; Bertram, R. P.; Benter, N.; Hieringer, W.; Andreasen, J. W.; Nielsen, M. M.; Johansen, P. M.; Buse, K., *Phys. Rev. E* **2005,** *72*, 036610.

## 7.8 Supporting information

**Table 7.S1.** $T_g$ values of the B10% and B40% blends of photopassive glasses ($gT_g$) with gDR1.

| **$gT_g$** | **$T_g$ (± 1 °C)** | |
|---|---|---|
| | **B10%** | **B40%** |
| **g94** | 88 | 81 |
| **g70** | 74 | 67 |
| **g54** | 62 | 58 |
| **g37** | 46 | 59 |
| **g21** | 46 | 55 |
| **g8** | 22 | 44 |
| **g-25** | 19 | 37 |

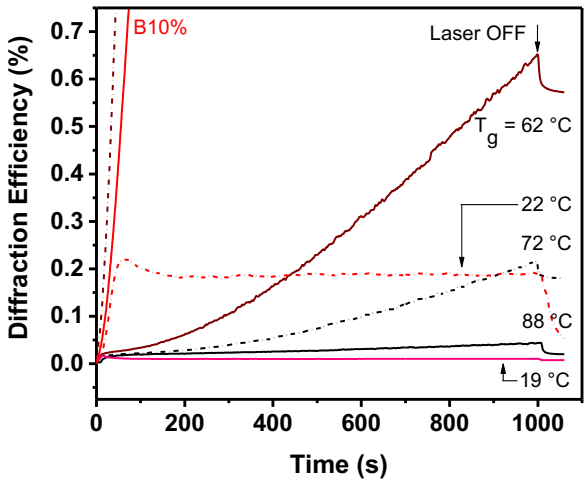


**Figure 7.S1.** Diffraction efficiency of B10% as a function of SRG inscription time showing an enlargement of Figure 7.3B of the main text to display more clearly the curves for samples with the lowest diffraction efficiencies.

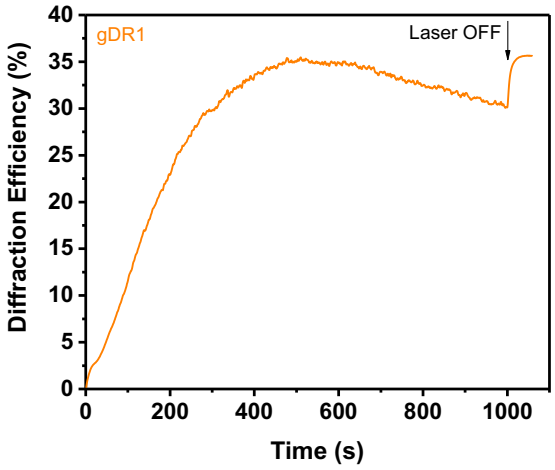


**Figure 7.S2.** Diffraction efficiency of pure gDR1 as a function of SRG inscription time.

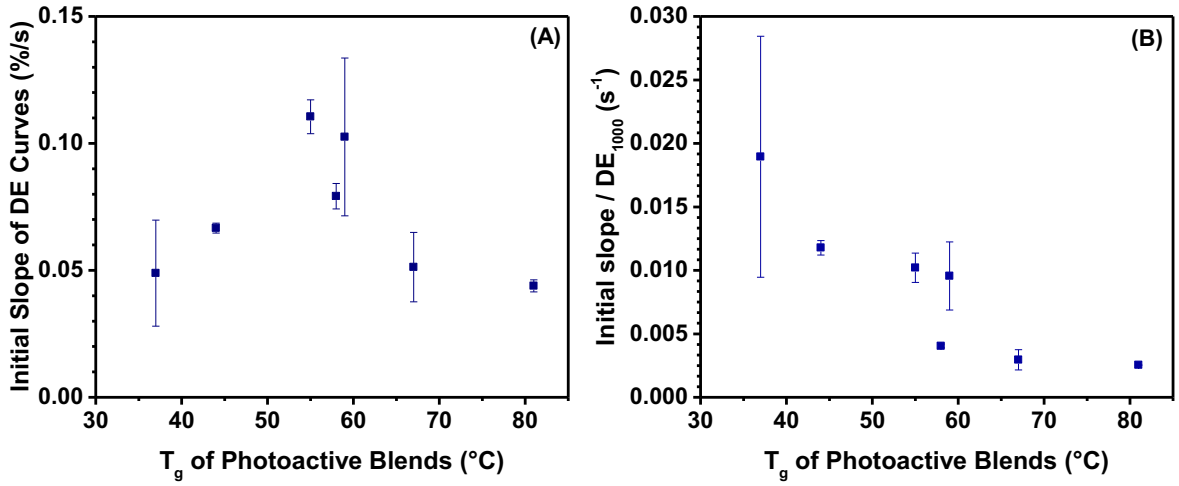


**Figure 7.S3.** A) Initial slopes of the SRG inscription curves (calculated in the linear portion between 10 and 20 s) of the B40% series as a function of their $T_g$. B) Initial slopes normalized by the corresponding $DE_{1000}$ as a function of $T_g$ of the B40% series.

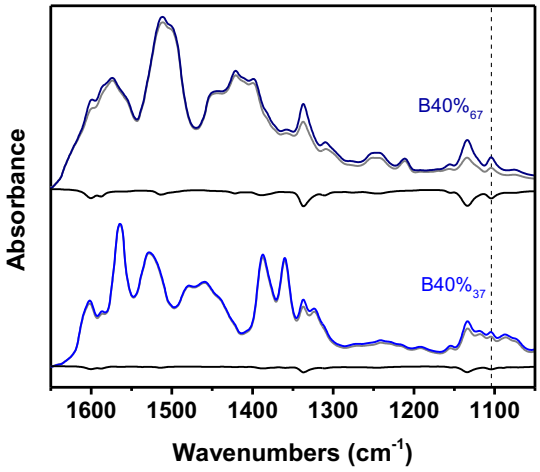


**Figure 7.S4.** Polarized ($A_p$ in grey and $A_s$ in blue) and dichroic difference (in black) spectra for the B40%$_{67}$ and B40%$_{37}$ blends. The dashed line indicates the 1104 $cm^{-1}$ band that was used to quantify DR1 orientation.

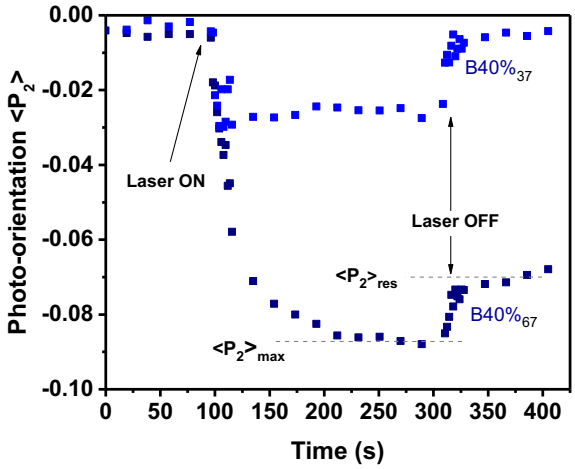


**Figure 7.S5.** Time evolution of the photo-orientation ($<P_2>$) of the azobenzene moiety (1104 $cm^{-1}$) for the B40%$_{67}$ and B40%$_{37}$ blends. The method to determine the value of the maximal photo-orientation ($<P_2>_{max}$) and the residual photo-orientation ($<P_2>_{res}$) is also shown.

# Chapitre 8: Conclusion

Le but principal de cette thèse consistait à établir des liens entre la structure des verres moléculaires étudiés et leurs propriétés, en vue d'optimiser leur préparation et leur utilisation dans diverses applications. Pour y arriver, le projet de recherche a été divisé en trois objectifs, qui ont chacun été couvert par deux travaux. Le présent chapitre effectue tout d'abord un retour global sur chacun d'entre eux, abordant de quelle façon ils sont interreliés et comment ils contribuent à l'atteinte du but principal. Par la suite, cinq grands axes de recherche qui découlent des conclusions tirées des travaux présentés sont suggérés.

## 8.1 Conclusions générales

### 8.1.1 Rôle des groupements substituants sur la triazine

À la suite des travaux du chapitre 2, qui comparaient le GFA, le GS et la $T_g$ d'une librairie de composés avec des groupements de tête NHMe et Et, et différents groupements auxiliaires (aromatiques ou aliphatiques), il en ressort que la possibilité d'établir des liaisons H à partir du groupement de tête est l'élément principal favorisant une valeur de $T_g$ élevée et la formation d'une phase vitreuse: 81% des composés substitués avec le groupe NHMe ont une vitesse de refroidissement critique inférieure à 0,5 °C/min, contre seulement 33% pour les composés substitués avec le groupe Et. Étant donné que le GFA des composés Et qui composent ce 33% ne peut être attribué à la possibilité d'établir des liaisons H au niveau du groupement de tête, il résulte probablement de la structure des groupements auxiliaires, combinée à la présence de groupements liants NH. Il ne peut être attribué uniquement à ces groupes NH puisque tous les composés de cette librairie possèdent les mêmes groupements liants NH.

La vaste gamme de groupements auxiliaires étudiés a permis de confirmer que les groupements aromatiques substitués avec des méthyles en position *meta* favorisent le plus le GFA des composés, alors que les halogènes (même s'ils se retrouvent en position *meta*), les méthyles substituants sur le phényle dans une autre position que *meta*, et les groupements aliphatiques diminuent le GFA et le GS. Le fait que le patron de substitution *meta* favorise le GFA est connu au sein de la communauté scientifique. Bien qu'Angell *et al.* ont suggéré que c'est la stabilité inférieure de 4 kJ/mol du cristal de 1,3-diméthylbenzène par rapport à celle des

cristaux des isomères 1,2- et 1,4-diméthylbenzène qui pourrait être à l'origine de ce phénomène,[1] cela demeure une question ouverte. Le nombre et la nature des substituants sur les groupements auxiliaires influencent également la $T_g$. Par exemple, l'ajout d'un groupement méthyle augmente la $T_g$, en moyenne, de 10 °C, et celle des composés halogénés augmente avec la polarisabilité de l'halogène.

Ces résultats mènent à la conclusion que la nature du groupement de tête influence majoritairement le GFA et la $T_g$ des composés, lorsque les groupements liants de ces derniers sont identiques, tel qu'il avait été mis de l'avant dans les études antérieures.[2-3] Il serait toutefois imprudent d'en venir à la même conclusion lorsque les groupements liants sont différents. C'est pour cette raison que les travaux du chapitre 3 concernent une autre librairie, constituée d'une série de molécules substituées avec un groupement de tête NHMe et une autre avec un groupement de tête OMe, pour lesquelles les groupements auxiliaires sont identiques (mexyles) mais qui présentent des groupements liants avec différentes caractéristiques. Il y a le groupe NH, pour étudier l'influence des liaisons H lorsqu'elles sont possibles au niveau des groupements liants, et les groupes NMe et O pour valider si l'encombrement stérique ou même la barrière énergétique de rotation de ces groupes peuvent affecter le GFA ou la $T_g$ des composés. Les résultats confirment qu'un groupement de tête donneur de liaisons H (NHMe) permet d'atteindre des valeurs de $T_g$ plus élevée qu'avec une tête seulement capable d'accepter des liaisons H (OMe) ou même sans capacité d'y participer (Et, chapitre 2).

Il se dégage de l'étude que la possibilité d'établir des liaisons H (surtout au niveau du groupement de tête) n'est pas essentielle pour qu'un composé possède un bon GFA. En effet, tous les composés de cette étude ont présenté un excellent GFA, à l'exception du composé substitué par un groupement de tête NHMe et des groupements liants O. Les liaisons H peuvent donc empêcher, de manière générale, la cristallisation lors du refroidissement depuis l'état liquide. Toutefois, lorsqu'elles sont utilisées en combinaison avec des groupements qui abaissent l'énergie des barrières de rotation (groupements O), ils ne sont pas suffisants (dans les cas étudiés) pour empêcher les molécules d'explorer leur profil énergétique et de cristalliser. Les groupements liants NMe, quant à eux, sont encombrants, ce qui élève la barrière énergétique de rotation et par le fait même, limite l'exploration du profil énergétique des molécules, favorisant ainsi leur GFA. Cette possibilité (ou impossibilité) s'applique également au GS des composés: seuls les composés avec des groupes NH ou O ont cristallisé à froid lors d'une

chauffe à 10 °C/min. Les groupements liants NMe sont donc les plus prometteurs pour mener à de bons GFA et GS, en entraînent toutefois des valeurs de $T_g$ plus faibles, étant donné l'absence de capacité à établir des liaisons H ou des interactions dipolaires.

### 8.1.2 Influences des liaisons H sur les propriétés des verres

Bien que la possibilité d'établir une (ou des) liaison(s) H ne soit pas la seule caractéristique qui permette aux molécules à base de triazine de former facilement une phase vitreuse, elle reste un paramètre clé qui nécessite une étude plus approfondie pour permettre de l'utiliser de manière plus rationnelle dans la conception et l'utilisation de nouveaux verres moléculaires, dont certains pourraient être éventuellement fonctionnels. Le chapitre 4 concernait un travail dans lequel des composés possédant à la fois des groupements capables de participer à des liaisons H et à des empilements π-π impliquant des dérivés stilbènes perfluorés et non fluorés. Ce type de motif est particulièrement intéressant dans l'industrie de l'opto-électronique puisqu'il a été utilisé avec succès dans des dispositifs à base de matériaux moléculaires amorphes.[4-6] Étant donné que, dans le cas des molécules étudiées au chapitre 4, l'énergie des liaisons H et des empilements π-π est du même ordre de grandeur, le composé avec le groupement de tête NHMe, capable d'établir des liaisons H, réussit à empêcher l'empilement plus directionnel des dérivés stilbènes perfluorés, ce qui n'est pas le cas lorsque le groupement de tête n'est pas un donneur de liaisons H ($NMe_2$). Bien qu'intéressant, il serait risqué de procéder à une généralisation hâtive du phénomène observé, puisque les interactions menant aux empilements impliquent la triazine et le cycle aromatique perfluoré, contrairement à l'alternance typiquement observée entre le cycle aromatique non fluoré et celui perfluoré.[7] Néanmoins, le concept d'introduire des liaisons H dans la structure d'une molécule qui porte déjà un substituant capable d'interactions directionnelles d'énergie similaire ou inférieure à celles des liaisons H peut être applicable à d'autres composés.

Il était également d'un intérêt particulier de préparer des films amorphes avec les composés à base de triazine à l'aide de la méthode PVD, puisque cette technique est entre autres utilisée dans l'industrie de l'opto-électronique.[8] Au chapitre 5, une étude portant spécifiquement sur l'influence de la capacité d'établir des liaisons H sur la stabilité cinétique des verres atteignable par PVD est présentée, constituant le premier travail à ce sujet impliquant des verres avec une $T_g$ supérieure à la température ambiante. Seulement le groupement de tête (NHMe,

OMe et Et) des composés est modifié de manière systématique, alors que les groupements auxiliaires et liants sont identiques. Bien que ces trois verres à base de triazine préparés par PVD présentent une densité plus importante et une certaine anisotropie (propriétés absentes pour les verres préparés par refroidissement à partir de l'état liquide), la présence d'un groupement donneur de liaisons H (NHMe) diminue de plus d'un ordre de grandeur leur stabilité cinétique (à $T_g$ + 4 K). Ce phénomène serait dû au fait que les liaisons H limitent la diffusion de surface des molécules, les empêchant ainsi d'explorer les coordonnées de leur profil énergétique.[9] Ce changement important de propriété est un résultat très utile, dont pourrait bénéficier le domaine du PVD, puisqu'il pourrait à la fois orienter le choix des groupements fonctionnels mais aussi le type d'utilisations possibles des verres PVD selon la stabilité désirée et/ou nécessaire au bon fonctionnement de certains dispositifs.

### 8.1.3 Comportement des matériaux photosensibles à l'état vitreux

Finalement, les chapitres 6 et 7 ont permis d'étudier la photosensibilité des azos dans différents contextes d'irradiation, respectivement non polarisée et polarisée sous forme de patron d'interférence, dans le but d'optimiser l'utilisation des verres moléculaires photosensibles pour certaines applications, mais aussi des matériaux photoactifs en général. Les connaissances tirées des chapitres 2 et 3 à propos de l'influence de la nature et de la position des substituants ont permis de guider la sélection du gDR1 comme verre modèle, avec son groupement de tête NHMe, ses groupements liants NH et l'un de ses groupements auxiliaires mexyle, l'autre étant un dérivé du colorant azo DR1. Le chapitre 6 a permis de faire ressortir le gradient d'environnement moléculaire créé lors de la photoisomérisation de l'azo, un phénomène qui se produit autant pour le verre moléculaire gDR1 que pour le polymère pDR1A. En effet, dans les deux cas, une différence d'environnement moléculaire correspondant à l'équivalent de chauffer le matériau à plus de 100 °C est rapportée.

Dans cette étude, il a été possible d'observer que le déplacement de la position de la bande utilisée pour déterminer la $T_{eff}$ était mieux défini pour le gDR1 que pour le pDR1A. Ce phénomène résulte de l'une des caractéristiques des verres moléculaires, i.e. leur isomolécularité. Cet avantage intrinsèque a permis de mettre au point le système modèle pour compléter l'étude du chapitre 7, qui implique un mélange de verres moléculaires photoactifs et photopassifs pour mieux découpler l'effet de la $T_g$ et du contenu en azo sur l'inscription des

SRGs, sans devoir tenir compte des facteurs dont l'influence est difficile à évaluer, comme l'enchevêtrement des chaînes polymères ou les différences de propriétés optiques des matériaux. Encore une fois, les connaissances acquises grâce aux travaux des chapitres 2 et 3 ont permis la sélection de verres photopassifs avec de bons GFA et GS pour éviter les risques de cristallisation des matériaux. Il a été possible de conclure que l'intervalle idéal de $T_g$ pour une inscription rapide de SRGs efficaces, lorsque des matériaux contenant 40 mol% de gDR1 sont utilisés, se situe entre ~45 et 60 °C. Ce résultat a un impact direct sur le choix des groupements fonctionnels lors de la conception d'un nouveau verre moléculaire (qui peut être guidée par les tendances observées aux chapitres 2 à 4), mais aussi sur la sélection de molécules photosensibles, utilisées seules, ou dans un mélange, pouvant aussi inclure les complexes polymères avec des molécules organiques de petite taille, pour optimiser la préparation de tels matériaux.

## 8.2 Optimisation de la préparation et de l'utilisation des verres moléculaires

À la suite de ce survol des travaux ayant couvert les trois objectifs de la thèse, il est possible de faire un retour sur le but principal, qui consistait à établir des liens entre la structure des verres moléculaires et leurs propriétés pour optimiser leur préparation et leur utilisation. Les travaux présentés ont permis de dégager quelques lignes directrices, un peu à la manière de celles retrouvées dans les travaux de Shirota[10] ou de Naito.[11] L'élément le plus important à retenir dans ce processus de réflexion est que chaque changement dans la nature ou la position du groupement peut avoir une influence sur le GFA, le GS ou la $T_g$ des verres moléculaires, et ce, même s'il peut sembler subtil. Ainsi, les lignes directrices ou les prédictions proposées dans le Tableau 8.1 ne sont pas des règles absolues, mais bien des indications qui peuvent guider les hypothèses lors de la conception de nouveaux composés, qu'ils soient fonctionnels ou non. Le tableau classe le GFA et la $T_g$ des composés dans différentes catégories: possibilité ou non d'établir des liaisons H au niveau des groupements de tête et liants, et structure aromatique ou aliphatique pour les groupements auxiliaires. La couleur verte est utilisée pour un bon GFA et une $T_g$ élevée, alors que la couleur rouge est employée pour un mauvais GFA et une valeur faible de $T_g$.

**Tableau 8.1.** Sommaire de l'influence de la nature et de la position des groupements substituants sur la triazine. Dans le cas du GFA, le vert indique une bonne capacité du composé à former une phase vitreuse et le rouge, une mauvaise. Dans le cas de la $T_g$, le vert indique une valeur élevée, alors que le rouge indique une valeur faible. L'italique est utilisé pour les hypothèses.

| **Groupements auxiliaires** | **Groupement de tête** | | | | | |
|---|---|---|---|---|---|---|
| | Possibilité de liaisons H | | | Impossibilité de liaisons H | | |
| | **Groupements liants** | | | | | |
| | Possibilité de liaisons H | Encombrant | Barrière de rotation faible (O) | Possibilité de liaisons H | Encombrant | Barrière de rotation faible (O) |
| Aromatiques (sans halogène, substitution 3,5) | **GFA** $T_g$ | **GFA** $T_g$ | **GFA** $T_g$ | **GFA** $T_g$ | ***GFA*** $T_g$ | **GFA** $T_g$ |
| Aliphatiques | **GFA** $T_g$ | ***GFA*** $T_g$ | ***GFA*** $T_g$ | **GFA** $T_g$ | ***GFA*** $T_g$ | ***GFA*** $T_g$ |

Pour concevoir un composé avec un bon GFA et une $T_g$ élevée, il serait avantageux d'employer les liaisons H, autant au niveau des groupements liants que du groupement de tête, combinées à des groupements auxiliaires aromatiques, de préférence substitués en *meta*. Les groupements encombrants au niveau des groupements liants peuvent également favoriser un bon GFA, avec le compromis d'une $T_g$ plus faible. Le choix d'un groupement liant capable d'abaisser la barrière énergétique de rotation comme le O pour augmenter la $T_g$ sans utiliser de liaison H est possible, mais avec la mise en garde que les composés pourront explorer leur profil énergétique et cristalliser plus facilement (diminuant ainsi le GS des composés). Le choix d'un groupement aliphatique abaisse la $T_g$, tout en rendant pire le GFA des composés, surtout lorsque les liaisons H sont possibles.

Ces indications mènent à la conclusion que la nature et la position de chaque groupement affectent les propriétés des verres et que le choix dépend réellement des propriétés désirées selon les applications. Par exemple, si les circonstances exigent que le groupement de tête du composé ne soit pas capable d'établir des liaisons H mais que la $T_g$ du composé soit élevée avec un bon GFA, e.g. pour une meilleure stabilité cinétique lorsque préparés par PVD pour un usage au-dessus de la température ambiante, des groupements auxiliaires aromatiques substitués avec des méthyles pourraient être envisageable. Toutefois, on peut supposer que ces groupements ne seraient pas nécessaires dans le cas où des groupements liants encombrants, de type NMe, soient employés lorsqu'une $T_g$ faible et un bon GFA sont requis. Ces lignes directrices s'appliquent

tout particulièrement dans le cas où des verres moléculaires à base de triazine fonctionnalisés avec un azo seraient préparés par PVD. Une hypothèse serait que l'obtention de verres encore plus photostables pourrait être possible avec des composés qui ne présentent pas de capacité à établir des liaisons H, avec des groupements liants O et un groupement auxiliaire fonctionnalisé par des méthyles à la position *meta* pour conserver une $T_g$ élevée et permettre un bon GFA.

## 8.3 Méthodes et caractérisations développées pendant la thèse

Outre l'exploration des différentes influences des groupements sur les propriétés des verres à base de triazine, la thèse a également permis la mise au point de quelques méthodes de caractérisation se révélant être intéressantes pour la suite du projet, apportant ainsi une autre dimension aux travaux présentés. De manière générale, elles ont permis de rendre plus quantitatives les observations qualitatives rapportées précédemment, offrant ainsi un référentiel facilitant les comparaisons des travaux futurs. Tout d'abord, l'échelle de GFA présentée au chapitre 2 permet d'établir une classification des composés non équivoque, tout en offrant une certaine flexibilité par rapport aux bornes des vitesses de refroidissement critiques attribuées à chaque niveau de GFA, qui pourraient être ajustées au besoin. Elle permet également de mettre en contexte les vitesses de refroidissement critiques en évaluant comment elles se comparent à celles d'autres matériaux amorphes.

Les travaux des chapitres 3 à 5 ont bénéficié des mesures de spectroscopie IR à température variable combinées aux analyses chimiométriques, pour quantifier les liaisons H, dont l'importance était soulignée dans les hypothèses provenant des travaux antérieurs, mais de manière qualitative. Cela a permis de confirmer que les liaisons H sont bien présentes à l'état visqueux (par exemple, pour le composé avec le groupement de tête NHMe, les deux groupements liants NH et les deux groupements auxiliaires mexyles, 65% des groupements NH étaient liés à près de 40 °C au-dessus de sa $T_g$) tout en révélant davantage d'information sur leur dynamique: en refroidissement, le début de la transition vitreuse coïncide avec l'arrêt de l'augmentation de la fraction de NH liés. Bien que les fractions rapportées ne soient pas nécessairement exactes, elles sont assez reproductibles pour être corrélées à la $T_g$ de molécules provenant de différentes librairies, comme c'est le cas entre celles des chapitres 3 et 4. La méthode donne aussi accès à l'enthalpie de formation de la liaison H, une valeur qui peut être

utile pour évaluer si les résultats des travaux de simulation sont d'un ordre de grandeur raisonnable.

Ces nombres relatifs aux liaisons H sont très pertinents pour approfondir le lien entre les liaisons H et la stabilité cinétique observée lors de la préparation des verres par PVD. Cette méthode pourrait aider à établir des corrélations quantitatives, dans un contexte où, à l'heure actuelle, seules des hypothèses découlant d'observations qualitatives sont utilisées pour tenter de relier les interactions intermoléculaires, la stabilité cinétique, et le coefficient de diffusion de surface d'un composé. D'ailleurs, le stage que l'auteure de cette thèse a effectué dans le groupe de recherche Ediger a permis de démarrer un projet, présentement en cours dans le groupe de recherche Yu (*University of Wisconsin-Madison*), impliquant des mesures de diffusion de surface sur les dérivés à base de triazine, rendues possible grâce à la $T_g$ des composés supérieure à la température ambiante, facilitant les mesures.

Finalement, la méthode de spectroscopie IR développée au chapitre 6 est particulièrement intéressante, puisqu'elle n'introduit pas de molécules susceptibles de perturber l'environnement qui doit être étudié, comme c'est parfois le cas avec des molécules sondes fluorescentes.[12] Toutefois, une méthode IR impliquant des mesures en transmission (au lieu de type ATR) gagnerait à être développée pour s'assurer de sonder l'ensemble de l'échantillon. Finalement, le choix d'exploiter un mélange de molécules organiques de petite taille, comme c'est le cas au chapitre 7, permet à la fois d'exploiter l'excellent GFA des verres tout en mettant à profit leur isomolécularité pour mieux cibler l'influence de paramètres autrement difficiles à dissocier d'autres facteurs. Dans les deux cas, des applications supplémentaires seront discutées dans les axes de recherches proposés dans la section suivante, pour faire ressortir leur importance respective.

## 8.4 Perspectives

La Figure 8.1 présente l'écosystème simplifié des verres moléculaires, afin de mettre en valeur les contributions originales de l'auteure de cette thèse à l'avancement des connaissances dans le domaine. Ces dernières sont en caractère gras, autant pour les travaux qui ont été présentés (chapitres 2 à 7) que ceux qui sont à venir (fond jaune). Le système modèle choisi a

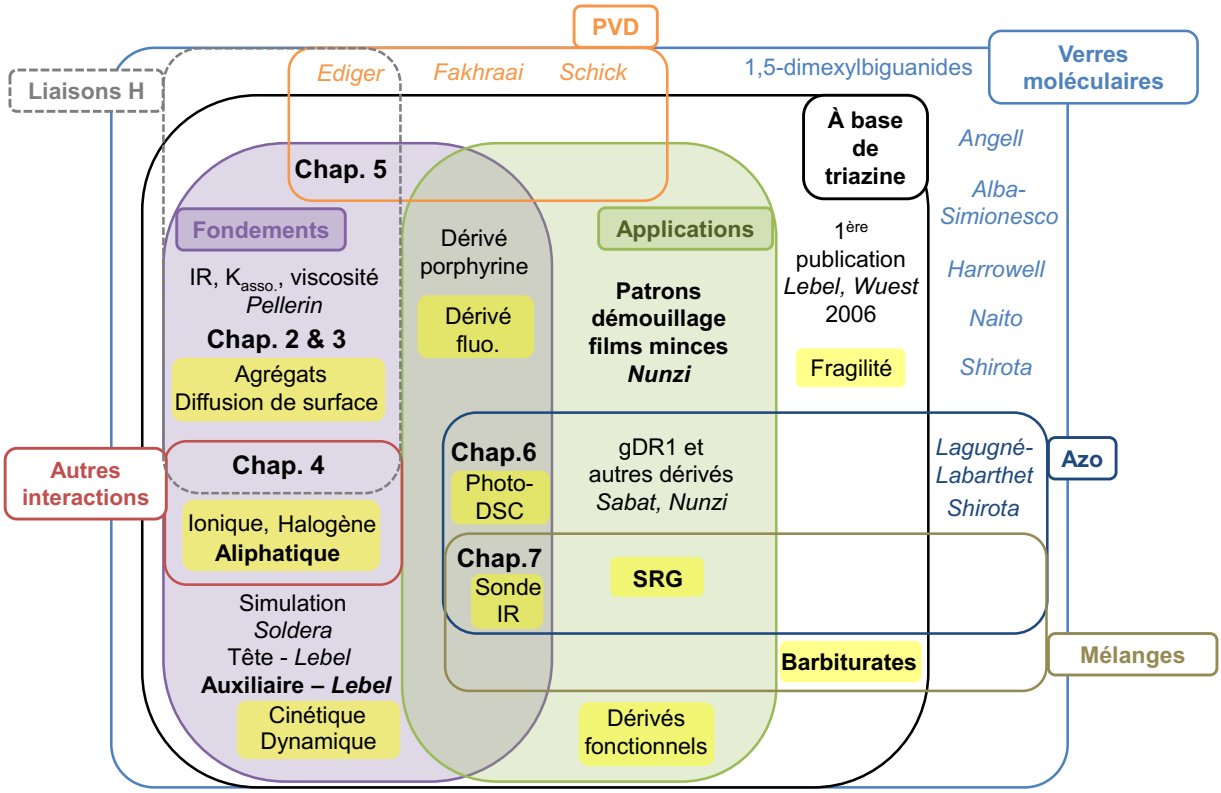


**Figure 8.1.** Écosystème simplifié du domaine des verres moléculaires. Le gras est utilisé pour représenter les contributions de l'auteure de cette thèse. Les encadrés jaunes indiquent quelques-uns des projets suggérés. L'italique est utilisé pour identifier quelques-uns des directeurs de groupes de recherche reliés au domaine.

permis d'explorer des sphères de recherche relatives autant aux fondements qu'aux applications, de complémenter et de rendre possible de nouvelles collaborations, mais aussi d'étudier des matériaux avec une certaine fonctionnalité. Le grand nombre de sous-espaces explorés, qui se reflètent par la publication des six chapitres de discussion dans six périodiques différents, démontre la polyvalence du système modèle. Cette dernière donne la latitude nécessaire pour explorer les axes de recherche discutés ci-dessous, et bien d'autres. Cette discussion a pour but d'ouvrir la voie à d'autres projets, mais aussi à la création d'autres sous-espaces de recherche pour venir enrichir l'écosystème présenté. Les lignes directrices qui ressortiront de ces études futures feront progresser celles dégagées au cours de cette thèse et permettront ainsi d'accéder

à un plus grand « coffre à outils » pour concevoir des verres moléculaires adaptés selon la condition de préparation voulue et les propriétés recherchées.

### 8.4.1 Autres interactions intermoléculaires

Étant donné que l'une des deux hypothèses provenant des travaux antérieurs concernait le rôle des liaisons H pendant la vitrification, il était logique de poursuivre les travaux de cette thèse à ce sujet. Toutefois, l'influence d'autres types d'interactions intermoléculaires gagnerait à être étudiée pour qu'elles soient introduites dans la structure des verres en ayant une meilleure idée de leur rôle. Par exemple, les liaisons ioniques, déjà abordées dans le cas des verres à base de 1,5-dimexylebiguanides[13] ou même très brièvement dans la préparation de films avec différents patrons de démouillage,[14] mériteraient d'être étudiées plus en profondeur. C'est aussi le cas pour les interactions impliquant des halogènes.[15] Leur directionnalité est déjà employée en tectonique moléculaire pour obtenir des cristaux et co-cristaux[16] ou même en chimie supramoléculaire.[17] Il serait justement pertinent d'évaluer si les liaisons H propres aux verres à base de triazine nuisent à cette directionnalité (un peu comme c'est le cas avec les dérivés stilbènes discutés au chapitre 4). Sachant que la polarisabilité des halogènes influence la $T_g$ (chapitre 2), il serait intéressant de confirmer comment ils affectent le GFA et le GS des composés.

De plus, une étude est présentement en cours pour vérifier l'influence des groupements cycliques mais non aromatiques (dans ce cas précis, le cyclohexyle) à la position des groupements auxiliaires. On suppose que l'encombrement stérique supplémentaire qu'ils provoquent, un peu à la manière des groupes liants NMe, pourraient favoriser le GFA des composés, permettant la présence de liaisons H pour obtenir une valeur de $T_g$ élevée, sans nécessiter la présence de groupements auxiliaires mexyles. En plus de reprendre le concept d'échelle de GFA du chapitre 2, des études sur la cinétique de cristallisation sont envisagées pour évaluer le GS d'une manière plus quantitative et ainsi pouvoir mieux déterminer si ce paramètre peut être corrélé à d'autres.

### 8.4.2 Liaisons H et agrégats

Regardés sous un autre angle, les travaux du chapitre 5 permettent d'évaluer l'influence de la méthode de préparation sur le nombre de liaisons H formées. Dans la même lignée, il serait intéressant d'employer la méthode chimiométrique développée au chapitre 3 pour quantifier le nombre de groupes NH liés lorsque les verres à base de triazine sont refroidis à partir de leur état liquide avec des vitesses ultrarapides à l'aide d'un appareil de flash DSC.[18] Même si un suivi *in situ* n'est pas possible, le nombre de liaisons H à l'état vitreux pourrait être comparé pour différents verres moléculaires refroidis à différentes vitesses pour évaluer s'il existe une limite inférieure de groupes NH liés pour que le composé passe à l'état vitreux. Des expériences analogues pourraient être faites avec des expériences d'évaporation de solvant à vitesse contrôlée.

Le thème de l'agrégation des molécules, qui constituait la deuxième hypothèse découlant des travaux antérieurs à cette thèse, mériterait d'être revisité. Entre autres abordée à la suite de mesures de viscosité,[2] la présence d'agrégats à l'état liquide et à l'état vitreux pourrait être évaluée grâce à des mesures de spectroscopie infrarouge à température variable combinées à des mesures de cisaillement. Ce genre de mesures permettrait de suivre l'évolution du nombre de liaisons H et corréler leur variation (ou changement de variation) aux transitions qui sont observées d'un point de vue rhéologique, un peu à la manière de ce qui a été fait à la Figure 3.3. Ce type d'études a déjà été réalisé, mais de façon computationnelle,[19] puisque les mesures présentent un défi technique non négligeable. Une des études a modélisé le comportement d'un réseau de molécules en deux dimensions liées entre elles par des liaisons H en vue d'évaluer leur potentiel lubrifiant, une propriété qui pourrait être exploitée pour des verres à base de triazine. Des mesures en cisaillement donneraient également accès aux temps de relaxation des matériaux à différentes températures, ce qui permettrait de calculer leur fragilité. Bien que Baird *et al.*[20] n'aient pas ressorti de corrélation directe entre la fragilité des composés et leur GFA, le nombre de liaisons H serait un nouveau paramètre avec lequel certaines corrélations pourraient être tentées.

### 8.4.3 Dynamique intra- et intermoléculaire

Les mesures de viscosité discutées dans la section précédente pourraient apporter des informations sur la dynamique du verre. Dans le même ordre d'idée, un autre type de mesures qui pourraient renseigner sur la dynamique et les temps de relaxation seraient celles combinant des mesures de spectroscopie IR à température variable avec des mesures de spectroscopie diélectrique, qui présentent encore une fois un défi technique. Ces mesures permettraient d'attribuer des groupements fonctionnels, ou l'établissement d'interactions entre des groupements fonctionnels, aux fréquences des transitions observées en spectroscopie diélectrique. Le groupe de recherche Kremer s'est d'ailleurs intéressé à de telles corrélations, sans toutefois que les mesures soient réalisées de manière simultanée.[21] La dynamique du fucose, un saccharide, a été étudiée lors de son vieillissement physique (en dessous de sa $T_g$) et à une température équivalente à 1,16 $T_g$. Les résultats ont montré que l'établissement d'interactions entre les groupements CH et O était impliqué dans la transition vitreuse, alors que seul un réarrangement du réseau de liaisons H se produisait pendant le vieillissement physique. De tels résultats à propos de verres à base de triazine seraient très enrichissants pour approfondir notre compréhension de leur dynamique intra- et intermoléculaire.

La poursuite des travaux de simulation avec le groupe de recherche Soldera serait également appropriée pour mieux comprendre l'influence des rotations des groupements auxiliaires et évaluer si cette dynamique intramoléculaire pourrait être reliée à la fragilité et/ou au GFA des composés. De tels résultats computationnels auraient avantage à être combinés à des résultats expérimentaux de résonance magnétique nucléaire (RMN) du $^{1}H$, du $^{13}C$ ou même du $^{15}N$ à l'état solide. Cette approche est notamment utilisée par le groupe de recherche de Taylor en complément des mesures de spectroscopie IR pour mieux comprendre les interactions entre le principe actif et le polymère utilisé comme stabilisant.[22-23] D'ailleurs, d'autres techniques spectroscopiques gagneraient à être explorées, comme la spectroscopie dans le domaine du terahertz, puisque Sibik *et al.* suggèrent que les fréquences enregistrées dans ce domaine en dessous de la $T_g$ du naproxène, un anti-inflammatoire capable d'établir des liaisons H, pourraient être corrélées à son GS.[24]

### 8.4.4 Mélanges de verres moléculaires

Employé au chapitre 7 pour mieux contrôler les paramètres étudiés, le concept de mélanges de verres photopassifs et photoactifs pourrait être repris pour, par exemple, évaluer à la fois l'influence de la concentration de fluorophores et de la $T_g$ sur les propriétés d'émission des matériaux fluorescents. Des mélanges à base de verres fluorescents (par exemple, avec une unité pyrène liée comme groupement auxiliaire sur la triazine) et de verres photopassifs possédant différentes $T_g$ seraient faisables. Toutefois, cela implique la synthèse d'un nouveau composé. Bien que les synthèses employées pour la préparation des composés à base de triazine soient relativement simples et mènent à un bon rendement, il serait encore plus efficace de pouvoir mélanger physiquement un verre et une molécule présentant la fonctionnalité désirée, sans avoir recours à des stratégies de synthèse particulières. Toutefois, ces molécules organiques de petite taille qui présentent la fonctionnalité souhaitée ont souvent un mauvais GFA (une très forte propension à cristalliser) et ont tendance à s'agréger, causant une séparation de phase au sein du mélange.[25] À la suite des résultats du chapitre 4, il serait pertinent d'évaluer si les liaisons H peuvent empêcher l'agrégation et la cristallisation de ces molécules fonctionnelles lorsqu'il n'y a pas de lien covalent entre le dérivé de triazine et le composé reconnu pour sa capacité à cristalliser.

Le premier projet[*] de mélange exploré impliquait des dérivés de triazine et de barbiturates. Les dérivés de barbiturates ont été choisis puisque plusieurs travaux ont déjà exploité la complémentarité des interactions possibles avec des dérivés de triazine. Par exemple, le groupe de recherche Whitesides a utilisé des dérivés de mélamine et d'acide barbiturique pour préparer des co-cristaux en forme de rosette ou de ruban;[26] celui de Leblanc a employé la spectroscopie IR polarisée pour étudier l'arrangement à l'interface air-eau de mélanges de triaminotriazine et d'acide barbiturique[27] et celui de Leibler s'en est servi pour concevoir des matériaux supramoléculaires.[28] Notre étude a montré que des mélanges impliquant le verre avec le groupement de tête NHMe, les groupements liants NH et des mexyles comme groupements auxiliaires, et un dérivé barbiturate pouvaient former une phase amorphe même si la

[*] Projet partiellement réalisé par Dominic Lauzon, dans le cadre d'un stage de recherche à l'été 2014, sous la supervision de l'auteure de cette thèse.

concentration de barbiturate dépassait 90 mol%. Toutefois, une séparation de phases menant à la cristallisation du dérivé barbiturate se produit lorsque la longueur de la chaîne alkyle augmente sur le groupement de tête. Ce comportement est probablement dû à la diminution de l'accessibilité du groupe NH, restreignant les possibilités de liaison H avec le dérivé barbiturate.

Dans la même lignée, un deuxième projet[†] de mélange, cette fois-ci entre des verres photopassifs capables d'établir des liaisons H et des dérivés azos photosensibles (aussi capables d'établir, dans une certaine mesure, des liaisons H), a permis d'évaluer le potentiel de ce type de mélange pour l'inscription de SRG. Les résultats ont entre autres démontré que les groupements substituants sur le dérivé azo influencent grandement les propriétés du mélange résultant. En déterminant la $T_g$ des mélanges en fonction de la concentration de dérivé azo, il a été possible de sélectionner les matériaux les plus prometteurs en ayant comme ligne directrice la zone optimale de $T_g$ déterminée au chapitre 7. Les performances d'inscription et de diffraction des SRGs préparés sont tout de même acceptables, compte tenu du fait qu'aucune interaction spécifique n'est établie entre la matrice de verre et l'azo, contrairement, par exemple, aux complexes impliquant la poly(4-vinylpyridine) (P4VP) et des dérivés azo sélectionnés sur la base de leur capacité à interagir avec l'azote de la pyridine.[29]

### 8.4.5 Matériaux fonctionnels

Finalement, les matériaux fonctionnels à base de dérivés de triazine peuvent encore faire l'objet de nombreuses études, qu'elles soient fondamentales ou appliquées. Au niveau des matériaux photosensibles, la méthode IR développée au chapitre 6 pourrait servir à étudier les gradients d'environnements moléculaires créés en fonction de la polarisation de l'illumination. Ces travaux pourraient être poursuivis avec le gDR1, mais il serait intéressant de comparer les gradients pour la série de dérivés triazine fonctionnalisés avec différents type d'azos, ou même de l'appliquer aux complexes P4VP-azo mentionnés dans la section précédente. Des mesures de DSC sous ou après illumination pourraient également être un complément intéressant aux

[†] Projet partiellement réalisé par Sébastien Néron, dans le cadre d'un stage de recherche à l'été 2015, sous la supervision de l'auteure de cette thèse.

résultats obtenus avec la méthode IR, permettant de faire un pont entre des résultats moléculaires (IR) et macroscopiques (DSC).

Il a brièvement été mentionné dans la section précédente que d'autres dérivés que ceux de type azo pourraient être liés de manière covalente à la triazine. Il a été question de verre fonctionnalisé avec un groupement pyrène fluorescent, ce qui peut être intéressant dans la mesure où Chung *et al.* ont préparé des matériaux moléculaires amorphes mécanochromiques, pour lesquels le cisaillement provoquait la cristallisation qui était accompagnée d'une augmentation de la fluorescence d'un facteur de 25.[30] Ce type de dérivés avec des propriétés pouvant mener à des applications sont possibles avec les verres moléculaires à base de triazine. En effet, les groupes de recherche Lebel et Nunzi ont déjà démontré qu'il était possible de lier de manière covalente des dérivés de porphyrine ou même de pérylène diimide (PDI) tout en conservant l'excellent GFA des matériaux.[31] Les performances photovoltaïques de ces dérivés PDI ont d'ailleurs déjà été évaluées. La mise au point de molécules destinées à des systèmes électroluminescents serait à considérer compte tenu des propriétés électroniques de la triazine, déjà employée pour de tels dispositifs,[32-34] d'autant plus que la structure des composés pourrait être optimisée pour mener à des films amorphes déposés par PVD présentant une très grande stabilité cinétique.

## 8.5 Références


1. Angell, C. A.; Busse, L. E.; Cooper, E. I.; Kadiyala, R. K.; Dworkin, A.; Ghelfenstein, M.; Szwarc, H.; Vassal, A., *Journal de Chimie Physique et de Physico-Chimie Biologique* **1985,** *82*, 267-274.
2. Plante, A.; Mauran, D.; Carvalho, S. P.; Pagé, J. Y. S. D.; Pellerin, C.; Lebel, O., *J. Phys. Chem. B* **2009,** *113*, 14884-14891.
3. Wang, R.; Pellerin, C.; Lebel, O., *J. Mater. Chem.* **2009,** *19*, 2747-2753.
4. Kim, T.-D., et al., *J. Am. Chem. Soc.* **2007,** *129*, 488-489.
5. Gray, T.; Kim, T.-D.; Knorr, D. B.; Luo, J.; Jen, A. K. Y.; Overney, R. M., *Nano Lett.* **2008,** *8*, 754-759.
6. Zhou, X.-H., et al., *Adv. Mater.* **2009,** *21*, 1976-1981.

7. Coates, G. W.; Dunn, A. R.; Henling, L. M.; Ziller, J. W.; Lobkovsky, E. B.; Grubbs, R. H., *J. Am. Chem. Soc.* **1998,** *120*, 3641-3649.
8. Tang, C. W.; VanSlyke, S. A., *Appl. Phys. Lett.* **1987,** *51*, 913-915.
9. Chen, Y.; Zhang, W.; Yu, L., *J. Phys. Chem. B* **2016,** *120*, 8007-8015.
10. Shirota, Y., *J. Mater. Chem.* **2005,** *15*, 75-93.
11. Naito, K.; Miura, A., *J. Phys. Chem.* **1993,** *97*, 6240-6248.
12. Arai, S.; Lee, S.-C.; Zhai, D.; Suzuki, M.; Chang, Y. T., *Sci. Rep.* **2014,** *4*, 6701.
13. Meunier, A.; Lebel, O., *Org. Lett.* **2010,** *12*, 1896-1899.
14. Melito, E.; Laventure, A.; Aldea-Nunzi, G.; Pellerin, C.; Buncel, E.; Lebel, O.; Nunzi, J.-M., *J. Mater. Chem. C* **2015,** *3*, 4729-4736.
15. Cavallo, G.; Metrangolo, P.; Milani, R.; Pilati, T.; Priimagi, A.; Resnati, G.; Terraneo, G., *Chem. Rev.* **2016,** *116*, 2478-2601.
16. Aakeroy, C. B.; Chopade, P. D.; Desper, J., *Cryst. Growth Des.* **2013,** *13*, 4145-4150.
17. Gilday, L. C.; Robinson, S. W.; Barendt, T. A.; Langton, M. J.; Mullaney, B. R.; Beer, P. D., *Chem. Rev.* **2015,** *115*, 7118-7195.
18. Poel, G. V.; Istrate, D.; Magon, A.; Mathot, V., *J. Therm. Anal. Calorim.* **2012,** *110*, 1533-1546.
19. Whyte, S. A.; Mosey, N. J., *J. Phys. Chem. C* **2015,** *119*, 350-364.
20. Baird, J.; Santiago-Quinonez, D., *Pharm. Res.* **2012,** *29*, 271-84.
21. Kossack, W., et al., *Phys. Chem. Chem. Phys.* **2013,** *15*, 20641-50.
22. Nie, H.; Su, Y.; Zhang, M.; Song, Y.; Leone, A.; Taylor, L. S.; Marsac, P. J.; Li, T.; Byrn, S. R., *Mol. Pharm.* **2016,** *13*, 3964-3975.
23. Yuan, X.; Xiang, T.-X.; Anderson, B. D.; Munson, E. J., *Mol. Pharm.* **2015,** *12*, 4518-4528.
24. Sibik, J.; Löbmann, K.; Rades, T.; Zeitler, J. A., *Mol. Pharm.* **2015,** *12*, 3062-3068.
25. Pajula, K.; Taskinen, M.; Lehto, V.-P.; Ketolainen, J.; Korhonen, O., *Mol. Pharm.* **2010,** *7*, 795-804.
26. Zerkowski, J. A.; Seto, C. T.; Whitesides, G. M., *J. Am. Chem. Soc.* **1992,** *114*, 5473-5475.
27. Huo, Q.; Dziri, L.; Desbat, B.; Russell, K. C.; Leblanc, R. M., *J. Phys. Chem. B* **1999,** *103*, 2929-2934.

28. Cortese, J.; Soulié-Ziakovic, C.; Tencé-Girault, S.; Leibler, L., *J. Am. Chem. Soc.* **2012,** *134*, 3671-3674.
29. Vapaavuori, J.; Heikkinen, I. T. S.; Dichiarante, V.; Resnati, G.; Metrangolo, P.; Sabat, R. G.; Bazuin, C. G.; Priimagi, A.; Pellerin, C., *Macromolecules* **2015,** *48*, 7535-7542.
30. Chung, K., et al., *ACS Cent. Sci.* **2015,** *1*, 94-102.
31. Adhikari, T.; Ghoshouni Rahami, Z.; Nunzi, J.-M.; Lebel, O., *Org. Electron.* **2016,** *34*, 146-156.
32. Fink, R.; Frenz, C.; Thelakkat, M.; Schmidt, H.-W., *Macromolecules* **1997,** *30*, 8177-8181.
33. Murase, T.; Fujita, M., *J. Org. Chem.* **2005,** *70*, 9269-9278.
34. Wagner, D.; Hoffmann, S. T.; Heinemeyer, U.; Münster, I.; Köhler, A.; Strohriegl, P., *Chem. Mater.* **2013,** *25*, 3758-3765.

# Annexe I: Caractérisation des composés 2b-q et 4a-q – Chapitre 2

*2-Methylamino-4,6-bis[(2-methylphenyl)amino]-1,3,5-triazine (**2b**)*

The mixture was refluxed for 3 days. Yield: 62 %; $T_g$ 55 °C, $T_c$ 128 °C, $T_m$ 149 °C; FTIR (ATR/$CH_2Cl_2$) 3422, 3262, 3165, 3060, 2952, 1573, 1502, 1487, 1451, 1412, 1397, 1359, 1293, 1251, 1190, 1172, 1117, 1047, 1007, 989, 938, 859, 810, 748, 717 $cm^{-1}$; $^1H$ NMR (300 MHz, DMSO-$d_6$, 298 K) δ 8.23 (br s, 1H), 8.10 (br s, 1H), 7.55 (d, $^3J$ = 7.0 Hz, 1H), 7.43 (d, $^3J$ = 7.0 Hz, 1H), 7.16 (d, $^3J$ = 7.0 Hz, 2H), 7.10 (d, $^3J$ = 7.6 Hz, 2H), 7.00 (t, $^3J$ = 7.0 Hz, 2H), 6.76 (br q, $^3J$ = 5.3 Hz, 1H), 2.73 (d, $^3J$ = 4.7 Hz, 3H), 2.23 (s, 3H), 2.20 (s, 3H) ppm; $^1H$ NMR (400 MHz, DMSO-$d_6$, 363 K) δ 7.75 (s, 2H), 7.58 (d, $^3J$ = 7.8 Hz, 2H), 7.16 (d, $^3J$ = 7.3 Hz, 2H), 7.11 (t, $^3J$ = 7.1 Hz, 2H), 7.00 (t, $^3J$ = 7.6 Hz, 2H), 6.41 (br s, 1H), 2.77 (d, $^3J$ = 4.7 Hz, 3H), 2.24 (s, 6H) ppm; $^{13}C$ NMR (75 MHz, DMSO-$d_6$) δ 166.4, 164.9, 137.6, 132.3, 131.8, 129.9, 125.9, 125.6, 124.1, 124.0, 27.1, 18.1 ppm; HRMS (ESI, $MNa^+$) calcd. for $C_{18}H_{20}NaN_6$ *m/e*: 343.1642, found: 343.1644.

*2-Methylamino-4,6-bis[(3-methylphenyl)amino]-1,3,5-triazine (**2c**)*

Yield: 77 %; $T_g$ 60 °C; FTIR (ATR/$CH_2Cl_2$) 3411, 3277, 3183, 3050, 2950, 2920, 1580, 1558, 1511, 1487, 1426, 1400, 1361, 1294, 1256, 1243, 1178, 1167, 1092, 1036, 1000, 975, 924, 892, 866, 809, 777, 748, 691 $cm^{-1}$; $^1H$ NMR (300 MHz, DMSO-$d_6$, 298 K) δ 9.07 (br s, 1H), 8.92 (br s, 1H), 7.60 (m, 4H), 7.13 (t, $^3J$ = 7.6 Hz, 2H), 6.93 (br s, 1H), 6.76 (d, $^3J$ = 7.6 Hz, 2H), 2.85 (d, $^3J$ = 4.7 Hz, 3H), 2.27 (s, 6H) ppm; $^1H$ NMR (400 MHz, DMSO-$d_6$, 363 K) δ 8.54 (s, 2H), 7.57 (m, 4H), 7.13 (t, $^3J$ = 7.3 Hz, 2H), 6.78 (d, $^3J$ = 7.8 Hz, 2H), 6.54 (br s, 1H), 2.89 (d, $^3J$ = 4.8 Hz, 3H), 2.29 (s, 6H) ppm; $^{13}C$ NMR (75 MHz, DMSO-$d_6$) δ 166.0, 164.2, 163.9, 140.2, 137.3, 128.1, 122.2, 120.4, 117.0, 27.3, 21.2 ppm; HRMS (ESI, $MNa^+$) calcd. for $C_{18}H_{20}NaN_6$ *m/e*: 343.1642, found: 343.1644.

*2-Methylamino-4,6-bis[(4-methylphenyl)amino]-1,3,5-triazine (**2d**)*

Yield: 82 %; $T_g$ 67 °C, $T_c$ 139 °C, $T_m$ 169 °C; FTIR (ATR/$CH_2Cl_2$) 3415, 3280, 3199, 3109, 3026, 2945, 2921, 2868, 1575, 1496, 1419, 1403, 1361, 1312, 1292, 1241, 1181, 1168, 1148, 1122, 1076, 1040, 1019, 936, 809, 736, 706, 672 $cm^{-1}$; $^1H$ NMR (300 MHz, DMSO-$d_6$, 298 K) δ 9.02 (br s, 1H), 8.88 (br s, 1H), 7.67 (br s, 4H), 7.05 (d, $^3J$ = 8.2 Hz, 4H), 6.89 (br s, 1H), 2.83 (d, $^3J$ = 4.7 Hz, 3H), 2.25 (s, 6H) ppm; $^1H$ NMR (400 MHz, DMSO-$d_6$, 363 K) δ 8.51 (s, 2H), 7.63 (d, $^3J$ = 8.6 Hz, 4H), 7.06 (d, $^3J$ = 8.1 Hz, 4H), 6.50 (br s, 1H), 2.87 (d, $^3J$ = 4.5 Hz, 3H), 2.27 (s, 6H) ppm; $^{13}C$ NMR (75 MHz, DMSO-$d_6$) δ 166.0, 164.0, 163.8, 137.8, 130.2, 128.6, 119.8, 27.3, 20.3 ppm; HRMS (ESI, $MNa^+$) calcd. for $C_{18}H_{20}NaN_6$ *m/e*: 343.1642, found: 343.1645.

*2-Methylamino-4,6-bis[(2,3-dimethylphenyl)amino]-1,3,5-triazine (**2e**)*

The mixture was refluxed for 3 days. Yield: 76 %; $T_g$ 70 °C; FTIR (ATR/$CH_2Cl_2$) 3419, 3255, 3163, 3064, 3028, 2944, 2919, 1575, 1501, 1457, 1410, 1398, 1359, 1276, 1189, 1152, 1111, 1095, 1074, 1044, 1018, 992, 895, 811, 767, 738, 708 $cm^{-1}$; $^1H$ NMR (300 MHz, DMSO-

$d_6$, 298 K) δ 8.30 (br s, 1H), 8.15 (br s, 1H), 7.24 (br d, $^3J$ = 5.3 Hz, 1H), 7.12 (br d, $^3J$ = 5.9 Hz, 1H), 6.99 (t, $^3J$ = 7.6 Hz, 2H), 6.92 (d, $^3J$ = 7.6 Hz, 2H), 6.67 (q, $^3J$ = 4.7 Hz, 1H), 2.70 (d, $^3J$ = 4.7 Hz, 3H), 2.22 (s, 6H), 2.06 (s, 3H), 2.03 (s, 3H) ppm; $^1$H NMR (400 MHz, DMSO-$d_6$, 363 K) δ 7.79 (s, 2H), 7.28 (d, $^3J$ = 7.8 Hz, 2H), 6.98 (t, $^3J$ = 7.8 Hz, 2H), 6.93 (d, $^3J$ = 7.1 Hz, 2H), 6,33 (br s, 1H), 2.74 (d, $^3J$ = 4.8 Hz, 3H), 2.25 (s, 6H), 2.10 (s, 6H) ppm; $^{13}$C NMR (75 MHz, DMSO-$d_6$) δ 166.4, 165.2, 137.5, 136.3, 132.0, 131.4, 126.0, 125.9, 124.7, 124.5, 124.1, 27.1, 20.2, 14.3 ppm; HRMS (ESI, $MNa^+$) calcd. for $C_{20}H_{24}NaN_6$ *m/e*: 371.1955, found: 371.1947.

*2-Methylamino-4,6-bis[(2,4-dimethylphenyl)amino]-1,3,5-triazine (**2f**)*

The mixture was refluxed for 3 days. Yield: 78 %; $T_g$ 54 °C, $T_m$ 170 °C; FTIR (ATR/$CH_2Cl_2$) 3417, 3262, 3168, 3012, 2945, 2921, 2860, 1573, 1490, 1448, 1399, 1377, 1359, 1294, 1266, 1219, 1173, 1157, 1126, 1035, 1013, 933, 872, 811, 736, 703 cm$^{-1}$; $^1$H NMR (300 MHz, DMSO-$d_6$, 298 K) δ 8.09 (br s, 1H), 7.96 (br s, 1H), 7.34 (d, $^3J$ = 6.4 Hz, 1H), 7.21 (d, $^3J$ = 7.6 Hz, 1H), 6.94 (s, 2H), 6.88 (d, $^3J$ = 7.0 Hz, 2H), 6.66 (br q, $^3J$ = 4.7 Hz, 1H), 2.67 (d, $^3J$ = 4.1 Hz, 3H), 2.22 (s, 6H), 2.16 (s, 3H), 2.13 (s, 3H) ppm; $^1$H NMR (400 MHz, DMSO-$d_6$, 363 K) δ 7.64 (s, 2H), 7.40 (d, $^3J$ = 8.1 Hz, 2H), 6.98 (s, 2H), 6.91 (d, $^3J$ = 8.1 Hz, 2H), 6.33 (br s, 1H), 2.75 (d, $^3J$ = 4.5 Hz, 3H), 2.26 (s, 6H), 2.20 (s, 6H) ppm; $^{13}$C NMR (75 MHz, DMSO-$d_6$) δ 166.3, 165.0, 135.0, 133.2, 132.9, 132.6, 131.9, 130.4, 126.1, 125.7, 27.1, 20.4, 18.0 ppm; HRMS (ESI, $MNa^+$) calcd. for $C_{20}H_{24}NaN_6$ *m/e*: 371.1955, found: 371.1952.

*2-Methylamino-4,6-bis[(2,5-dimethylphenyl)amino]-1,3,5-triazine (**2g**)*

The mixture was refluxed for 3 days. Yield: 61 %; $T_g$ 66 °C; FTIR (ATR/$CH_2Cl_2$) 3416, 3261, 3162, 3022, 2949, 2921, 2863, 1591, 1570, 1515, 1481, 1456, 1410, 1358, 1291, 1263, 1247, 1210, 1167, 1148, 1128, 1036, 997, 940, 877, 808, 736 cm$^{-1}$; $^1$H NMR (300 MHz, DMSO-$d_6$, 298 K) δ 8.15 (br s, 1H), 8.01 (br s, 1H), 7.35 (s, 1H), 7.22 (s, 1H), 7.03 (d, $^3J$ = 7.6 Hz, 2H), 6.81 (d, $^3J$ = 7.6 Hz, 2H), 6.75 (br q, $^3J$ = 4.7 Hz, 1H), 2.73 (d, $^3J$ = 4.7 Hz, 3H), 2.20 (s, 6H), 2.18 (s, 3H), 2.15 (s, 3H) ppm; $^1$H NMR (400 MHz, DMSO-$d_6$, 363 K) δ 7.68 (s, 2H), 7.38 (s, 2H), 7.03 (d, $^3J$ = 7.8 Hz, 2H), 6.81 (d, $^3J$ = 7.6 Hz, 2H), 6.41 (br s, 1H), 2.77 (d, $^3J$ = 4.8 Hz, 3H), 2.22 (s, 6H), 2.18 (s, 6H) ppm; $^{13}$C NMR (75 MHz, DMSO-$d_6$) δ 166.3, 164.8, 137.4, 134.6, 129.7, 129.1, 128.6, 126.3, 125.9, 124.8, 124.6, 27.0, 20.5, 17.5 ppm; HRMS (ESI, $MH^+$) calcd. for $C_{20}H_{25}N_6$ *m/e*: 349.2141, found: 349.2149.

*2-Methylamino-4,6-bis[(2,6-dimethylphenyl)amino]-1,3,5-triazine (**2h**)*

Dioxane was used as the solvent instead of THF, and the mixture was refluxed for 3 days. Yield: 81 %; $T_g$ 89 °C; FTIR (ATR/$CH_2Cl_2$) 3419, 3393, 3254, 3176, 3041, 3022, 2954, 2920, 2855, 1596, 1571, 1557, 1495, 1477, 1439, 1409, 1396, 1373, 1358, 1265, 1219, 1165, 1146, 1098, 1076, 1035, 989, 921, 875, 849, 811, 767, 736, 702, 690 cm$^{-1}$; $^1$H NMR (400 MHz, DMSO-$d_6$, 363 K) δ 7.67 (s, 2H), 7.01 (s, 6H), 6.18 (br s, 1H), 2.64 (d, $^3J$ = 4.5 Hz, 3H), 2.17 (s, 12H) ppm; $^{13}$C NMR (75 MHz, DMSO-$d_6$) δ 166.5, 165.2, 136.7, 136.0, 127.4, 125.6, 27.0, 18.5 ppm; HRMS (ESI, $MNa^+$) calcd. for $C_{20}H_{24}NaN_6$ *m/e*: 371.1955, found: 371.1957.

*2-Methylamino-4,6-bis[(3,4-dimethylphenyl)amino]-1,3,5-triazine (**2i**)*

Yield: 82 %; $T_g$ 71 °C; FTIR (ATR/$CH_2Cl_2$) 3400, 3277, 3185, 3021, 2967, 2940, 2920, 2862, 1572, 1497, 1450, 1412, 1359, 1305, 1253, 1211, 1163, 1122, 1078, 1021, 998, 872, 810, 706, 661 cm$^{-1}$; $^1$H NMR (300 MHz, DMSO-$d_6$, 298 K) δ 8.99 (br s, 1H), 8.85 (br s, 1H), 7.57

(br s, 1H), 7.50 (d, $^3J$ = 7.0 Hz, 3H), 7.00 (d, $^3J$ = 8.2 Hz, 2H), 6.93 (br s, 1H), 2.84 (d, $^3J$ = 4.7 Hz, 3H), 2.18 (s, 6H), 2.16 (s, 6H) ppm; $^1$H NMR (600 MHz, DMSO-$d_6$, 363 K) δ 8.45 (s, 2H), 7.49 (s, 2H), 7.44 (d, $^3J$ = 8.2 Hz, 2H), 7.00 (d, $^3J$ = 8.2 Hz, 2H), 6.53 (br s, 1H), 2.87 (s, 3H), 2.20 (s, 6H), 2.19 (s, 6H) ppm; $^{13}$C NMR (75 MHz, DMSO-$d_6$) δ 165.4, 163.6, 163.2, 137.7, 135.6, 129.2, 129.1, 121.2, 117.5, 27.2, 19.5, 18.5 ppm; HRMS (ESI, $MH^+$) calcd. for $C_{20}H_{25}N_6$ *m/e*: 349.2141, found: 349.2141.

*2-Methylamino-4,6-bis[(2,4,6-trimethylphenyl)amino]-1,3,5-triazine (**2j**)*

Dioxane was used as the solvent instead of THF, and the mixture was refluxed for 3 days. Yield: 82 %; $T_g$ 83 °C, $T_c$ 180 °C, $T_{dec}$ 249 °C; FTIR (ATR/$CH_2Cl_2$) 2415, 3381, 3250, 3185, 3163, 3004, 2953, 2919, 2857, 2731, 1569, 1558, 1492, 1436, 1411, 1396, 1374, 1360, 1309, 1264, 1229, 1174, 1155, 1140, 1077, 1035, 1012, 974, 937, 851, 811, 775, 736, 701, 679, 647 cm$^{-1}$; $^1$H NMR (400 MHz, DMSO-$d_6$, 363 K) δ 7.53 (s, 2H), 6.83 (s, 4H), 6.14 (br s, 1H), 2.65 (d, $^3J$ = 4.5 Hz, 3H), 2.24 (s, 6H), 2.14 (s, 12H) ppm; $^{13}$C NMR (75 MHz, DMSO-$d_6$) δ 166.6, 165.4, 135.7, 134.5, 134.1, 128.0, 27.1, 20.4, 18.4 ppm; HRMS (ESI, $MNa^+$) calcd. for $C_{22}H_{28}NaN_6$ *m/e*: 399.2268, found: 399.2270.

*2-Methylamino-4,6-bis[(3,5-difluorophenyl)amino]-1,3,5-triazine (**2k**)*

The mixture was refluxed for 3 days. Yield: 65 %; $T_g$ 54 °C, $T_c$ 84°C, $T_m$ 182, 191 °C; FTIR (ATR/$CH_2Cl_2$) 3460, 3428, 3290, 3223, 3123, 2954, 1625, 1594, 1559, 1516, 1478, 1436, 1412, 1364, 1304, 1255, 1216, 1186, 1170, 1153, 1115, 1082, 1034, 997, 983, 966, 837, 808, 747, 668 cm$^{-1}$; $^1$H NMR (300 MHz, DMSO-$d_6$, 298 K) δ 9.66 (br s, 1H), 9.54 (br s, 1H), 7.61 (br m, 4H), 7.40 (br s, 1H), 6.74 (br m, 2H), 2.85 (d, $^3J$ = 4.7 Hz, 3H) ppm; $^1$H NMR (400 MHz, DMSO-$d_6$, 363 K) δ 9.25 (s, 2H), 7.56 (d, $^3J_{H\text{-}F}$ = 8.3 Hz, 4H), 7.02 (br s, 1H), 6.64 (t, $^3J_{H\text{-}F}$ = 9.3 Hz, 2H), 2.90 (d, $^3J$ = 4.8 Hz, 3H) ppm; $^{13}$C NMR (75 MHz, DMSO-$d_6$) δ 165.8, 163.9, 163.5, [164.0, 163.8, 160.9, 160.6 (dd, $^1J_{C\text{-}F}$ = 241 Hz, $^2J_{C\text{-}F}$ = 15 Hz)], [143.1, 142.9, 142.7 (t, $^2J_{C\text{-}F}$ = 14 Hz)], [102.3, 102.2, 101.9, 101.8 (dd, $^2J_{C\text{-}F}$ = 29 Hz, $^3J_{C\text{-}F}$ = 7 Hz)], [96.7, 96.6, 96.3, 96.2, 96.0, 95.9 (dt, $^2J_{C\text{-}F}$ = 27 Hz, $^3J_{C\text{-}F}$ = 8 Hz)], 27.3 ppm; HRMS (ESI, $MNa^+$) calcd. for $C_{16}H_{12}F_4NaN_6$ *m/e*: 387.0952, found: 387.0956.

*2-Methylamino-4,6-bis[(3,5-dichlorophenyl)amino]-1,3,5-triazine (**2l**)*

Yield: 87 %; $T_g$ 83 °C, $T_c$ 135, 195 °C, $T_m$ 190, 212 °C; FTIR (ATR/$CH_2Cl_2$) 3242, 3415, 3396, 3275, 3178, 3113, 2958, 1606, 1570, 1519, 1500, 1413, 1358, 1303, 1267, 1253, 1226, 1170, 1150, 1114, 1082, 1015, 993, 924, 841, 807, 738, 691, 668 cm$^{-1}$; $^1$H NMR (300 MHz, DMSO-$d_6$, 298 K) δ 9.61 (br s, 1H), 9.46 (br s, 1H), 7.91 (br d, 4H), 7.38 (br s, 1H), 7.10 (t, $^4J$ = 1.7 Hz, 2H), 2.86 (d, $^3J$ = 4.7 Hz, 3H) ppm; $^1$H NMR (600 MHz, DMSO-$d_6$, 363 K) δ 9.17 (s, 2H), 7.88 (s, 4H), 7.06 (t, $^4J$ = 1.7 Hz, 2H), 7.01 (br s, 1H), 2.90 (d, $^3J$ = 4.7 Hz, 3H) ppm; $^{13}$C NMR (75 MHz, DMSO-$d_6$) δ 165.7, 163.8, 163.4, 142.6, 133.7, 120.5, 117.4, 27.2 ppm; HRMS (ESI, $MH^+$) calcd. for $C_{16}H_{13}Cl_4N_6$ *m/e*: 430.9922, found: 430.9932.

*2-Methylamino-4,6-bis[(3,5-dibromophenyl)amino]-1,3,5-triazine (**2m**)*

Yield: 79 %; $T_g$ 94 °C; FTIR (ATR/$CH_2Cl_2$) 3402, 3275, 3174, 3093, 2956, 2857, 1605, 1559, 1519, 1496, 1407, 1359, 1297, 1256, 1226, 1170, 1150, 1103, 1081, 1012, 988, 904, 840, 808, 749, 741, 688, 667 cm$^{-1}$; $^1$H NMR (300 MHz, DMSO-$d_6$, 298 K) δ 9.57 (br s, 1H), 9.41 (br s, 1H), 8.11 (br s, 2H), 8.03 (br s, 2H), 7.40 (br s, 1H), 7.36 (s, 2H), 2.85 (d, $^3J$ = 4.1 Hz, 3H)

ppm; $^{1}$H NMR (400 MHz, DMSO-$d_6$, 363 K) δ 9.15 (s, 2H), 8.06 (s, 4H), 7.32 (t, $^{4}J$ = 1.8 Hz, 2H), 7.02 (br s, 1H), 2.90 (d, $^{3}J$ = 4.8 Hz, 3H) ppm; $^{13}$C NMR (75 MHz, DMSO-$d_6$) δ 165.7, 163.8, 163.4, 143.0, 125.8, 122.0, 120.8, 120.6, 27.2 ppm; HRMS (ESI, $MH^+$) calcd. for $C_{16}H_{13}Br_4N_6$ *m/e*: 608.7890, found: 608.7891.

*2-Methylamino-4,6-bis[(3,5-diiodophenyl)amino]-1,3,5-triazine (**2n**)*

Yield: 74 %; $T_g$ 128 °C; FTIR (ATR/$CH_2Cl_2$) 3398, 3266, 3172, 3078, 2947, 2902, 1604, 1548, 1513, 1490, 1414, 1401, 1355, 1291, 1262, 1223, 1169, 1149, 1108, 1077, 1009, 990, 882, 840, 807, 764, 750, 709, 684, 668, 651 $cm^{-1}$; $^{1}$H NMR (300 MHz, DMSO-$d_6$, 298 K) δ 9.41 (br s, 1H), 9.26 (br s, 1H), 8.28 (br s, 2H), 8.15 (br s, 2H), 7.61 (s, 2H), 7.35 (br s, 1H), 2.85 (d, $^{3}J$ = 4.1 Hz, 3H) ppm; $^{1}$H NMR (400 MHz, DMSO-$d_6$, 363 K) δ 8.99 (br s, 2H), 8.21 (s, 4H), 7.63 (t, $^{4}J$ = 1.3 Hz, 2H), 6.96 (br s, 1H), 2.90 (s, 3H) ppm; $^{13}$C NMR (75 MHz, DMSO-$d_6$) δ 165.7, 163.7, 163.4, 142.7, 137.0, 136.7, 127.1, 126.8, 95.5, 27.2 ppm; HRMS (ESI, $MH^+$) calcd. for $C_{16}H_{13}I_4N_6$ *m/e*: 796.7375, found: 796.7395.

*2-Methylamino-4,6-bis[(3,5-dimethoxyphenyl)amino]-1,3,5-triazine (**2o**)*

Yield: 64 %; $T_g$ 65 °C; FTIR (ATR/$CH_2Cl_2$) 3380, 3286, 3132, 2999, 2956, 2939, 2907, 2838, 1591, 1556, 1513, 1480, 1451, 1421, 1355, 1262, 1248, 1202, 1175, 1151, 1087, 1063, 1021, 992, 974, 928, 833, 809, 735, 702, 682, 647 $cm^{-1}$; $^{1}$H NMR (300 MHz, DMSO-$d_6$, 298 K) δ 9.01 (br s, 1H), 8.86 (br s, 1H), 7.09 (br d, 4H), 7.02 (br s, 1H), 6.11 (s, 2H), 3.71 (s, 12H), 2.85 (d, $^{3}J$ = 4.7 Hz, 3H) ppm; $^{1}$H NMR (600 MHz, DMSO-$d_6$, 363 K) δ 8.54 (s, 2H), 7.06 (d, $^{4}J$ = 1.8 Hz, 4H), 6.64 (br s, 1H), 6.13 (t, $^{4}J$ = 2.1 Hz, 2H), 3.73 (s, 12H), 2.89 (d, $^{3}J$ = 4.7 Hz, 3H) ppm; $^{13}$C NMR (75 MHz, DMSO-$d_6$) δ 165.9, 164.0, 163.7, 160.1, 141.9, 98.2, 98.0, 93.8, 93.6, 54.8, 27.2 ppm; HRMS (ESI, $MH^+$) calcd. for $C_{20}H_{25}N_6O_4$ *m/e*: 413.1932, found: 413.1937.

*2-Methylamino-4,6-bis[(3,4,5-trimethoxyphenyl)amino]-1,3,5-triazine (**2p**)*

Yield: 69 %; $T_g$ 94 °C; FTIR (ATR/$CH_2Cl_2$) 3549, 3344, 3293, 3214, 3132, 2995, 2939, 2838, 1586, 1499, 1450, 1416, 1292, 1231, 1203, 1185, 1127, 1048, 1005, 972, 925, 832, 810, 786, 735 $cm^{-1}$; $^{1}$H NMR (300 MHz, DMSO-$d_6$, 298 K) δ 8.96 (br s, 1H), 8.81 (br s, 1H), 7.18 (br d, 4H), 7.02 (br s, 1H), 3.73 (s, 12H), 3.61 (s, 6H), 2.86 (d, $^{3}J$ = 4.7 Hz, 3H) ppm; $^{1}$H NMR (600 MHz, DMSO-$d_6$, 363 K) δ x ppm; $^{13}$C NMR (75 MHz, DMSO-$d_6$) δ 165.9, 163.9, 163.6, 152.4, 136.2, 132.2, 98.0, 97.5, 60.0, 55.5, 27.3 ppm; HRMS (ESI, $MH^+$) calcd. for $C_{22}H_{29}N_6O_6$ *m/e*: 473.2143, found: 473.2149.

*2-Methylamino-4,6-bis[(3,5-di-tert-butylphenyl)amino]-1,3,5-triazine (**2q**)*

Yield: 60 %; $T_g$ 129 °C, $T_c$ 173 °C, $T_m$ 234 °C; FTIR (ATR/$CH_2Cl_2$) 3467, 3270, 3216, 3138, 2963, 2905, 2868, 1706, 1666, 1601, 1558, 1523, 1476, 1429, 1395, 1362, 1307, 1275, 1248, 1223, 1204, 1170, 1132, 1087, 1025, 982, 946, 900, 867, 810, 792, 764, 750, 707 $cm^{-1}$; $^{1}$H NMR (300 MHz, $CDCl_3$, 298 K) δ 7.45 (br s, 2H), 7.34 (br d, 4H), 7.12 (s, 2H), 5.66 (br s, 1H), 2.91 (d, $^{3}J$ = 4.7 Hz, 3H), 1.31 (s, 36 H) ppm; $^{13}$C NMR (75 MHz, $CDCl_3$) δ 165.8, 163.7, 162.9, 151.2, 137.9, 137.4, 118.0, 117.4, 116.0, 115.1, 34.9, 31.4, 27.8 ppm; HRMS (ESI, $MH^+$) calcd. for $C_{32}H_{49}N_6$ *m/e*: 517.4013, found: 517.4017.

*2-Ethyl-4,6-bis(phenylamino)-1,3,5-triazine (**4a**)*

Yield: 76 %; $T_g$ 27 °C, $T_c$ 52 °C, $T_m$ 162 °C; FTIR (ATR/$CH_2Cl_2$) 3251, 3160, 3084, 3032, 2981, 2944, 2879, 1624, 1599, 1574, 1549, 1515, 1495, 1458, 1443, 1429, 1389, 1309, 1291, 1283, 1243, 1212, 1172, 1158, 1121, 1103, 1077, 1038, 988, 944, 904, 867, 827, 772, 754, 710, 690 $cm^{-1}$; $^1H$ NMR (300 MHz, DMSO-$d_6$, 298 K) δ 9.71 (s, 2H), 7.77 (d, $^3J$ = 5.9 Hz, 4H), 7.30 (t, 3$J$ = 7.6 Hz, 4H), 7.01 (t, $^3J$ = 7.6 Hz, 2H), 2.57 (q, $^3J$ = 7.6 Hz, 2H), 1.26 (t, $^3J$ = 7.0 Hz, 3H) ppm; $^{13}C$ NMR (75 MHz, DMSO-$d_6$) δ 178.8, 163.9, 139.4, 128.3, 122.3, 120.3, 31.3, 11.5 ppm; HRMS (ESI, $MNa^+$) calcd. for $C_{17}H_{17}NaN_5$ *m/e*: 314.1376, found: 314.1381.

*2-Ethyl-4,6-bis[(2-methylphenyl)amino]-1,3,5-triazine (**4b**)*

Yield: 76 %; $T_m$ 169 °C; FTIR (ATR/$CH_2Cl_2$) 3411, 3225, 3119, 3064, 3027, 2974, 2937, 2878, 1612, 1596, 1565, 1504, 1455, 1426, 1348, 1291, 1247, 1212, 1191, 1158, 1115, 1098, 1048, 1036, 986, 940, 824, 751, 719, 679 $cm^{-1}$; $^1H$ NMR (300 MHz, DMSO-$d_6$, 298 K) δ 8.84 (s, 2H), 7.40 (d, $^3J$ = 7.6 Hz, 2H), 7.16 (d, $^3J$ = 7.0 Hz, 2H), 7.11 (t, $^3J$ = 7.6 Hz, 2H), 7.03 (t, $^3J$ = 7.6 Hz, 2H), 2.44 (q, $^3J$ = 7.6 Hz, 2H), 2.19 (s, 6H), 1.17 (t, $^3J$ = 7.6 Hz, 3H) ppm; $^{13}C$ NMR (75 MHz, DMSO-$d_6$) δ 178.8, 164.8, 136.9, 132.4, 130.0, 126.0, 125.6, 124.7, 31.2, 18.0, 11.5 ppm; HRMS (ESI, $MNa^+$) calcd. for $C_{19}H_{21}NaN_5$ *m/e*: 342.1689, found: 342.1698.

*2-Ethyl-4,6-bis[(3-methylphenyl)amino]-1,3,5-triazine (**4c**)*

Yield: 91 %; $T_g$ 19 °C, $T_c$ 94 °C, $T_m$ 112 °C; FTIR (ATR/$CH_2Cl_2$) 3387, 3269, 3168, 3115, 3048, 2973, 2938, 2877, 1599, 1577, 1550, 1513, 1488, 1462, 1423, 1347, 1302, 1284, 1254, 1206, 1170, 1118, 1091, 1043, 984, 939, 892, 867, 823, 777, 689 $cm^{-1}$; $^1H$ NMR (300 MHz, DMSO-$d_6$, 298 K) δ 9.64 (s, 2H), 7.55 (s, 4H), 7.17 (t, $^3J$ = 7.6 Hz, 2H), 6.83 (d, $^3J$ = 7.6 Hz, 2H), 2.55 (q, $^3J$ = 7.0 Hz, 2H), 2.26 (s, 6H), 1.25 (t, $^3J$ = 7.6 Hz, 3H) ppm; $^{13}C$ NMR (75 MHz, DMSO-$d_6$) δ 178.7. 163.9. 139.3. 137.5. 128.2. 123.1. 120.8. 117.5. 31.2. 21.2. 11.5 ppm; HRMS (ESI, $MNa^+$) calcd. for $C_{19}H_{21}NaN_5$ *m/e*: 342.1689, found: 342.1695.

*2-Ethyl-4,6-bis[(4-methylphenyl)amino]-1,3,5-triazine (**4d**)*

Yield: 86 %; $T_g$ 35 °C, $T_c$ 61,109 °C, $T_m$ 152 °C; FTIR (ATR/$CH_2Cl_2$) 3391, 3265, 3189, 3101, 3028, 2974, 2938, 2922, 2875, 1613, 1569, 1499, 1464, 1434, 1409, 1352, 1312, 1291, 1239, 1205, 1189, 1104, 1040, 1020, 985, 936, 817, 748 $cm^{-1}$; $^1H$ NMR (300 MHz, DMSO-$d_6$, 298 K) δ 9.59 (s, 2H), 7.64 (br s, 4H), 7.09 (d, $^3J$ = 8.2 Hz, 4H), 2.54 (q, $^3J$ = 7.6 Hz, 2H), 2.26 (s, 6H), 1.24 (t, $^3J$ = 7.6 Hz, 3H) ppm; $^{13}C$ NMR (75 MHz, DMSO-$d_6$) δ 178.6, 163.8, 136.9, 131.2, 128.7, 120.3, 31.3, 20.4, 11.6 ppm; HRMS (ESI, $MNa^+$) calcd. for $C_{19}H_{21}NaN_5$ *m/e*: 342.1689, found: 342.1697.

*2-Ethyl-4,6-bis[(2,3-dimethylphenyl)amino]-1,3,5-triazine (**4e**)*

Yield: 82 %; $T_g$ 46 °C, $T_c$ 73 °C, $T_m$ 169 °C; FTIR (ATR/$CH_2Cl_2$) 3378, 3229, 3120, 3070, 2973, 2940, 2920, 1609, 1566, 1550, 1509, 1465, 1423, 1382, 1347, 1273, 1214, 1190, 1165, 1128, 1100, 1067, 1018, 987, 825, 783, 745, 707 $cm^{-1}$; $^1H$ NMR (300 MHz, DMSO-$d_6$, 298 K) δ 8.87 (s, 2H), 7.10 (d, $^3J$ = 7.0 Hz, 2H), 6.94 (m, 4H), 2.40 (q, $^3J$ = 7.0 Hz, 2H), 2.17 (s, 6H), 1.97 (s, 6H), 1.14 (t, $^3J$ = 7.0 Hz, 3H) ppm; $^{13}C$ NMR (75 MHz, DMSO-$d_6$) δ 178.6, 165.0, 136.7, 136.5, 131.9, 126.4, 124.8, 31.2, 20.1, 14.3, 11.6 ppm; HRMS (ESI, $MNa^+$) calcd. for $C_{21}H_{25}NaN_5$ *m/e*: 370.2002, found: 370.2008.

*2-Ethyl-4,6-bis[(2,4-dimethylphenyl)amino]-1,3,5-triazine (**4f**)*

Yield: 94 %; $T_g$ 39 °C, $T_c$ 59, 88, 114 °C, $T_m$ 121, 158 °C; FTIR (ATR/$CH_2Cl_2$) 3435, 3229, 3129, 3059, 3018, 2973, 2938, 2922, 1604, 1570, 1504, 1464, 1452, 1428, 1376, 1289, 1266, 1222, 1157, 1126, 1099, 1058, 986, 871, 824, 734, 719, 678 $cm^{-1}$; $^1H$ NMR (300 MHz, DMSO-$d_6$, 298 K) δ 8.67 (s, 2H), 7.21 (d, $^3J$ = 8.2 Hz, 2H), 6.96 (s, 2H), 6.89 (d, $^3J$ = 8.2 Hz, 2H), 2.38 (q, $^3J$ = 7.6 Hz, 2H), 2.22 (s, 6H), 2.12 (s, 6H), 1.12 (t, $^3J$ = 7.6 Hz, 3H) ppm; $^{13}C$ NMR (75 MHz, DMSO-$d_6$) δ 178.6, 164.9, 134.2, 133.7, 132.5, 130.5, 126.1, 126.0, 31.2, 20.4, 17.9, 11.5 ppm; HRMS (ESI, $MNa^+$) calcd. for $C_{21}H_{25}NaN_5$ *m/e*: 370.2002, found: 370.2008.

*2-Ethyl-4,6-bis[(2,5-dimethylphenyl)amino]-1,3,5-triazine (**4g**)*

Yield: 93 %; $T_g$ 32 °C, $T_c$ 121 °C, $T_m$ 136 °C; FTIR (ATR/$CH_2Cl_2$) 3437, 3372, 3231, 3133, 3047, 3022, 2973, 2937, 2923, 1596, 1566, 1516, 1485, 1464, 1416, 1376, 1349, 1291, 1262, 1214, 1163, 1132, 1096, 1040, 985, 949, 878, 824, 805, 721 $cm^{-1}$; $^1H$ NMR (300 MHz, DMSO-$d_6$, 298 K) δ 8.73 (s, 2H), 7.16 (s, 2H), 7.02 (d, $^3J$ = 7.6 Hz, 2H), 6.82 (d, $^3J$ = 7.0 Hz, 2H), 2.43 (q, $^3J$ = 7.6 Hz, 2H), 2.15 (s, 6H), 2.12 (s, 6H), 1.16 (t, $^3J$ = 7.6 Hz, 3H) ppm; $^{13}C$ NMR (75 MHz, DMSO-$d_6$) δ 178.6, 164.8, 136.6, 134.6, 129.8, 129.2, 126.2, 125.4, 31.2, 20.5, 17.6, 11.5 ppm; HRMS (ESI, $MNa^+$) calcd. for $C_{21}H_{25}NaN_5$ *m/e*: 370.2002, found: 370.2013.

*2-Ethyl-4,6-bis[(2,6-dimethylphenyl)amino]-1,3,5-triazine (**4h**)*

Dioxane was used as the solvent instead of THF, and the mixture was refluxed for 3 days. Yield: 72 %; $T_{dec}$ 240 °C; FTIR (ATR/$CH_2Cl_2$) 3386, 3211, 3046, 2977, 2938, 2923, 1613, 1597, 1525, 1467, 1421, 1375, 1299, 1268, 1223, 1163, 1121, 1094, 1068, 1036, 985, 919, 884, 844, 825, 7665, 704, 664 $cm^{-1}$; $^1H$ NMR (400 MHz, DMSO-$d_6$, 363 K) δ 8.25 (s, 2H), 7.02 (s, 6H), 2.35 (q, $^3J$ = 7.6 Hz, 2H), 2.13 (s, 12H), 1.09 (t, $^3J$ = 7.6 Hz, 3H) ppm; $^{13}C$ NMR (75 MHz, DMSO-$d_6$) δ 178.6, 165.2, 165.0, 135.8, 135.6, 127.7, 127.4, 126.1, 125.8, 31.1, 18.4, 18.2, 11.6 ppm; HRMS (ESI, $MNa^+$) calcd. for $C_{21}H_{25}NaN_5$ *m/e*: 370.2002, found: 370.2008.

*2-Ethyl-4,6-bis[(3,4-dimethylphenyl)amino]-1,3,5-triazine (**4i**)*

Yield: 88 %; $T_g$ 31 °C, $T_c$ 74, 126 °C, $T_m$ 135, 144 °C; FTIR (ATR/$CH_2Cl_2$) 3385, 3268, 3170, 3105, 3023, 2970, 2938, 2921, 2879, 1606, 1568, 1552, 1497, 1439, 1408, 1344, 1304, 1252, 1210, 1169, 1124, 1107, 1046, 1021, 1000, 985, 960, 873, 823, 758, 733, 708 $cm^{-1}$; $^1H$ NMR (300 MHz, DMSO-$d_6$, 298 K) δ 9.53 (s, 2H), 7.51 (br s, 4H), 7.04 (d, $^3J$ = 8.2 Hz, 2H), 2.54 (q, $^3J$ = 7.6 Hz, 2H), 2.17 (s, 12H), 1.25 (t, $^3J$ = 7.6 Hz, 3H) ppm; $^1H$ NMR (400 MHz, DMSO-$d_6$, 363 K) δ 9.04 (s, 2H), 7.48 (s, 2H), 7.44 (d, $^3J$ = 8.1 Hz, 2H), 7.03 (d, $^3J$ = 8.3 Hz, 2H), 2.55 (q, $^3J$ = 7.6 Hz, 2H), 1.26 (t, $^3J$ = 7.6 Hz, 3H) ppm; $^{13}C$ NMR (75 MHz, DMSO-$d_6$) δ 178.5, 163.9, 137.1, 135.9, 130.0, 129.3, 121.6, 117.9, 31.3, 19.6, 18.7, 11.6 ppm; HRMS (ESI, $MNa^+$) calcd. for $C_{21}H_{25}NaN_5$ *m/e*: 370.2002, found: 370.1998.

*2-Ethyl-4,6-bis[(2,4,6-trimethylphenyl)amino]-1,3,5-triazine (**4j**)*

Dioxane was used as the solvent instead of THF, and the mixture was refluxed for 3 days. Yield: 84 %; $T_g$ 60 °C, $T_{dec}$ 240 °C; FTIR (ATR/$CH_2Cl_2$) 3373, 3350, 3216, 3055, 3007, 2974, 2945, 2921, 1614, 1568, 1520, 1487, 1467, 1421, 1375, 1311, 1279, 1234, 1218, 1157, 1114, 1062, 1034, 1012, 986, 937, 846, 826, 738, 672 $cm^{-1}$; $^1H$ NMR (400 MHz, DMSO-$d_6$, 363 K) δ 8.13 (s, 2H), 6.84 (s, 4H), 2.34 (q, $^3J$ = 7.6 Hz, 2H), 2.24 (s, 6H), 2.10 (s, 12H), 1.09 (t, $^3J$ = 7.6 Hz, 3H) ppm; $^{13}C$ NMR (75 MHz, DMSO-$d_6$) δ 178.4, 165.3, 165.1, 135.4, 135.2, 135.0,

134.6, 133.2, 128.3, 128.0, 31.1, 20.4, 18.2, 18.1, 11.6 ppm; HRMS (ESI, $MNa^+$) calcd. for $C_{23}H_{29}NaN_5$ *m/e*: 398.2315, found: 398.2320.

*2-Ethyl-4,6-bis[(3,5-difluorophenyl)amino]-1,3,5-triazine (**4k**)*

Yield: 86 %; $T_g$ 25 °C, $T_c$ 69 °C, $T_m$ 153 °C; FTIR (ATR/$CH_2Cl_2$) 3423, 3275, 3218, 3121, 2981, 2943, 1611, 1586, 1552, 1516, 1475, 1436, 1350, 1307, 1256, 1214, 111, 1117, 1057, 994, 983, 972, 935, 837, 823, 751, 668, 643 $cm^{-1}$; $^1H$ NMR (300 MHz, DMSO-$d_6$, 298 K) δ 10.17 (s, 2H), 7.54 (s, 4H), 6.79 (t, $^3J$ = 8.8 Hz, 2H), 2.61 (q, $^3J$ = 7.6 Hz, 2H), 1.25 (t, $^3J$ = 7.6 Hz, 3H) ppm; $^{13}C$ NMR (75 MHz, DMSO-$d_6$) δ 179.4, 163.7, [164.1, 163.9, 160.9, 160.7 (dd, $^1J_{C\text{-}F}$ = 242 Hz, $^2J_{C\text{-}F}$ = 15 Hz)], [142.2, 142.0, 141.8 (t, $^2J_{C\text{-}F}$ = 14 Hz)], [102.8, 102.5 (d, $^2J_{C\text{-}F}$ = 27 Hz)], [97.5, 97.2, 96.9 (t, $^2J_{C\text{-}F}$ = 27 Hz)], 31.2, 11.2 ppm; HRMS (ESI, $MH^+$) calcd. for $C_{17}H_{14}F_4N_5$ *m/e*: 364.1180, found: 364.1190.

*2-Ethyl-4,6-bis[(3,5-dichlorophenyl)amino]-1,3,5-triazine (**4l**)*

Yield: 83 %; $T_g$ 52 °C, $T_c$ 109 °C, $T_m$ 169 °C; FTIR (ATR/$CH_2Cl_2$) 3404, 3269, 3152, 3111, 2979, 2940, 1592, 1568, 1545, 1502, 1445, 1413, 1343, 1306, 1263, 1228, 1203, 1116, 1053, 989, 965, 948, 918, 841, 823, 806, 737, 691, 667 $cm^{-1}$; $^1H$ NMR (300 MHz, DMSO-$d_6$, 298 K) δ 10.14 (s, 2H), 7.85 (s, 4H), 7.18 (s, 2H), 2.63 (q, $^3J$ = 7.6 Hz, 2H), 1.26 (t, $^3J$ = 7.6 Hz, 3H) ppm; $^{13}C$ NMR (75 MHz, DMSO-$d_6$) δ 179.4, 163.6, 141.8, 133.9, 121.5, 118.0, 31.2, 11.1 ppm; HRMS (ESI, $MH^+$) calcd. for $C_{17}H_{14}Cl_4N_5$ *m/e*: 429.9970, found: 429.9971.

*2-Ethyl-4,6-bis[(3,5-dibromophenyl)amino]-1,3,5-triazine (**4m**)*

Yield: 83 %; $T_g$ 66 °C, $T_c$ 135-140 °C, $T_m$ 191 °C; FTIR (ATR/$CH_2Cl_2$) 3396, 3374, 3267, 3147, 3110, 2977, 2937, 1587, 1555, 1497, 1463, 1437, 1407, 1372, 1345, 1303, 1262, 1230, 1202, 1100, 1050, 1020, 987, 957, 898, 840, 822, 750, 738, 686, 665 $cm^{-1}$; $^1H$ NMR (300 MHz, DMSO-$d_6$, 298 K) δ 10.08 (s, 2H), 8.02 (s, 4H), 7.39 (s, 2H), 2.63 (q, $^3J$ = 7.6 Hz, 2H), 1.26 (t, $^3J$ = 7.6 Hz, 3H) ppm; $^{13}C$ NMR (75 MHz, DMSO-$d_6$) δ 179.3, 163.6, 142.1, 126.7, 122.2, 121.2, 31.1, 11.0 ppm; HRMS (ESI, $MH^+$) calcd. for $C_{17}H_{14}Br_4N_5$ *m/e*: 607.7937, found: 607.7950.

*2-Ethyl-4,6-bis[(3,5-diiodophenyl)amino]-1,3,5-triazine (**4n**)*

Yield: 80 %; $T_g$ 96 °C, $T_c$ 166 °C, $T_m$ 196 °C; FTIR (ATR/$CH_2Cl_2$) 3391, 3263, 3154, 3125, 3082, 2973, 2934, 1593, 1574, 1544, 1492, 1462, 1402, 1344, 1298, 1263, 1231, 1202, 1117, 1095, 1048, 990, 951, 881, 840, 821, 738, 708, 685, 666 $cm^{-1}$; $^1H$ NMR (300 MHz, DMSO-$d_6$, 298 K) δ 9.91 (br s, 2H), 8.18 (s, 4H), 7.68 (s, 2H), 2.62 (q, $^3J$ = 7.0 Hz, 2H), 1.27 (t, $^3J$ = 7.0 Hz, 3H) ppm; $^{13}C$ NMR (75 MHz, DMSO-$d_6$) δ 179.2, 163.5, 141.8, 137.8, 127.4, 95.6, 31.1, 10.9 ppm; HRMS (ESI, $MH^+$) calcd. for $C_{17}H_{14}I_4N_5$ *m/e*: 795.7422, found: 795.7431.

*2-Ethyl-4,6-bis[(3,5-dimethoxyphenyl)amino]-1,3,5-triazine (**4o**)*

Yield: 93 %; $T_g$ 35 °C, $T_c$ 108 °C, $T_m$ 126 °C; FTIR (ATR/$CH_2Cl_2$) 3335, 3283, 3234, 3124, 2995, 2961, 2938, 2909, 2838, 1607, 1581, 1550, 1514, 1479, 1453, 1421, 1345, 1295, 1248, 1204, 1169, 1153, 1111, 1067, 990, 930, 823, 736, 681 $cm^{-1}$; $^1H$ NMR (300 MHz, DMSO-$d_6$, 298 K) δ 9.62 (s, 2H), 7.06 (s, 4H), 6.18 (s, 2H), 3.69 (s, 12H), 2.58 (q, $^3J$ = 7.0 Hz, 2H), 1.26 (t, $^3J$ = 7.0 Hz, 3H) ppm; $^{13}C$ NMR (75 MHz, DMSO-$d_6$) δ 178.8, 163.9, 160.3, 141.0, 98.6, 94.4, 54.9, 31.2, 11.4 ppm; HRMS (ESI, $MNa^+$) calcd. for $C_{21}H_{25}NaN_5O_4$ *m/e*: 434.1799, found: 434.1802.

*2-Ethyl-4,6-bis[(3,4,5-trimethoxyphenyl)amino]-1,3,5-triazine (**4p**)*

Yield: 73 %; $T_g$ 63 °C, $T_c$ 117 °C, $T_m$ 186 °C; FTIR (ATR/$CH_2Cl_2$) 3329, 3128, 2964, 2938, 2839, 1604, 1576, 1498, 1451, 1415, 1349, 1233, 1197, 1128, 1059, 1036, 1006, 924, 824, 785, 737 $cm^{-1}$; $^1H$ NMR (300 MHz, DMSO-$d_6$, 298 K) δ 9.57 (br s, 2H), 7.10 (br d, 4H), 3.75 (br s, 6H), 3.62 (s, 12H), 2.57 (br s, 2H), 1.26 (t, $^3J$ = 7.0 Hz, 3H) ppm; $^1H$ NMR (400 MHz, DMSO-$d_6$, 363 K) δ 9.10 (s, 2H), 7.11 (s, 4H), 3.73 (s, 12H), 3.68 (s, 6H), 2.59 (q, $^3J$ = 7.6 Hz, 2H), 1.28 (t, $^3J$ = 7.6 Hz, 3H) ppm; $^{13}C$ NMR (75 MHz, DMSO-$d_6$) δ 178.6, 163.7, 152.5, 135.3, 132.9, 98.4, 60.0, 55.6, 31.2, 11.3 ppm; HRMS (ESI, $MNa^+$) calcd. for $C_{23}H_{29}NaN_5O_6$ *m/e*: 494.2010, found: 494.2008.

*2-Ethyl-4,6-bis[(3,5-di-tert-butylphenyl)amino]-1,3,5-triazine (**4q**)*

Yield: 78 %; $T_m$ 215 °C; FTIR (ATR/$CH_2Cl_2$) 3429, 3256, 3082, 2963, 2905, 2868, 1587, 1553, 1521, 1510, 1437, 1422, 1363, 1307, 1247, 1204, 1134, 1054, 1026, 986, 943, 900, 868, 824, 706 $cm^{-1}$; $^1H$ NMR (300 MHz, $CDCl_3$, 298 K) δ 7.40 (s, 4H), 7.30 (br s, 2H), 7.17 (s, 2H), 2.68 (q, $^3J$ = 7.6 Hz, 2H), 1.36 (t, $^3J$ = 7.6 Hz, 3H), 1.32 (s, 36H) ppm; $^{13}C$ NMR (75 MHz, $CDCl_3$) δ 179.9, 164.0, 151.3, 137.2, 118.1, 115.7, 34.9, 31.4, 11.3 ppm; HRMS (ESI, $MH^+$) calcd. for $C_{33}H_{49}NaN_5$ *m/e*: 538.3880, found: 538.3884.

# Annexe II: Synthèses – Chapitre 3

*EXPERIMENTAL SECTION*

*2-Methylamino-4-mexylamino-6-(3,5-dimethylphenoxy)-1,3,5-triazine (**4**)*

2-Methylamino-4-mexylamino-6-chloro-1,3,5-triazine (0.264 g, 1.00 mmol) was dissolved in dioxane (5 mL) in a round-bottomed flask equipped with a magnetic stirrer and a water-jacketed condenser. $K_2CO_3$ (0.152 g, 1.10 mmol) and 3,5-dimethylphenol (0.134 g, 1.10 mmol) were successively added, and the mixture was refluxed for 2 days. After allowing to cool down to ambient temperature, ethyl ether and $H_2O$ were added, and the resulting precipitate was collected by filtration, washed with $H_2O$ and ethyl ether, and allowed to completely dry to give 0.244 g of compound 4 in acceptable purity (0.698 mmol, 70 %). $T_g$ 42 °C, $T_c$ 122 °C, $T_m$ 178 °C; FT-IR (ATR/$CH_2Cl_2$) 3384, 3274, 3149, 3014, 2950, 2919, 2859, 1617, 1579, 1554, 1530, 1464, 1393, 1348, 1244, 1192, 1189, 1172, 1090, 1038, 1000, 929, 888, 843, 811, 687, 662, 648 $cm^{-1}$; $^1H$ NMR (400 MHz, DMSO-$d_6$, 363 K) δ 8.98 (br s, 1H), 7.29 (s, 2H), 7.10 (br s, 1H), 6.86 (s, 1H), 6.80 (s, 2H), 6.60 (s, 1H), 2.88 (s, 3H), 2.30 (s, 6H), 2.19 (s, 6H) ppm; $^{13}C$ NMR (75 MHz, DMSO-$d_6$) δ 171.2, 170.8, 167.9, 167.7, 165.7, 165.1, 152.8, 140.1, 139.1, 137.6, 127.0, 124.0, 120.0, 117.9, 27.8. 27.6. 21.5. 21.2 ppm; HRMS (ESI, $MNa^+$) calcd. for $C_{20}H_{23}NaN_5O$ *m/e*: 372.1795, found: 372.1801.

*2-Methylamino-4,6-bis(3,5-dimethylphenoxy)-1,3,5-triazine (**5**)*

2-Methylamino-4,6-dichloro-1,3,5-triazine (1.00 g, 5.59 mmol) was dissolved in dioxane (20 mL) in a round-bottomed flask equipped with a magnetic stirrer and a water-jacketed condenser. $K_2CO_3$ (1.70 g, 12.3 mmol) and 3,5-dimethylphenol (1.50 g, 12.3 mmol) were successively added, and the mixture was refluxed for 2 days. After allowing to cool down to ambient temperature, the mixture was poured into $H_2O$ and stirred 20 min at ambient temperature. The resulting precipitate was collected by filtration, washed with 1M aq. NaOH, $H_2O$ and hexanes, and allowed to dry completely in air to give 0.924 g of pure compound 5 (2.64 mmol, 47 %). $T_g$ 41 °C, $T_c$ 58, 100 °C, $T_m$ 180 °C; FT-IR (ATR/$CH_2Cl_2$) 3277, 3150, 3016, 2977, 2917, 2871,1640, 1619, 1598, 1580, 1553, 1468, 1437, 1416, 1385, 1368, 1288, 1254, 1175, 1146, 1083, 1036, 1000, 948, 925, 895, 850, 808, 739, 699, 680, 656, 643 $cm^{-1}$; $^1H$ NMR (300 Mhz, $CDCl_3$, 298 K) δ 6.83 (s, 2H), 6.79 (s, 2H), 6.74 (s, 2H), 6.27 (br s, 2H), 2.90 (d, $^3J$ = 4.1 Hz, 3H), 2.29 (s, 6H), 2.28 (s, 6H) ppm; $^{13}C$ NMR (75 MHz, $CDCl_3$) δ 172.5, 171.7, 168.8, 151.9, 151.8, 139.0, 138.8, 127.2, 127.1, 119.2, 27.8, 21.3 ppm; HRMS (ESI, $MNa^+$) calcd. for $C_{20}H_{22}NaN_4O_2$ *m/e*: 373.1635, found: 373.1644.

*2-Methoxy-4-mexylamino-6-(3,5-dimethylphenoxy)-1,3,5-triazine (**6**)*

2-Methoxy-4,6-dichloro-1,3,5-triazine (2.00 g, 11.1 mmol) was dissolved in acetone (30 mL) in a round-bottomed flask equipped with a magnetic stirrer. $Na_2CO_3$ (1.18 g, 11.1 mmol) was added, then the flask was placed in an ice bath. A solution of 3,5-dimethylaniline (1.39 mL, 1.35 g, 11.1 mmol) in acetone (20 mL) was then slowly added at 0-5 $^oC$ under vigorous stirring, after which the ice bath was removed and the mixture was stirred for 1h at ambient temperature, after which $H_2O$ was added. The product was extracted with ethyl ether, the organic layer was washed with brine, dried over $Na_2SO_4$, filtered, and the solvent was evaporated under reduced pressure. Recrystallization from hot hexanes afforded 2.31 g of the 2-methoxy-4-mexylamino-

6-chloro-1,3,5-triazine precursor (8.73 mmol, 79 %). $T_m$ 104 °C; FT-IR (ATR/$CH_2Cl_2$) 3360, 3279, 3235, 3190, 3142, 3008, 2951, 2917, 2866, 1618, 1557, 1487, 1457, 1389, 1364, 1281, 1205, 1171, 1095, 1046, 917, 881, 841, 808, 733, 682 $cm^{-1}$; $^1H$ NMR (300 MHz, $CDCl_3$, 298 K) δ 7.65 (br s, 1H), 7.17 (s, 2H), 6.80 (s, 1H), 4.02 (s, 3H), 2.32 (s, 6H) ppm; $^{13}C$ NMR (75 MHz, $CDCl_3$) δ 171.5, 170.6, 165.2, 138.7, 136.5, 126.7, 118.9, 55.5, 21.4 ppm; HRMS (ESI, $MNa^+$) calcd. for $C_{12}H_{13}ClNaN_4O$ *m/e*: 287.0670, found: 287.0681.

2-Methoxy-4-mexylamino-6-chloro-1,3,5-triazine (0.265 g, 1.00 mmol) was dissolved in dioxane (5 mL) in a round-bottomed flask equipped with a magnetic stirrer and a water-jacketed condenser. $K_2CO_3$ (0.152 g, 1.10 mmol) and 3,5-dimethylphenol (0.134 g, 1.10 mmol) were successively added, and the mixture was refluxed for 2 days. After allowing to cool down to ambient temperature, ethyl ether and $H_2O$ were added, and both layers were separated. The organic layer was washed with 1M aqueous NaOH and brine, dried over $Na_2SO_4$, filtered, and the solvent was evaporated under reduced pressure and dried thoroughly to give 0.259 g of pure compound 6 (0.739 mmol, 74 %). $T_g$ 37 °C; FT-IR (ATR/$CH_2Cl_2$) 3367, 3284, 3233, 3150, 3014, 2953, 2919, 2865, 1619, 1570, 1550, 1458, 1407, 1372, 1357, 1323, 1291, 1270, 1247, 1195, 1182, 1149, 1118, 1092, 1036, 1000, 973, 927, 889, 845, 814, 687, 660 $cm^{-1}$; $^1H$ NMR (400 MHz, DMSO-$d_6$, 363 K) δ 9.64 (br s, 1H), 7.20 (s, 2H), 6.92 (s, 1H), 6.84 (s, 2H), 6.66 (s, 1H), 3.94 (s, 3H), 2.31 (s, 6H), 2.17 (s, 6H) ppm; $^{13}C$ NMR (75 MHz, DMSO-$d_6$) δ 172.6, 172.4, 166.2, 152.4, 139.3, 139.0, 137.8, 127.6, 124.9, 119.8, 118.8, 117.9, 55.0, 21.2 ppm; HRMS (ESI, $MNa^+$) calcd. for $C_{20}H_{22}NaN_4O_2$ *m/e*: 373.1635, found: 373.1639.

*2-Methylamino-4-mexylamino-6-(N,3,5-trimethylphenylamino)-1,3,5-triazine (**7**)*

2-Methylamino-4-mexylamino-6-chloro-1,3,5-triazine (0.527 g, 2.00 mmol) was dissolved in dioxane (15 mL) in a round-bottomed flask equipped with a magnetic stirrer and a water-jacketed condenser. N,3,5-trimethylaniline (0.297 g, 2.20 mmol) were successively added, and the mixture was refluxed for 2 days. After allowing to cool down to ambient temperature, 1M aqueous HCl and $CH_2Cl_2$ were added, and both layers were separated. The organic layer was recovered, and hexanes was added until an off-white precipitate had completely formed. The precipitate was collected by filtration, washed with hexanes, and redissolved in $CH_2Cl_2$. The solution was washed with 1M aqueous NaOH, dried over $Na_2SO_4$, filtered, and the solvent was evaporated under reduced pressure and dried thoroughly to give 0.555 g of compound 7 (1.53 mmol, 77 %). $T_g$ 63 °C; FT-IR (ATR/$CH_2Cl_2$) 3411, 3279, 3170, 3131, 3011, 2946, 2917, 2864, 1604, 1581, 1547, 1516, 1495, 1439, 1390, 1328, 1301, 1256, 1228, 1203, 1178, 1138, 1114, 1067, 1034, 999, 905, 891, 840, 809, 737, 710, 698, 690, 656 $cm^{-1}$; $^1H$ NMR (400 MHz, DMSO-$d_6$, 363 K) δ 8.33 (br s, 1H), 7.27 (s, 2H), 6.95 (s, 2H), 6.87 (s, 1H), 6.52 (s, 1H), 6.41 (br s, 1H), 3.43 (s, 3H), 2.85 (d, $^3J$ = 4.1 Hz, 3H), 2.30 (s, 6H), 2.15 (s, 6H) ppm; $^{13}C$ NMR (75 MHz, DMSO-$d_6$) δ 166.5, 165.8, 164.3, 145.5, 140.9, 138.2, 137.3, 127.5, 125.2, 123.0, 117.3, 38.1, 27.7, 27.4, 21.5, 21.3 ppm; HRMS (ESI, $MNa^+$) calcd. for $C_{21}H_{26}NaN_6$ *m/e*: 385.2117, found: 385.2124.

*2-Methylamino-4,6-bis(N,3,5-trimethylphenylamino)-1,3,5-triazine (**8**)*

2-Methylamino-4,6-dichloro-1,3,5-triazine (0.358 g, 2.00 mmol) was dissolved in dioxane (15 mL) in a round-bottomed flask equipped with a magnetic stirrer and a water-jacketed condenser. N,3,5-trimethylaniline (0.595 g, 4.40 mmol) were successively added, and the mixture was refluxed for 2 days. After allowing to cool down to ambient temperature, 1M

aqueous HCl and $CH_2Cl_2$ were added, and both layers were separated. The organic layer was recovered, dried over $Na_2SO_4$, filtered, and the solvent was evaporated under reduced pressure and dried thoroughly to give 0.359 g of compound 8 (0.954 mmol, 48 %). $T_g$ 21 °C; FT-IR (ATR/$CH_2Cl_2$) 3423, 3277, 3164, 3009, 2924, 2917, 2866, 1608, 1580, 1540, 1492, 1478, 1452, 1380, 1329, 1266, 1241, 1201, 1172, 1116, 1038, 919, 883, 845, 810, 702, 692, 664 $cm^{-1}$; $^1H$ NMR (300 MHz, $CDCl_3$, 298 K) δ 7.01 (s, 4H), 6.84 (s, 2H), 5.06 (br s, 1H), 3.46 (s, 6H), 2.82 (d, $^3J$ = 4.1 Hz, 3H), 2.33 (s, 12H) ppm; $^{13}C$ NMR (75 MHz, $CDCl_3$) δ 166.7, 165.6, 144.8, 137.7, 126.7, 124.2, 37.4, 27.4, 21.3 ppm; HRMS (ESI, $MNa^+$) calcd. for $C_{22}H_{28}NaN_6$ *m/e*: 399.2273, found: 399.2284.

*2-Methoxy-4-mexylamino-6-(N,3,5-trimethylphenylamino)-1,3,5-triazine (**9**)*

2-Methoxy-4,6-bis(mexylamino)-1,3,5-triazine (2.00 g, 5.72 mmol) was dissolved in anhydrous DMF (20 mL) in a flame-dried round-bottomed flask equipped with a magnetic stirrer. NaH (60 wt%, 0.206 g, 8.59 mmol) was added, and the mixture was stirred 30 min at ambient temperature until hydrogen evolution had stopped. Iodomethane (0.535 mL, 1.22 g, 8.59 mmol) was slowly added, and the mixture was stirred at ambient temperature for 12 h. The mixture was then poured into $H_2O$ and stirred 20 min, then the precipitate was collected by filtration and abundantly washed with $H_2O$. The crude product was chromatographed on silica (AcOEt/Hexanes 1:4) to give 1.13 g of compound 9 (3.11 mmol, 54 %) as well as 0.241 g of bis(N,3,5-trimethylphenylamino) derivative 10 (0.638 mmol, 11 %). Alternatively, compound 9 could be isolated by recrystallization from hexanes, which gave 0.863 g (2.37 mmol, 42 %). $T_g$ 44 °C, $T_c$ 126 °C, $T_m$ 148 °C; FT-IR (ATR/$CH_2Cl_2$) 3374, 3282, 3233, 3192, 3120, 3011, 2979, 2950, 2918, 2864, 1606, 1588, 1564, 1541, 1504, 1458, 1400, 1390, 1377, 1354, 1326, 1302, 1267, 1221, 1207, 1184, 1162, 1123, 1103, 1071, 1054, 1037, 999, 990, 932, 904, 888, 842, 812, 771, 715, 690, 655 $cm^{-1}$; $^1H$ NMR (400 MHz, DMSO-$d_6$, 363 K) δ 8.96 (br s, 1H), 7.24 (s, 2H), 6.96 (s, 2H), 6.92 (s, 1H), 6.57 (s, 1H), 3.87 (s, 3H), 3.45 (s, 3H), 2.30 (s, 6H), 2.15 (s, 6H) ppm; $^{13}C$ NMR (75 MHz, DMSO-$d_6$) δ 170.8, 166.9, 165.0, 144.6, 140.1, 138.4, 137.5, 128.2, 125.0, 123.9, 117.5, 54.0, 38.3, 38.2, 21.4, 21.3 ppm; HRMS (ESI, $MNa^+$) calcd. for $C_{21}H_{25}NaN_5O$ *m/e*: 386.1951, found: 386.1958.

*2-Methoxy-4,6-bis(N,3,5-trimethylphenylamino)-1,3,5-triazine (**10**)*

2-Methoxy-4,6-bis(mexylamino)-1,3,5-triazine (1.07 g, 3.06 mmol) was dissolved in anhydrous DMF (20 mL) in a flame-dried round-bottomed flask equipped with a magnetic stirrer. NaH (60 wt%, 0.367 g, 9.18 mmol) was added, and the mixture was stirred 30 min at ambient temperature until hydrogen evolution had stopped. Iodomethane (0.571 mL, 1.30 g, 9.18 mmol) was slowly added, and the mixture was stirred at ambient temperature for 12 h. Hexanes and $H_2O$ were then added, and both layers were separated. The aqueous layer was extracted twice with hexanes, the organic extracts were combined, washed with $H_2O$ and brine, dried over $Na_2SO_4$, filtered, and the volatiles were evaporated under vacuum. Filtration on a short silica plug (AcOEt/Hexanes 1:4) gave 1.10 g of pure compound 10 (2.91 mmol, 95 %). $T_g$ -25 °C; FT-IR (ATR/$CH_2Cl_2$) 3009, 2948, 2918, 2866, 1608, 1561, 1529, 1475, 1458, 1385, 1359, 1322, 1269, 1230, 1215, 1162, 1116, 1086, 1039, 1000, 983, 950, 915, 881, 847, 811, 749, 727, 702, 662 $cm^{-1}$; $^1H$ NMR (300 MHz, $CDCl_3$, 298 K) δ 6.95 (s, 4H), 6.85 (s, 2H), 3.81 (s, 3H), 3.45 (s, 6H), 2.31 (s, 12H) ppm; $^{13}C$ NMR (75 MHz, $CDCl_3$) δ 170.9, 166.5, 144.3,

137.9, 127.3, 124.2, 53.7, 37.8, 21.3 ppm; HRMS (ESI, $MNa^+$) calcd. for $C_{22}H_{27}NaN_5O$ *m/e*: 400.2108, found: 400.2117.

*2-Methylamino-4-(N,3,5-trimethylphenylamino)-6-(3,5-dimethylphenoxy)-1,3,5-triazine (**11**)*

2-Methylamino-4-mexylamino-6-(3,5-dimethylphenoxy)-1,3,5-triazine (1.00 g, 2.86 mmol) was dissolved in anhydrous DMF (10 mL) in a flame-dried round-bottomed flask equipped with a magnetic stirrer. NaH (60 wt%, 0.172 g, 4.29 mmol) was added, and the mixture was stirred 30 min at ambient temperature until hydrogen evolution had stopped. Iodomethane (0.267 mL, 0.609 g, 4.29 mmol) was slowly added, and the mixture was stirred at ambient temperature for 12 h. Ethyl ether and $H_2O$ were then added, and both layers were separated. The organic layer was recovered, washed with $H_2O$ and brine, dried over $Na_2SO_4$, filtered, and the volatiles were evaporated under vacuum. The product was purified by recrystallization from hot hexanes to give 0.651 g of compound 11 (1.79 mmol, 63 %). $T_g$ 33 °C, $T_c$ 126 °C, $T_m$ 152 °C; FT-IR (ATR/$CH_2Cl_2$) 3421, 3267, 3179, 3140, 3011, 2946, 2918, 2866, 1606, 1576, 1539, 1492, 1427, 1405, 1386, 1358, 1322, 1291, 1266, 1232, 1218, 1191, 1167, 1146, 1132, 1116, 1055, 1033, 999, 977, 950, 931, 907, 888, 846, 810, 736, 695, 685 $cm^{-1}$; $^1H$ NMR (400 MHz, DMSO-$d_6$, 363 K) δ 6.97 (br s, 1H), 6.91 (s, 2H), 6.84 (s, 1H), 6.80 (s, 1H), 6.75 (s, 2H), 3.38 (s, 3H), 2.76 (d, $^3J$ = 4.3 Hz, 3H), 2.26 (s, 12H) ppm; $^{13}C$ NMR (75 MHz, DMSO-$d_6$) δ 170.6, 167.8, 167.3, 166.9, 166.5, 152.7, 152.7, 144.5, 144.4, 138.9, 138.5, 138.1, 137.9, 127.5, 126.6, 124.6, 119.6, 38.0, 27.5, 21.2 ppm; HRMS (ESI, $MNa^+$) calcd. for $C_{21}H_{26}N_5O$ *m/e*: 364.2132, found: 364.2142.

*2-Methoxy-4-(N,3,5-trimethylphenylamino)-6-(3,5-dimethylphenoxy)-1,3,5-triazine (**12**)*

2-Methoxy-4-mexylamino-6-(3,5-dimethylphenoxy)-1,3,5-triazine (1.00 g, 2.85 mmol) was dissolved in anhydrous DMF (10 mL) in a flame-dried round-bottomed flask equipped with a magnetic stirrer. NaH (60 wt%, 0.171 g, 4.28 mmol) was added, and the mixture was stirred 30 min at ambient temperature until hydrogen evolution had stopped. Iodomethane (0.266 mL, 0.608 g, 4.28 mmol) was slowly added, and the mixture was stirred at ambient temperature for 12 h. Ethyl ether and $H_2O$ were then added, and both layers were separated. The organic layer was recovered, washed with $H_2O$ and brine, dried over $Na_2SO_4$, filtered, and the volatiles were evaporated under vacuum. The product was purified by recrystallization from hot hexanes to give 0.640 g of compound 12 (1.76 mmol, 62 %). $T_g$ 8 °C, $T_m$ 129 °C; FT-IR (ATR/$CH_2Cl_2$) 3012, 2952, 2919, 2867, 1607, 1574, 1534, 1468, 1412, 1363, 1321, 1292, 1260, 1228, 1199, 1184, 1146, 1121, 1101, 1055, 1000, 931, 888, 848, 813, 713, 697, 684 $cm^{-1}$; $^1H$ NMR (400 MHz, DMSO-$d_6$, 363 K) δ 6.92 (s, 2H), 6.89 (s, 1H), 6.84 (s, 1H), 6.77 (s, 2H), 3.81 (s, 3H), 3.40 (s, 3H), 2.27 (s, 12H) ppm; $^{13}C$ NMR (75 MHz, DMSO-$d_6$) δ 172.2, 171.8, 167.5, 152.2, 143.6, 138.9, 138.3, 128.2, 128.1, 127.2, 127.0, 124.4, 124.3, 119.5, 119.4, 54.7, 38.4, 38.3, 21.2 ppm; HRMS (ESI, $MNa^+$) calcd. for $C_{21}H_{24}NaN_4O_2$ *m/e*: 387.1791.1642, found: 387.1802.

*SUPPORTING INFORMATION*

To confirm the observed trends in the thermal behavior of compounds **1-12**, analogues **13-15** where both mexylamino ancillary groups are replaced by phenylamino groups were

synthesized in 62-85 % yield from the corresponding bis(phenylamino)chlorotriazines and sodium methoxide in methanol (Scheme II.S1) following a previously published procedure.[1]

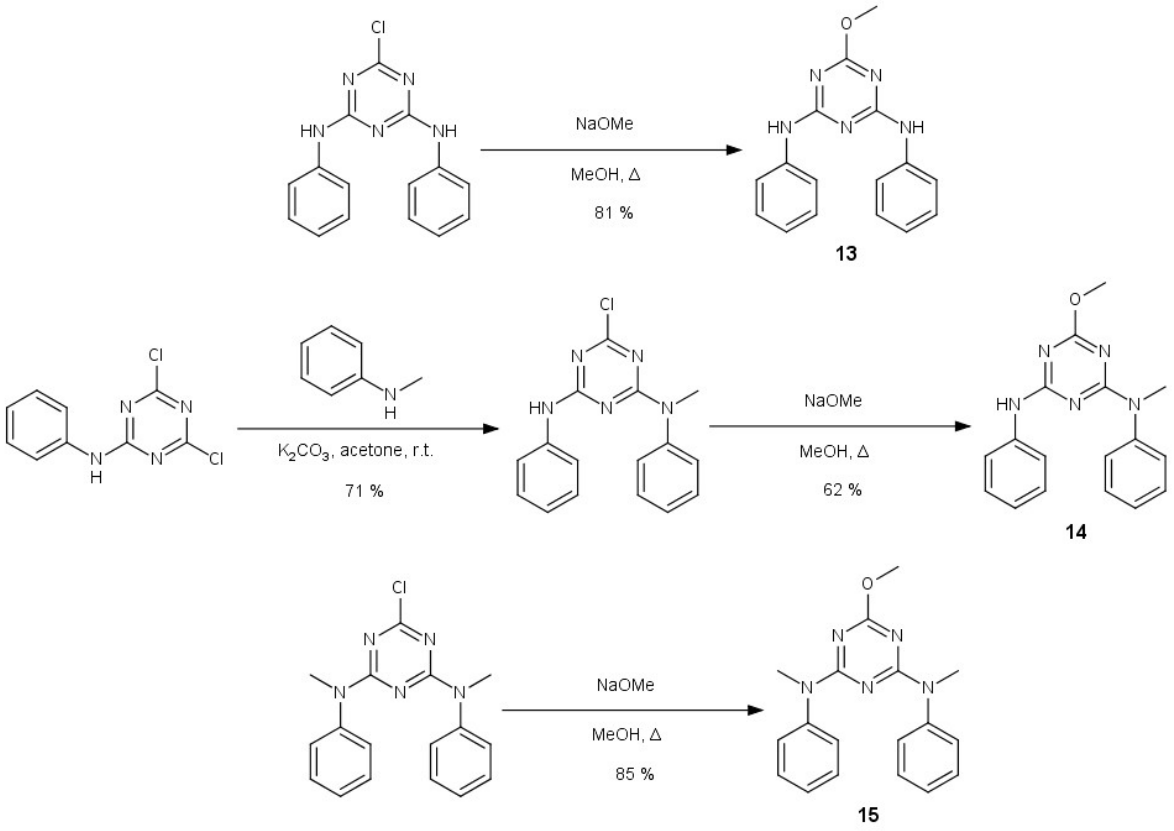


**Scheme II.S1.** Syntheses of compounds 13-15

*2-Methoxy-4-phenylamino-6-(N-methylphenylamino)-1,3,5-triazine (**14**)*

2-Phenylamino-4,6-dichloro-1,3,5-triazine (1.00 g, 4.15 mmol) was dissolved in acetone (20 mL) in a round-bottomed flask equipped with a magnetic stirrer. $K_2CO_3$ (0.574 g, 4.15 mmol) was added, then the flask was placed in an ice bath. A solution of N-methylaniline (0.450 mL, 0.445 g, 4.15 mmol) in acetone (10 mL) was then slowly added at 0-5 $^oC$ under vigorous stirring, after which the ice bath was removed and the mixture was stirred for 18h at ambient temperature, after which $H_2O$ was added. The product was extracted with ethyl ether, the organic layer was washed successively with 1M aqueous HCl, aqueous $NaHCO_3$ and brine, dried over $Na_2SO_4$, filtered, and the solvent was evaporated under reduced pressure. Recrystallization from hot hexanes afforded 0.914 g 2-chloro-4-phenylamino-6-(N-methylphenylamino)-1,3,5-triazine (2.93 mmol, 71 %). $T_m$ 126 °C; FT-IR (ATR/$CH_2Cl_2$) 3393, 3275, 3204, 3166, 3121, 3094, 3061, 3037, 2952, 2929, 2870, 1602, 1574, 1524, 1497, 1446, 1404, 1388, 1353, 1317, 1250, 1228, 1162, 1114, 1097, 1027, 976, 931, 900, 837, 800, 757, 735, 695, 627 $cm^{-1}$; $^1H$ NMR (400 MHz, DMSO-$d_6$, 363 K) δ 9.76 (s, 1H), 7.53 (d, $^3J$ = 7.8 Hz, 2H), 7.47 (t, $^3J$ = 8.1 Hz, 2H), 7.37

(m, 3H), 7.18 (t, $^3J$ = 7.6 Hz, 2H), 6.99 (t, $^3J$ = 7.1 Hz, 2H), 3,48 (s, 3H) ppm; $^{13}$C NMR (75 MHz, DMSO-$d_6$) δ 168.7, 165.5, 163.2, 143.9, 139.1, 129.5, 128.8, 127.3, 127.1, 123.2, 120.1, 38.6 ppm; HRMS (ESI, $MNa^+$) calcd. for $C_{16}H_{14}ClNaN_5$ *m/e*: 334.0835, found: 334.0839.

2-chloro-4-phenylamino-6-(N-methylphenylamino)-1,3,5-triazine (0.814 g, 2.61 mmol) was dissolved in methanol (20 mL) in a round-bottomed flask equipped with a magnetic stirrer and a water-jacketed condenser. A methanolic NaOMe solution (25 wt%, 0.846 mL, 3.92 mmol) was added, and the mixture was refluxed for 18 h. The volatiles were concentrated under vacuum, then $CH_2Cl_2$ and $H_2O$ were added, and both layers were separated. The organic layer was recovered, dried over $Na_2SO_4$, filtered, and the solvent was evaporated under reduced pressure. Recrystallization from hot hexanes afforded 0.494 g of pure compound **14** (1.61 mmol, 62 %). $T_g$ 30 °C, $T_c$ 102 °C, $T_m$ 141 °C; FT-IR (ATR/$CH_2Cl_2$) 3391, 3275, 3191, 3158, 3100, 3061, 3033, 3011, 2994, 2951, 2906, 2868, 1610, 1602, 1577, 1561, 1539, 1494, 1462, 1443, 1405, 1389, 1358, 1299, 1265, 1245, 12010, 1180, 1156, 1120, 1097, 1052, 1028, 989, 961, 901, 853, 810, 756, 736, 694, 670 $cm^{-1}$; $^1$H NMR (400 MHz, DMSO-$d_6$, 363 K) δ 9.17 (br s, 1H), 7.61 (d, $^3J$ = 8.1 Hz, 2H), 7.43 (t, $^3J$ = 8.1 Hz, 2H), 7.37 (d, $^3J$ = 7.1 Hz, 2H), 7.29 (t, $^3J$ = 7.1 Hz, 1H), 7.17 (t, $^3J$ = 8.1 Hz, 2H), 6.94 (t, $^3J$ = 7.3 Hz, 1H), 3.86 (s, 3H), 2.50 (s, 3H) ppm; $^{13}$C NMR (75 MHz, DMSO-$d_6$) δ 170.9, 166.8, 165.1, 144.6, 140.1, 129.2, 128.6, 127.3, 126.4, 122.4, 120.0, 54.1, 38.1 ppm; HRMS (ESI, $MNa^+$) calcd. for $C_{17}H_{17}NaN_5O$ *m/e*: 330.1331, found: 330.1336.

*2-Methoxy-4,6-bis(N-methylphenylamino)-1,3,5-triazine (**15**)*

2-chloro-4,6-bis(N-methylphenylamino)-1,3,5-triazine (1.44 g, 4.43 mmol) was dissolved in methanol (30 mL) in a round-bottomed flask equipped with a magnetic stirrer and a water-jacketed condenser. A methanolic NaOMe solution (25 wt%, 1.44 mL, 6.65 mmol) was added, and the mixture was refluxed for 18 h. The volatiles were concentrated under vacuum, then $CH_2Cl_2$ and $H_2O$ were added, and both layers were separated. The organic layer was recovered, dried over $Na_2SO_4$, filtered, and the solvent was evaporated under reduced pressure and dried thoroughly to yield 1.22 g of compound 15 (3.79 mmol, 85 %). $T_g$ -21 °C; FT-IR (ATR/$CH_2Cl_2$) 3090, 3061, 3035, 3010, 2980, 2948, 2895, 2866, 2808, 2790, 1603, 1561, 1528, 1494, 1477, 1460, 1444, 1385, 1358, 1299, 1270, 1212, 1162, 1105, 1028, 996, 977, 955, 906, 835, 810, 764, 735, 696 $cm^{-1}$; $^1$H NMR (300 MHz, $CDCl_3$, 298 K) δ 7.30 (m, 8H), 7.17 (t, $^3J$ = 7.0 Hz, 2H), 3.78 (s, 3H), 3.45 (s, 6H) ppm; $^{13}$C NMR (75 MHz, $CDCl_3$) δ 170.7, 166.3, 144.3, 128.5, 126.4, 125.5, 53.8, 37.7 ppm; HRMS (ESI, $MNa^+$) calcd. for $C_{18}H_{19}NaN_5O$ *m/e*: 344.1487, found: 344.1493.

*REFERENCE*

1. Lebel, O.; Maris, T.; Perron, M.-È.; Demers, E.; Wuest, J. D., *J. Am. Chem. Soc.* **2006**, *128*, 10372-10373.

# Annexe III: Synthèses – Chapitre 4

*EXPERIMENTAL SECTION*

*2-Dimethylamino-4-phenylamino-6-[(3-formylphenyl)amino]-1,3,5-triazine (**1b**)*

A solution of 2-dimethylamino-4-phenylamino-6-dichloro-1,3,5-triazine (3.41 g, 13.7 mmol) and 3-aminobenzaldehdye diethylacetal (3.47 g, 17.8 mmol) in THF (50 mL) in a round-bottomed flask equipped with a magnetic stirrer and a water-jacketed condenser was refluxed for 18 h, at which point 1M aqueous HCl (20 mL) was added and the reflux was continued an additional 1h. Ethyl ether and $H_2O$ were added, causing a precipitate to form. The precipitate was collected by filtration, washed with $H_2O$ and ethyl ether, then the crude product was recrystallized from hot toluene to give 1.55 g pure compound **1b** (4.64 mmol, 34 %). $T_g$ 51 °C, $T_m$ 178 °C; FT-IR (ATR/$CH_2Cl_2$) 3404, 3286, 3201, 3109, 3057, 2931, 2868, 1693, 1617, 1582, 1547, 1525, 1509, 1496, 1483, 1434, 1418, 1403, 1367, 1318, 1305, 1265, 1231, 1175, 1087, 1062, 996, 976, 897, 805, 787, 753, 735, 691 $cm^{-1}$; $^1H$ NMR (300 MHz, DMSO-$d_6$, 298 K) δ 9.95 (s, 1H), 9.41 (br s, 1H), 9.13 (br s, 1H), 8.45 (s, 1H), 8.02 (br s, 1H), 7.77 (d, $^3J$ = 8.2 Hz, 2H), 7.48 (d, $^3J$ = 5.3 Hz, 2H), 7.25 (t, $^3J$ = 7.6 Hz, 2H), 6.94 (t, $^3J$ = 7.6 Hz, 1H), 3.14 (s, 6H) ppm; $^{13}C$ NMR (75 MHz, DMSO-$d_6$) δ 193.5, 165.6, 164.3, 141.7, 140.6, 137.0, 129.6, 128.8, 125.9, 123.3, 122.1, 120.5, 120.3, 36.4 ppm; HRMS (ESI, $MNa^+$) calcd. for $C_{18}H_{18}NaN_6O$ *m*/*e*: 357.1434, found: 357.1446.

*3-(2-Methylamino-4-mexylamino-1,3,5-triazin-6-yl)aminostilbene (**2a**)*

Benzyltriphenylphosphonium chloride (0.428 g, 1.10 mmol) was dissolved in dry DMF (10 mL) under $N_2$ atmosphere in a dry round-bottomed flask equipped with a magnetic stirrer. NaH (60 wt% in mineral oil, 0.048 g, 1.20 mmol) was added, and the mixture was stirred 45 min at ambient temperature. 2-Methylamino-4-mexylamino-6-[(3-formylphenyl)amino]-1,3,5-triazine **1** (0.458 g, 1.00 mmol) was added, and the mixture was stirred for 18 h at 60 °C under $N_2$ atmosphere, after which the mixture was poured into $H_2O$ and stirred 5 minutes at ambient temperature. The resulting precipitate was collected by filtration, washed with $H_2O$ and redissolved in $CH_2Cl_2$. The solution was dried over $Na_2SO_4$, filtered, and the volatiles were evaporated under reduced pressure. Chromatography on silica using AcOEt/hexanes 1:1 as eluent yielded 0.286 g compound **2a** as a 3:1 mixture of *E*/*Z* isomers that could not be satisfactorily separated (0.677 mmol, 68 %). $T_g$ (*E*/*Z*) 78 °C; FT-IR (ATR/$CH_2Cl_2$) 3411, 3279, 3191, 3081, 3057, 3024, 2973, 2947, 2917, 2866, 1578, 1557, 1513, 1427, 1398, 1360, 1323, 1301, 1241, 1211, 1185, 1167, 1085, 1030, 998, 960, 883, 841, 809, 782, 748, 693 $cm^{-1}$; $^1H$ NMR (*E*, 400 MHz, DMSO-$d_6$, 363 K) δ 8.71 (br s, 1H), 8.53 (br s, 1H), 8.03 (s, 1H), 7.69 (d, $^3J$ = 7.6 Hz, 1H), 7.40 (s, 2H), 7.26 (m, 3H), 7.21 (d, $^3J$ = 7.8 Hz, 2H), 7.15 (s, 2H), 6.62 (s, 1H), 6.61 (d, $^3J$ = 7.1 Hz, 1H), 2.93 (d, $^3J$ = 4.5 Hz, 3H), 2.25 (s, 6H) ppm; $^1H$ NMR (*Z*, 400 MHz, DMSO-$d_6$, 363 K) δ 8.62 (br s, 1H), 8.43 (br s, 1H), 7.71 (d, $^3J$ = 7.8 Hz, 1H), 7.64 (s, 1H), 7.39 (s, 2H), 7.26 (m, 3H), 7.21 (d, $^3J$ = 7.8 Hz, 2H), 7.15 (s, 2H), 6.82 (d, $^3J$ = 7.3 Hz, 1H), 6.62 (s, 1H), 6.62 (s, 1H), 6.51 (br s, 1H), 2.87 (d, $^3J$ = 4.3 Hz, 3H), 2.25 (s, 6H) ppm; $^{13}C$ NMR (75 MHz, $CDCl_3$) δ 166.7, 164.3, 139.5, 138.6, 138.3, 137.9, 137.3, 130.3, 130.1, 128.8, 128.8, 128.6, 128.1, 127.6, 127.1, 126.5, 124.9, 123.2, 121.2, 120.4, 119.4, 119.0, 118.4, 27.7, 21.4 ppm; HRMS (ESI, $MNa^+$) calcd. for $C_{26}H_{26}NaN_6$ *m*/*e*: 445.2111, found: 445.2123.

*SUPPORTING INFORMATION*

*3-(2-Dimethylamino-4-phenylamino-1,3,5-triazin-6-yl)aminostilbene (**2b**)*

The title compound was synthesized from 2-dimethylamino-4-phenylamino-6-[(3-formylphenyl)amino]-1,3,5-triazine **3** (1.55 g, 4.64 mmol) and benzyltriphenylphosphonium chloride (1.98 g, 5.10 mmol) by a procedure similar to the one used for compound **2a**. The reaction mixture was poured into $H_2O$, then the solution was extracted twice with ethyl ether. The organic extracts were washed twice with $H_2O$ and brine, dried over $Na_2SO_4$, filtered, and the volatiles were evaporated under reduced pressure. The crude product was purified by chromatography on silica with AcOEt/hexanes 3:7 as eluent to yield 1.19 g pure compound **2b** (2.91 mmol, 63 %) as a 1:1 mixture of E/Z isomers. A small sample of pure E isomer (approximately 0.100 g) could be separated from the mixture by chromatography using the same conditions. $T_g$ (E) 50 °C; FT-IR (ATR/$CH_2Cl_2$) 3399, 3282, 3202, 3122, 3103, 3081, 3057, 3026, 2954, 2930, 2870, 1598, 1581, 1546, 1524, 1509, 1495, 1421, 1401, 1369, 1308, 1271, 1229, 1177, 1064, 1029, 997, 896, 806, 781, 752, 692 $cm^{-1}$; $^1H$ NMR (E, 400 MHz, $CDCl_3$, 298 K) δ 7.91 (s, 1H), 7.84 (s, 1H), 7.78 (s, 1H), 7.55 (d, $^3J$ = 7.8 Hz, 2H), 7.39 (d, $^3J$ = 7.8 Hz, 2H), 7.39 (s, 1H), 7.22 (m, 6H), 7.08 (d, $^3J$ = 7.6 Hz, 1H), 6.98 (s, 2H), 6.95 (t, $^3J$ = 7.3 Hz, 1H), 3.16 (s, 6H) ppm; $^{13}C$ NMR (E, 75 MHz, CDCl3) δ 165.7, 164.2, 139.9, 139.5, 137.9, 137.4, 129.0, 128.8, 128.7, 127.6, 126.6, 122.7, 121.1, 120.1, 119.3, 117.9, 36.6 ppm; HRMS (ESI, $MNa^+$) calcd. for $C_{25}H_{24}NaN_6$ m/e: 431.1955, found: 431.1973.

*3-(2-Methylamino-4-mexylamino-1,3,5-triazin-6-yl)amino-2',3',4',5',6'-pentafluorostilbene (**3a**)*

The title compound was synthesized from 2-methylamino-4-mexylamino-6-[(3-formylphenyl)amino]-1,3,5-triazine 1 (1.50 g, 4.31 mmol) and 2,3,4,5,6-pentafluorobenzyltriphenylphosphonium bromide (2.48 g, 4.74 mmol) by a procedure similar to the one used for compound **2a**. 1.63 g of pure compound **3a** were thusly obtained after chromatography on silica using AcOEt/Hex 1:1 as eluent (3.18 mmol, 74 %). $T_g$ 78 °C, $T_m$ 204 °C; FT-IR (ATR/$CH_2Cl_2$) 3248, 3278, 3197, 3134, 3019, 2952, 2921, 2866, 1578, 1557, 1519, 1497, 1428, 1398, 1363, 1323, 1300, 1264, 1182, 1168, 1145, 1131, 1084, 1032, 1004, 968, 884, 841, 809, 782, 739, 724, 686 $cm^{-1}$; $^1H$ NMR (400 MHz, DMSO-$d_6$, 363 K) δ 8.75 (br s, 1H), 8.49 (br s, 1H), 8.07 (s, 1H), 7.82 (d, $^3J$ = 7.6 Hz, 1H), 7.37 (s, 2H), 7.32 (d, $^3J_{trans}$ = 16.6 Hz, 1H), 7.31 (s, 1H), 7.20 (d, $^3J$ = 7.1 Hz, 1H), 6.92 (d, $^3J_{trans}$ = 16.6 Hz, 1H), 6.61 (br s, 1H), 6.58 (s, 1H), 2.92 (d, $^3J$ = 3.5 Hz, 3H), 2.24 (s, 6H) ppm; $^{13}C$ NMR (75 MHz, DMSO-$d_6$) δ 166.5, 164.6, 164.3, 146.2, 142.9, 141.4, 140.4, 139.3, 137.8, 137.5, 136.4, 136.0, 129.2, 123.7, 120.8, 118.3, 117.4, 112.5, 112.1, 27.7, 21.2 ppm; $^{19}F$ NMR (400 MHz, DMSO-$d_6$) δ -175.6 (d, J = 21 Hz), -175.7 (d, J = 21 Hz), -189.6 (t, J = 21 Hz), -195.9 (t, J = 21 Hz) ppm; HRMS (ESI, $MNa^+$) calcd. for $C_{26}H_{21}F_5NaN_6$ m/e: 535.1640, found: 535.1659.

*3-(2-Dimethylamino-4-phenylamino-1,3,5-triazin-6-yl)amino-2',3',4',5',6'-pentafluorostilbene (**3b**)*

The title compound was synthesized from 2-dimethylamino-4-phenylamino-6-[(3-formylphenyl)amino]-1,3,5-triazine 3 (1.17 g, 3.49 mmol) and 2,3,4,5,6-pentafluorobenzyltriphenylphosphonium bromide (2.01 g, 3.84 mmol) by a procedure similar to the one used for compound **2a**. The reaction mixture was poured into a mixture of ethyl ether

and $H_2O$, causing a white precipitate to form. The precipitate was collected by filtration, washed abundantly with $H_2O$ and ethyl ether, and allowed to dry to give 0.827 g pure compound **3b** (1.66 mmol, 48 %). $T_g$ 67 °C, $T_c$ 139 °C, $T_m$ 202 °C; FT-IR (ATR/$CH_2Cl_2$) 3427, 3285, 3207, 3126, 3104, 3058, 3032, 2937, 2871, 1619, 1581, 1546, 1520, 1496, 1433, 1418, 1405, 1368, 1337, 1303, 1275, 1229, 1180, 1168, 1144, 1131, 1065, 1031, 1006, 968, 959, 914, 806, 782, 753, 723, 689 $cm^{-1}$; $^1H$ NMR (400 MHz, DMSO-$d_6$, 363 K) δ 8.82 (br s, 1H), 8.72 (br s, 1H), 8.15 (s, 1H), 7.77 (m, 3H), 7.30 (m, 4H), 7.18 (d, $^3J$ = 6.8 Hz, 1H), 6.95 (m, 2H), 3.17 (s, 6H) ppm; $^{13}C$ NMR (75 MHz, DMSO-$d_6$) δ 166.1, 164.6, 146.0, 143.6, 141.5, 140.8, 139.1, 138.3, 136.6, 129.2, 128.6, 122.1, 121.3, 121.2, 120.6, 118.2, 112.9, 112.3, 36.3 ppm; $^{19}F$ NMR (400 MHz, DMSO-$d_6$) δ -175.7 (d, $J$ = 21 Hz), -189.5 (t, $J$ = 21 Hz), -195.8 (t, $J$ = 21 Hz) ppm; HRMS (ESI, $MNa^+$) calcd. for $C_{25}H_{19}F_5NaN_6$ *m*/*e*: 521.1484, found: 521.1505.